Imperial College
London

The Utilisation of Biomass as a fuel for Chemical Looping Combustion

Matthew Edward Boot-Handford

Supervised by: Dr. Paul Fennell and Dr Nick Florin

Department of Chemical Engineering
Imperial College London of Science, Technology and Medicine

Thesis submitted for the degree of Doctor of Philosophy (PhD) to Imperial College London of Science, Technology and Medicine

September 2015

Abstract

Development of a commercially viable carbon capture and sequestration (CCS) technology for fossil fuel power generation is vital if the anticipated effects of global warning are to be avoided. Chemical-looping combustion (CLC) is an indirect combustion process that utilises a regenerable solid oxygen sorbent (oxygen carrier, OC), typically a metal oxide, to transfer oxygen from the combustion air to the fuel such that direct contact between air and fuel is avoided. CLC is a variant on an oxy-fuel carbon capture system that offers the potential for a much lower energy penalty as CO_2 separation is achieved intrinsically such that additional energy-intensive gas separation steps are avoided (Boot-Handford, 2014). Our research focuses on the development and optimisation of OCs for CLC systems using biomass and biomass derived fuels. The development of a CLC process utilising biomass is of particular interest as it has the potential to result in negative CO_2 emissions *i.e.* a net removal of CO_2 from the atmosphere.

Thermochemical conversion of biomass typically results in the formation of significant quantities of refractory tar compounds which are difficult to combust and can lead to reduced fuel conversion efficiencies (Mendiara, 2011). Decomposition of the tars on the surface of the OC can result in severe coking and temporary deactivation. Coking of the OC also limits the overall CO_2 capture efficiency of the process as regeneration of the OC in air produces CO_2 which cannot be captured (Corbella, 2005).

This thesis documents the progress made towards the development of a robust laboratory based system for testing the effects of biomass tars on the long term performance of a chemical-looping combustion process. The work completed in this thesis can be divided into two main areas: the first involved developing optimised fabrication strategies for the production of inexpensive iron-based oxygen carrier particles of high reactivity and robust physical characteristics that could be used in CLC systems utilising biomass as the fuel. The second research focus involved the development of a reactor and analysis protocol for studying the interactions between biomass pyrolysis tars and the cheap, synthetic iron-based oxygen carrier materials.

A range of pure iron oxide and iron oxide supported with 40 wt.% Al_2O_3 oxygen carrier materials were prepared via simple scalable fabrication techniques based on wet granulation for use in CLC systems utilising biomass or gasified biomass as a fuel. The oxygen carrier particles were subjected to rigorous testing using a range of analytical methods to assess their physical and chemical properties and suitability for use in large-scale systems. The effect of fabrication method and alumina precursor material used for producing the supported iron oxide materials were found to have a considerable effect on the physical characteristics and reactivity of the oxygen carrier material.

The reduction kinetics (the rate limiting step in the CLC of gaseous fuels) of the different OC materials prepared in this work were assessed using a thermogravimetric analyser (TGA). A simple particle model based on the concept of effectiveness factor was applied to determine the intrinsic kinetic information. Preparation of the Al_2O_3 supported iron oxide oxygen carrier material using a $Al(OH)_3$ alumina precursor gave the most porous oxygen carrier material with the highest surface area. This oxygen carrier was also the most reactive particularly at temperatures above 973 K and demonstrated very good thermal stability at temperatures up to 1173 K. The activation energy of the oxygen carrier was found to increase from 73 kJ mol^{-1} for the temperature range 823-1073 K to 123 kJ mol^{-1} at temperatures of 1073-1173 K. The increase in the activation energy was attributed to further conversion of Fe_3O_4 to $FeAl_2O_4$ which was more pronounced at the higher temperature range. Here we propose that the formation of $FeAl_2O_4$ was beneficial, acting to enhance the thermal stability, reactivity and oxygen transfer capacity of the iron oxide based oxygen carrier material.

A new 500W laboratory-scale, two-stage fixed-bed reactor for simulating CLC with ex situ solid fuel gasification has been designed and constructed. Preliminary studies of the interactions between OC materials consisting of pure iron oxide and 60 wt.% Fe_2O_3 iron oxide supported on Al_2O_3 and a gas stream produced from the pyrolysis of biomass to emulate a fuel gas containing large quantities of tars were carried out. The presence of both OC materials at 973 K was found to significantly reduce the amount of biomass tars by up to 71 wt.% in the case of the 60 wt.% Fe_2O_3/40 wt.% Al_2O_3 OC material compared with analogous experiments in which the biomass tars were exposed to an inert bed of sand. Exposing the pyrolysis vapours to the oxygen carriers in their oxidised form favoured the production of CO_2. The production of CO was favoured when the oxygen carriers were in their reduced forms. Both oxygen carrier materials were affected by carbon deposition. Carbon deposition was removed in the subsequent oxidation phase with no obvious deleterious effects on the reactivity of the oxygen carrier materials after exposure to the pyrolysis gases and vapours.

Declaration of Originality

I certify, to the best of my knowledge, that the work presented in this thesis is primarily my own and that I am the primary person responsible for the preparation of this manuscript. Any work that was the result of a collaborative effort has been highlighted and acknowledged in the acknowledgments section at the beginning of this thesis.

Matthew Edward Boot-Handford, September 2015.

Copyright Declaration

Acknowledgement

First and foremost I would like to thank my PhD project supervisors Dr Paul Fennell and Dr Nick Florin for their invaluable advice and support whilst I was conducting this research. In particular I'd like to thank Paul for designing, funding and providing me with the opportunity to take on such an interesting, relevant and challenging project. At times, this project was deeply frustrating, at others highly enjoyable but always thoroughly rewarding. Thank you Paul and Nick for giving me the freedom and trust to develop and pursue my own ideas allowing me to truly own the work described in this thesis.

I am sincerely grateful to Dr John Blamey, Dr Zili Zhang, Dr Nigel Paterson and Prof. Rafael Kandiyoti for their massive help and advice while I was designing, constructing and commissioning my reactor. Dr John Blamey and Dr Zili Zhang also deserve a thank you for the assistance they provided when I was writing and troubleshooting both my Matlab data processing and Agilent Vee reactor control codes. An additional big thank you goes to Dr Zili Zhang and Jonson Cao for their help during the early stages of my oxygen carrier particle preparation work. I'd also like mention and thank Erik Tropp for his very kind assistance with some of the particle crushing and SEM work that he did during the later stages of my PhD.

Others that deserve a special thanks include Dr Cesar Berrueco, Dr Esther Lorente, Dr Kairul Rostani, Dr Beatrice Fidalgo and Dr Pedro Arcelus-Arillaga for their assistance (particularly during the early days) with SEC, UVF and GC analysis of my tar samples.

I have also received significant assistance from many of the Chemical Engineering support staff at Imperial College without whom, the completion of my work and PhD thesis would not have been possible. A big thank you goes to Richard Wallington and Tony Meredith of the workshop team; Chin Lang of electronics/electrical workshop; Patricia Carry and Andrew Macy of analytical services; Keith Walker and Ben Kitnash of the Chemical Engineering stores; and Sarah Payne, Susi Underwood, Jessica Baldock and Louise Le Cornu for their administrative support.

To my office buddies Dr Zili Zhang and Dr Tom Hills- it has been an absolute pleasure. I can't thank you enough for all the help, discussions and support you have provided throughout my time at Imperial College and for all those shared experiences that I probably shouldn't mention (but I will)- the countless drinking sessions, the trip to China (and the silver suits), the missed airplane and night spent in Frankfurt airport, the Chinese club incident, Boujis…

I'd also like to thank the rest of my friends and colleagues (past and present) at Imperial College for making my time at Imperial College so enjoyable and memorable (in no particular order): Felix Donat, Dr Charles Dean, Dr Kelvin Okpoko, Dr Belen Gonzalez Garcia, Dr Danlu Tong, Xin Zhou, Joe Yao, Peter Clough, Eneritz Fernandez Puertas, Clementine Chambon, Vivi Filipousi, Florence Gschwend, Dr Anthe George, Dr Jason Hallett, Dr Niall MacDowell, Dr Jose Bermudez Menendez, Dr Tomás

Ramirez Reina, Dr Mario Villanueva, Javier Remón Núñez, Xiangyi Long, Dr Liya Zheng, Dr Anastassia Sivena, Dr Salman Masoudi Soltani, Dr Jie Yu, Johnny Ball, Lorena Souza, Dr Elaine Virmond and Dr Michelle Di Domenico. My sincerest apologies if I have missed anyone.

I would like to thank my family and friends (outside of Imperial) for all of the support, encouragement and love they have given and for sticking with me throughout this rather long and all-consuming ordeal. To my mum Pip, my dad Ray, my brothers Rob and Chris, my sister in-law Sarah, Amy (Chris's girlfriend), grandma Joyce, grandad Bob and my friends Ben, James (Scouse), Elisah and Dan (Parky)- thank you so much, I love you all.

Last but not least, I'd like to give the biggest thank you to my fiancée and future wife Laura. Thank you for all the love, generosity and patience you have shown me. I don't deserve you but I am so happy that you have stuck with me throughout these very tough few years. I love you very much and will endeavour to spend much more time with you in the future and be the best husband I can be.

Best wishes to you all,

Matt Boot-Handford
September 2015

Table of Contents

Nomenclature

A_o	Pre-exponential factor	(m^3 s^{-1} g^{-1})
Ar_i	Relative atomic mass of species '*i*'	-
$C_{char,g}$	Carbon content of the char	(wt.%)
D_b	bulk, gas phase diffusion coefficient	(m^2 s^{-1})
D_{eff}	Effective diffusivity within a porous particle	(m^2 s^{-1})
D_H	Hydrodynamic diameter of a tube	m
D_K	Knudsen diffusion coefficient	(m^2 s^{-1})
D_p	Pore diameter	nm
$E_{a,\,i}$	Activation energy calculated from the intrinsic rate constants (k_i)	(kJ mol^{-1})
$E_{a,\,obs}$	Activation energy calculated from the observed rate constants (k_o)	(kJ mol^{-1})
$\Delta H_T^{\ominus}$	Standard enthalpy of reaction at T = T K and 1.01 bar_a	(kJ mol^{-1})
K_{eq}	Equilibrium constant	(s^{-1})
M_{Act}	Actual mass of oxygen carrier	(g)
M_{ox}	Mass of oxidised oxygen carrier material	(g)
M_{Red}	Mass of reduced oxygen carrier material	(g)
Mr_i	Relative molecular mass of species *i*	-
N_{Bi}	Biot number, $N_{Bi} = hR/3\lambda_e$	-
N_i	Flux a gaseous species 'i' within a porous particle	(mol s^{-1})
Nu	Nussult number, $Nu = hd_p/\lambda_{mix}$	-
P	Total system pressure	(bar_a)
P_i	Partial pressure of species 'i'	(bar_a)
$Q_{out,s}$	Total flow at exit of reactor at standard conditions (i.e. 1.01 bara, 293 K)	(ml s^{-1})
R	Spherical particle radius	(m)

R	Ideal gas constant	(J mol^{-1} K^{-1})
R_e	Reynold's number for the flow of gas through a cylindrical tube, $Re_D = (\rho_g U D_H) / \mu$	-
R_{max}	Normalised maximum char reactivity	(s^{-1})
R_o	Theoretical oxygen mass ratio of oxygen carrier material	-
Sc	Schmidt number, $Sc = \mu / (\rho_g D_b)$	-
T	Absolute temperature	(K)
T_b	Bulk temperature of the bulk fluid	(K)
T_m	Melting temperature	(K)
T_{Tammen}	Tammen temperature	(K)
U	Volumetric flow rate	(m^3 s^{-1})
V_p	Volume of pores	(cm^3)
Sh	Sherwood number $Sh = 0.91Re^{0.49}Sc^{0.33}$	-
W_{char}	Weight of char	(g)
W_o	Initial weight of char	(g)
X	Fractional conversion (oxidation extent) of oxygen carrier material	-
ΔX	Conversion difference of oxygen carrier material (between the air reactor and fuel reactor)	-
X_{AR}	Average fractional conversion of oxygen carrier in the air reactor	-
X_{FR}	Average fractional conversion of oxygen carrier in the fuel reactor	-
c_i	Concentration of gaseous species 'i' within a porous spherical particle	(mol m^3)
$c_{i,S}$	Concentration of gaseous species 'i' at the surface of the particle	(mol m^3)
c_v	Coefficient of variance	-
d_p	Particle diameter	(m)
H	convective heat transfer coefficient of the fluid	(W m^{-1} K^{-1})

$k_{g,i}$	External mass transfer coefficient for the bulk gas phase	(m s^{-1})
k_i	Forward intrinsic rate constant for the reaction of CO with Fe_2O_3	(s^{-1})
k_o	Observed (or overall) rate constant for the forward reaction between CO and Fe_2O_3	(mol s^{-1} g^{-1})
N	reaction order	-
r'	Rate of reaction per unit mass of Fe_2O_3	(mol s^{-1} g^{-1})
R	radial position within a particle	(m)
r_e	Pore radius	(m)
T	Time	(s)
U	Atomic unit	-
$\bar{x}$	Average (mean) value	-
$x_{C,char}$	Mass fraction of C in char	-
x_i	Mole fraction of species i	-

Greek symbols

Υ_i	Gas yield of species ‘i’	-
μ	Dynamic viscosity	(kg m^{-1} s^{-1})
ε_{Fe2O3}	Porosity of Fe_2O_3 component of the oxygen carrier particle	-
H	Effectiveness factor for a spherical particle	-
λ_e	thermal conductivity of the solid (*i.e.* Fe_2O_3)	(W m^{-1} K^{-1})
λ_{mix}	thermal conductivity of the fluid (calculated using the Chapman-Enskog model)	(W m^{-1} K^{-1})
ρ_{Fe2O3}	Envelope density of the Fe2O3 component of the particle	(kg m^{-3})
ρ_g	Gas density	(kg m^3)
Σ	Standard deviation	-
$\sigma_{(1,2)}$, $\varepsilon_{(1,2)}$	Force constants in the Lennard-Jones potential function for a binary gas mixture	(K)
Τ	Tortuosity factor	-
Φ	Thiele modulus for an irreversible reaction	-
$\Omega^{(1,1)*}$	Collission integral between 2 molecules of gas species 1	(kg s^D m^{-3} m^{-D} s^{-1})

Abbreviations

BECCS	Bio-energy with carbon capture and storage
BET	Brunauer-Emmett-Teller (surface area)
BJH	Barrett-Joyner-Halenda (porosity)
BRH	Brazilian rice husk
BW	Beech wood
CCS	Carbon capture and storage
CLC	Chemical-looping combustion
CLC	Chemical-Looping Combustion
CLOU	Chemical-looping with oxygen uncoupling
CLR	Chemical-Looping Reforming
DFB	Dual-fluidised bed
EIA	Energy Information Administration (U.S.A)
HAT	Humid air turbine
HHV	Higher heating value
ID	Internal Diameter
IEA	International Energy Agency
IGCC	Intergrated gasification combined cycle
IPCC	Intergovernmental Panel on Climate Change
LHV	Lower heating value
LLGHG	Long-lived greenhouse gas
MEA	Monoethanolamine
MIP	Mercury Intrusion Porosimetry
MFC	Mass Flow Controller
MSW	Municipal solid waste

NAA	Neutron activation analysis
NB	Nominal Bore
NMP	n-methyl-2-pyrolidinone
OC	Oxygen carrier
OD	Outer Diameter
PC	Pulverised coal
PID	Proportional-Integral-Derivative (feedback control mechanism)
RETs	Renewable Energy Technologies
SEC	Size exclusion chromatography
SEM	Scanning Electron Microscopy
SER	Sorbent Enhanced Reforming
TCD	Thermal Conductivity Detector
TGA	Thermogravimetric analyser
TIR	Textile industry residue
TIT	Turbine inlet temperature
TRH	Thai rice husk
UV	Ultraviolet
UVF	Ultraviolet fluorescence (spectroscopy analysis)
XRD	X-ray diffraction analysis
XRF	X-ray fluorescenece analysis
Ar	As received
daf	Dry, ash-free basis
Db	dry basis

List of Figures

List of Tables

Chapter 1

Introduction

1.1 Background

Global primary energy consumption has increased by around 165 % since 1970; yet the way in which energy is generated remains predominantly unchanged (BP, 2015). Fossil fuels are used to supply more than 85 % of the global energy demand for reasons that fossil fuels are a cheap, efficient, and reliable source of energy. However increased fossil fuel use due to growing global energy demands has resulted in a 125 % rise in energy related CO_2 emissions during the same period with emissions reaching an all-time high of 32.4 Gt-CO_2 in 2013-2014 (IEA, 2015) with total annual CO_2 emissions from fossil fuel combustion, cement production and flaring of 34.8 GtCO_2/yr in 2011 (Pachauri et al., 2014). The IEA projects, assuming moderate population growth and strong economic growth in the developing world, that the global primary energy demand will increase a further 20 % by 2030. Assuming that the COP21 countries stick to their nationally determined CO_2 contribution pledges, energy related CO_2 emissions will rise by 8 % to 34.8 Gt-CO_2/yr.

At present, CO_2 emissions from fossil fuel combustion for the production of energy and industrial processes account for ~78 % of total anthropogenic CO_2 emissions and represent the main source of increased levels of atmospheric CO_2 (Pachauri et al., 2014). Energy related emissions include emissions arising from electricity, heat and fuel use by the industrial, commercial, public, domestic and transport sectors (IEA, 2010b). Other significant sources of anthropogenic CO_2 emissions include land use changes (deforestation) and industrial processes; such as the calcination of limestone for cement manufacture, the use of coke in the iron and steel industry for the extraction of iron from ores and chemical production (IPCC, 2005).

Increasing anthropogenic emissions has caused the atmospheric concentration of CO_2 to rise from a pre-industrial concentration of 280 ppm to 390 ppm in 2011 with a marked increase in growth rate to ~2ppm/year observed over the last 60 years in line with the increasing global energy consumption (Pachauri et al., 2014). There is now substantial evidence that this increase in atmospheric CO_2 is the primary driver of global heating. Emissions of other long-lived greenhouse gases (LLGHG) such as CH_4, N_2O, SF_6 also contribute, but to a lesser extent. Total atmospheric concentrations of all the major LLGHGs was 430 ppm CO_2-eq in 2011.

Elevated levels of atmospheric LLGHGs have already caused the average global combined land and sea surface temperature to rise by 0.85 °C over the period ranging from 1880 to 2012 (Pachauri et al., 2014). Although this temperature rise is considered to be within the tolerable range; further heating in excess of 2 ˚C above pre-industrial temperatures (upper safe limit for heating as defined by Pachauri et al. (2014)), is potentially devastating and irreversible. The consequences would include increased melting of glaciers, ice caps and sea ice which would cause sea levels to rise further and at a faster rate. If all sea ice were to melt; at least 4 million km^2 of land currently home to 5% of the World's population could be lost to the sea (Stern, 2006). Rising sea levels will also intensify constraints on water supplies in coastal areas due to salination of groundwater and underground reservoirs. Furthermore, global heating will affect local and continental weather systems causing more frequent and intense extreme weather events such as droughts, flooding, cyclones and heat waves. Ultimately, this will lead to a loss of arable and currently populated land, food and water shortages, ocean acidification, significantly reduced biodiversity, increased human mortality rates due to malnutrition, changes in infectious disease vectors and mass migration on a scale unprecedented in human history. The effects of climate change will affect the third world and poorest communities hardest- the people least equipped to adapt to global and local climatic changes and who ironically are the least responsible for anthropogenic climate change.

It is clear that if the anticipated effects of climate change are to be avoided, a significant global effort is required to reduce CO_2 emissions. The IPCC in its fifth assessment report recommends that global CO_2 emissions should to be reduced by 40-70 % of the 2010 emissions before 2050 to stabilise the atmospheric CO_2 concentration between 350-400 ppm (445-490 ppm-CO_2eq) and limit heating to 2 °C or less (IPCC, 2014).

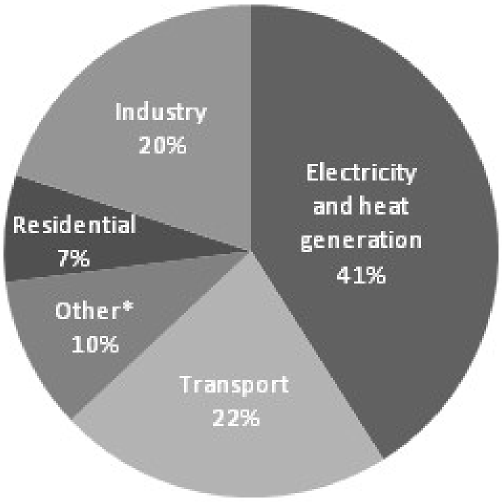

Figure 1.1: Global CO_2 emissions by sector in 2008 (IEA, 2010b).

*Other includes commercial/public services, agriculture/forestry, fishing, energy industries other than electricity and heat generation, and other emissions not specified elsewhere.

As can be seen in figure 1.1, electricity and heat production is responsible for the largest contribution to global CO_2 emissions; therefore cutting/eliminating emissions related to this sector is essential. Below is a brief summary of the different approaches for reducing CO_2 emissions from this sector (IPCC, 2005).

- Substituting fossil fuel power stations for zero carbon alternatives such as renewable energy technologies (RETs) including wind turbines, solar photovoltaics, concentrating solar power, geothermal and hydroelectric generators or low carbon alternatives such as nuclear.
- Substituting fossil fuels for sustainable biomass such as forestry and agricultural residue and municipal solid waste (MSW).
- Substituting fossil fuels with a high carbon content for one with a lower carbon content e.g. coal for natural gas.
- Improving the efficiency of the power generation process and the transmission system.
- Reduce electricity and heat demand by improving the energy efficiency of the technologies that consume the electricity, improving insulation in building and educating consumers to use energy more efficiently.
- Carbon capture and sequestration (CCS) - capturing CO_2 from the flue stream of power stations and storing it in deep geological formations.

Whilst the complete substitution of fossil fuels for RETs, nuclear and sustainable biomass is the ultimate goal, the fact remains that fossil fuels are the cheapest (if the costs associated with the negative environmental impacts are not accounted for) and most reliable source of energy. Growing energy demands in the developing world and an increased use of fossil fuels is likely to overwhelm improvements in energy intensity and carbon intensity arising from efficiency savings and substitution of coal to natural gas power generation (approaches iv and v) (EIA, 2011). Therefore, the development of a commercially viable carbon capture and storage system in the next 1 to 2 decades is crucial if the required CO_2 emissions reductions are to be achieved whilst meeting growing global energy demands (IPCC, 2014).

1.2 Carbon Capture and Storage

Carbon capture and storage is a multi-step process that involves separating CO_2 from the flue streams of large point source emitters such as power plants and large industrial processes, compressing, and then transporting the captured CO_2 to a suitable storage site where it is injected into geological formations deep underground or under the seabed (Boot-Handford et al., 2014). In 2000, emissions from large (> 0.1 $GtCO_2$/yr) point sources suitable for integration with CCS amounted to ~ 45 % of global CO_2 emissions (IPCC, 2005). The increased use of centrally produced energy vectors such as electricity and hydrogen by distributed and mobile CO_2 sources in place of fossil fuels is expected to further increase the proportion of global CO_2 emissions that can be mitigated using CCS. In addition, the integration of CCS with biomass power generation (BECCS) could potentially result in negative CO_2 emissions as the CO_2 produced and subsequently stored in biomass CCS is equal to the amount of CO_2 removed from the atmosphere by the biomass during photosynthesis. This approach may become increasingly practiced, particularly if mitigation efforts fall short of targets and atmospheric LLGHG concentrations reach dangerous levels or take a trajectory towards stabilisation at dangerous levels (as they already are). Co-firing of biomass with coal is already commonly practised by the power generation sector as it reduces fuel costs and the carbon intensity of the plant (IEA-ETN, 2010b). At present, it is possible to substitute 10-20% (in energy content) of the coal in PCC or IGCC plants for biomass without significantly affecting the plant operation (IEA-ETN, 2010a). Co-firing at CCS integrated power plants can help to reduce the carbon intensity of the plant further by offsetting fugitive emissions. The IPCC (2007) projects that by 2050, CO_2 emissions reductions of 21-45 % could be achieved through the integration of CCS technology with power stations and large scale industrial processes.

CO_2 capture is the most energy intensive and therefore most expensive component of the CCS chain. Current CO_2 capture technologies are able to capture between 85-95 % of the CO_2 produced from power stations; however processes equipped with CCS require between 10-40 % more energy than an equivalent process without CCS (IPCC, 2005). The extra CO_2 generated as a consequence of the extra fuel consumption has the effect of lowering the CO_2 capture efficiency to 80-90 % for a constant power output. It is estimated that CO_2 capture with currently commercial CCS technologies would increase the cost of electricity by between 20-85 % (IPCC, 2005). As a result a significant research effort is being invested in the development of less energy intensive, more efficient and therefore cheaper CO_2 capture processes.

Chemical-looping combustion (CLC) is one such technology, in which a regenerable solid sorbent (oxygen carrier, OC), typically a metal oxide is used to transfer oxygen from the combustion air to the fuel such that direct contact between the air and the fuel is avoided. As a consequence two flue streams are generated, one comprising of oxygen depleted air, the other, CO_2 and H_2O. Cooling of the combustion flue stream causes the water vapour to condense out yielding a near-pure stream of CO_2 for sequestration. The summation of the enthalpies of oxygen carrier oxidation (in air) and oxygen carrier reduction (by the fuel) is equal to the enthalpy of fuel combustion. Hence CO_2 separation is achieved without the energy penalty typically associated with CO_2 capture.

1.3 Project aims and objectives

Most CLC research has focused on gaseous fuels and extended pilot scale trials have demonstrated the feasibility of natural gas CLC for large scale power generation (Lyngfelt, 2011), however CLC of solid fuels is more complex and less well understood. Solid fuels need to be gasified first since direct reactions between the solids do not take place at an appreciable rate. The gasification step can either be carried out in-situ in the fuel reactor or ex-situ in a separate gasifier prior to the fuel reactor. The gas produced from the gasification of solid fuels typically contains much higher quantities of problematic impurities (compared with natural gas) such as particulates (unreacted char and ash), tar vapours, alkali compound vapours and sulphur and nitrogen containing compounds such as H_2S, NH_3 and HCN. Tars are particularly problematic when considering biomass as a fuel since biomass gasification tends to produce a gas containing much larger quantities of tars (typically 0.1-10 wt.% of initial biomass weight) compared with coal.

The development and commercialisation of biomass gasification processes is particularly hindered by the presence and interfering nature of tar. Tar can condense and deposit in pipelines and downstream processing equipment causing clogging and blockages in both the technology used to convert biomass and the engines, gas turbines and fuel cells that burn the fuel gas to generate energy. Tar is a greater problem for more advanced technologies such as fuel cells that have very low tolerances < 80 ppb tar contamination. Biomass tar is also highly acidic (typical pH < 2) which means that its presence can lead to a whole range of corrosion related problems.

In the context of CLC, tar formation is of particular concern as it is difficult to combust and can lead to reduced fuel conversion efficiencies (Mendiara *et al*., 2011). In addition, decomposition of the tars on the surface of the OC can result in severe coking and temporary deactivation. Coking of the OC also limits the overall CO_2 capture efficiency of the process as regeneration of the OC in air produces CO_2 which cannot be captured (Corbella *et al.,* 2005). However, to date, research focussing on the potential utilisation of biomass as a fuel for chemical-looping processes and the effects tar may have on the CLC process is limited. The overarching aim of this project was to develop a robust system to investigate the effect and fate of tar compounds in chemical looping combustion systems using iron-based oxygen carrier materials. In order to achieve these aims, the following experimental objectives were set:

- Design, construct and implement a new 2-stage fixed-bed reactor for studying the discrete interactions between biomass tars and CLC oxygen carrier materials. The reactor was an upgraded version of a pre-existing 2-stage, fixed-bed reactor the reactor. The design was modified to allow for experiments simulating a chemical-looping combustion of solid fuels process with ex situ gasification of biomass to be conducted. Biomass was pyrolysed in the first stage, generating a simulated fuel gas (containing large quantities of tars) for use in the 2nd stage packed with an oxygen carrier bed. Ensuring the oxygen carrier particles, and chars and ash were kept separate allowed more accurate measurement of the discreet interactions that took place between tars and the oxygen carriers.

- Develop and optimise cheap, scalable fabrication strategies for the production of low-cost, highly reactive and robust iron-based oxygen carrier materials for use in CLC systems employing biomass or gasified biomass as a fuel.
- Develop a rigorous testing protocol for the assessment of the different oxygen carrier materials produced in this work to determine their physical and chemical properties and suitability for use in large-scale systems.

1.4 Thesis outline

Chapter 2 provides a literature review of recent developments in the area of CLC and solid fuel utilisation. The chapter begins by introducing the concept of chemical-looping combustion for integrated power generation and CO_2 capture. A brief description of the main problems associated with CLC of solid fuels is then presented which is followed by sections that discuss process and oxygen carrier development for the purpose of chemical-looping combustion of solid fuels. The final section discusses how common contaminants produced during the combustion and gasification of solid fuels effect the CLC process and oxygen carrier performance.

Chapter 3 reports and discusses the results from experimental investigations into the effects of biomass type, elevated temperatures (973-1173 K) and presence of cheap potentially catalytic solid material on the product distribution from the slow pyrolysis of biomass. This work was carried out as part of the initial training into: (i) the operation of high-temperature hot-rod reactors; (ii) procedures for conducting biomass pyrolysis experiments to achieve repeatable results; (iii) protocols for treating and isolating pyrolysis tars; and (iv) protocols for handling and analysing the pyrolysis tars and other recoverable pyrolysis products. It was also the intention to use the experience gained conducting the preliminary work discussed in chapter 3 to assess the suitability of the pre-exisitng 2-stage fixed-bed reactor for studying interactions between biomass tars and chemical-looping oxygen carriers at conditions relevant to large scale CLC systems.

Chapter 4 discusses the limitations with the pre-existing 2-stage fixed-bed reactor and describes how the upgraded reactor was designed to overcome these limitations such that it was capable of being used for studies into the effects of biomass tars on the chemical-looping process and oxygen carrier materials. Biomass pyrolysis commissioning experiments are also presented, discussed and compared with the results from the existing reactor.

Chapter 5 explores the development and optimisation of fabrication strategies based on wet granulation for the production of cheap, highly reactive and mechanically robust iron oxide-based oxygen carrier materials for CLC systems utilising biomass or gasified biomass as a fuel. A rigorous testing protocol was established to assess the physical and chemical properties of the synthesised oxygen carrier materials and their suitability for use in large-scale systems. The reduction kinetics (the rate limiting step in the CLC of gaseous fuels) of the different OC materials prepared in this work were assessed using a thermogravimetric analyser (TGA). A simple particle model based on the concept of effectiveness factor was applied to determine the intrinsic kinetic information.

Chapter 6 presents preliminary experimental work investigating interactions between iron oxide-based oxygen carrier materials and biomass tars in the upgraded 2-stage, fixed-bed reactor. The effect of exposing volatile biomass pyrolysis products to iron-based oxygen carrier materials loaded into the 2nd stage on the product distribution, carbon deposition and reactivity of the OC material after exposure are discussed.

Chapter 7 provides a summary of conclusions and suggestions for further work.

Chapter 2

Literature Review

2.1 Chemical-Looping Combustion

Chemical-looping combustion (CLC) is a flameless combustion process that intrinsically generates a flue stream of near-pure CO_2 circumventing the need for expensive and energy intensive gas separation processes. It is expected that CO_2 capture efficiencies of 98 % could be achieved from a CLC power plant (Boot-Handford et al., 2014). This would be a significant improvement on current state of the art CO_2 separation technologies which have capture efficiencies in the range of 80-90 %.

In a CLC process, direct contact between fuel and air is prevented; instead a solid oxygen carrier, typically a metal oxide, is used to transfer oxygen from air to the fuel (eq. 2.1). Oxidation of the oxygen carrier in air is always exothermic, whilst reduction of the oxygen carrier by the fuel can be either exothermic or endothermic and will depend on the type of oxygen carrier and fuel used. The overall enthalpy change for the oxidation and reduction components of a CLC process is equal to the enthalpy of combustion of the fuel in the traditional manner.

$$(2\mathrm{n} + \mathrm{m})\mathrm{MeO} + \mathrm{C_nH_{2m}} \Rightarrow (2\mathrm{n} + \mathrm{m})\mathrm{Me} + \mathrm{mH_2O} + \mathrm{nCO_2} \qquad \text{(Equation 2.1)}$$

Where MeO is the oxidised form of metal oxide and Me is the reduced form of metal oxide

The most established chemical-looping combustor configuration involves two fluidised bed reactors (a fuel reactor and an air reactor) which are interconnected to allow continuous cycling of the oxygen carrier between the reactors (fig. 2.1). This configuration is also known as a dual-fluidised bed (DFB) chemical-looping combustor. Gaseous fuels are used to fluidise the oxygen carrier bed in the fuel reactor. The fuel is oxidised by the oxygen carrier generating a flue stream of CO_2 and steam. Cooling of the fuel reactor flue stream causes the steam to condense out yielding near pure CO_2 for sequestration. The reduced oxygen carrier is transferred to the air reactor where it is re-oxidised. The air reactor is operated as a high velocity riser providing the driving force for particle circulation. The volumetric flow of gas into the air reactor is typically 10 times higher than the flow of gaseous fuel into the fuel reactor which is operated as a bubbling fluidised bed (Lyngfelt et al., 2001). The oxygen carrier particles are entrained in the air flow and transported up through the reactor to the exit. The oxygen carrier particles are separated from the air reactor flue stream (consisting of oxygen-depleted air) by a cyclone situated at the exit of the air reactor and recycled back into the fuel reactor. In the case where fuel oxidation is endothermic, the heat conveyed by the circulating solid is used to maintain the temperature in the fuel reactor. Complete oxidation/reduction of the oxygen carrier during the CLC process is not necessarily achieved neither is it essential. Loop seals fluidised with steam prevents the crossover of gases between the two reactor fluidised beds.

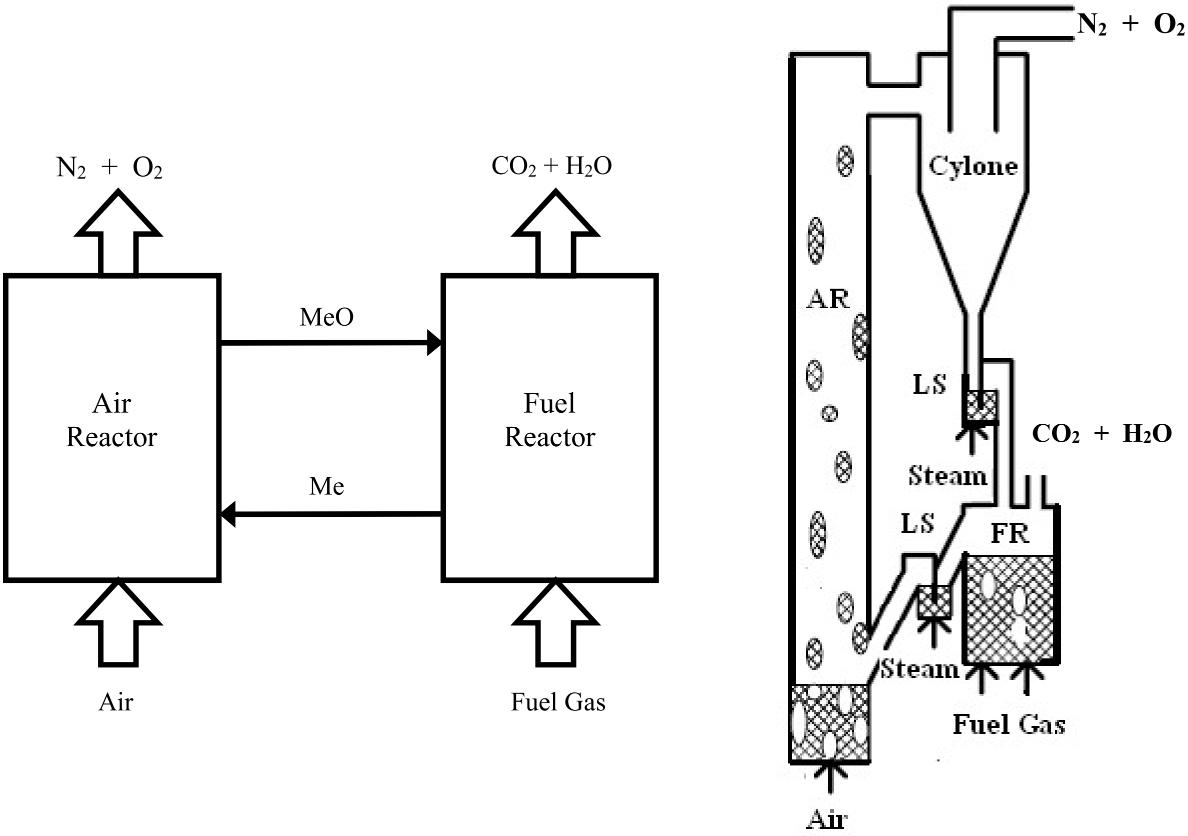

Figure 2.1: **Left**: The chemical-looping combustion process where Me and MeO denotes the circulating metal and metal oxide particles (Lyngfelt et al., 2001). **Right**: Schematic of a dual fluidized bed chemical-looping combustion reactor. Where AR is the air reactor, FR is the fuel reactor and LS is loop seal.

It is also possible to use a single fluidised bed (Dennis and Scott, 2010) or packed bed reactor (Noorman et al., 2007) configuration for CLC where the gas inlet is periodically alternated between air and the fuel (for more details see section 2.3).

Chemical-looping combustion was first proposed in a patent by Lewis and Gilliland (1954) as a means for producing pure CO_2 from carbonaceous materials using metal oxides as the oxidising agent. The application of CLC as a more efficient method for the combustion of carbonaceous fuels for power generation was later proposed in 1983 by Richter and Knoche (1983). Thermodynamics state that in order to obtain the maximum amount of work from a chemical reaction, the process has to be reversible i.e. at equilibrium. Due to the limitations of the materials used for combustors and turbines, combustion temperatures are restricted to ≤ 1200 °C (Ishida et al., 1987). This is significantly lower than the temperatures required for reversible combustion and as a result the process is highly irreversible with considerable exergy destruction due to increased entropy generation. For a CLC process where the enthalpies of oxidation and reduction of the metal oxide are exothermic, the thermal energy is released in two steps at intermediate temperatures, reducing the irreversibly of combustion and the associated exergy destruction. In the case where reduction of the metal oxide is endothermic, the fuel reactor can be utilised as a heat sink for recovering low temperature heat in the exhaust gases so that more high temperature heat can be generated in the air reactor per unit of fuel. In both cases CLC offers an enhanced power generation efficiency compared to conventional single cycle combustion power generation (Richter and Knoche, 1983). However, when comparing CLC power generation to modern power stations utilising improved heat integration systems, more efficient turbines and combined cycle power generation processes, the efficiency enhancement offered by CLC is marginal (Anheden and Svedberg, 1998).

Today, chemical-looping combustion receives attention due to its potential as a power generation process that inherently separates CO_2 from the other flue gases without imposing a severe energy penalty on the power generation process. Wolf et al. (2005) performed an exergy analysis to compare the electrical efficiencies of 800 MW natural gas power stations based on a conventional combined cycle combustion process, a combined cycle CLC process and a conventional combined cycle combustion process with a near-commercial MEA absorption process for CO_2 capture. For the processes that include CO_2 capture, compression of the CO_2 to 150 bar for sequestration was included in the analysis. The MEA absorption process is reported to have a CO_2 capture efficiency of 80-90 % and imposes an 8-10 % point penalty on the electrical efficiency of the power plant. Wolf et al. reported electrical efficiencies of 52-53 % could be achieved by a combined cycle CLC plant employing NiO/Ni or alumina supported Fe_2O_3/FeO as oxygen carriers, operating at 13 bar with an air reactor temperature of 1200 °C. This was found to be 2 % points lower than the conventional combustion combined cycle process, but at least 5 % points higher than the combined cycle combustion process with state of the art MEA absorption technology for CO_2 capture. These findings are consistent with other exergy analyses by Brandvoll and Bolland (2004) who reported that an efficiency of 55.9 % could be achieved using a natural gas CLC plant with humid air turbine (HAT) operated at 20 bar with an air reactor outlet temperature/turbine inlet temperature of 1200 °C. This study did not take into account exergy losses due to compression of the CO_2 for sequestration, which is assumed to lower the efficiency by ~ 2 % points.

Anheden and Svedberg (1998) compared exergetic efficiencies of conventional combustion and CLC power generation processes using coal syngas as the fuel. They found that the efficiency of a CLC power plant using Fe_2O_3 as an oxygen carrier was higher than that of a conventional combustion power plant or CLC power plant with NiO/Ni as the oxygen carrier. However, this study only considered single cycle gas turbine energy generation. The physical exergy lost in the exhaust of the conventional combustion power plant and CLC power plant using the Ni/NiO oxygen carrier was larger than that of the CLC power plant using Fe_2O_3/FeO as an oxygen carrier. They concluded that similar efficiencies could be achieved by all processes if the exergy in the exhaust was efficiently recovered using a combined cycle or advanced turbine such as an evaporative gas turbine or HAT.

Like Brandvoll and Bolland's exergy analysis, this study did not take into account exergy losses due to compression of the CO_2 stream for sequestration. Further exergy penalties may also be imposed on the power generation process if additional gas conditioning steps are required. Coal syngas often contains a higher concentration of impurities than natural gas (BP, 2011) and these impurities may have to be removed prior to or post CLC to prevent poisoning of the oxygen carrier, and to ensure safe, efficient transport and storage/reuse of the captured CO_2. As a consequence, it is likely that the exergy losses from a CLC power generation process using coal syngas as a fuel would be slightly greater than if natural gas was to be used.

All of the discussed exergy studies found that the turbine inlet temperature (TIT)/air reactor outlet temperature had a significant effect on the efficiency of the CLC process. If the air reactor temperature was limited to $\leq$ 1000 °C due to the thermal instability of the oxygen carrier, the efficiency of the CLC process would be reduced a further 5 % points (Wolf et al., 2005). A potential solution to this would be top firing to increase the turbine inlet temperature to 1200 °C, however the CO_2 released as a consequence cannot be captured and the CO_2 capture efficiency would be reduced. It is therefore highly desirable that oxygen carriers have high thermal stabilities that can withstand temperatures $\geq$ 1200 °C. Increasing the process pressure was also found to offer enhanced efficiencies although above 20 bar, Brandvoll and Bolland found that the further efficiency improvements were cancelled out by the increased energy consumed by gas compression. It should however be noted that the exergy studies discussed above do not detail specific reactor designs, therefore, the efficiencies quoted may not be achievable on a commercial scale.

In the EU project ENCAP, an initial design for a 455 MWe CLC natural gas power plant has been proposed with the potential of an energy penalty of ~ 4.5 % compared with a reference case state of the art natural gas combined cycles power plant without CO_2 capture which has an efficiency of 56.5 % (Ekström et al., 2009). In this case the CLC reactor outlet temperature was limited to 1000°C, therefore potentially higher efficiencies could be achieved if the outlet temperature was increased to 1200 °C. Furthermore, the investigation considers designs for a 455 MWe CLC solid fuel power plant and suggests that the energy penalty would be even lower, ~ 2-3 % points, compared with a state of the art pulverised coal (PC) power station with steam cycle which has an electrical efficiency of 44 %. The estimated CO_2 capture costs associated with the CLC power plant were also low of ~ 10 €/ton of CO_2 compared with ~ 20 €/ton of CO_2 for a 455 MWe oxy-fuel power plant and 25 €/ton of CO_2 for a 455 MWe pre-combustion IGCC power plant.

A further benefit of CLC is that thermal NO_X emissions are also intrinsically avoided (Ishida and Jin, 1996). NO_X formation as a consequence of the oxidation of nitrogen in the air increases dramatically with increasing reaction temperatures above ~1500 °C (Baukal Jr, 2012). In normal combustors, flame temperatures often exceed 2000 °C leading to significant NO_x generation. CLC processes operate at temperatures far below those required for thermal NO_X formation and a high heat capacity of the oxygen carrier particles prevents significant local temperature increases. NO_X gases may still form due to oxidation of nitrogen containing impurities in the fuel, but the NO_X gases generated in the fuel reactor are captured along with the CO_2.

2.2 CLC of Solid Fuels

CLC of gaseous fuels is relatively well understood and has demonstrated its commercial feasibility with extended pilot scale trials (Lyngfelt, 2011); however, CLC of solid fuels is a more complicated process. Solid-solid reactions between the oxygen carrier and solid fuel are either negligible or do not occur, therefore solid fuels must first be gasified to transfer the carbon into the gas phase to allow it to react with the oxygen carrier (Jin and Ishida, 2004).

Most of the research concerning CLC has focused on natural gas (methane) as a fuel; however, gasification of solid fuels produces a syngas that consists primarily of H_2 and CO with CH_4 and CO_2 as minor components. Whilst the commonly studied oxygen carrier systems tend to be more reactive towards CO and H_2 (the main components of syngas) than CH_4, syngas contains much high concentrations of impurities such as light hydrocarbons, tar vapours, alkali compound vapours and sulfur and nitrogen containing compounds such as H_2S, NH_3 and HCN (Higman and van der Burgt, 2008). The presence of these impurities can cause significant detriment to the oxygen carrier and CLC process (Mendiara et al., 2011, Shen et al., 2010, Weerachanchai et al., 2009). The effects of some of these impurities on the oxygen carrier and CLC process are discussed in section 2.6. Therefore, the optimum process, oxygen carriers and operating conditions used for CLC of solid fuels will differ from natural gas CLC processes. The following sections discuss process and oxygen carrier development for the purpose of chemical-looping combustion of solid fuels.

2.2.1 CLC Processes for Solid Fuel Utilisation

Solid fuel can either be gasified upstream of the CLC reactor in a separate gasifier or in situ in the fuel reactor. Four methods (i-iv) for CLC of solid fuels have been identified from the literature. A description of each is provided below.

2.2.2 Pre-gasification of the solid fuel in a separate gasifier to generate a fuel gas (syngas) for use in a conventional DFB CLC reactor.

This approach requires installation of a gasifier upstream of the CLC combustor to convert the solid fuel into syngas that can then be utilised in a conventional DFB CLC combustor. Air cannot be used as the gasification agent because this introduces nitrogen into the fuel gas which would dilute the CO_2 stream generated by the CLC process. It is possible to use pure O_2 as a component of the gasification agent; however an air separation process is required which is energy intensive and expensive. Although the amount of O_2 that is needed is less than 25 % of the O_2 required in an oxy-fuel combustion process, the increased costs and reduced process efficiency associated with air separation negatively affects the commercial competitiveness of solid fuel CLC compared with other power generation and CO_2 capture technologies (Mattisson et al., 2009b).

As a consequence, solid fuels are typically pre-gasified in a mixture of steam and/or CO_2 (Berguerand and Lyngfelt, 2009). This approach however is not without its problems. Gasifying solid fuels with steam and/or CO_2 is endothermic and slow; therefore to ensure reasonable rates of fuel gasification, a high gasifier temperature needs to be maintained (800-900 ˚C) (Higman and van der Burgt, 2008). Maintaining such high temperatures is a significant technical issue that requires a complex system for high temperature heat integration (Brown, 2010).

The benefits of a CLC process with pre-gasification of solid fuels are that fuel contaminants can be removed in a gas conditioning step prior to the CLC reactor. Furthermore solid fuel particles and oxygen carrier particles are kept separate which means that solid separation between the reactors to prevent unreacted fuel particles from crossing over into the air reactor is not necessary. The presence of ash in the system which could cause agglomeration, defluidisation of the bed and deactivation of the oxygen carrier is also avoided.

However, the addition of a gasifier and a gas conditioning facility prior to the CLC reactor into the setup increases the capital cost and land space required for construction of a commercial scale CLC plant.

2.2.3 Pre-gasification of the solid fuel for use in a CLC combustor based on a packed bed reactor

Attrition of the oxygen carrier particles is a serious problem associated with using fluidised bed reactors for CLC (Johansson, 2007). Fragmentation and attrition caused by the stresses of fluidisation results in a loss of oxygen carrier from the system as small particles are elutriated with the flue gases. The loss of oxygen carrier from the system can cause blockages downstream of the combustor and increased equipment wear (Kumar et al., 2009). A purge of fresh oxygen carrier is required to compensate for these losses increasing the cost associated with the oxygen carrier material.

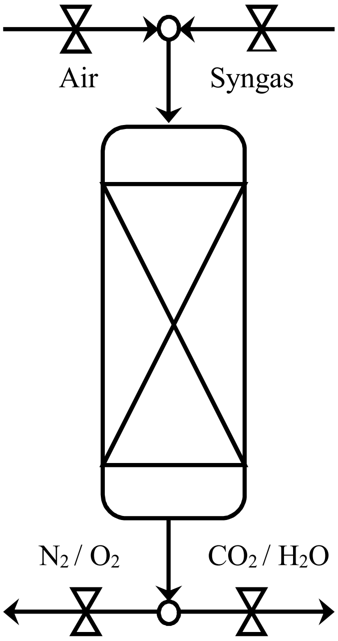

Figure 2.2: Schematic of a packed bed chemical-looping combustion (Noorman et al., 2007) reactor.

In packed bed CLC reactors, particle attrition as well as the need for complex solid-solid and gas-solid separations are intrinsically avoided (fig. 2.2). Other benefits of packed bed chemical-looping combustors include that the reactors are more compact, easier to operate and cheaper to construct than fluidised bed reactors (Warnecke, 2000). Packed bed reactors also allow for better utilisation of the oxygen carrier as a higher degree of oxygen carrier oxidation/reduction is achieved (Noorman et al., 2007).

Since solid fuels cannot be directly introduced into a packed bed CLC reactor, the fuels must be gasified first to generate a syngas (as in approach 2.3.1). The syngas is then supplied to the packed bed combustor containing a stationary bed of an oxidised oxygen carrier which is progressively reduced in the direction of the gas flow. Once the bed is completely reduced, the fuel gas is switched to air and the oxygen carrier is re-oxidised for the next cycle. In order to generate continuous, high temperature flue streams for power generation and CO_2 compression and transport, a number of packed bed combustors operated in parallel and out of phase are required.

As is the case for approach 2.3.1 the fuel needs to be gasified prior to CLC. Therefore a system for high temperature heat integration is required to maintain high gasifier temperatures. There are also potential technical issues associated with the requirement for high temperature, high gas flow switching and the potential gas leakage at the beginning and end of each reduction and oxidation periods (Noorman et al., 2007).

2.2.4 Gasification of solid fuel in situ

Gasification of solid fuels for use in a CLC process can also be performed in situ in the fuel reactor (Berguerand and Lyngfelt, 2009). In this case, solid fuel is fed continuously into the bed which is fluidised by the gasification agent consisting of CO_2 and/or steam. At the high temperatures experienced within the fuel reactor (800-1000 ˚C) the solid fuel is partially oxidised by the gasification agent, generating syngas. The syngas is then oxidised to CO_2 and H_2O by the oxygen carrier.

Gasification of solid fuels occurs in two stages. The fuel particles first undergo pyrolysis where volatile components are released leaving a residual solid consisting predominantly of carbon known as char. The second stage is gasification of the char. Under normal CLC fuel reactor conditions, pyrolysis and subsequent oxidation of the volatile matter by the oxygen carrier is fast, however the rate of char gasification is often much slower and rate limiting. To ensure an acceptable fuel conversion, the residence time of the fuel particles in the fuel reactor needs to be extended. It is also important to prevent crossover of the fuel particles into the air reactor where the fuel would be combusted generating CO_2 that cannot be recovered. Berguerand and Lyngfelt (2009) achieved this by modifying the fuel reactor. This approach also requires that the particle size of the fuel is smaller than the oxygen carrier. A schematic view of the modified fuel reactor chambers can be seen in figure 2.3. The fuel reactor is divided into 3 chambers, a high velocity chamber (HIVEL), low velocity chamber (LOVEL) and a carbon stripper (CS). In the low velocity chamber, the fuel is gasified and subsequently oxidised by the oxygen carrier. The high velocity chamber is located below a fuel reactor riser and is where unreacted fuel particles are elutriated in the flow and carried back to the fuel reactor cyclone where the particles are reintroduced back into the fuel reactor. This process helps to improve fuel conversion as it increases the residence time of the fuel particles in the fuel reactor. The carbon stripper is located at the exit of the LOVEL chamber which separates the fuel particles from the oxygen carrier particles. The fuel particles are re-circulated back into the LOVEL section whilst the reduced oxygen carrier proceeds to the air reactor for regeneration.

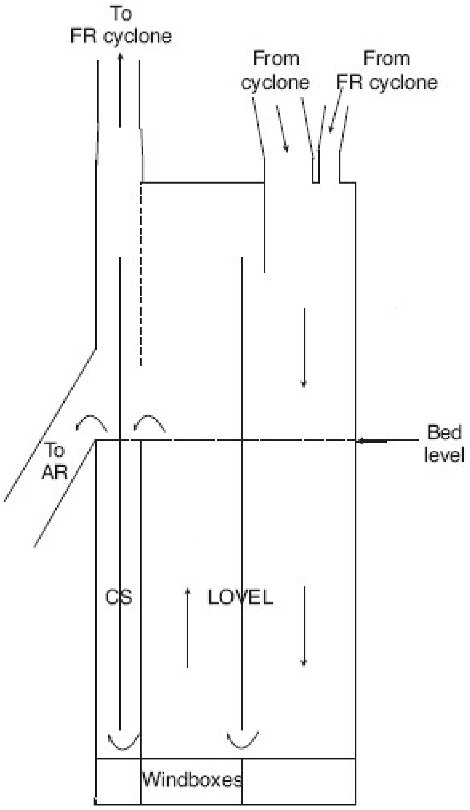

Figure 2.3: (Berguerand et al., 2011): Schematic of the modified fuel reactor of a dual fluidised bed chemical-looping combustion reactor for solid fuel utilization.

Initial tests demonstrated that although char particles were prevented from entering the air reactor, the fuel conversion and CO_2 capture efficiencies were low. This was attributed to the low reactivity of the fuel and the fact that the fuel was fed into the bed from above. It was found that significant devolatisation occurred before the fuel entered the bed and so the volatiles that were released during the fuel feeding process did not come into contact with the oxygen carrier bed and were therefore not combusted. It is expected that significant improvements in the fuel conversion and CO_2 capture efficiencies could be achieved by feeding the fuel into the bottom of the bed.

A distinct advantage of this approach is that the temperature differentiation caused by gasifying the fuel in situ is intrinsically balanced by the heat transferred from the air reactor by the circulating solids. A potential drawback though is that construction of a commercial scale plant that operates in this manner would be more expensive to construct due the complexity of the equipment required. In addition, it is not possible to remove fuel impurities prior to the CLC process therefore oxygen carriers are more likely to deactivate quicker. Ash will also be present. If the ash has a low melting point, interactions between the ash and oxygen carrier particles can result in agglomeration and de-fluidisation of the bed (Weerachanchai et al., 2009).

Recently, a new type of oxygen carrier has been developed with the ability to release gaseous O_2 in the fuel reactor (Mattisson et al., 2009b). The new process has been termed chemical-looping oxygen-uncoupling (CLOU). CLOU oxygen carriers provide a novel way of avoiding the slow and endothermic gasification step as the O_2 released in the fuel reactor can react directly with the fuel dramatically improving fuel conversion rates. However, CLOU oxygen carriers are in the early stages of development and at present, their use is restricted to lower temperatures (~950 °C) (Mattisson et al., 2009b). CLOU oxygen carriers are discussed in more detail in section 2.5.7.

2.2.5 Gasification of the fuel in situ in a single fluidised bed operated in a semi-batch manner

Chemical-looping combustion reactors do not necessarily have to be configured as two interconnected fluidised bed reactors. An approach recently developed by Scott et al. (Scott et al., 2006) involves consolidating the CLC process into a single fluidised bed reactor which is operated in a three stage cycle (fig. 2.4). In the first stage, the solid fuel is fed into a hot bed (800-1000 ˚C) of the oxidised oxygen carrier which is fluidised by CO_2 and/or steam. Under these conditions the fuel is gasified and the syngas produced is oxidised by the oxygen carrier. Before complete depletion of the oxidised oxygen carrier is reached, the fuel feed is stopped and the remaining char inventory is gasified (stage 2). Once the char inventory has been sufficiently reduced, the fluidising gas is switched to air and the depleted oxygen carrier is regenerated (stage 3). Stage 1 follows stage 3 and a new cycle begins.

This combustor configuration is simpler than a conventional CLC combustor, although to generate a continuous hot flue streams for power generation, a number of reactors operating in parallel and at different phases of the cycle are required. Laboratory scale testing of this combustor configuration has produced promising results; however further testing on a larger scale is required to determine whether the heat generated in the reactor during the oxidation period is able to balance the endothermic gasification processes of stages 1 and 2 (Brown, 2010). The net cooling of the reactor during stages 1 and 2 will limit the time period in which gasification reactions can occur, which in turn restricts the types of fuel and oxygen carrier that can be used. There may also be issues with gas leakage at the beginning and end of each of the oxidation and reduction periods (as in approach 2.3.2) which would affect the carbon capture efficiency of the process.

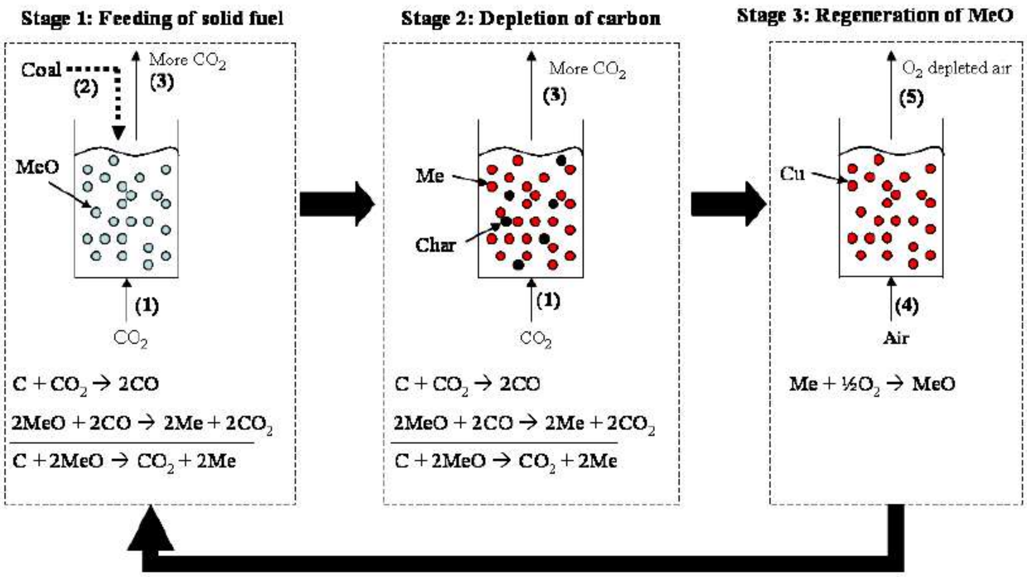

Figure 2.4 (Brown, 2010): The chemical-looping combustion process utilising solid fuels in a single fluidised bed, operated in a semi batch manner.

2.3 Oxygen Carrier Systems

The oxygen carrier is the salient feature of a CLC process; hence the majority of CLC research focuses on oxygen carrier development. The reactivity of a particular oxygen carrier and its oxygen carrying capacity are important characteristics that directly influence the design and operation of the CLC combustor. Materials suitable for use as a CLC oxygen carrier require certain chemical and physical properties. These properties are listed below (Hossain and de Lasa, 2008).

- Large oxygen carrying capacity
- High reactivity- fast oxidation and reduction rates
- Thermal, physical and chemical stability for repeated oxidation/reduction cycles at high temperatures (800-1200 ˚C)
- High gas yield- a high selectivity towards complete fuel conversion to CO_2 and H_2O
- Low material and production cost
- Environmentally benign

Due to high oxygen carrying capacities and favourable oxidative and reductive thermodynamic properties, transition metal oxides, such as those of Ni, Cu, Co, Fe and Mn, are the most commonly researched materials for commercial CLC oxygen carrier applications (Adanez et al., 2004). The

$CaSO_4$/CaS calcium sulfate system has also received attention on account of its large oxygen carrying capacity (Song et al., 2008b).

Oxygen carrier particles can either consist of the pure metal oxide, or the metal oxide can be supported on an inert porous material. Production costs are lower if pure metal oxides are used; however pure metal oxides generally have a low reactivity and poor thermal and mechanic stability (Adanez et al., 2004). If an inert support is used effectively, the supported metal oxide will have a larger reactive surface area due to an increased porosity, enhanced ion conductivity and improved thermal and mechanical stability for increased resistance to agglomeration, sintering, particle fragmentation and attrition. The increased porosity of supported metal oxygen may also improve the fluidisability of the particles. The most commonly studied support/binder materials include Al_2O_3, SiO_2, TiO_2, ZrO_2, YSZ, $NiAl_2O_4$ and $MgAl_2O_4$ (Hossain and de Lasa, 2008). Supporting a metal oxide reduces its oxygen carrying capacity, but it can significantly enhance its reactivity and durability for repeated cycling. A brief description of the key oxygen carrier properties that influence the design and operation of the CLC process is provided below.

2.3.1 Oxygen Carrying Capacity

The oxygen carrying capacity of an oxygen carrier is usually stated in terms its oxygen ratio, R_o (Lyngfelt et al., 2001). The oxygen ratio (2) is the mass difference between the fully oxidised and fully reduced oxygen carrier (eq. 2.2). R_o gives the theoretical maximum amount of oxygen that can be transferred from the air reactor to the fuel reactor per unit mass of the fully oxidised oxygen carrier. The actual oxygen carrying capacity will vary with repeated cycling and is heavily influenced by the mechanical and thermal stability of the particle as well as the particle size and porosity. For supported oxygen carriers, the oxygen carrying capacity will also depend on metal loading (Adanez et al., 2004). R_o values provide a means for comparing the oxygen carrying capacities of different oxygen carrying systems. A list of R_o values for commonly investigated metal oxide oxygen carrier systems can be found in table 2.1.

$$R_o = \frac{(M_{ox} - M_{red})}{M_{ox}} \qquad \text{(Equation 2.2)}$$

M_{ox} is the molar mass of the fully oxidised oxygen carrier and M_{red} is the molar mass of the fully reduced oxygen carrier.

Table 2.1: A list of commonly investigated oxygen carriers and their theoretical oxygen carrying capacities R_o.

Oxygen carrier system	**R_o**
NiO / Ni	0.22
CuO / Cu	0.22
CuO/Cu_2O	0.12
Cu_2O/Cu	0.14
Fe_2O_3 / Fe	0.32
Fe_2O_3 / Fe_3O_4	0.04
Fe_3O_4 / FeO	0.07
MnO_2/ Mn	0.39
MnO_2/Mn_2O_3	0.20
Mn_2O_3/Mn_3O_4	0.04
Mn_3O_4/MnO	0.07
MnO/Mn	0.24
Co_3O_4/Co	0.28
Co_3O_4/CoO	0.07
CoO/Co	0.23
$CaSO_4/CaS$	0.47

2.3.2 Oxygen Carrier Reactivity

The rate of oxidation r_{ox} or reduction r_{red} can be expressed as the change in the extent of oxidation of the oxygen carrier as a function of time (eq. 2.3).

$$r' = \frac{dX}{dt} \qquad \text{(Equation 2.3)}$$

Where X is the extent of oxidation of the oxygen carrier (or conversion) and is the ratio of the actual mass of bound oxygen to the mass of oxygen when the oxygen carrier is fully oxidised (eq. 2.4).

$$X = \frac{M_{Act} - M_{Red}}{M_{Ox} - M_{Red}} \qquad \text{(Equation 2.4)}$$

It is often useful to present fuel conversions or rates of reduction as a function of the change in degree of oxidation of the oxygen carrier (or conversion difference), *ΔX* (eq. 2.5), especially if there are multiple oxidation/reduction steps between the fully oxidised and fully reduced states. This makes it possible to present how oxidation and reduction rates as well as fuel conversion efficiencies change with the oxidation states of the oxygen carrier.

$$\Delta X = X_{AR} - X_{FR} \qquad \text{(Equation 2.5)}$$

ΔX is the conversion difference (between the air reactor and fuel reactor), X_{AR} is the average conversion of the OC material in the air reactor and X_{FR} is the average conversion of the oxygen carrier in the fuel reactor.

The reactivity or rate at which the oxygen carrier reacts with the fuel and oxygen and its oxygen carrying capacity have a large influence on the amount of oxygen carrier bed material (solids inventory) required in the CLC system (Johansson, 2007). For oxygen carriers that have a large oxygen carrying capacity and a high rate of reaction for a wide conversion range ΔX, less bed material and lower solid circulation rates (in DFB combustors) are required for complete combustion of the fuel. Smaller systems, constructed at a lower capital cost, can be used and material and oxygen carrier production costs would be lower. Process costs of DFB CLC would also be reduced as less energy is required for bed fluidisation and circulation. However, reduction of the oxygen carrier by the fuel is often endothermic (especially if CH_4/natural gas is used as the fuel). In a DFB CLC reactor, if the solid circulation rate is too slow, the temperature drop in the fuel reactor will be large causing the oxygen carrier reduction rate (fuel oxidation rate) to fall with a consequential decrease in fuel conversion. In other combustor configurations (approaches 2.3.1 and 2.3.4), shorter reduction and oxidation periods are required to prevent the temperature falling too much during the reduction period.

2.3.3 Fuel Conversion/Gas Yield

The fuel conversion or gas yield, γ_{red}, is also very important as complete fuel conversion to H_2O and CO_2 is required to ensure efficient CLC power generation. The fuel conversion or gas yields for the combustion of CH_4, CO and H_2 are given by (eq. 2.6-2.8) (Lyngfelt et al., 2001).

$$\gamma_{\mathrm{CH_4}} = \frac{x_{H_2O} + x_{CO_2}}{x_{CH_4} + x_{H_2O} + x_{CO_2} + x_{CO} + x_{H_2}} \qquad \text{(Equation 2.6)}$$

$$\gamma_{CO} = \frac{x_{CO_2}}{x_{CO} + x_{CO_2}} \qquad \text{(Equation 2.7)}$$

$$\gamma_{H_2} = \frac{x_{H_2O}}{x_{H_2} + x_{H_2O}} \qquad \text{(Equation 2.8)}$$

When complete combustion of the fuel is not achieved, which may be a consequence of thermodynamic constraints of the oxygen carrier or limitations associated with the CLC process or operating parameters, the unconverted gas must either be re-circulated back into the fuel reactor or combusted by introducing oxygen downstream of the fuel reactor (Johansson, 2007). These options introduce increased process complexity resulting in a higher process cost and should therefore be avoided.

2.3.4 Thermal and Physical Stability of the Oxygen Carrier

As mentioned earlier, to ensure CLC power generation is more efficient and cheaper than other methods of power generation with CO_2 capture, the process has to generate flue streams at temperatures ≥ 1200 °C (Wolf et al., 2005). Therefore, it is highly desirable that oxygen carriers have a high thermal stability and can operate at temperatures of at least 1200 °C without sintering, agglomeration and fracturing.

A high physical stability is required especially in CLC processes that use fluidised bed reactors as the mechanical stress imposed on the oxygen carriers as a consequence of fluidisation can lead to attrition and fracturing of the particles and a loss of oxygen carrier from the system due to entrainment of the smaller particles in the flue gases. However, the physical strength of an oxygen carrier particle tends to be inversely proportional to its reactivity as higher strength particles generally tend to have lower porosities and/or been prepared using higher temperature sintering steps (Adanez et al., 2004) (Mattisson et al., 2004).

2.4 Oxygen Carrier Development

Jerndal et al. (2006) conducted a thermal analysis to investigate the suitability of a range of potential oxygen carriers for CLC of CH_4, H_2 and CO at temperatures of 800 °C and 1000 °C. The study concluded that the metal oxide systems Mn_2O_3/MnO, Fe_2O_3/Fe_3O_4 and CuO/Cu were the best candidates for CLC applications. Full conversion of the fuel gases to CO_2 and H_2O (also known as gas yield) could be achieved at acceptable rates for use as CLC oxygen carriers. The NiO/Ni system is also promising as it is the most reactive metal oxide system especially in terms of CH_4 oxidation; however thermodynamic limitations result in slightly lower fuel conversions to CO_2 and H_2O of ~ 99 % with the rest converted to CO and H_2. The CoO/Co system may not be feasible since the analysis found this system gave gas yields between 93-97 %. The lower gas yields were achieved at higher temperatures and pressures. In addition, Co-based oxygen carriers are expensive and hazardous to human health and the environment.

2.4.1 Ni-based Oxygen Carriers

The NiO/Ni system is the most reactive metal oxide in terms of the rate at which NiO is reduced by the fuel (usually the rate limiting step) and has a high oxygen carrying capacity ($R_o = 0.22$) (Hossain and de Lasa, 2008). However, Ni has a tendency to agglomerate at CLC operating temperatures of ~ 950-1000 ˚C, which reduces the surface area of Ni available for re-oxidation (Ishida and Jin, 1996). As a result, the oxygen carrying capacity of pure Ni/NiO decreases with number of oxidation/reduction cycles.

Alumina (Al_2O_3) is the most commonly investigated support for Ni-based oxygen carriers as it is cheap, it has a high thermal stability and good fluidisation characteristics. Ni/NiO exists as a dispersed phase on the alumina surface; this reduces the particles susceptibility to sintering and agglomeration (Hossain and de Lasa, 2008). However, alumina supported Ni/NiO has a tendency to form nickel aluminate ($NiAl_2O_4$), which cannot be reduced below 1000 ˚C (a difficult temperature to reach in the fuel reactor). As a result, the oxygen carrying capacity of Ni/Al_2O_3 decreases with $NiAl_2O_4$ formation (Cho et al., 2004). Problems associated with $NiAl_2O_4$ formation can be avoided by using an excess of Nickel when preparing Ni/Al_2O_3 to compensate for losses of the reactive Nickel species (Cho et al., 2005). Alternatively, $NiAl_2O_4$ could be used as the support. It has also been found that incorporating Magnesium into a $NiAl_2O_4$ support can further enhance the thermal stability of a Ni/NiO oxygen carrier (Villa et al., 2003) (Mattisson et al., 2006b). The presence of Mg stabilises Ni^{2+} in both cubic NiO and spinel $NiAl_2O_4$ structures such that the supported oxygen carrier is stable for repeated oxidation/reduction cycles at temperatures in excess of 1300 ˚C.

Gayán (2008) prepared α-Al_2O_3 via thermal pre-treatment of γ-Al_2O_3 at 1150 °C and $CaAl_2O_4$ and $MgAl_2O_4$ via dry impregnation of γ-Al_2O_3 particles with CaO or MgO nitrate solutions followed by high temperature sintering. NiO loading were between 11-38 % NiO and MgO or CaO loading were between 5-9 %. It was found that NiO/Ni supported on α-Al_2O_3, $CaAl_2O_4$ and $MgAl_2O_4$ demonstrated much higher methane combustion selectivity to CO_2 and H_2O for repeated cycling (> 50 oxidation and reduction cycles in a batch fluidised bed operated at 950 °C) than NiO/ γ-Al_2O_3 particles as interactions between NiO and the support to form aluminates were minimised.

YSZ, Bentonite and TiO_2 have also been investigated as potential supporting materials for Ni-based oxygen carriers, although Ni/NiO supported on Bentonite and TiO_2, is less reactive than alumina supported Ni/NiO (Son and Kim, 2006). In addition, Bentonite supported Ni/NiO is thermally less stable, whilst Ni/NiO on TiO_2 is more susceptible to coking. In contrast, YSZ supported Ni/NiO has shown promise demonstrating high reactivity and stable oxygen carrying capacity over repeated cycling but is more expensive than Al_2O_3 (Ishida et al., 1996).

Leion et al. (Leion et al., 2009b) investigated the use of oxygen carrier particles consisting of 60 wt.% NiO and 40 wt.% $NiAl_2O_4$ prepared by a spin flash dryer for CLC of a range of solid fuels. Cyclic experiments were carried out in a single fluidised bed operated at 950 °C. For a low sulfur Indonesian coal, fuel conversions close to the thermodynamic limit were achieved. In addition, fuel oxidation rates were faster than the rates observed when ilmenite was used as the oxygen carrier. However, fuel conversions and conversion rates were much lower when the Ni-based oxygen carrier was used for combusting pet coke and a South African coal that have higher sulfur contents. This was attributed to the formation of nickel sulfides and sulfates that deactivated the oxygen carrier. On account of the high price of nickel, it was concluded that Ni-based oxygen carriers are not suitable for CLC of solid fuels.

Ni-based oxygen carriers offer the benefits of a high oxygen carrying capacity, fast oxidation/reduction kinetics and a high thermal stability however, Nickel is expensive and toxic which undermines the development of a commercially viable Ni-based CLC oxygen carrier.

2.4.2 Fe-based Oxygen Carriers

Iron has received a great deal of attention for commercial CLC oxygen carrier applications; it is naturally high in abundance, cheap, environmentally benign and has a high theoretical oxygen carrying capacity (R_o = 0.30 for reduction of Fe_2O_3 to Fe (Hossain and de Lasa, 2008). However, Fe_2O_3/Fe_3O_4, which has much lower oxygen carrying capacity (R_o = 0.04), is the only iron-based redox system that is currently feasible for CLC applications because gas yields for the reductions of Fe_3O_4/FeO and FeO/Fe with both CH_4 and syngas are low and rates of fuel conversion are too slow (Jerndal et al., 2006).

Mattisson et al (2001) investigated the use of hematite (a natural Fe_2O_3 ore) as an oxygen carrier for CLC of methane in a lab-scale packed bed reactor operated at 950 °C. The reactivity of the hematite particles was initially low but improved with successive cycles. High gas yields of ~99 % were achieved by operating with a large solid inventory and short reduction periods such that ΔX was limited to < 0.04 (i.e. reduction of Fe_2O_3 limited to Fe_3O_4). The increase in reactivity with successive cycling was attributed to attrition and fragmentation of the particles exposing a larger reactive surface area. Agglomeration was not observed.

Subsequently, Mattisson et al. (2004) synthesised a range of supported Fe_2O_3 oxygen carriers and investigated the effects of different supporting materials and metal oxide loadings had on the reactivity and methane combustion efficiency of the Fe_2O_3/Fe_3O_4 system. Enhanced reactivities were reported for Fe_2O_3/Fe_3O_4 supported on Al_2O_3, ZrO_2, TiO_2 and $MgAl_2O_4$ with mass ratios of (60:40) prepared via freeze granulation and sintering at 950-1300 °C. The physical durability of the particles increased with the preparation sintering temperature although the reactivity of the particle tended to be lower. The Fe_2O_3/Al_2O_3 particle was the most reactive of the particles sintered at 1300 °C. Metal loadings ranging between 40-90 % have also been investigated, although it is generally accepted that a loading of 60 wt.% Fe_2O_3 (40 wt.% alumina or other supporting material) is an optimal compromise between reactivity enhancement (due to the increased reactive surface area) and oxygen carrying capacity (Cho, 2002).

Abad et al. (2007a) investigated the chemical-looping combustion of methane and a simulated syngas (50 % CO and 50 % H_2) in a continuously operated dual-fluidised bed combustor using an alumina supported Fe-based oxygen carrier. The oxygen carrier comprised of 60 wt.% Fe_2O_3 and 40 wt.% Al_2O_3 and was prepared by freeze granulation followed by sintering at 1100 °C for 6 hours. Combustion efficiencies of 97 % and 99 % were achieved for methane and syngas respectively. The reactivity and crushing strength of the oxygen carrier did not seem to be affected by the 60 hours of continuous operation and they reported no signs of agglomeration or carbon deposition.

Fe-based oxygen carriers have also been investigated for CLC of solid fuels where the solid fuels are introduced directly into the fuel reactor. Leion et al. (2007) studied CLC of petroleum coke using a

60 wt.% Fe_2O_3/ 40 wt.% $MgAl_2O_4$ oxygen carrier and found that the oxygen carrier reacted rapidly with the intermediate gasification products such as CO and H_2 enhancing the rate of gasification.

Deactivation and agglomeration of oxygen carrier particles used for direct CLC of solid fuels is likely to occur at a faster rate as a consequence of interactions with ash, tars and other fuel impurities (Leion et al., 2009b). It is therefore desirable to use cheap oxygen carriers for direct CLC of solid fuels to minimise any process cost increases associated with lower oxygen carrier lifetimes. Berguerand and Lyngfelt (2009) investigated a low cost oxygen carrier prepared from Ilmenite, an iron and titanium ore ($FeTiO_3$), for direct CLC of petroleum coke in a 10 kW_{th} continuously operated dual fluidised bed chemical-looping combustor with a fuel reactor operating temperature of 950 °C. Fuel conversion varied between 55 % and 75 % and CO_2 capture efficiencies varied between 68 % and 87 %. The low conversion and CO_2 capture efficiencies were attributed to the poor reactivity of the fuel and reactor design issues associated with feeding the fuel into the bed (previously discussed in section 2.3.3).

Teyssié et al. (2011) investigated the effect of adding lime (CaO) to an ilmenite based oxygen carrier bed for the CLC of petroleum coke. Moderate improvements in the fuel combustion efficiency and a halving of the CO concentration in the flue gas was observed when a bed consisting of 80 wt.% ilmenite with 20 wt.% lime. The improved fuel combustion efficiency was due to CaO catalysing the water gas shift reaction. Thus CO reacted with steam generating CO_2 and H_2. H_2 is much more reactive with ilmenite than CO.

Other potential sources of low cost oxygen carrier precursor materials are Fe_2O_3 containing waste products from the iron and steel industries. Rydén et al. (2009) prepared oxygen carriers from red and brown iron oxide powders, waste products from steel sheet production, and iron oxide scales produced during the rolling of steel sheets. The oxygen carriers were tested for the CLC of methane in a batch fluidised bed reactor at 850 °C and 950 °C. By themselves, the oxygen carriers demonstrated low reactivities towards methane combustion; however a significant enhancement in reactivity and methane combustion efficiency was reported with the addition of 5 wt.% $NiO/MgAl_2O_4$. The methane combustion efficiency of the iron oxide scale at 950 °C increased from 50.1 % to 95.8 % when the Ni-based oxygen carrier was introduced. It was concluded that the addition of small amounts of Ni catalyses the conversion of methane to CO and H_2 which react with the iron oxide at a considerably higher rate. These experiments demonstrate that low cost oxygen carriers can be produced with sufficient reactivities and combustion efficiencies for CLC applications.

Finally Fe-based oxygen carriers have also been used as an oxygen carrier in a CLC process for combined heat and hydrogen production in a packed bed CLC reactor (Bohn et al., 2008). The process is comprised of three main steps. In the first step, Fe_2O_3 is reduced using syngas. Since this process is carried out in a packed bed reactor, complete combustion can be achieved for a higher oxygen carrier conversion range $\Delta X > 0.04$; hence some of the Fe_2O_3, particularly at the end of the bed closest to the gas inlet, is reduced to FeO and Fe. Once all of the bed has been reduced to at least Fe_3O_4, the gas flow is switched to steam which partially re-oxidises Fe and FeO to Fe_3O_4 generating a high purity H_2 stream (once the unreacted steam has been condensed out). In the final step the gas flow is switched to air and the Fe_3O_4 is oxidised back to Fe_2O_3 producing useful heat which could be used to raise steam for power generation.

Bohn et al. (2008) found that the capacity of unsupported Fe_2O_3 to produce H_2 deteriorated significantly with repeated cycles if reduced completely to Fe whilst if reduction was limited to FeO, stable yields of H_2 over 10 cycles were obtained. Deactivation of the Fe_2O_3/Fe system was due to a significant (~70 %) increase in the molar density of the particles when reduced from FeO to Fe causing a severe contraction of the iron lattice when the oxygen was removed. Thus the reactive surface area of the particle was significantly decreased. It is highly desirable to reduce Fe_2O_3 to Fe, since four times as much H_2 can be produced during re-oxidation with steam than if reduction is limited to FeO (eq. 2.9-2.10).

$$3Fe + 4H_2O \leftrightarrow Fe_3O_4 + 4H_2 \qquad \text{(Equation 2.9)}$$

$$3FeO + H_2O \leftrightarrow Fe_3O_4 + H_2 \qquad \text{(Equation 2.10)}$$

In a subsequent study Bohn et al. (2010) prepared a number of modified Fe_2O_3 particles by impregnating Fe_2O_3 with either Al, Cr, Mg or Si in an attempt to improve the stability of the Fe_2O_3/Fe system. Their results showed that the addition of 10 mol.% to Al_2O_3 provided the best improvement producing stable H_2 yields close to the theoretical limit for Fe_2O_3/Fe over 10 redox cycles at 850 °C.

Although this concept is based on the steam-iron process (one of the oldest methods of producing hydrogen), CLC in packed beds for combined power and hydrogen production is a relatively new concept. Further work is required to determine the efficiency of combustion, CO_2 capture and H_2 production.

2.4.3 Cu-based Oxygen Carriers

The CuO/Cu system offers a number of favourable oxygen carrying features; (i) CuO/Cu has a high oxygen carrying capacity ($R_o = 0.21$); (ii) it has a high reactivity for both oxidation and reduction cycles which allows systems to operate with lower solid inventories (Abad et al., 2007a); (iii) the oxidation and reduction of the CuO/Cu system using CH_4, CO and H_2 as fuels are both exothermic, therefore lower circulation rates and a higher oxygen carrier conversion range (ΔX) can be utilised (de Diego et al., 2007); (iv) complete fuel combustion of gaseous fuels such as CH_4, CO and H_2 is achievable using Cu-based oxygen carriers (García-Labiano et al., 2004); and (v) copper is reasonably inexpensive compared with other potential oxygen carrier materials (Hossain and de Lasa, 2008). However, metallic copper has a low melting point of 1045 °C and CuO decomposes to Cu_2O at high temperatures and low O_2 partial pressures; at 944 °C CuO decomposes at partial pressures of O_2 below 0.04 (Jerndal et al., 2006). Therefore, CLC processes utilising Cu-based oxygen carriers are generally limited to lower temperatures of around 900-950 °C.

De diego et al. (2004) compared the reactivity of a pure CuO oxygen carrier and supported CuO using a range of different inert supporting materials and preparation techniques in a TGA at 800 °C. Initially the reactivity of the unsupported CuO oxygen carrier was high, but dropped rapidly and after 3 cycles and the methane combustion efficiency was reduced to ~10 %. Alumina supported CuO prepared via mechanical mixing and co-precipitation techniques maintained a high level of reactivity achieving complete methane combustion, but significant particle fragmentation was observed. They concluded that impregnation was the best preparation technique generating durable, high reactivity particles that completely combusted methane during repeated cycling. However, they assert that metal loadings should be ≤ 10 % to prevent particle agglomeration.

Chuang et al. (2008) reported a significant enhancement of the mechanical stability of co-precipitated alumina supported CuO oxygen carriers during fluidised bed CLC cycling when precipitation was carried out at a higher pH ~ 9.7 as opposed to a pH of 7.1. Furthermore, it was found that particles prepared via co-precipitation did not agglomerate even with high CuO loadings of 82.5 wt.% after 18 oxidisation and reduction cycles in a fluidised bed operated at 900 °C.

In terms of solid fuel CLC, Cu-based oxygen carriers offer the advantage that they react exothermically with gaseous hydrocarbons, therefore the heat released as they are reduced can be used to balance the endothermic gasification of solid fuels in CO_2 and/or steam. Dennis et al. investigated CLC of lignite coal (Dennis and Scott, 2010) and bituminous coal (Dennis et al., 2010) using Cu_2O/CuO-based oxygen carriers prepared via impregnation in a single fluidised bed reactor operated in a semi batch manner at 930 °C. It was found that the presence of the Cu-based oxygen carrier significantly enhanced the rate of gasification for both fuels. They argued that the gasification rate enhancement was most likely a consequence of the Cu_2O reacting with the gasification products (CO and H_2), therefore lowering the concentration of CO and H_2 surrounding the char particles which are known to inhibit gasification (Liu and Niksa, 2004). Furthermore, it was found that an even larger enhancement of the gasification rate was possible if the temperature was reduced from 930 °C to 830 °C (Dennis and Scott, 2010). At this temperature, CuO was formed during oxidation, which decomposed to Cu_2O releasing gaseous O_2 during the reduction period in a CLOU type process (section 2.5.7). Gasification rates were enhanced since both Cu_2O and O_2 could react with the gasification products and O_2 could also react directly with the char. No agglomeration or deactivation of the particles by the ash species was observed but the BET surface area of the particles decreased from ~ 60 $m^2 g^{-1}$ to ~ 6 $m^2 g^{-1}$ after 20 cycles at 930 °C. This did not seem to affect combustion rates since gasification of the fuel was the rate limiting process.

The CuO/Cu system has a number of highly desirable characteristics for direct CLC of solid fuels, but its low thermal stability is a significant disadvantage limiting operating temperatures to ~ 950 °C. In order to achieve high thermal efficiencies from a CLC power generation process utilising a Cu-based oxygen carrier, top-firing of the flue gases would be required which reduces the CO_2 capture efficiency of the process.

2.4.4 Mn-based oxygen carriers

Mn-based oxygen carriers have high reactivities and are able to completely convert fuels such as CH_4, H_2 and CO to CO_2 and H_2O (Jerndal et al., 2006). In addition manganese oxide is a cheap and non-toxic oxygen carrier precursor. However, the oxygen carrying capacity of Mn-based oxygen carriers is limited since Mn_2O_3 decomposes to Mn_3O_4 in air at ~ 900 °C and the reactivity of MnO with gaseous fuels is far too slow. Mn_3O_4/MnO is therefore the only redox system that can be utilised in a conventional high temperature CLC process although Mn_2O_3/MnO has attracted attention as a potential CLOU oxygen carrier system (Mattisson et al., 2009b) (section 2.4.7). It should be noted that whilst the oxygen carrying capacity of Mn_3O_4/MnO is low ($R_o = 0.07$), it is almost twice that of the much more extensively studied Fe_2O_3/Fe_3O_4 system ($R_o = 0.04$). Mn_3O_4/MnO is also more reactive than Fe_2O_3/Fe_3O_4 (Johansson, 2007).

Adandez et al. (2004) tested a range of supporting materials for Mn-based oxygen carriers including Al_2O_3, Sepiolite, SiO_2, TiO_2 and ZrO_2 in a TGA operated at temperatures up to 1100 °C. Only Mn_3O_4/MnO supported on ZrO_2 maintained a high reactivity and crushing strength after 5 oxidation and reduction cycles. Mattisson et al. (2003) found that the reactivity of alumina supported Mn_3O_4 was poor due to the formation of $MnAl_2O_4$ spinels during sintering.

Johansson et al. (2006) synthesised Mn-based oxygen carriers supported on ZrO_2 and ZrO_2 stabilised with CaO, MgO and CeO. All the oxygen carriers maintained high reactivities and only limited physical changes were observed after 16 oxidation and reduction cycles in a fluidised bed operated at 950 °C. It was concluded that Mn_3O_4/MnO supported on MgO-ZrO_2 had the highest reactivity. Zafar et al.(2007) tested MgO-ZrO_2 supported Mn_3O_4/MnO oxygen carrier particles in a 300 W_{th} continuously operated dual fluidised bed. Combustion efficiencies were > 99 % for syngas and slightly lower for methane. Attrition rates were low and no agglomeration was detected after 70 hours of operation at 1000 °C.

Mn-based oxygen carriers have been successfully utilised for CLC of gaseous fuels; however at present only a small amount of work has been published detailing investigations that involve using Mn-based oxygen carriers for direct CLC of solid fuels.

2.4.5 $CaSO_4$ based oxygen carriers

$CaSO_4$ is cheap and has a higher oxygen carrying capacity (R_o = 0.47) than any of the previously discussed metal oxide systems. In a recent study, Song et al. (2008b) found that $CaSO_4$ particles prepared from a natural anhydrite ore demonstrated a high reactivity and stability during repeated oxidation and reduction with methane in a fixed-bed reactor operated at 950 °C. Higher temperatures led to increased methane combustion efficiencies although decomposition of $CaSO_4$ to SO_2, H_2S and CaO was also more prevalent at higher temperatures. In a subsequent paper, Song et al. (2008a) investigated CLC of coal gas in a fluidised bed reactor at 950 °C using $CaSO_4$ as the oxygen carrier. Initially the combustion efficiency was high, however after ~ 15 cycles the reduction rate and combustion efficiency fell with successive cycles due to $CaSO_4$ decomposition.

Song et al. (2008b) found that the rate of $CaSO_4$ decomposition can be minimised by operating at low temperatures (< 950 °C), higher pressures and/or higher partial pressures of sulfur containing species. Furthermore, the addition of small amounts of lime (CaO), which is commonly used in gas conditioning for the removal of sulfur containing gases, can be used to extend the lifetime of a $CaSO_4$ oxygen carrier bed (Shen et al., 2008). In this case, CaO is used to capture SO_2 before it exits the bed and the products $CaSO_4$ and CaS act as oxygen carriers in subsequent cycles.

At present there are very few published papers that have investigated supporting $CaSO_4$ for CLC applications. Ding et al. (2011) tested an alumina supported $CaSO_4$ particle for a single reduction with methane in a fixed-bed reactor at 950 °C. The supported $CaSO_4$ had a higher surface area and demonstrated a higher reactivity and thermal stability compared to pure $CaSO_4$; however further work is required to determine the performance of this oxygen carrier during repeated high temperature cycling.

$CaSO_4$/CaS is a promising system for CLC oxygen carrying applications and may be particularly suitable as an oxygen carrier for CLC of high sulfur containing gaseous or solid fuels. However, further work is required to develop more reactive and thermally stable supported $CaSO_4$ oxygen carriers.

2.4.6 Mixed Metal Oxide Oxygen Carriers

In attempts to improve the reactivity and stability of certain metal oxide oxygen carriers, a range of mixed metal oxides have been synthesised. Jin et al. (Jin et al., 1998) were the first researchers to investigate the potential of bi-metallic oxides for CLC oxygen carrier applications. The double metal oxide of CoO-NiO supported on YSZ was found to demonstrate a higher reactivity and regenerability during repeated oxidation and reduction cycles than either of the individual metal oxides supported on YSZ; however CoO-NiO/YSZ was not considered further on account of its low thermal stability. Hossain and de Lasa (2007) developed a bimetallic cobalt and nickel oxygen carrier supported on α-Al_2O_3 for use in a fluidised bed chemical-looping combustor. It was found that Co preferentially reacted with the alumina support suppressing $NiAl_2O_4$ formation. The presence of Co also helped to maintain a consistent Ni dispersion enhancing the particle's resistance to sintering and agglomeration. The particle demonstrated an enhanced reactivity however, reactivity was only tested up to 750 °C and further work is required to determine reactivity and stability at the higher temperatures more likely to be experienced in a CLC process.

Adánez et al. (2006) tested mixed Ni-Cu oxygen carriers supported on alumina in a TGA and a batch operated fluidised bed at 900-1100 °C. Unlike monometallic Ni-based oxygen carriers, the Ni-Cu-oxygen carrier was able to completely convert CH_4 to CO_2 and H_2O during the initial part of the reduction cycles as CuO was reduced before NiO. In addition, they reported that the presence of Ni improved the thermal stability of Cu allowing operation up to 950 °C without sintering or agglomeration.

As mentioned previously the addition of NiO significantly enhanced the methane combustion efficiency of Fe-based oxygen carriers produced from steel industry waste products. Johansson et al. (2006) observed a doubling of CH_4 combustion rates when 3 % of a $NiO/MgAl_2O_4$ oxygen carrier was added to an $Fe_2O_3/MgAl_2O_3$ bed in a continuously operated DFB chemical-looping combustor at 950 °C. The increase in rate was attributed to a synergic effect between the two metal oxide systems where NiO/Ni catalysed the decomposition of CH_4 to CO and H_2 which were more easily oxidised by the Fe_2O_3 oxygen carrier. The addition of small amounts of NiO was also found to improve the reactivity and combustion efficiency of natural ilmenite based oxygen carriers (Ryden et al., 2010).

Bimetallic oxygen carriers containing manganese are also of considerable interest due to their ability to release small amounts of gaseous O_2 under reducing/inert conditions at higher temperatures than monometallic manganese based oxygen carriers. These oxygen carriers are discussed further in the following section (section 2.5.7).

2.4.7 Oxygen Carriers for Chemical-Looping Oxygen Uncoupling (CLOU)

Chemical-looping with oxygen uncoupling (CLOU) as a technology for the production of power with integrated CO_2 capture was first proposed by Mattisson et al. (2009b) although the origins of the technology date back to the Brin process- a process operated commercially between 1886 to 1906 for the production of concentrated O_2 using barium oxide as the oxygen sorbent (eq. 2.11) (Jensen, 2009). The reaction was discovered by Guy-Lussac and Thenard (1811) and first investigated for O_2 production applications by Boussingault (1852).

Brin Process: $$2BaO_{(s)} + O_{2\,(g)} \leftrightarrow 2BaO_{2\,(s)} \qquad \Delta H^{\ominus} = -44.3\ kJ.mol^{-1} \qquad \text{(Equation 2.11)}$$

CLOU is a variant on CLC that involves using oxygen carriers that are able to release gaseous O_2 in the fuel reactor which can directly react with the fuel. This process is of particular interest for the CLC of solid fuels. CLOU involves three steps in two reactors (fig. 2.5). In the air reactor, the CLOU oxygen carrier captures O_2 in the combustion air according to (eq. 2.14). The oxygen carrier is then transferred to the fuel reactor where it releases the O_2 captured in the air reactor (eq. 2.12). In the third step, the O_2 reacts with the gaseous/solid fuel according to normal combustion (eq. 2.13).

CLOU offers the advantage that the slow, endothermic gasification step required in conventional CLC of solid fuels is avoided. The rates of fuel conversion are significantly higher and as a consequence, higher combustion efficiencies can be achieved with a much lower oxygen carrier solids inventory. Also, since fuel combustion in O_2 is exothermic, both the air reactor and fuel reactor processes are exothermic.

CuO/Cu_2O and Mn_2O_3/Mn_3O_4 are the most promising oxygen carrier candidates for CLOU combustion of solid fuels (Mattisson et al., 2009b). The release of oxygen from these systems is a function of the operating temperature and O_2 partial pressure. CuO and Mn_2O_3 are stable in air up to temperatures of 1028 °C and 899 °C respectively; however the temperature at which these systems decompose decreases with the O_2 partial pressure. It is important that the reduced metal oxides can be oxidised at high temperatures and O_2 partial pressures lower than air as O_2 concentrations in the air reactor will vary between 21% at the air inlet and ~ 5 % at the air reactor outlet. At an O_2 partial pressure of 0.05, CuO and Mn_2O_3 will only form at temperatures up to 955 °C and 820 °C respectively. The low temperatures at which these systems can operate represents the main drawback with CLOU processes.

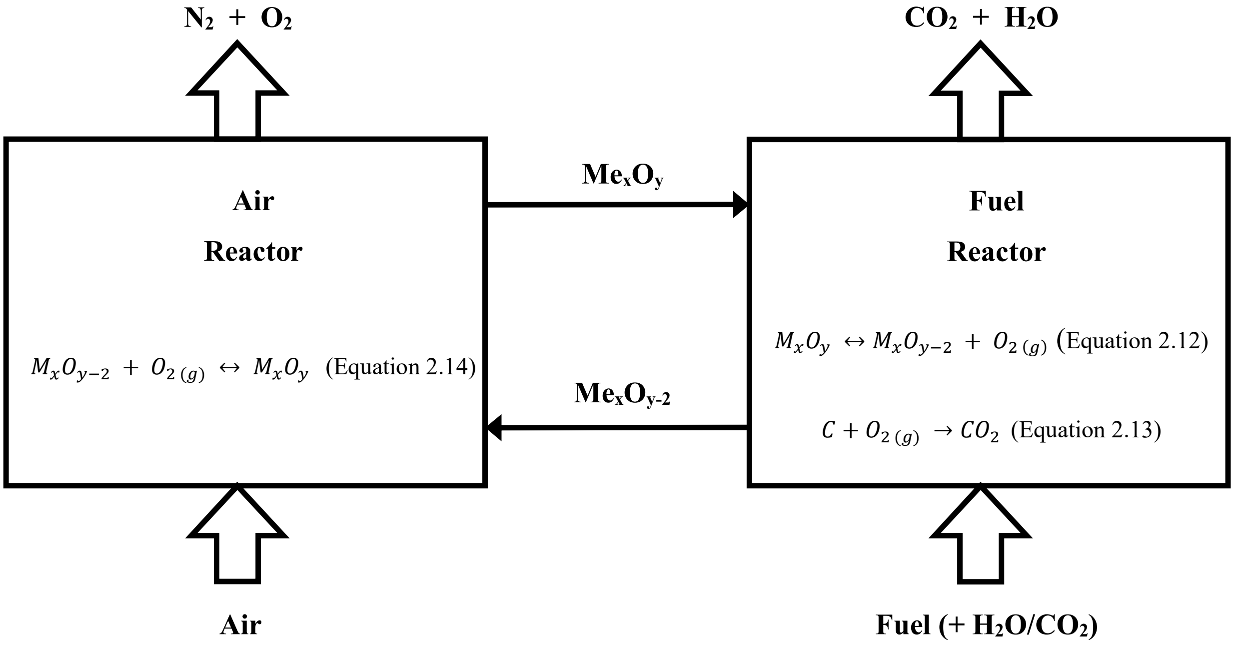

Figure 2.5: The chemical-looping with oxygen uncoupling process where Me_xO_{y-2} and Me_xO_y denotes the reduced and oxidised metal oxide particles.

Mattisson et al. (2009a) investigated CLOU of petroleum coke in a batch operated lab scale fluidised bed at 950 °C using a CuO-oxygen carrier supported on ZrO_2. Very high fuel combustion efficiencies of ~ 95 % were attained and the rates of fuel conversion were 50 times higher than fuel conversion rates in an equivalent process utilising $Fe_2O_3/MgAl_2O_4$ as the oxygen carrier. The slightly lower than complete conversion efficiency was attributed to release of volatiles in the freeboard of the fluidised bed reactor as the fuel was fed into the bed. Entrainment of the volatiles in the gases exiting the reactor will have reduced the residence time of the volatiles in the reactor and contact with the bed material, limiting the combustion efficiency of the solid fuel's volatile components.

Due to the low thermal stability of Mn_2O_3 at typical air reactor O_2 partial pressures Mn_2O_3/Mn_3O_4 CLOU oxygen carriers are normally considered less suitable than CuO/Cu_2O (Mattisson et al., 2009b). However, the addition of other metallic cations into the manganese oxide frameworks can alter the thermodynamic properties of manganese oxides, in some cases stabilising the Mn^{3+} and Mn^{4+} cations in either a spinel (Shulman et al., 2009) or perovskite structure (Leion et al., 2009a, Ryden et al., 2011).

Shulman et al. (2009) tested oxygen carriers consisting of 20 wt.% Fe_2O_3 or 20 wt.% NiO with 80 wt.% Mn_3O_4 in a single fluidised bed at 900 °C. It was found that the presence of Ni and Fe in the structure of Mn_2O_3 had a stabilising effect such that Mn_3O_4 could be oxidised to Mn_2O_3 at 900 °C in 10 % O_2. Reaction rates were high and complete methane combustion could be achieved by the Fe_2O_3/Mn_2O_3 system at 900 °C. Rydén et al. (2011) investigated the potential of the 20 wt.% Fe_2O_3/ 80 wt.% Mn_2O_3 oxygen carrier for high temperature CLOU of methane in a continuously operated DFB reactor at temperatures between 800-1000 °C. The tests were not successful as the experiments had to be aborted after 4 hours due to the low mechanical stability of the particles which collapsed during operation. Results from the first few cycles revealed that the bimetallic particles were able to transfer much larger quantities of O_2 to the fuel reactor than monometallic Mn-based oxygen carriers, although it was not enough for complete combustion of methane. As a consequence combustion efficiencies were more dependent on the reactivity of the conventional CLC reactions between methane and the oxygen carrier. High solid circulation rates (and a more mechanically stable Mn/Fe-based oxygen carrier) would therefore be required to supply enough gaseous O_2 for complete combustion of the methane.

$CaMnO_3$ is another manganese containing compound with oxygen carrier potential, however like Mn_2O_3, $CaMnO_3$ decomposes to Ca_2MnO_4 and $CaMn_2O_4$ at typical CLC temperatures which restricts the full oxidation potential of this material (Bakken et al., 2004). Leion et al. (2009a) investigated substituting Ti at some of the Mn sites in the $CaMnO_3$ structure in an attempt to stabilise the Mn^{4+} in a perovskite structure. The compound with chemical formula $CaMn_{0.875}Ti_{0.125}O_3$ was deemed the most interesting for CLOU investigations. The reactivity of $CaMn_{0.875}Ti_{0.125}O_3$ was investigated in a TGA and lab scale fluidised bed with methane and petroleum coke. It was found that the rate of petroleum coke combustion using $CaMn_{0.875}Ti_{0.125}O_3$ was much lower than CLC of petroleum coke when CuO/Al_2O_3 was used, however it was still three times faster than combustion by $Fe_2O_3/MgAl_2O_3$. In addition, oxidation of $CaMn_{0.875}Ti_{0.125}O_3$ seemed to be less affected by temperature than the CuO/Cu_2O and released roughly the same amount of O_2 at 900 °C and 950 °C. Rydén et al. (2011) tested $CaMn_{0.875}Ti_{0.125}O_3$ for CLOU combustion of methane in a continuously operated DFB reactor at 950 °C and found that combustion efficiencies as high as 99.8 % could be achieved. The particles retained their reactivity for 70 hours of operation and only limited physical changes were observed.

CLOU offers distinct advantages for CLC of solid fuels however further work is required to develop a CLOU process that can operate at temperatures between 1000 °C and 1200 °C. With this aim, bimetallic Mn-containing oxygen carriers have shown promise demonstrating improved thermal stabilities compared with single metallic Mn- and Cu- oxygen carrier materials.

2.5 Oxygen Carrier Fouling

As mentioned previously gasification of solid fuels generates a syngas which contain impurities such as tar vapours, sulfur and nitrogen containing gases and alkali compound vapours (Higman and van der Burgt, 2008). The relative amounts of these species are determined by fuel type and gasification/CLC process conditions. The presence of such impurities can have significant effects on the CLC process and in some cases lead to deactivation of the oxygen carrier. In this section, the possible mechanisms for oxygen carrier deactivation by common syngas impurities and methods for limiting such interactions are discussed. Ash will also be present if the fuel is gasified in situ and therefore the effects of ash on the CLC/gasification process and oxygen carrier will also be discussed.

2.5.1 Tar Interactions and Carbon Deposition

Tar is a broad term used to describe all organic compounds formed during pyrolysis and gasification of solid fuels with the exception of hydrocarbons that are gases at standard temperature and pressure. Tars are predominantly formed during the pyrolysis stage of a gasification process. Pyrolysis is the first stage of the gasification process and refers to the thermal breakdown of solid carbonaceous fuel in the absence of air (anaerobic devolatisation) at temperatures between 350 °C and 800 °C to produce a mixture of gas, oil, and char (containing ash) (Reed et al., 2001). For coal pyrolysis, ~ 20-40 % of the initial fuel mass is converted into pyrolysis vapour (the collective term for pyrolysis gases and oils), whilst for biomass pyrolysis, vapour yields are much higher, typically between 75-90 % (Reed et al., 2001). Most of the primary tars generated during pyrolysis will be cracked/reformed into combustible gases (such as CO, H_2, CH_4 and other light hydrocarbons), CO_2 and H_2O in subsequent high temperature gasification reactions (700 – 1200 °C); however a small amount of secondary and tertiary tars are also formed which exit the gasifier with the syngas (Milne et al., 1998). The exact amount and constitution of tars exiting the gasifier will differ depending on the fuel type, gasifier type and operating conditions used. Generally, tars include single ring to 5-ring aromatic compounds, oxygenates, olefins and complex poly-aromatic hydrocarbons (PAHs) (Devi et al., 2003). Due to the much higher volatile content of biomass compared to coal, tar formation is more of a problem for biomass gasification where 0.1-10 % of the initial biomass mass exits the gasifier as tar (Higman and van der Burgt, 2008).

Tars are problematic for a number of reasons. Firstly, certain high molecular weight tar compounds start to condense at temperatures < 450 °C (McKendry, 2002b). This can lead to clogging and blockages in gas lines and filters and a reduced gasification efficiency since the energy content of the tars cannot be recovered (Milne et al., 1998). Furthermore, removal of the condensed tars is energy intensive and expensive. In the context of CLC, the presence of tar can lead to significant coking of the oxygen carriers

(Mendiara et al., 2011). Coking will not permanently deactivate oxygen carriers as the carbon is burnt off in the subsequent oxidation step; however the CO_2 that is released is not captured thus reducing the CO_2 capture efficiency of the CLC process (Corbella et al., 2005a, Corbella et al., 2005b).

Coking can occur via three main pathways: the Boudouard reaction (eq. 2.14), the reverse water-gas reaction (15), or thermal/catalytic decomposition of a hydrocarbon species on the surface of a solid (Mendiara et al., 2011). A generalised reaction scheme for the decomposition of a hydrocarbon on the surface of a solid is provided in (eq. 2.15). Coke formation via the Boudouard and reverse water-gas reaction is favoured at low temperatures, whilst coke formation via hydrocarbon decomposition is more prevalent at higher temperatures. In the case of high molecular weight hydrocarbons such as tars, reaction (eq. 2.16) can be considered irreversible. In a CLC process utilising solid fuels and operating at 800-1200 °C, coking of the oxygen carrier will be predominantly caused by tar decomposition (Mendiara et al., 2011).

$$2CO \overset{surf}{\longleftrightarrow} C_{(s)} + CO_2 \qquad \text{(Equation 2.15)}$$

$$CO + H_2 \overset{surf}{\longleftrightarrow} C_{(s)} + H_2O \qquad \text{(Equation 2.16)}$$

$$C_nH_{2n+2} \overset{surf}{\longleftrightarrow} nC_{(s)} + (n+1)H_2 \qquad \text{(Equation 2.17)}$$

In a recent publication, Mendiara et al. (2011) investigated the interactions between toluene (a model tar compound) and four different oxygen carriers (60 wt.% $NiO/MgAl_2O_4$, 40 wt.% $NiO/NiAl_2O_4$, 40 wt.% $Mn_3O_4/Mg\text{-}ZrO_2$ and the iron ore ilmenite ($FeTiO_3$)). The objective of the research was to develop a chemical-looping process for the selective reforming of tars present in biomass syngas thus improving the quality/heating value of the syngas. Experiments were performed in a TGA and fixed-bed reactor operated at temperatures between 600-800 °C. The $NiO/NiAl_2O_4$ and $Mn_3O_4/Mg\text{-}ZrO_2$ oxygen carrier particles were the most promising candidates for tar reforming applications demonstrating high and stable reactivities towards toluene for repeated redox cycles. The reactivity of ilmenite was much lower, but improved with successive cycling, whilst $NiO/MgAl_2O_4$ did not react with toluene at any of the investigated temperatures.

Carbon deposition was observed for all the oxygen carriers that reacted with toluene although it was most severe for $NiO/NiAl_2O_4$. It was found that coking increased at higher temperatures and in the case of $NiO/NiAl_2O_4$ and ilmenite, a longer time period for the reduction step also resulted in increased coke formation. The fact that coking was enhanced at higher temperatures suggests that the main path for carbon deposition is through toluene decomposition as in reaction (eq. 2.16). The introduction of steam was found to be effective at decreasing carbon deposition however very high H_2O/C_7H_8 ratios of > 26.4 were required. This is significantly higher than the H_2O/CH_4 ratio of ~ 2 required to prevent carbon deposition caused by methane decomposition. Operating at such high H_2O/tar ratios is impractical and would impose a significant energy penalty on the process.

If the fuel is gasified in a separate gasifier upstream of the chemical-looping combustor, tar could potentially be removed from the syngas in a gas conditioning step before it is introduced into the fuel reactor. However, if the fuel is gasified in situ in the fuel reactor, interactions between tars and the oxygen carrier particles are unavoidable. Therefore development of an oxygen carrier that is highly reactive towards tars whilst resistant to coke formation is highly desirable.

2.5.2 Nitrogen and Sulfur Containing Compounds

Both coal and biomass contain certain amounts of sulfur and nitrogen. Sulfur content in coal ranges from 0.5-6 wt.% whilst sulfur content in biomass is much lower, typically less than 0.5 wt.% (Higman and van der Burgt, 2008). The nitrogen contents of coal and biomass are similar ranging between 0.5 – 3 wt.%. During the gasification process, the nitrogen in the solid fuel is converted to NH_3, HCN and N_2 and the sulfur is converted predominantly to H_2S and SO_2. The presence of gases such as NH_3 HCN and H_2S in the fuel gas of a CLC process is undesirable as these gases are also oxidised by the oxygen carriers. Therefore to ensure complete combustion of a fuel gas containing high concentrations of sulfur and nitrogen containing gases, a greater amount of oxygen needs to be supplied to the fuel by increasing the circulation rate of the oxygen carrier (Berguerand and Lyngfelt, 2009).

H_2S and SO_2 will also react with metal oxide oxygen carriers forming sulfides and sulfates which could potentially deactivate the oxygen carrier. In a thermodynamic analysis that compared chemical-looping combustion using different oxygen carriers, Jerndal et al. (2006) found that of the most commonly studied metal oxide oxygen carrier systems, only Ni and Co based oxygen carriers were susceptible to sulfide and sulfate formation at SO_2 and H_2S partial pressures and temperatures that are encountered in CLC processes.

Recently, Shen et al.(2010) investigated the effect of H_2S in a synthetic syngas (H_2 + CO) on a NiO/Al_2O_3 oxygen carrier in a 1 kW prototype DFB CLC reactor. It was found that H_2S reacted with the Ni to form Ni_3S_2 and that the extent of Ni_3S_2 formation increased with fuel reactor temperature. The process was reversible and the oxygen carrier was fully regenerated in the air reactor; however, the sulfur was oxidised to SO_2 which exited the air reactor in the flue gases. Since the air reactor exhaust is released back into the atmosphere, downstream gas conditioning would be required to ensure SO_2 emissions to the atmosphere are in line with environmental legislation. In addition, Ni_3S_2 has a low melting point (789 °C), which caused sintering and loss of fine grain surface structure. As a result, the reactivity of the particles decreased with successive cycling. Ni-based oxygen carriers are therefore not suitable for use with fuels with high sulfur contents. In the case where the CLC fuel contains high levels of sulfur compounds, $CaSO_4/CaS$ may be more suitable as high H_2S and SO_2 partial pressures have been found to limit deactivation via the thermal decomposition of $CaSO_4$ into CaO and SO_2 (Song et al., 2008b).

2.5.3 Ash and other Particulate Matter

Ash is the inorganic residue that remains after combustion of a solid fuel and will be present in the chemical-looping combustor if the fuel is gasified in situ. The ash content of coal varies drastically; it can be as low as 2 wt.% or > 75 wt.%. Coal ash consists primarily of minerals such as silica, Al_2O_3, Fe_2O_3, CaO and smaller amounts of magnesia, titanium oxide and alkali and sulfur compounds (Higman and van der Burgt, 2008). The presence of coal ash in the CLC process is not expected to cause significant problems as it has a high melting point typically between 1200-1600 °C. The ash will therefore exist as particulates at CLC operating temperatures of 800-1200 °C. Particulate contamination of the fuel reactor flue gas can be a problem as particulates will deposit in downstream equipment and gas lines causing blockages and increased wear, however this can be largely avoided by using filters and cyclone separators (Kumar et al., 2009).

Rubel et al. (2011) studied CLC of a high ash containing coal in a TGA using a Fe-based oxygen carrier. Reportedly, the presence of ash caused no detriment to the oxygen carrier and it was found that some of ash components such as iron oxide and sulfate compounds were able to act as extra oxygen carriers increasing the oxygen carrying capacity of the sample. These findings suggest that ash could potentially be utilised as a low cost precursor for the production of cheap oxygen carriers.

Biomass ash is different from coal ash and consists primarily of salts. The major biomass ash components are potassium, calcium and phosphorous with smaller amounts of sodium, magnesium, iron, silicon and trace elements (Higman and van der Burgt, 2008). Biomass ashes are considered much more problematic than coal ashes as they typically have much lower melting temperatures. For example, some rice husk ashes have melting points of around 800 °C. Therefore even in CLC processes operating at low temperatures the presence of biomass ash can lead to agglomeration and de-fluidisation of the oxygen carrier bed (Weerachanchai et al., 2009). In addition, biomass generally has higher alkali metal contents which form vapours at temperatures above 700 °C (McKendry, 2002a). Alkali vapours will interact with the silica in the either the ash or soil (present as a biomass feed contaminant) to produce a highly aggressive slurry which can corrode the metal surfaces of a gasifier/chemical-looping combustor. As a consequence certain biomass varieties may not be suitable for use in a CLC process where the fuel is gasified in situ.

2.6 Literature Review: Key Findings

- Chemical-looping combustion of natural gas is relatively well understood and has demonstrated its commercial feasibility with extended pilot scale trials (Lyngfelt, 2011).
- The energy penalty associated with CO_2 capture from a CLC power plant is potentially much lower (~ 2-4.5 % points) (Ekström et al., 2009) than other near commercial CO_2 capture technologies such as MEA CO_2 capture (8-10 % points) (Wolf et al., 2005) and oxy-fuel combustion (15-20 %) (Shah and Christie, 2007).
- CLC CO_2 capture efficiencies are also potentially much higher (~ 98 %) (Johansson, 2002) compared to the other near commercial CO_2 capture technologies which have CO_2 capture efficiencies ranging between (80-90 %) (IPCC, 2005).
- Exergy studies found that to ensure a high process efficiency, the CLC reactor must be pressurised (20-30 bar) and generate high temperature flue streams (≥ 1200 °C) (Anheden and Svedberg, 1998, Brandvoll and Bolland, 2004, Ishida et al., 1987, Wolf et al., 2005). Therefore oxygen carriers must be able to withstand temperatures ≥ 1200 °C without sintering, fracturing or agglomerating.
- CLC of solid fuels is a more complex process that natural gas CLC and less well understood. Solid-solid reactions between the oxygen carrier and solid fuel are either negligible or do not occur, therefore solid fuels must first be gasified to transfer the carbon into the gas phase to allow it to react with the oxygen carrier (Jin and Ishida, 2004).
- The fuel can either be gasified in situ in the CLC reactor or ex situ in an upstream gasifier. The fuel is normally gasified in H_2O and CO_2; however the process is exothermic and slow. To

ensure reasonable rates of fuel gasification, high gasifier/CLC fuel reactor temperatures need to be maintained. If the fuel is gasified ex situ, heat needs to be transferred from the CLC process. This represents a significant technical issue that requires a complex system for high temperature heat integration (Brown, 2010).

- Gasifying the fuel in situ in a dual fluidised bed CLC reactor is beneficial as the endothermicity of the gasification process is intrinsically balanced by the heat conveyed by the circulating oxygen carrier particles. However a more complicated (and expensive) reactor is required that prevents the crossover of residual fuel particles to the air reactor where the fuel would be combusted generating CO_2 which cannot be recovered (Berguerand and Lyngfelt, 2009).

- Gasification of solid fuels produces syngas that primarily consists of CO and H_2 with CH_4 and CO_2 as minor components. Whilst CO and H_2 are more reactive towards the commonly studied oxygen carriers than CH_4 (major component of natural gas), solid fuel syngas is dirtier than natural gas containing higher levels of impurities. Tar vapours, alkali compound vapours and sulfur and nitrogen containing compounds such as H_2S, NH_3 and HCN are particularly problematic and can cause significant detriment to the CLC process and oxygen carrier (Higman and van der Burgt, 2008).

- The presence of tars in the fuel gas reduces fuel conversion efficiencies as they are difficult to combust in a CLC process. In addition decomposition of the tars on the surface of the oxygen carriers can lead to severe coking and temporary deactivation the oxygen carrier (Mendiara et al., 2011). Coking of the oxygen carrier also limits the overall CO_2 capture efficiency of the process as regeneration of the oxygen carrier in the air reactor produces CO_2 which cannot be captured (Corbella et al., 2005a, Corbella et al., 2005b).

- Sulfur and nitrogen containing gases such as H_2S, COS, NH_3 and HCN are also oxidised by the oxygen carriers. High levels of these gases can lead to reduced fuel conversion efficiencies if excess oxygen is not supplied to the fuel by way of a higher solid circulation rate (Berguerand and Lyngfelt, 2009). In addition H_2S and SO_2 will also react with Ni- and Co- based oxygen carriers to form sulfides and sulfates which deactivate the oxygen carriers (Shen et al., 2010). The sulfides and sulfates will also decompose at the higher temperatures in the air reactor (1000-1200 °C) releasing SO_x gases. Gas conditioning of the air reactor flue is therefore required to remove SO_x from the air reactor flue stream in line with environmental legislation.

- If the fuel is gasified in situ, ash will also be present in the CLC combustor. The presence of ash that melts at temperatures < 1200 °C can lead to agglomeration and de-fluidisation of the oxygen carrier (Weerachanchai et al., 2009).

- In order to limit the increased process costs associated with the shorter lifetimes of oxygen carriers used for CLC of solid fuels, cheap oxygen carriers are preferred. Oxygen carriers based on iron and manganese oxides, and $CaSO_4$ are particularly suitable as they are cheap, environmentally benign and they have high thermal stabilities (Mattisson et al., 2006a, Song et al., 2008a). Ilmenite (an iron and titanium ore, $FeTiO_3$) and Fe_2O_3-containing waste from iron and steel industry have also demonstrated potential as very low cost oxygen carrier precursors (Berguerand et al., 2011, Ryden et al., 2009).

- Ni- and Cu-based oxygen carriers are the most reactive of the commonly investigated oxygen carriers however it was concluded in this literature review that neither was suitable for applications as solid fuel CLC oxygen carriers. Ni-based oxygen carriers are expensive, toxic and are deactivated as a result of sulfide and sulfate formation when used as an oxygen carrier for medium to high sulfur containing fuels. In addition NiO/Ni is much more susceptible to coking than the other commonly studied oxygen carriers (Leion et al., 2009b). Cu-based oxygen carriers are unsuitable due to the low melting temperature of Cu (1045 °C) which limits CLC operating temperatures to > 950 °C (Jerndal et al., 2006).

- An alternative approach to using low cost oxygen carriers is to use highly reactive synthetic oxygen carriers. In particular, CLOU oxygen carriers have shown great potential for solid fuel CLC applications (Mattisson et al., 2009b). CLOU oxygen carriers provide a novel way of avoiding the slow and endothermic gasification step as the O_2 released by the CLOU oxygen carriers in the fuel reactor can react directly react with fuel dramatically improving fuel conversion rates. CuO/Cu_2O and Mn_2O_3/Mn_3O_4 are the most commonly investigated CLOU systems, but the low melting point of Cu (1045 °C) and the fact that CuO and Mn_2O_3 decompose at temperatures of 955 °C and 820 °C at an O_2 partial pressure of 0.05, limits operating temperatures to ~ 900°C and 950°C. Recently it was reported that mixed metal oxides based on 20 wt% Fe_2O_3/80 wt% Mn_2O_3 and $CaMn_{0.875}Ti_{0.125}O_3$ have the effect of stabilising the Mn^{3+}, and Mn^{4+} cations respectively, potentially allowing these CLOU systems to be used at temperatures > 1000 °C (Shulman et al., 2009, Ryden et al., 2011).

Chapter 3

Assessing the Suitability of Different Biomass Feedstocks for Processing via Gasification

3.1 Introduction

Biomass utilisation has received renewed interest over recent years in response to growing concerns over volatile fossil fuel prices, energy security, waste management and climate change (Demirbas et al., 2009). Biomass is widely considered to be a renewable source of energy, chemicals and fuels which is often available in large quantities and at a low cost as a by-product of agriculture and forestry. The use of responsibly sourced biomass[1] is potentially CO_2 neutral as the amount of CO_2 released during combustion is equal to the amount removed from the atmosphere during photosynthesis (although emissions from fertiliser, transport, farming and pre-treatment usually result in its use being slightly CO_2 positive). Furthermore, biomass utilisation coupled with carbon capture and storage (BECCS) can potentially result in negative CO_2 emissions *i.e.* a net removal of CO_2 from the atmosphere (van Vuuren et al., 2013, Gough and Upham, 2011, Azar et al., 2013). The use of biomass for the production of heat and power also offers advantages over other renewable energy sources such as wind and solar in that it is capable of providing uniform and uninterrupted distribution and can be easily integrated with fossil fuel power plants.

Gasification is one of the most efficient and flexible methods for processing biomass, providing a means to convert 60-90 % of the energy content of the biomass into a versatile gas with significantly improved distribution characteristics (*i.e.* can be transported *via* pipeline) (Reed et al., 1988). The gas that is produced can be used directly as a fuel in a gas turbine or fuel cell for heat and power generation, or as a feedstock for the production of liquid transportation fuels or chemicals. Gasification also enables the extraction of energy from a much wider range of materials that may not be considered fuels in the conventional sense, such as municipal solid waste (MSW) and sewage (Yassin et al., 2005, Fytili and Zabaniotou, 2008).

---

[1] Responsibly sourced biomass refers to either waste organic matter such as agricultural and forestry residues and MSW, sewage etc, or dedicated energy crops that have been grown on marginal or arid land that would not or cannot otherwise be used for crop/food production. The rate of use should not outstrip supply or rate of production.

Gasification is a complex process involving numerous parallel reactions resulting in a mixture of both useful and problematic products. Pyrolysis is the first step of the gasification process which involves the thermal decomposition of a solid fuel in the absence of oxygen to produce a complex mixture of gases, tars (oils), and char (containing ash). These species further react in gasification reactions with limited amounts of oxygen, steam and/or CO_2 to produce a gas with high concentrations of H_2 and CO.

Biomass pyrolysis yields significant amounts of vapour (typically 75-90 % of the initial weight compared with 20-40 wt.% for coal) a large proportion of which is tar (Reed et al., 2001). Whilst most of the primary tar compounds produced during pyrolysis are cracked and reformed into useful, combustible gases in subsequent high temperature gasification and combustion reactions, small amounts of secondary and tertiary tars are also formed which exit the gasifier with the product gas. Tars are operationally defined as any organic material in the product stream that is condensable in the gasifier, downstream processing steps or conversion devices (Milne et al., 1998). Its presence can lead to a whole host of downstream operational issues, particularly in advanced technologies such as fuel cells that have very low tolerances < 80 ppb tar contamination. The high tar content of gas produced from biomass gasification represents a substantial obstacle to commercialisation and wide scale deployment of the technology as downstream conditioning to remove tars exacts substantial economic and efficiency penalties on the process thus research focused on controlling and eliminating tar is important.

Our research at Imperial College has had two main focuses: the first being the development of a simple protocol for assessing the suitability of different biomass feedstocks for use as a fuel for gasification. The second involved investigating the impact of operating conditions such as temperature and presence of low-cost materials with potential catalytic activity on the pyrolysis product distribution with the aim of minimising or even eliminating residual tar compounds exiting the process.

This work employed a laboratory-scale fixed-bed reactor that could be operated in either a single stage or two-stage configuration with independent heating of the two stages (fig. 3.1) to gain new fundamental insights into the discrete tar conversion steps that take place during a pyrolysis or gasification process. For the first part of our work, the fixed bed reactor was operated in its single stage configuration to pyrolyse biomass feedstocks. The products obtained *i.e.* char and tars were then characterised using a range of analytical techniques to determine their chemical and physical properties. These experiments were targeted at gaining information to aid in the design of an optimal process for the gasification of a particular biomass or waste feedstock, informing on the most appropriate operating conditions and gasifier type.

The second strand of our research made use of the reactor in its two-stage configuration. Here, the first stage was employed as a tar generating zone and the 2nd stage as a tar cracking zone. The 2nd stage was operated empty to assess the effect of elevated temperatures (973-1173 K) on the tar yield, and loaded with a bed of either sand; sand and calcined limestone; or sand and calcined dolomite to investigate whether any additional cracking could be achieved by these materials.

This work was carried out as part of the training into hot-rod reactor operation biomass pyrolysis experimental design, biomass tar and other product recovery protocols (described in section 3.2). It was intended that the experience gained conducting this work would inform on the design of an upgraded version of the reactor for the specific purpose of investigating interactions between biomass tars and CLC oxygen carrier materials.

3.2 Experimental

The development and operation of the 2-stage reactor employed in this work has been reported in detail in a number of previous publications (Bolton et al., 1987, Pindoria et al., 1997, Collot et al., 1999, Monteiro Nunes et al., 2007, Monteiro Nunes et al., 2008, Dabai et al., 2010) and will be described only briefly here. The version of the reactor employed in this work is the same as that described by Dabai *et al.* (Figure 3.1) (Dabai et al., 2010).

3.2.1 Reactor Description

The first stage consisted of a 12 mm ID (2mm wall thickness) stainless steel tube, 200 mm in length with a welded flange connection at its base to allow for connection to the 2nd stage or directly to the tar trap (fig. 3.1). A Swagelok Tee fitting was connected to the top of the first stage which acted as the inlet for the 1st stage gas supply and allowed for placement of a thermocouple for 1st stage temperature control. Before each experimental run, 1 g of biomass (106-150 µm) was loaded into the 1st stage and supported in position with a strip of stainless steel wire mesh.

Figure 3.1: Diagram of the 2-stage, fixed-bed reactor, reproduced from Monteiro Nunes *et al*. (2007).

The 2^{nd} stage was made up of a 12 mm ID (2mm wall thickness) Incoloy 800 HT tube, 150 mm in length with welded top and bottom flanges. The top flange was designed to incorporate three equally spaced, lateral gas inlets such that the gas velocity could be varied independently of the 1^{st} stage. A spigot welded to the outside of the 2^{nd} stage allowed for placement of a thermocouple inside the 2^{nd} stage for controlling the temperature. For experiments investigating the effect of the different solids on the tar yield, 20 mm beds comprised of a 10 mm section of either 20 wt.% limestone or 20 wt.% dolomite (355-425 µm) mixed with 80 wt.% sand (500-710 µm) positioned between two 5 mm sections of sand were loaded into the 2^{nd} stage prior to assembly. The beds were held in position with a wire mesh plug.

The tar trap was a 12 mm ID, stainless steel U-tube fitted with a stainless steel flange to enable connection of the trap to either the 1^{st} or 2^{nd} stage. The tar trap was submerged in a liquid nitrogen bath for the duration of the experiment to condense as many of the tars and other volatile products as possible for analysis. The exit of the trap was packed with wire mesh to enhance the internal surface area of the tar trap and ensure efficient trapping of the volatile products in the form of aerosol droplets.

The reactor was heated via four copper electrodes that were attached to the outside of the reactor body at the top and bottom of each of the two stages. The reactor body acted as a resistance heater. The electrode that attached to the top of the 1st stage was rigid and acted as a support for the reactor. The other three electrodes were flexibly attached to the reactor with woven copper cables to allow for thermal expansion of the reactor body.

3.2.2 Materials

The biomass and waste samples used in this study were beech wood (BW), a rice husk originating from Brazil (BRH), a rice husk originating from Thailand (TRH) and a dried solids residue (sludge) obtained from waste water treatment at a textile manufacturing facility in Brazil (Textile Industry Residue, TIR). The BW and TRH samples have been used in previous pyrolysis and gasification related studies involving the hot-rod and wire-mesh reactors at Imperial College (Dabai et al., 2010, Dabai et al., 2014, Somrang, 2012). These samples were chosen as base-case biomass materials that could be used during preliminary investigations such that the results obtained could be directly compared with previous work, providing a direct measure of the training progress. Training was deemed complete when the user could provide reproducible (RSD < 5 %) mass balances for the pyrolysis of the different biomass materials that were consistent with the results produced by previous users. Furthermore, global rice production represent one of the largest sources of agricultural residue (~ 1000 Mt/y between 2006 and 2008) which predominantly comprised of rice husk (Bentsen et al., 2014). The scale at which rice husk is produced makes its exploitation as a fuel for the production of both centralised and decentralised power and fuel production a highly attractive pursuit. Here, two rice husks sourced from different geographical locations (Thailand and Brazil) were investigated to determine whether the location from which the rice husk was source affected the thermochemical breakdown behaviour of the rice husk and assess the potential of each material as a fuel for a gasification process. The textile industry residue was selected for reasons that (a) its chemical and elemental structure is significantly different from the traditional lignocellulosic biomass types investigated in this chapter (table 3.1); and (b) the textile industry produces significant quantities[2] of solid waste and yet very little work has focused on investigating its potential as a fuel for power and liquid fuel production.

Biomass samples were prepared by grinding in a high-shear cutting mill followed by sieving to obtain a size fraction of 106-150 μm. The ground and sieved biomass samples were then dried in small batches in an air-circulating oven at 308 K for 16 hours to remove the free moisture. Their ultimate and proximate analyses can be found in table 3.1.

The sand used in this investigation was supplied by David Balls Sand. Samples were prepared by sieving to a size fraction of 500-710 μm. The limestone originated from Purbeck, UK and the dolomite was supplied by Steetley Dolomite, ltd. The limestone and dolomite samples were prepared by grinding in a hammer mill followed by sieving to a size fraction of 355-425 μm. Different size fractions of sand and calcined limestone/dolomite were chosen so that they may be easily separated after the experiment for analysis. The XRF analyses of the sand, dolomite and limestone are present in table 3.2.

Table 3.1: Proximate and ultimate analyses of the biomass samples used in this study.

Feed	**Ultimate Analysis ^{daf}**						**Proximate Analysis**		
	C	**H***	**N**	**O^**	**S**	**Cl**	**Ash**	**Moisture**	**Volatiles**
Beech wood	49.3	5.5	0.3	44.9	<0.04	0.01	0.5	11.6	75
Brazilian rice husk	43.1	5.6	0.4	50.9	0.00	0.02	13.4	6.9	45.2
Thai rice husk	47.0	5.9	0.8	46.0	0.05	0.40	16.8	10.1	64.5
Textile Industry Residue	57.5	9.0	4.9	22.3	3.99	1.65	29.0	11.9	53.0

Values for the proximate analyses are calculated on the "as received" moisture.

^{daf} dry, ash-free basis.

* denotes that the value has been corrected for moisture content *i.e.* it does not include the hydrogen in the moisture.

^ the oxygen content was determined by difference.

The analysis for beech wood and Thai rice husk was carried out by TES Bretby, UK.

The analysis for the Brazilian rice husk and textile sludge residue was carried out by H. Jorge, Private Comm, 2010.

---

[2] Quantifying total solid waste produced by the textile industry is very difficult as data is fragmented and record keeping is poor (Lopes, 2013). To give some perspective, Lopes (2013) estimated that the solid residue produced by the clothing sector in the area of Bom Retiro, Sao Paulo, Brazil is ~ 175, 000 tons/year which is equivalent to ~ 2 % of annual solid waste production in Brazil.

Table 3.2: XRF Analysis of the Sand, Dolomite and Purbeck Limestone used in this study.

Constituent	Sand [wt.%]	Limestone [wt.%]	Dolomite [wt.%]
CaO	0.20	93.15	65.25
SiO_2	98.41	8.46	0.14
MgO	0.00	0.76	34.47
Fe_2O_3	0.10	0.55	0.04
Al_2O_3	1.09	0.47	0.08
P_2O_5	0.00	0.22	0.00
SO_3	0.00	0.15	0.00
K_2O	0.17	0.11	0.00
SrO	0.00	0.07	0.02
MnO	0.00	0.05	0.00
NiO	0.00	0.01	0.00
TiO_2	0.03	0.00	0.00

3.2.3 Operating Conditions

A standard set of conditions (summarised in table 3.3) was used when operating the reactor in either its single or 2-stage configuration. A heating rate of 1 K s^{-1} was used to heat the biomass sample in the 1st stage of the reactor from ambient to 773 K where it was held for 900 s to ensure complete pyrolysis of the sample. A flow of helium with superficial velocity of 0.1 m s^{-1} at 773 K was introduced at the top of the reactor to sweep the evolving volatiles from the sample bed downstream to the 2nd stage or tar trap.

The operating conditions of the 2nd stage were varied depending on the variable that was being tested. In all cases, the 2nd stage was heated to the experimental temperature (773-1173 K) prior to starting the first stage temperature program. When limestone or dolomite was used, the 2nd stage was heated to 1173 K for 300 s to ensure the dolomite and limestone was fully calcined before the 2nd stage was allowed to cool to the experimental temperature. During this period, the tar trap was not cooled, so as not to trap any of the CO_2 or H_2O released in the calcination period which would interfere with the product analysis. An additional flow of He was added through gas inlets in the 2nd stage flange such that the total superficial flow through the 2nd was controlled at 0.25 m s^{-1}.

3.2.4 Product Recovery

After each experiment, the reactor was dismantled and each of the reactor components was carefully washed with a 4:1 (v/v) solution of chloroform and methanol (150 ml) to recover any tars. The washings were then filtered into a flask using a pre-weighed Whatman no. 1 filter paper to collect any chars that were removed in the washing process. The bulk of the solvent was removed by evaporation on a rotary evaporator (BUCHI-Rotavapor 3000) operated at 353 K (80 °C) at 40 rpm for 10 minutes. The tars were then transferred to an aluminium beaker and placed in a recirculating air oven at 35 °C (308 K) for 2 hours (along with the chars that were removed from the 1st stage after the washing step) to ensure complete solvent removal from the samples. The tars and chars were then weighed to determine their respective gravimetric yields as a percentage of the initial weight of the biomass sample.

Table 3.3: Summary of experimental operating parameters.

Operating Conditions	1st Stage	2nd stage
Fuel type	Beech wood Thai Rice Husk Brazilian Rice Husk Textile Industry Residue	**N/A**
Fuel weight	1.000 g	**N/A**
Fuel Particle Size	106-150 µm	**N/A**
Bed type	N/A	**Variable: No bed** **20 mm Sand (500-710 µm)** **20 mm Sand & calcined Dolomite (10-40 wt.%)^** **20 mm Sand & calcined Limestone (20 wt.%)^**
Heating Rate	1 K s^{-1}	**Preheated to experimental temperature**
Hold Temperature	773 K	**Variable- 973 K** **1073 K** **1173 K**
Hold Time	900 s	**N/A**
Pressure	2.2 bar$_a$	**2.0 bar$_a$**
Carrier Gas	Helium	**Helium**
Superficial Velocity	0.1 m s^{-1}	**0.25 m s^{-1}**

^Limestone and dolomite 355-425 µm

3.2.5 Gaseous product detection

The concentration of CO_2, CO and CH_4 were measured in the outlet gas of the reactor after the tar trap via online gas detectors (table 3.4). CO_2 was condensed in the tar trap during the experiments and therefore had to be measured after the experiments when the tar trap was allowed to warm up to room temperature.

Table 3.4: Online gas analyser specifications.

Gas	Type	Model	Range	Accuracy
CO_2	Infrared	Servomex xentra 4200	0 – 100 vol.%	± 1 % of measured value
CO	Infrared	Servomex xentra 4201	0 – 25 vol.%	± 1 % of measured value
CH_4	Infrared	ADC	0 – 20 vol.%	± 1 % of measured value

3.2.6 Product Characterisation

Size exclusion chromatography (SEC)

Size exclusion chromatography (SEC) was used to determine the molecular size distribution of the tar samples. The SEC setup consists of a Mixed D column (300mm long, 7.5mm ID) with a polydivinylbenzene packing (5 µm particle size) supplied by Polymer Laboratories UK. The polydivinylbenzene packing acts as the stationary phase and n-methyl-2-pyrolidinone (NMP) is the mobile phase. The column is operated at 80 °C (353 K) and an NMP flow rate of 0.5 ml min^{-1}. Tar samples are dissolved in NMP and a 20 µL aliquot was injected into the column. The injected sample is separated as a function of the hydrodynamic volume of the individual sample components. Elution from the column is monitored with a Kauner diode array smartline 2600 detector. The detector measures UV absorbance at 300 nm of the separated sample as it elutes from the column. At this wavelength, NMP is partially transparent permitting reasonable monitoring of the eluent. Data is recorded and normalised, to enable comparison of tar samples generated under different conditions, with software developed at Imperial College.

Ultraviolet-Fluorescence (UV-F) Analysis

A Perkin-Elmer LS50 luminescence spectrometer was used to perform synchronous UV-F analysis on the tars generated in this investigation. Tar samples were dissolved in NMP and irradiated with UV light. The excitation wavelengths at which the sample was irradiated and the wavelength at which emissions form the sample were detected were varied between 250-800 nm. Emissions were detected at a wavelength 20 nm lower than the excitation wavelength to account for Stokes shift. UV-F analysis of the tar samples provides information on the degree of conjugation and to an extent, the size of tar components. Both the wavelengths of light that a sample component absorbs and that is subsequently fluoresced increase with degree of conjugation. A limitation of UV-F analysis is that it is insensitive to components with molecular masses exceeding 1000 atomic units (u) and will not detect components with a molecular mass greater than 3000 u (Kandiyoti et al., 2006).

Elemental Analysis

Elemental analysis of the tar and char samples to determine the concentration of carbon, hydrogen, nitrogen, sulfur and oxygen (by difference) was carried out using a Perkin Elmer 2400 at the University of Sheffield. Trace element analysis of the chars was carried out via neutron activation analysis (NAA) at the Centre for Analytical Research in the Environment, Silwood Park, Ascot (Asif and Parry, 1989).

Surface Area and Porosity Analysis

Pore surface area (BET) and pore volume distribution (BJH) measurements of the recovered chars and bed materials were determined using a Micromeritics Tristar 3000 N_2 sorption analyzer. Pore volume distribution in the macroporous range was investigated via mercury porosimetry using a Micromeretics IV 9500 series analyser. A more detailed description of both N_2 sorption and MIP analyses are provided in appendix A (sections A.1.1-A.1.3).

SEM Analysis

The sample's morphology was observed with a Hitachi S3400 SEM with 20 kV of accelerating voltage under high vacuum. The samples were coated with gold before SEM examination and images obtained by secondary electrons are presented here.

Char Reactivity Analysis

Char reactivity measurements with air or CO_2 were carried out conducted using a TGA (TA Q5000). 3-5 mg of the char sample was loaded onto a platinum pan and heated up under a flow of N_2 (25 ml.min^{-1}) to either 773 K or 1173 K for reactivity measurements with air or CO_2 respectively. The temperature was held at the set-point temperature for 5 minutes before the gas purge was switched to either air or CO_2. The weight loss of the chars was measured until constant weight was obtained. The normalised maximum reactivity (R_{max}) was obtained from the maximum slope of a plot of normalized weight against time, according to (eq 3.1).

$$R_{max} = -\frac{1}{W_o}\left(\frac{dW}{dt}\right) \qquad \text{(Equation 3.1)}$$

Here W_o is the initial weight of the char (daf basis), and (dW/dt) is the rate of weight loss, obtained from the first derivative of the weight loss curve. The repeatability of the R_{max} determination was ± 9 % of the value quoted. Only single determinations have been reported as repeatabilities are usually high and well within ± 5 % of the measured reactivity value.

3.3 Results

3.3.1 Single Stage Pyrolysis Experiments

Product Distribution

The product distributions for the pyrolysis of the different biomass feedstocks (fig. 3.2) demonstrated similar trends to those observed in the proximate analysis (table 3.1). Beech wood (BW) produced the largest quantity of volatiles (liquids and gases) with the textile industry residue (TIR) exhibiting the reverse trend producing the largest amount of char and least volatiles. Pyrolysis of the two rice husk species produced similar amounts of char and volatiles to the beech wood although; the Thai rice husk (TRH) produced approximately 40 % less tars than the Brazilian rice husk (BRH). BW pyrolysis yielded a similar amount of tars to the BRH at 35.5 wt.%. The tar yield in the case of the TIR pyrolysis was lower at 24 wt.% than the BW and BRH pyrolysis but higher than the tar yield of the TRH pyrolysis at 21.9 wt.%.

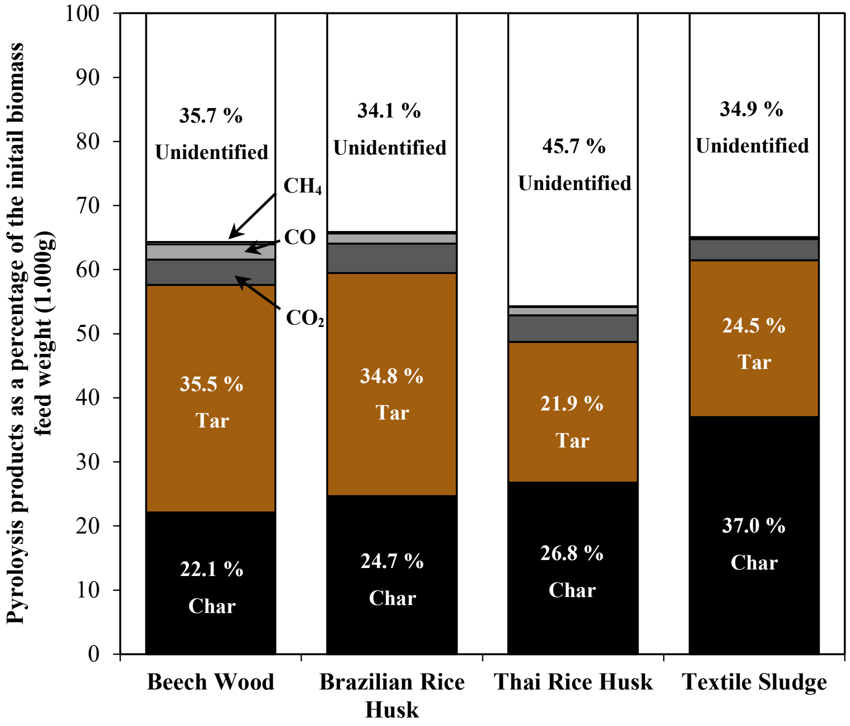

Figure 3.2: Distribution of the products generated during pyrolysis of four types of biomass feed in the single stage reactor presented on a dry, ash-free basis. All errors were within 0.5 % relative to the mean. **Gas Yields:** CO_2 = 3.9 % 4.6 % 4.2 %, 3.3 %; CO = 2.4 %, 1.6 %, 1.3 %, 0.2 %; CH_4 = 0.3 %, 0.2 %, 0.1 %, 0.2 % for BW, BRH, TRH and TS respectively. **Experimental Parameters**: ***1st stage***: **Feed** = Variable (1.000 g, 106-150 μm), **carrier gas** = He, **superficial velocity** = 0.1 m.s^{-1}, **inlet pressure** = 2.2 bar$_a$, **heating rate** = 1 K s^{-1}, **hold temperature** = 773 K, **hold time** = 900 s.

The amount of char produced during pyrolysis increased with increasing ash content as determined by proximate analysis (table 3.1). This is consistent with previous works that have concluded a high ash content favours char forming reactions (Zanzi et al., 2002, Venderbosch and Prins, 2010). Yields of the measured combustible gases (CO and CH_4) were relatively low in all cases ranging from 0.3 wt.% for TIR to 2.7 wt.% for beech wood. CO_2 yields were slightly higher in the region of 3-5 wt.%.

Between 35-45 wt.% of the pyrolysis products could not be accounted for. It is likely that the unidentified products include compounds such as light tar species, light hydrocarbons, alcohols, water and hydrogen that were either not efficiently trapped during the experiment or lost during the product recovery procedure. Previous work with the same reactor showed that a large fraction (in the region of 20 wt.% depending on the biomass variety) of the products produced during the pyrolysis of dried biomass was H_2O (Dabai et al., 2010). The implications of these results are discussed in section 3.3.2.

Tar Analysis

Size Exclusion Chromatography (SEC) Analysis

SEC was employed to provide information on the molecular size distribution of the tars. Each of the chromatograms has two peaks separated by a region of low absorption intensity revealing that the tar samples have a bimodal molecular size distribution (fig. 3.3). The first (excluded) peaks correspond to the elution of high molecular mass tar constituents that are either completely or partially excluded from the porosity of the column. Here, the maxima of the first peaks are all just within the calibrated range of the column (elution times of 11.4-11.7 minutes) corresponding to molecular masses in the region of 440-550 x 10^3 u.

The second (retained) peaks in the SEC chromatograms correspond to the elution of lower molecular mass tar constituents which are retained and can therefore be fully resolved by the column. The molecular mass corresponding to the maximum peak intensities have been estimated and are provided in figure 3.3.

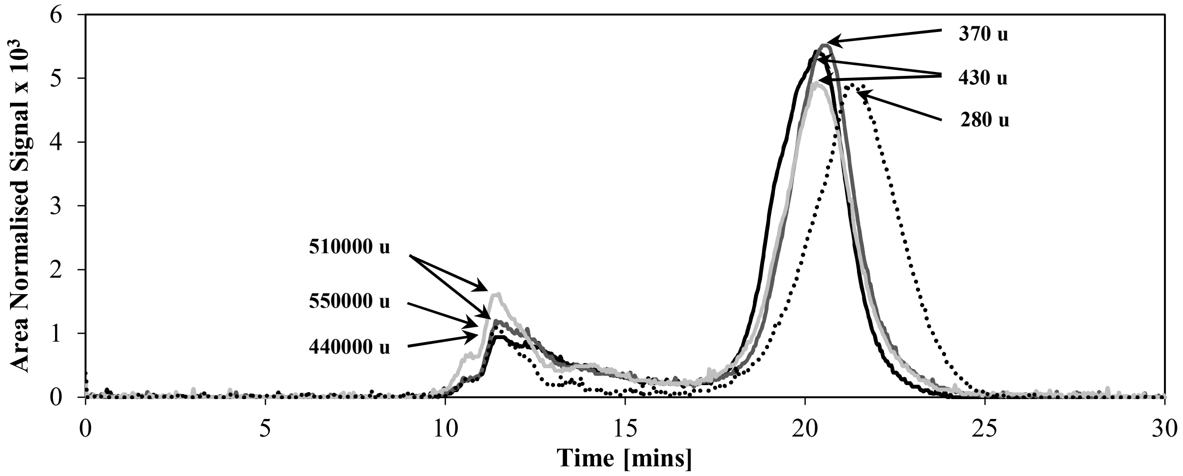

Figure 3.3: SEC analyses of the tars recovered after pyrolysis of the four types of biomass feed in the single stage reactor. **Experimental Parameters**: ***1st stage***: **Feed** = Variable (1.000 g, 106-150 μm), **carrier gas** = He, **superficial velocity** = 0.1 m.s^{-1}, **inlet pressure** = 2.2 bar$_a$, **heating rate** = 1 K s^{-1}, **hold temperature** = 773 K, **hold time** = 900 s.

▬ BW; ▬ BRH; ▬ TRH; ········ TIR

The most notable difference in the SEC chromatograms is in the elution time of the lighter fraction (2nd peak) of the TIR tars. The maximum intensity appears almost one minute after the equivalent peaks in the chromatograms of the other tars indicating that the lighter fraction of the TIR tars has a lower average molecular mass compared with the tars produced from pyrolysis of the more conventional biomass varieties.

Subtle differences can also be observed in the SEC chromatograms of the pyrolysis tars of the two rice husk species. The TRH appears to have a slightly larger proportion of the heavier tar fraction relative to the lighter fraction compared with the Brazilian variant. The maximum peak intensity of the retained peak in the chromatogram of the TRH tars also appears at a slightly shorter elution time than the BRH indicating that the lighter fraction of the TRH tars has a higher average molecular mass of 430 u compared with 370 u in the case of the BRH tars.

Ultraviolet Fluorescence (UVF) Analysis

Ultraviolet fluorescence (UVF) spectroscopy was used to provide information on the degree of conjugation and to some extent, the size of the different species in the tar samples (fig. 3.4). UVF is only able to detect compounds with molecular masses < 3000 u and so does not provide any information on the tar species characterised by the excluded peaks in SEC spectrums. The UVF spectra of the three biomass samples consist of a broad emission spectrum between ~270–450 nm with two maxima at ~320 nm and ~350-360 nm (the small peaks in each of the spectra at ~290 nm is caused by fluorescence emissions from the solvent- NMP). The presence of the two, relatively well defined peaks indicates that the lighter tar fraction of the biomass tars (as characterised by SEC) broadly consist of two molecular groups that differ by extent of conjugation.

There are notable differences between the UVF spectra of the tars derived from the two rice husk species (fig. 3.4). The first peak in the spectra of the BRH tars at ~320 nm is far more intense than the second peak at the higher wavelength of ~355 nm whereas the two peaks in the spectra of the tars derived from the Thai variant are of equal intensity. This finding suggests there is a larger proportion of the less conjugated tar species in the BRH tars relative to the more conjugated tar species; whereas the tars derived from the Thai variant appears to contain similar quantities of the two conjugated molecular groups.

The spectra of the pyrolysis tars derived from the TIR is distinctly different from the spectra of the three biomass derived tars- it is broader and consists of a large central peak at around 340 nm flanked by two less intense peaks at 310 nm and 390 nm. This means that there is more variation in the conjugation extents of the tar species that make up the lighter tar fraction of the pyrolysis tars derived from the TIR.

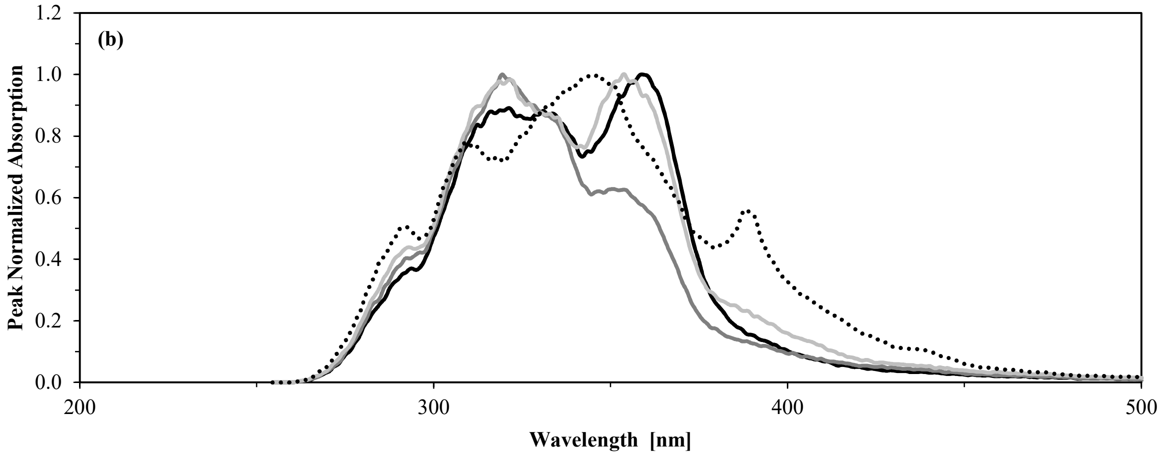

Figure 3.4: UVF analyses of the tars recovered after pyrolysis of the four types of biomass feed in the single stage reactor. **Experimental Parameters**: ***1st stage***: **Feed** = Variable (1.000 g, 106-150 μm), **carrier gas** = He, **superficial velocity** = 0.1 m.s^{-1}, **inlet pressure** = 2.2 bar$_a$, **heating rate** = 1 K s^{-1}, **hold temperature** = 773 K, **hold time** = 900 s. ——— BW; ——— BRH; ——— TRH; ········ TIR

Elemental Analysis

Elemental analysis of the different pyrolysis tars (table 3.5) revealed that in all cases, the tars have slightly higher carbon contents and slightly lower oxygen contents than the parent biomasses. The compositional trends in the carbon and oxygen contents of the different pyrolysis tars are the same as those observed for the different parent biomass feedstocks. The BW and BRH tars have similar carbon and oxygen contents of around 55 wt.% and 40 wt.% respectively whereas the TRH and TIR tars have slightly higher carbon contents of around 60 wt.% and lower oxygen contents of 33 wt.% and 22 wt.% respectively.

The high oxygen contents of the lignocellulosic biomass derived tars are similar to those stated elsewhere in the literature of around 35-40 wt.% suggesting that these tars are highly acidic and polar in nature (Oasmaa and Czernik, 1999, Lu et al., 2009). The pH of biomass derived tars with similar elemental compositions is typically reported as being in the region of 2-3. A high oxygen content is also indicative of a high water content which typically ranges between 15 and 30 wt.% and is difficult to remove owing to the hydrophilic nature of the tars. The highly acidic nature and high water content of biomass derived tars is a highly problematic as it can lead to significant corrosion related issues in downstream pipelines and equipment of a biomass gasification or pyrolysis facility (Özçimen, 2013, Milne et al., 1998). Unfortunately, quantification of the water content and acidity of the tars was not possible at the time of this study.

The heating values of the tars were also estimated from the elemental compositions and are summarised in Table 3.5. Previous studies have found good agreement between experimentally obtained heating values and theoretical heating values of pyrolysis tars calculated from their elemental compositions using the modified Dulong's formula for bio-oils (eq. 3.2) (Demirbas et al., 1997). Information relating to the heating value of tars is particularly useful if the purpose of the thermochemical conversion process is to generate a bio-oil for fuel applications.

$$\text{HHV (MJ/kg)} = 0.335(\text{wt.\%C}) + 1.423(\text{wt.\%H}) - 0.154(\text{wt.\%O}) \qquad \text{(Equation 3.2)}$$

When the purpose of the thermo-chemical conversion process is to generate a bio-oil for fuel applications, a high oxygen content and related high acidity and water content tends to result in an unstable bio-oil with a short shelf life. Other consequences of a high oxygen containing bio-oil include high viscosity and boiling points, poor miscibility with conventional hydrocarbon fuels and reduced energy density (see table 3.5) which diminishes the capacity and commercial attractiveness of such an oil to fulfil applications as a drop-in renewable fuel substitute or additive.

The low oxygen content of the TIR derived tar might suggest that it possesses the most favourable characteristics as a potential bio-oil fuel in that it has the highest energy density and is likely to be less polar, less acidic and therefore more stable than the other tars investigated. However, the tar yield in the case of TIR pyrolysis was the lowest at 30.4 wt.% (or 15 wt.% if the ash content is also considered) and contains relatively large quantities of nitrogen which will contribute to increased NO_x emissions if burnt in a conventional internal combustion engine.

Table 3.5: Summary of the elemental analysis and calculated HHV values for the tars produced from the pyrolysis of the different biomass feedstocks in the single stage reactor.

Experimental Parameters: ***1st stage***: **Feed** = Variable (1.000 g, 106-150 μm), **carrier gas** = He, **superficial velocity** = 0.1 $m.s^{-1}$, **inlet pressure** = 2.2 bar_a, **heating rate** = 1 K s^{-1}, **hold temperature** = 773 K, **hold time** = 900 s.

Tars	Ultimate Analysis (wt.%) ^{daf}				Atomic Ratio			HHV (MJ kg^{-1})
	C	H	N	O*	O/C	H/C	N/C	
Beech wood	55.4	6.4	0.1	38.1	0.5	1.4	0.00	21.8
Brazilian rice husk	53.1	5.9	0.9	40.0	0.6	1.3	0.01	20.1
Thai rice husk	59.0	6.7	1.3	33.0	0.4	1.4	0.02	24.2
Textile industry residue	61.5	8.7	8.1	21.8	0.3	1.7	0.11	29.6

* The oxygen content was determined by difference

Char Analysis

A range of analytical techniques were employed to ascertain some important chemical and physical properties of the chars produced from pyrolysis of the different biomass feedstocks investigated in this study.

Elemental Analysis

Trends in the elemental analysis of the chars were different to those observed for the tars (table 3.6). The BW char had the highest carbon content and lowest oxygen content at 80.3 wt.% and 16.6 wt.% respectively. The carbon contents of the rice husk derived chars were slightly lower at 72-75 wt.%. The TIR char was found to have the lowest carbon content and highest oxygen content at 61.9 wt.% and 28.7 wt.% respectively. Interestingly, the ultimate analysis of the TIR char was very similar to that of the tar and it contained a larger proportion of oxygen compared with its respective tar.

Table 3.6: Summary of the elemental analysis and calculated HHV values for the tars produced from the pyrolysis of the different biomass feedstocks in the single stage reactor.

Experimental Parameters: ***1st stage***: **Feed** = Variable (1.000 g, 106-150 μm), **carrier gas** = He, **superficial velocity** = 0.1 m.s^{-1}, **inlet pressure** = 2.2 bar$_a$, **heating rate** = 1 K s^{-1}, **hold temperature** = 773 K, **hold time** = 900 s.

Chars	**Ultimate Analysis (wt.%) ^{daf}**				**Atomic Ratio**			**HHV (MJ kg^{-1}) ^{db}**
	C	**H**	**N**	**O***	**O/C**	**H/C**	**N/C**	
Beech wood	80.3	2.7	0.3	16.6	0.2	0.4	0.0	30.7
Brazilian rice husk	74.6	3.1	1.4	20.9	0.2	0.5	0.0	18.2
Thai rice husk	72.3	3.0	1.0	23.7	0.2	0.5	0.0	16.6
Textile industry residue	61.9	5.1	4.3	28.7	0.3	1.0	0.1	8.5

* The oxygen content was determined by difference

Trace Element Analysis

In addition to ultimate analysis, the concentrations of certain trace elements in the chars were determined via nuclear activation analysis (fig. 3.5). Determining the concentration of the alkali and alkaline earth metals such as K, Na, Ca and Mg is particularly important given their known catalytic activity during pyrolysis, char gasification and tar cracking interactions (Raveendran et al., 1995, Kannan and Richards, 1990, Senneca, 2007, Degroot et al., 1988, Bridgwater, 2008). The TIR char was found to contain the largest concentrations of sodium, calcium and magnesium however the TRH char contained the largest amount of potassium. The TRH char also contained more of all the alkaline and alkaline earth metals measured in this study (Na, K, Ca and Mg) than the BRH char, which in the case of potassium was over double the amount detected in the BRH char. The BW char also contained reasonably high concentrations of the alkali and alkaline earth metals particularly Ca of which it contained around 3-4 times more than the rice husk chars. The BW char contained less magnesium than the other chars but a similar amount of potassium to the BRH and TIR chars.

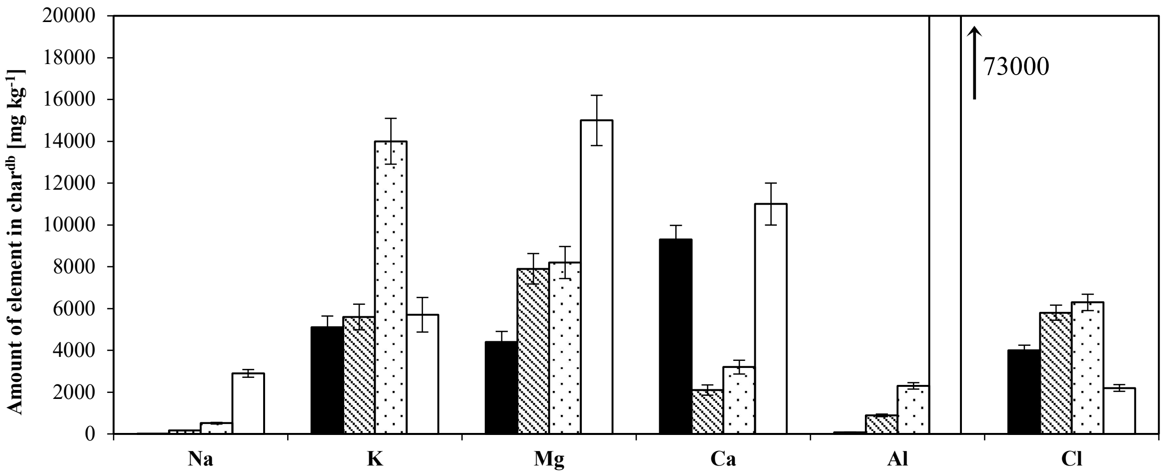

Figure 3.5: The amounts of certain important inorganic elements present in the chars produced during pyrolysis of the different biomass feedstocks in the single-stage hot-rod reactor determined via nuclear activation analysis. **Experimental Parameters:** ***1st stage***: **Feed** = Variable (1.000 g, 106-150 μm), **carrier gas** = He, **superficial velocity** = 0.1 m.s^{-1}, **inlet pressure** = 2.2 bar$_a$, **heating rate** = 1 K s^{-1}, **hold temperature** = 773 K, **hold time** = 900 s. BW; ▧ BRH; ⊡ TRH and☐ TIR.

BET/BJH and Mercury Intrusion Porosimetry (MIP) Analysis

Surface area and pore size distribution analysis of the char particles via BET/BJH N_2-adsorption analysis revealed that the TIR char had the highest surface area at 41 m^2 g^{-1} (table 3.1) and largest concentration of pores in the meso-porous region (fig. 3.6 (a)). The cumulative volume of pores of the TIR char as measured by BJH analysis was almost two orders of magnitude larger than the chars produced from the other biomass feedstocks at 0.11 cm^3 g^{-1}. The BW char was found to have the smallest surface area and lowest volume of mesopores. There were also some differences between the two rice husk species with the BRH char exhibiting almost double the surface area and volume of mesopores compared with the BRH char.

Analysis of the macroporosity via mercury porosimetry revealed that the TIR char had the least macro-porosity at 0.12 cm^3 g^{-1} compared with ~ 0.40-0.43 cm^3 g^{-1} for the other chars (Figure 3.6 (b), Table 3.1). The average pore sizes varied substantially for the 5-10^5 nm pore size range. The BW char was found to have the largest average pore size at 1482 nm. The average pore sizes of the rice husks were an order of magnitude smaller than the BW at 131 nm and 250 nm for the BRH and TRH chars respectively. The TIR char had the smallest average pore size which was an order of magnitude smaller again at 11 nm. A trend can be observed between the initial ash content of the parent biomass and the surface area, volume of mesopores and average pore size in both the meso- and macro- porosity regions of the char with the higher ash content appearing to favour smaller pores and a higher surface area.

Table 3.7: Summary of BET/BJH N_2-adsorption and MIP results for the chars obtained after pyrolysis of the different biomass feedstocks in the single-stage, hot-rod reactor.

Experimental Parameters: ***1st stage***: **Feed** = Variable (1.000 g, 106-150 μm), **carrier gas** = He, **superficial velocity** = 0.1 m.s^{-1}, **inlet pressure** = 2.2 bar$_a$, **heating rate** = 1 K s^{-1}, **hold temperature** = 773 K, **hold time** = 900 s.

Char	BW	BRH	TRH	TIR
Surface Area [m² g^{-1}]	1.17	12.22	6.90	41.32
Average Pore size (1.7 - 300 nm) [nm]	51	14	10	7
Cumulative vol. of pores (1.7 - 300 nm) [cm³ g^{-1}]	6.37 x 10^{-3}	2.78 x 10^{-2}	1.73 x 10^{-2}	0.106
Average Pore size (5 – 10^5 nm) [nm]	1482	131	250	11
Cumulative vol. of pores (5 – 10^5 nm) [cm³ g^{-1}]	0.433	0.401	0.431	0.115

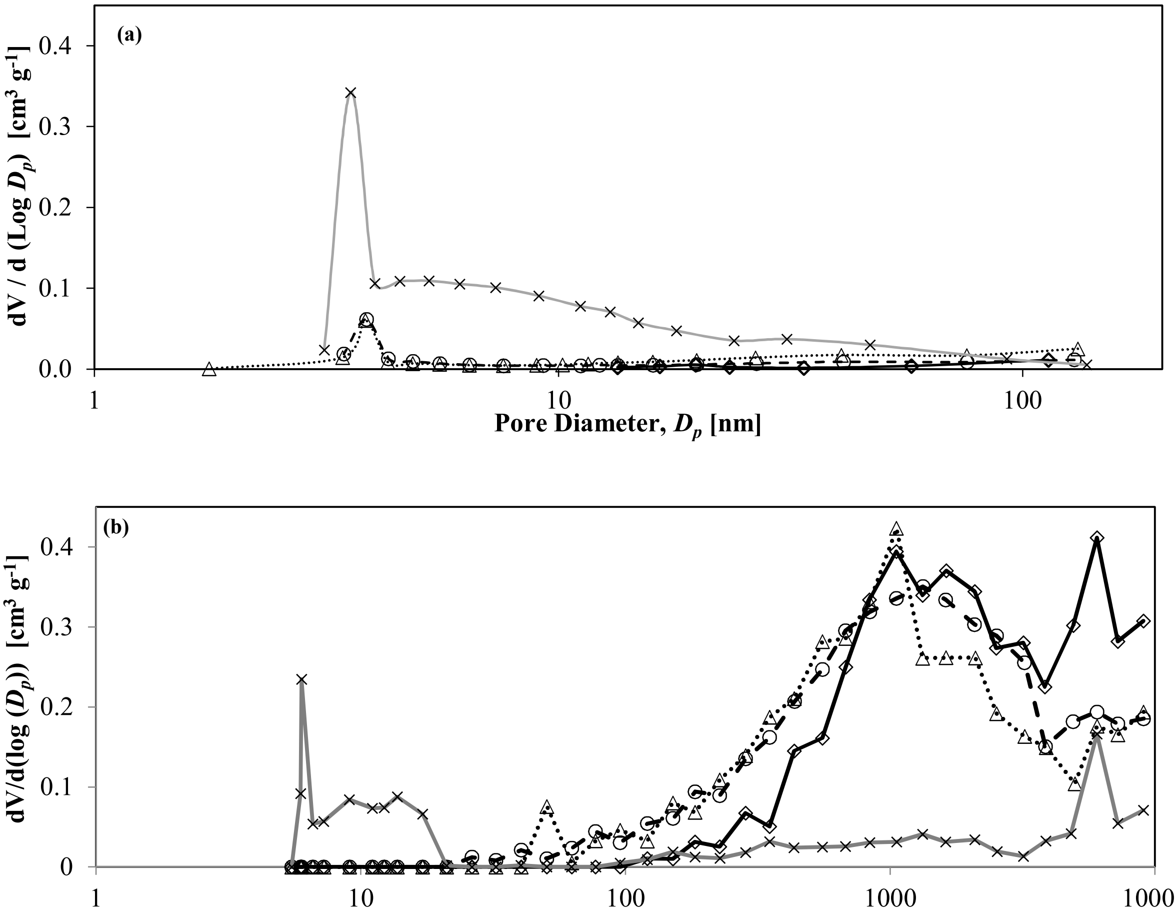

Figure 3.6: Pore size distributions for (a) the pore size range 1.7-300 nm as determined via BJH N_2 adsorption analysis and (b) the pore size range 5-10000 nm as determined via mercury porosimetry for the chars obtained after pyrolysis of the different biomass feedstocks in the single-stage, hot-rod reactor. **Experimental Parameters**: ***1st stage***: **Feed** = Variable (1.000 g, 106-150 μm), **carrier gas** = He, **superficial velocity** = 0.1 m.s^{-1}, **inlet pressure** = 2.2 bar$_a$, **heating rate** = 1 K s^{-1}, **hold temperature** = 773 K, **hold time** = 900 s. ―◇― BW; ···△··· BRH; – ○ – TRH and ―×―TIR.

SEM Analysis

Comparing the surface structures and morphologies of the different char particles via SEM analysis, it can be seen that the BW char particles appear to have the most fibrous structure and largest pores whilst the TIR chars have the smallest pores (fig. 3.7 (a,d)). The two rice husk chars appear to have slightly smaller pores (fig. 3.7 (b,c)) than the BW char. These observations are consistent with the trends in macroporosity determined via mercury-porosimetry. The surface of the rice husk and TIR chars also appear to be coated with a lot more ash (lighter-coloured areas in fig. 3.7 (a,d)) compared with the BW char particles which in the case of the rice husk chars appears to have formed some sort of molten phase.

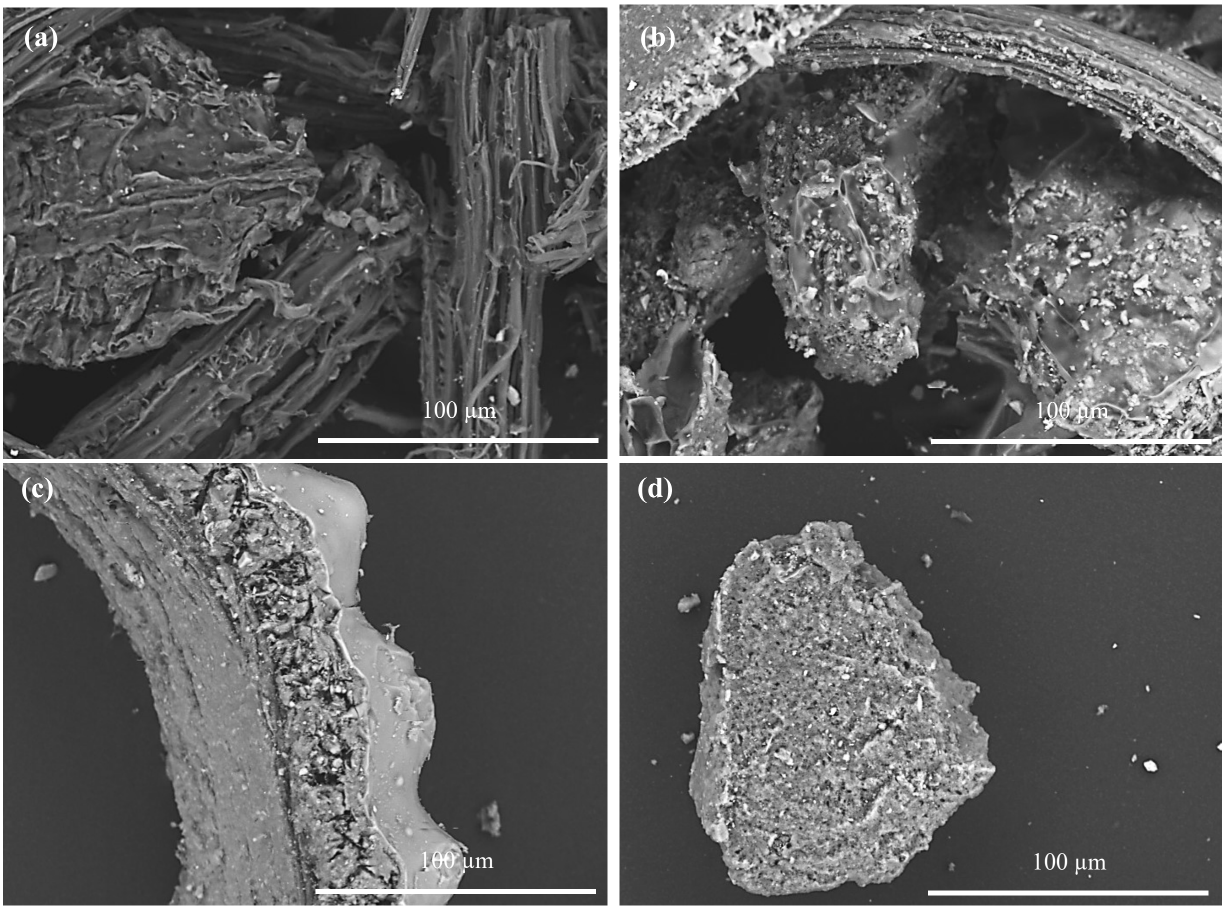

Figure 3.7: SEM images of the chars produced during the pyrolysis of the different feeds in the single stage reactor. (a) BW chars, (b) BRH chars, (c) TRH char, (d) TIR char. **Experimental Parameters**: ***1st stage***: **Feed** = Variable (1.000 g, 106-150 µm), **carrier gas** = He, **superficial velocity** = 0.1 m.s^{-1}, **inlet pressure** = 2.2 bar$_a$, **heating rate** = 1 K s^{-1}, **hold temperature** = 773 K, **hold time** = 900 s.

Char Reactivity Analysis

Thermogravimetric analysis of the chars was used to determine their relative reactivities in air at 773 K and CO_2 at 1173 K. Figure 3.8 depicts the thermogravimetric data for the CO_2 gasification experiments with the different chars. The chars underwent additional weight losses during the pre-heating section of the experiment. The weight loss experienced by each of the chars can be seperated into four distinct regions (A-D) corresponding to maxima in the normalised reactivity profiles, labelled A*-D* in (fig. 3.8).

The first weight-loss region (A) occured as the chars were heated from 323-1173 K and corresponds to the loss of unbound moisture. The second and third weight loss regions (B and C) occured as the chars were heated from 383-1173 K at a heating rate of 1 K s^{-1} under a 50 ml min^{-1} purge of N_2 and the final weight loss (D) is a result of char gasification as the gas purge was switch from N_2 to CO_2 1173 K. A clearer depiction of the weight loss and reactivity profiles with respect to temperature for the pre-heating step (323 K to 1173 K) of the gasification experiments is provided in Figure 3.9.

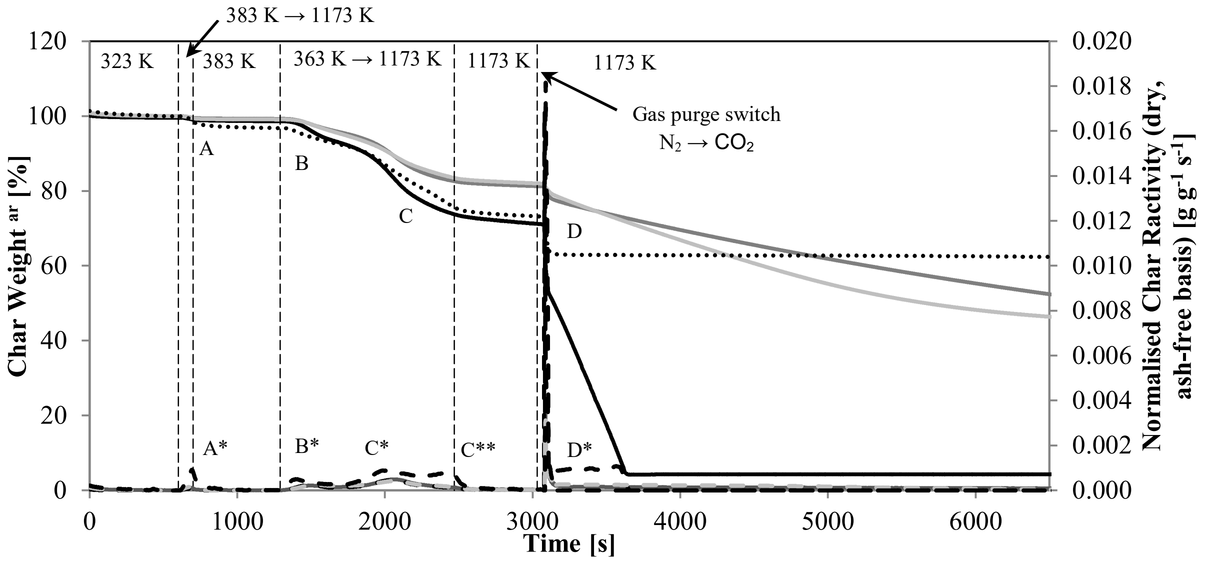

Figure 3.8: Depiction of the CO_2 gasification reactivity experiments for the different biomass chars via thermogravimetric analysis. Weight loss curves: ▬▬ BW; ▬▬ BRH; ▬▬ TRH; ········ TIR; normalized reactivates: dashed line equivalents, TIR is the dash and dot line.

The BW, BRH and TIR chars experienced weight losses equivalent to ~ 10 wt.% during heating from 383-1173 K, which increased further to 30 wt.% when heated to 1173 K. The weight loss in the case of the TIR char was more severe, equivalent to 20 wt.% at 773 K and 70 wt.% at 1173 K. The maximum rate of weight loss for the pre-heating region B (peak B*) occurred at ~500 K for the BW, BRH and

TRH chars and at the slightly lower temperature of ~460 K in the case of the TIR (fig. 3.8). This weight loss was likely caused by residual pyrolysis of the char matrix or vaporisation of secondary or tertiary tar compounds that had condensed in the char matrix during the initial pyrolysis of the chars.

The maximum in the normalised reactivity profile corresponding to the third weight loss region C (peak C*), occurred at the higher temperature of ~890 K for the BW and rice husk chars and 850 K in the case of the TIR char (fig. 3.9). There is also an additional peak (C**) in the normalised reactivity profile for the TIR char at ~ 1120 K. These weight losses were likely due to further pyrolysis of the char matrix and vaporisation/cracking of refractory secondary and tertiary tar compounds that condensed in the char matrix during the initial pyrolysis of the chars in addition to a small amount of pyrolytic gasification at the higher temperatures. The high O/C ratio of the TIR char compared with the other chars infers a less stable char matrix that through further pyrolytic decomposition would yield more-oxygenated products with greater oxidising potentials. The greater oxidising potential of the TIR char pyrolysis products in combination with the higher concentration of catalytic ash constituents is likely to have lead to more pronounced pyrolytic gasification at the higher temperatures explaining the greater extent of weight loss over the pre-heating period and the occurance of an additional peak (C**) in the normalised reactivity profile of the TIR char at 1120 K.

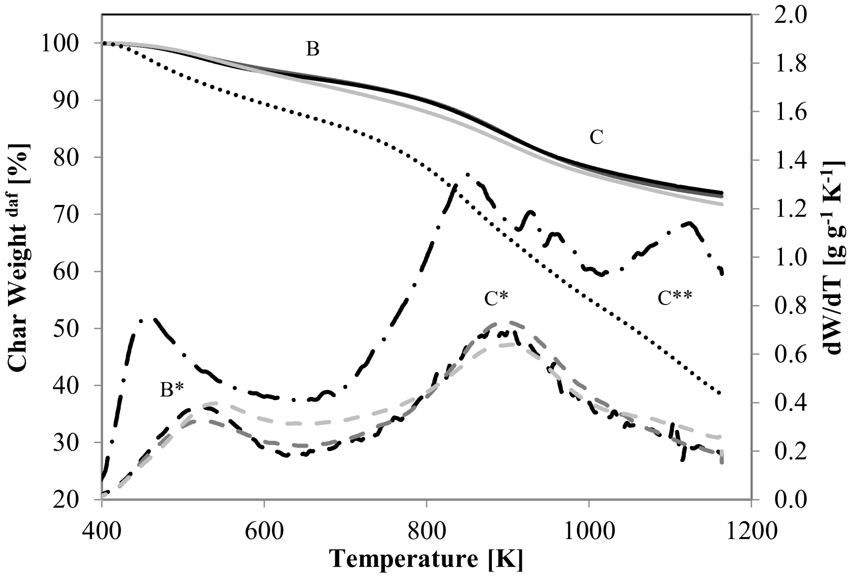

Figure 3.9: TGA/DTGA analysis of chars derived from pyrolysis of the different biomass varieties in the hot-rod reactor during heating to 1173 K at a heating rate of 1 K s^{-1} under a N$_2$ flow of 50 ml min^{-1}. —— BW; —— BRH; —— TRH; ······ TIR.

The isothermal normalised reactivities of the chars with air at 773 K (fig. 3.10) and CO$_2$ at 1173 K (fig. 3.11) as a function of conversion reveal some interesting behaviours. The BW and TRH chars exhibited the highest peak reactivites in air at 773 K exhibiting a maximum normalised reactivity of 0.012 g g^{-1}

s^{-1}; and observed similar reactivity profiles (fig. 3.10). In both cases, the combustion reaction rate increased reaching maxima at conversion values of 0.37 and 0.12 for the BW char and TRH char respectively.

The peak normalised reactivites of the BRH and the TIR chars were lower than those observed for the BW and TRH chars at 0.007 s^{-1}. These chars also exhbited similar combustion reactivity profiles (albeit different profiles to the BW and TIR chars) reaching maximum reactivities at a conversion of < 0.02 followed by a steady monotonous decline with increasing conversion.

The reactivity profiles of the chars with CO_2 at 1173 K were quite different to those observed for the air reactivity experiments at 773 K. In the case of the BW and rice husk chars, the reactivity profiles show an initial surge in reactivity coinciding with the entry of the reactive gas, which rapidly declines to a much lower stable value. The BW char transitioned to the post surge stable reactivity at a conversion of 0.27 and achieved complete char gasification conversion after 10 minutes. The BRH and TRH char gasification transitioned at a much lower conversion of around 0.05 and due to the much slower post-surge gasification reactivites required much longer time periods of 140 minutes and 70 minutes for the BRH and TRH respectively to achieve complete conversion. The reactivity profile for the TIR char was different to those observed by the other chars in that the initial surge persisted for close to the entire conversion range, transitioning to the post-surge reactivity behaviour at a conversion of ~0.89 achieving complete conversion after ~2 minutes.

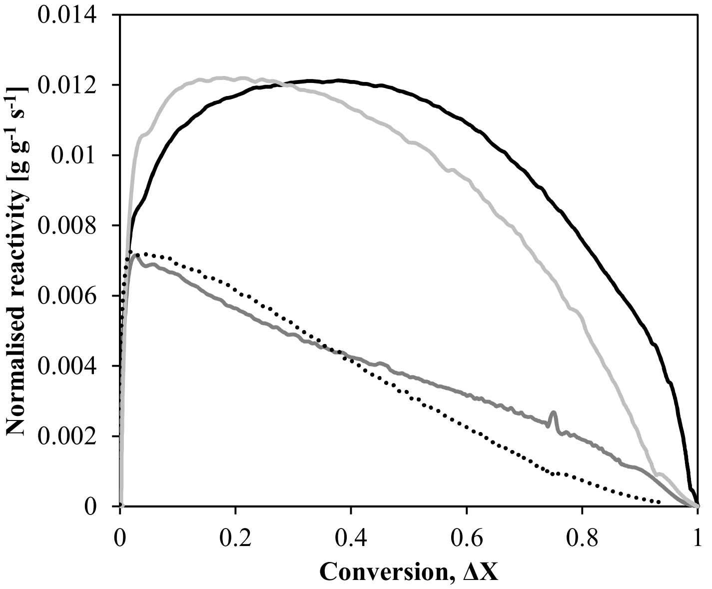

Figure 3.10: Normalised combustion reactivities of the four different chars with air at 773 K as a function of conversion. ——— BW; ——— BRH; ——— TRH; ········ TIR.

As indicated above, the TIR char exhibited the highest initial peak reactivity of 0.054 g g^{-1} s^{-1} with the BW char displaying the second highest reactivity of 0.024 g g^{-1} s^{-1}. The BRH and TRH chars were significantly less reactive with peak normalised reactivities of 0.005 g g^{-1} s^{-1}. The stable residual reactivities measured at a conversion of 0.5 (or 0.9 for the TIR char) were between 14-17 times lower than the maximum reactivities measured during the initial surge for the BW, TRH and TIR chars and 35 times lower in the case of the BRH char. The trend in residual char gasification reactivities with CO_2 at 1173 K was: TIR char > BW char > TRH char > BRH char.

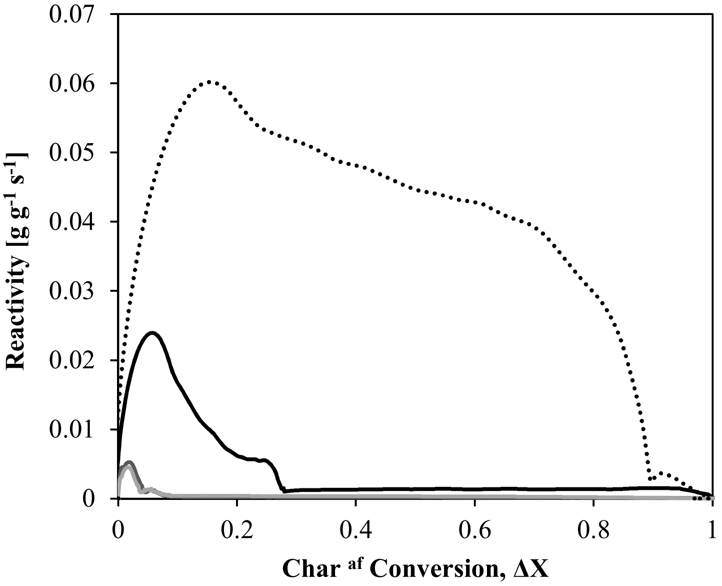

Figure 3.11: Normalised CO_2 gasification reactivities of the four different chars at 1173 K as a function of conversion. ——— BW; ——— BRH; ——— TRH; ········ TIR.

3.3.2 Discussion of Single Stage Pyrolysis Experiments

Pyrolytic decomposition of biomass and other carbonaceous materials is a complex process involving a multitude of different reactions. The resultant distribution and nature of the pyrolysis products depends on a range of different process parameters and fuel properties. In this work, the four different biomass varieties were prepared and tested in the same way such that any differences in the pyrolysis product distributions were a result of inherent differences in the properties of the parent biomass feeds. The O/C ratio of the parent biomass, lignocellulosic composition, ash content and morphology, pore structure and surface area development during pyrolysis have all been reported to affect the pyrolysis behaviour of a particular biomass fuel (Yaman, 2004, Yang et al., 2006, Zanzi et al., 2002, Raveendran et al., 1995, Raveendran et al., 1996, Raveendran and Ganesh, 1998, Bridgwater et al., 1999).

The most striking differences in the pyrolysis product distributions is between the two rice husks species with the Brazilian variant releasing ~ 40 wt.% more tar than the Thai rice husk. Whilst there were small differences in the elemental compositions of the parent biomasses as well as small differences in the surface areas and morphologies of the resultant chars; the most likely cause for the differences in the tar and gas yields between the TRH and BRH pyrolysis experiments was the difference in potassium concentration. The potassium concentration of the TRH was more than double the concentration of the other biomass varieties which all contained similar quantities.

Pyrolysis of biomass varieties containing large amounts of ash are typically found to produce less tar and more char due to the catalytic effect and higher surface area provided by the inorganic ash constituents on which secondary tar condensation/char forming reactions can take place (Bridgwater et al., 1999, Philpot, 1970). An exception to this rule is when the ash contains high concentrations of potassium which has been found to act as a strong gasification catalyst during pyrolysis promoting reactions between the evolving tars with other primary pyrolysis products such as CO_2 and H_2O (Raveendran et al., 1995, Jensen et al., 1998). These interactions have the effect of reducing liquid formation (and in some cases char formation) in favour of gas formation as was observed here (Raveendran et al., 1995).

The SEC results show that the TRH tars contain a larger proportion of the heavier tar fraction (characterised by the excluded peak in the SEC chromatogram) compared with the BRH tars. The peak corresponding to the lighter tar fraction also elutes at a shorter time which is most likely due to the larger proportion of a more conjugated group of tar compounds present in the TRH tars as indicated by UVF analysis. These findings suggest that the enhanced tar cracking afforded by the higher concentration of potassium in the TRH, favoured the cracking/gasification of the lighter, less conjugated tar fractions.

The pyrolysis behaviour of the TIR adhered far better to the trend typically observed for biomass containing large quantities of ash in that it produced more char and less tar whilst the amount of gas/unidentified products yield was similar to the BW and BRH.

The nature of the TIR tars (as characterized by SEC and UVF) appeared to be quite different to the tars derived from the other biomass feeds tested in this study. SEC indicated that the TIR tars contained a larger proportion of the lighter tar fraction (resolved peak in the SEC chromatogram) which also had a lower average molecular mass compared with the other tars. The UVF spectra of the pyrolysis tars derived from the TIR was also different- the spectra was broader and was comprised of three peaks compared to two.

One possible cause of the differences in the nature of the TIR tars can be deduced from the morphology of the resultant char. The N_2-adsorption and MIP analysis revealed that the TIR char had the highest surface area and a predominantly mesoporous pore structure compared with the other biomass derived chars which were largely macroporous in nature. These combined properties infer that the residence time of the volatiles within the char matrix and contact between the volatiles and char walls would have been greater than for the other biomass varieties. A greater residence time of the volatiles in the char in addition to the high concentration of inorganic matter would have caused enhanced secondary tar polymerisation and char forming reactions. This is particularly true for the larger primary tar compounds which are likely to have been hindered from exiting the char by the small pores resulting in the evolution of smaller, lower molecular weight tar compounds from the pyrolysing char matrix.

It should also be noted that the differences observed in the product distribution and nature of the tars and char could also be due to compositional differences (compared with the more conventional lignocellulosic biomass varieties tested here) and related differences in the thermo-chemical breakdown pathways. Unfortunately, it is not possible to expand further on the potential differences in the thermo-chemical breakdown pathways without more in depth compositional information of the different feeds which was not available at the time of this study.

The product distributions of BW and BRH pyrolysis and nature of the tars as determined by SEC and UVF analysis appear to be very similar despite the differences in the O/C ratios, ash content (particularly the inert ash component content), surface area and porosity of the resultant char. This indicates that these factors have less influence on the pyrolysis behaviour compared with the concentration of certain catalytically active ash constituents.

Determining the reactivity of the pyrolysis char is particularly important when designing a gasification process for a particular fuel. Here a few reactivity tests were carried out to determine the relative char reactivities with air at 773 K and CO_2 at 1173 K. The BW and TRH chars demonstrated the highest normalised reactivities in the combustion tests of 0.012 s^{-1} while the reactivities of the BRH and TIR were lower at 0.007 s^{-1}. There were also similarities in the reactivity profiles as a function of conversion between the more reactive BW and TRH chars and the less reactive BRH and TIR chars. The combustion reactivity profile of the BW and TRH chars initially increased, passing through a maximum reactivity at intermediate conversions of 0.37 and 0.12 respectively; whereas the profiles of the less reactive BRH and TIR chars observed monotonously decreasing relationships between reactivity and increasing conversion with the maximum reactivities attained at conversions of < 0.02. The type of reactivity profile observed by the more reactive BW and TRH chars is indicative of a reaction that involves the unblocking of dead pores caused by tar deposition and decomposition, and the widening of smaller pores, resulting in an increased exposure of active surface area with carbon conversion during the early stages and consistent with SEM and BET (Senneca, 2007). The reactivity profile of the less reactive chars on the otherhand, tends to indicate that the amount of reactive surface area decreased with increasing conversion.

The more reactive BW and TRH chars in the combustion tests also exhibited the smallest BET surface areas and largest average pore sizes in the macroporous region. These observations are in agreement with some previous studies investigating coal and biomass char oxidation reactivity where char oxidation was found to occur predominanly through the growth and extension of the meso- and macroporous network and that the microporous region is not significantly affected (Hurt et al., 1991, Aarna and Suuberg, 1998, Fushimi et al., 2003, Senneca, 2007). In addition to offering improved mass transfer properties by aiding the transport of the reactant and product gases through the char matrix, it is also believed that the surface area of macropores contains a higher concentration of active sites compared with micropores (Hurt et al., 1991). This can be rationalised by considering where the different porosity regions occur within the char structure. Micropores are believed to occur predominanalty between highly conjugated, graphene-like crystallite sheets of the char matrix whereas large meso- and macropores are formed at the bounderies of inorganic ash structures and around defects and edges in the graphitic crystallites where most of the oxygen containing functional groups tend to be located (Hurt et al., 1991, Lehmann and Joseph, 2012).

The propensity of a char to form larger meso- and macropores during pyrolysis and oxidation may go some way to explaining the different reactivities; particularly in the case of the BW char which had a considerably larger average pore size (in the macroporous region) and appeared to have the most open structure. This theory is also likely to explain the lower reactivity of the TIR char which exhibited the opposite morphological traits to the BW char. However the differences in the average pore size and pore size distributions of the rice husk chars is less pronounced. It is therefore more likely that the higher concentration of catalytically active inorganic matter, particularly potassium, present in the TRH was the dominant factor influencing the difference in combustion reactivities of the two rice husks.

The trends in the reactivities of the chars in the CO_2 gasification tests at 1173 K were different to those observed for the combustion tests at 773 K. The reactivity profiles as a function of conversion were also different exhibiting an initial surge in reactivity coinciding with the entry of CO_2 which rapidly decayed to a much lower stable value. This type of reaction profile is characteristic of CO_2 gasification of char experiments and is associated with the consumption of organic material at highly active sites within the char matrix (Kannan and Richards, 1990).

The TIR char was the most reactive char in the CO_2 gasification experiments, with the fast initial surge in reactivity persisting for close to the entire conversion range. The fast and persistent reaction rate is likely due to the improved catalytic activity of certain inorganic constituents (particularly the alkaline earth metals) at the higher temperature; an improvement in the accessible active surface area due to pore widening and the opening up of previously dead pores as a result of the additional thermal decomposition and pyrolysis at the higher temperatures; and the high ratio of ash/organic material of the TIR char. During the pre-heating step, the char lost 70 wt.% of its organic content such that prior to the CO_2 gasification reaction step, the organic content of the TIR char was 14 wt.% compared with 97 wt.%, 54 wt.% and 46 wt.% for the BW, BRH and TRH chars respectively. As a consequence, it is likely that the organic content of the TIR char existed as a disperse, highly active phase on a catalytically-active inorganic ash matrix.

Interestingly, the rice husk chars exhibited significantly lower surge and residual reactivities compared with the BW and TIR chars. The low reactivity is most likely due to increased deactivation and loss of the catalytically active potassium and sodium containing ash species during heating to 1173 K.

At temperatures of 700-850 ˚C (973-1123 K), potassium in the form of KCl and KOH is lost from the char through vaporization and at temperatures > 850 ˚C (1123 K), K_2CO_3 will decompose (Bridgwater, 2008, Jensen et al., 2000). K_2CO_3 decomposition will either result in the loss of potassium through the formation of KOH or alternatively the potassium can react with silica to form a deactivated potassium silicate phase. Potassium silicate eutectic melts can form at temperatures as low as 500 ˚C (773 K) in the presence of Na_2O (Pelton and Blander, 1986) and is the possible explanation for the appearance of the molten ash coating on the surface of the rice husk chars in the SEM images (Figure 3.7). The formation of potassium and other alkali metal silicate phases is exacerbated at high temperatures and in chars containing high concentrations of silica. In addition to deactivating the alkali metal towards char gasification, alkali silicate melts can form an impermeable coating that blocks access to small pores and activated surface sites of the char further impeding char gasification (Sørensen et al., 2000, Kannan and Richards, 1990, Moilanen, 2006). A low ash fusion temperature may also lead to other process problems including bed agglomeration and defluidisation in fluidised bed reactors and corrosion as a result of the acidic nature of the alkali silicates. As a consequence the potassium concentration of a char becomes less important for gasification reactions at high temperatures and when present in combination with large amounts of silica, can cause significant inhibition of the char gasification reactivity.

The BW char exhibited the second highest reactivity. The reasonably high reactivity is likely to be a result of the propensity of the BW char to form macropores and its high concentration of calcium and magnesium compared to the rice husk chars. There is also a clear trend between the combined Ca and Mg content of the chars and the CO_2 gasification reactivites demonstrated by the chars (fig. 3.12). Ca and Mg are less susceptible to silicate formation, such that their concentration becomes more important towards char gasification reactivites at the higher temperatures. The lower reactivity compared with the TIR char was likely due to the much lower ratio of organic to ash ratio and lower concentration of alkaline earth metals.

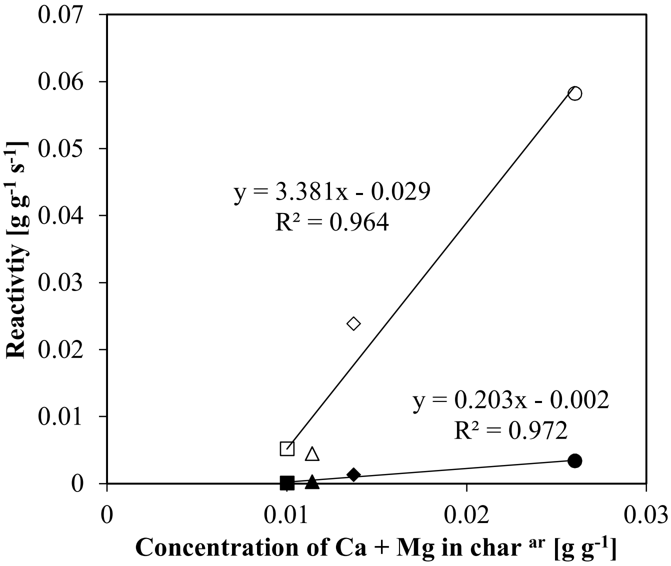

Figure 3.12: CO_2 gasification reactivity of the chars generated in the single stage pyrolysis of the different biomass feeds as a function of the char indigenous Ca and Mg concentration.

<u>**Experimental Parameters**</u>: ***1st stage***: **Feed** = Variable (1.000 g, 106-150 μm), **carrier gas** = He, **superficial velocity** = 0.1 m.s^{-1}, **inlet pressure** = 2.2 bar$_a$, **heating rate** = 1 K s^{-1}, **hold temperature** = 773 K, **hold time** = 900 s. Maximum initial rate: ◇ BW, △ BRH, □ TRH, ○ TIR; Rate at X=0.5 (solid fill).

3.3.3 Pyrolysis Experiments in the 2-Stage Fixed-Bed Reactor

Effect of 2nd Stage Temperature

For investigations into the effect of elevated temperature on the beech wood pyrolysis product distribution, the (empty) 2nd stage was preheated to 973 K, 1073 K or 1173 K before the first stage heating program was initiated. In this configuration the tars and volatiles, released during pyrolysis of the beech wood in the 1st stage undergo cracking, reforming and gasification reactions in the 2nd stage. It was chosen to narrow down the investigated biomass varieties down to beech wood as it produced the largest amount of tars in the single stage pyrolysis experiments. There was also an abundant supply of this beech wood within the department.

Tar yields from beech wood pyrolysis in the two-stage reactor were significantly lower than beech wood pyrolysis in the single stage reactor (fig. 3.13). When the 2nd stage was operated at 973 K the amount of tar exiting the reactor was reduced to 26 % of the amount exiting the single stage reactor. Further reductions in the tar yield were achieved by increasing the temperature of the 2nd stage to 1073 K and 1173 K (fig. 3.13). At a 2nd stage temperature of 1173 K, it was possible to eliminate 97 % of the tar generated in the 1st stage.

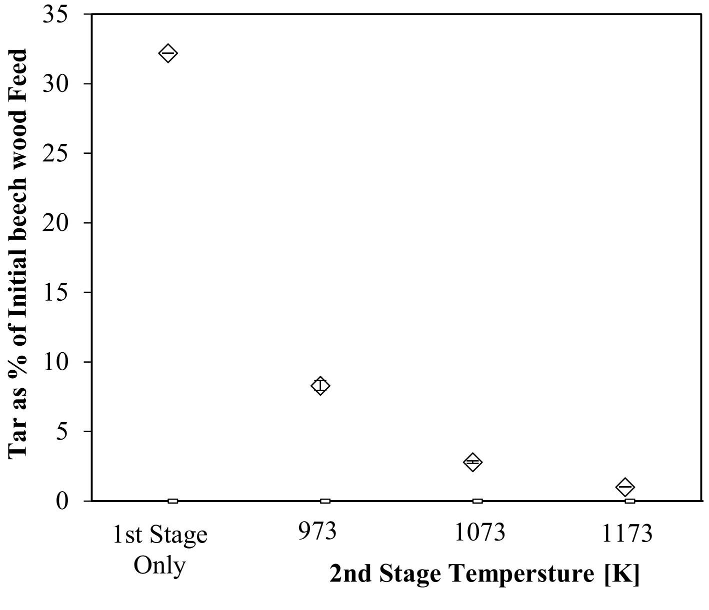

Figure 3.13: Tar recovered as a function of 2nd stage temperature.

Experimental Parameters: ***1st stage***: **Feed** = Beech wood (1.000 g, 106-150 μm), **carrier gas** = He, **superficial velocity** = 0.1 m s^{-1}, **inlet pressure** = 2.2 bar$_a$, **heating rate** = 1 K s^{-1}, **hold temperature** = 773 K, **hold time** = 900 s. ***2nd stage***: **Bed** = N/A, **superficial velocity** = 0.25 m s^{-1}, **inlet pressure** = 2.1 bar$_a$, **temperature** = variable.

The tars generated in the single stage and 2-stage reactors were characterised using size exclusion chromatography (fig. 3.14). The main difference in the chromatograms of the tars generated in the 2-stage reactor with a 2nd stage temperature of 973 K compared with the chromatogram of the tars generated in the single-stage reactor was that the excluded peak was more intense whilst the retained peak was less intense. This suggests that the lower molecular mass tars were more susceptible to thermal cracking in the 2nd stage at 973K than the higher molecular mass fraction. It is also the case that the maxima of the peaks for both fractions of the tars generated in the 2-stage reactor at 973 K occur at shorter elution times which indicates a slight increase in the average molecular mass of both tar fractions compared with the single stage reactor tars.

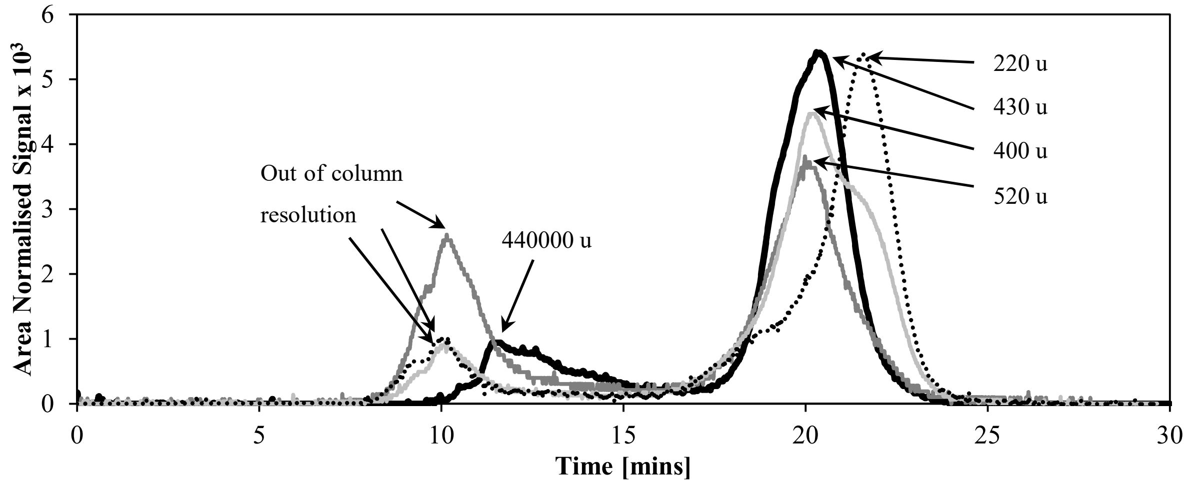

Figure 3.14: SEC chromatograms of tars recovered when the temperature of the empty 2nd stage was varied.
Experimental Parameters: ***1st stage***: **Feed** = Beech wood (1.000 g, 106-150 µm), **carrier gas** = He, **superficial velocity** = 0.1 m s^{-1}, **inlet pressure** = 2.2 bar$_a$, **heating rate** = 1 K s^{-1}, **hold temperature** = 773 K, **hold time** = 900 s. ***2nd stage***: **Bed** = N/A, **superficial velocity** = 0.25 m s^{-1}, **inlet pressure** = 2.1 bar$_a$, **temperature** = variable. 1st stage only . 2nd stage temperature = 973 K ——, 1073 K ——, 1173 K ·----·

In the chromatogram of the tars generated at 1073 K, the intensity of the excluded peak decreased back to a similar level as the excluded peak of the chromatogram for the single stage tars, whilst the retained peak became broader and more intense than the equivalent peak in the 973 K tars. The larger width of the retained peak was due to the development of a shoulder that eluted at a similar time to the peak of the retained peak of the 1173 K tars. The elution time of the retained peak was also slightly longer than the equivalent peak in the chromatogram of the 973 K tars.

Increasing the temperature of the 2nd stage to 1173 K caused a further shift in the elution time of the retained peak in the direction of the shoulder of the retained peak in the chromatogram of the 1073 K tars. The retained peak was also more intense and narrower than the equivalent peak in the chromatogram of the 1073 K tars.

These findings indicate that increasing the temperature of which the tars were exposed to enhanced the cracking of the larger, high molecular weight tars (as characterised by the excluded peak) into smaller, lighter tar compounds. Increasing the temperature of the 2nd stage also appeared to enhance the cracking of the less thermally stable heavier tars in the lower molecular mass fraction such that the average molecular mass (estimated from the elution time of the retained peak) decreased from 523 u to 399 u and 216 u for 2nd stage temperatures of 973 K, 1073 K and 1173 K respectively. This is also supported by the fact that as the 2nd stage temperature was increased from 1073 K to 1173 K, the retained peak became narrower and more intense corresponding to a decrease in the variety of tar species that have a high enough thermal stability to resist decomposition at 1173 K.

The concentrations of CH_4, CO and CO_2 were also measured in the reactor flue gas (fig. 3.15). CO production increased substantially from 2.9 % of the initial biomass feed in the single stage reactor to 15.5 % in the 2-stage reactor at 973 K. Increasing the temperature of 2nd stage to 1073 K and 1173 K resulted in further increases in the amount of CO detected. At a 2nd stage temperature of 1173 K, 22.8 wt.% of the initial beech wood feed was converted to CO. The trend in CH_4 production was similar to the trend observed for CO, however the amount of CH_4 that was released was much lower.

The total amount of CO_2 released in the 2-stage reactor at 973 K was similar to the amount released from beech wood pyrolysis in the single stage reactor. A small increase in CO_2 production was detected when the temperature of the 2nd stage was increased from 1073 K to 1173 K; however increasing the temperature to 1173 K had no further effect. This suggests that most of the detected CO_2 was produced during pyrolysis and that thermal tar cracking at elevated temperatures favours the production of the combustible gases CO and CH_4.

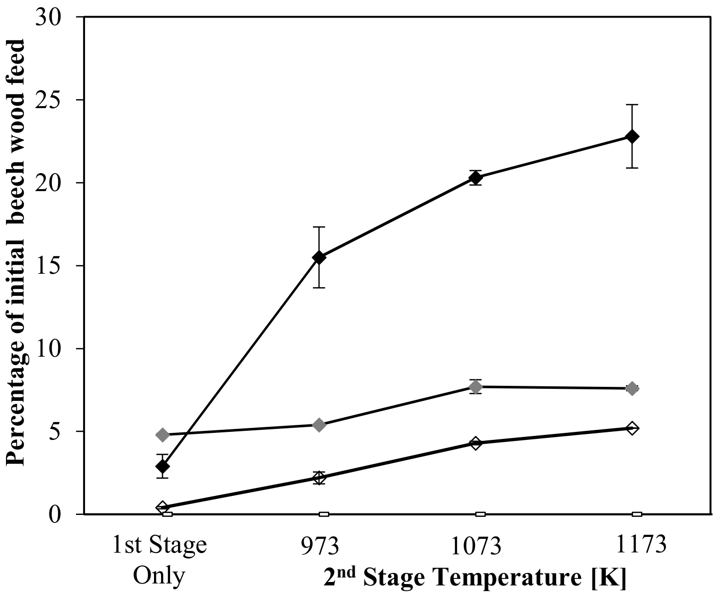

Figure 3.15: Gas production as a function of 2nd stage temperature.

Experimental Parameters: ***1st stage***: **Feed** = Beech wood (1.000 g, 106-150 μm), **carrier gas** = He, **superficial velocity** = 0.1 m s^{-1}, **inlet pressure** = 2.2 bar_a, **heating rate** = 1 K s^{-1}, **hold temperature** = 773 K, **hold time** = 900 s. ***2nd stage***: **Bed** = N/A, **superficial velocity** = 0.25 m s^{-1}, **inlet pressure** = 2.1 bar_a, **temperature** = variable. ◆ CO; ◇ CH_4; ◆ CO_2

The Effect of Inert Surface Area

To determine how non-catalytic reactive surface area affects the product distribution of beech wood pyrolysis; sand was loaded into the 2nd stage at 973 K to create sand beds of 20 mm, 30 mm and 40 mm in length. Sand is not normally present in a downdraft gasifier, but is commonly used as the bed material in fluidised bed gasifiers. Sand was chosen for these investigations as it is inert and has a high thermal capacity; therefore the surface area of the sand will remain consistent at high temperatures and will not chemically interact with the pyrolysis products generated in the 1st stage. Only the effect of bed length (i.e. extra inert surface area) on the product distribution is therefore observed. Table 3.8 presents a summary of the product distribution for pyrolysis of beech wood in the 2-stage reactor with a 2nd stage at 973 K packed with beds of sands varying in length.

Table 3.8: The effect of different 2nd stage sand bed lengths on the product distribution of beech wood pyrolysis.
Experimental Parameters: ***1st stage***: **Feed** = Beech wood (1.000 g, 106-150 μm), **carrier gas** = He, **superficial velocity** = 0.1 m s^{-1}, **inlet pressure** = 2.2 bar_a, **heating rate** = 1 K s^{-1}, **hold temperature** = 773 K, **hold time** = 900 s. ***2nd stage:*** **Bed = material =** sand (d_p = 500-700 μm), **bed length** = variable, **superficial velocity** = 0.25 m s^{-1}, **inlet pressure** = 2.1 bar_a, **temperature** = variable.

	Weight as percentage of initial biomass weight (1.000 g)					
2nd stage Bed	**Tars**	**Chars**	**CH_4**	**CO**	**CO_2**	**Unidentified**
N/A	8.3 ± 0.4	20.7 ± 0.8	2.2 ± 0.4	15.5 ± 1.8	5.4 ± 0	47.9
20 mm sand	8.0 ± 0.6	21.5 ± 1.1	2.3 ± 0.1	16.5 ± 1.1	5.9 ± 0.7	45.8
30 mm sand	7.8 ± 0.4	21.1 ± 1.0	2.2 ± 0.1	15.1 ± 1.8	5.1 ± 0.4	48.7
40 mm sand	8.4 ± 0.2	21.1 ± 1.3	2.2 ± 0	16.9 ± 0.4	4.6 ± 1.1	46.8

It is clear from table 3.8 that increasing the inert surface area within the 2nd stage at 973 K did not influence the pyrolysis product distribution further. This was also the case when 20 mm sand beds were inserted into the 2nd stage at 1073 K and 1173 K (Figure 3.16 (a)). This suggests that the tar species that are unstable at the investigated temperatures break down quickly and that tar cracking reactions proceed to completion within the time frame that the tars reside in the empty 2nd stage.

The Effect of Adding Small Amounts of Limestone and Dolomite to the 20 mm 2nd Stage Sand Beds

The last set of experiments involved investigating the effects of adding small amounts of cheap catalytically active solids to a 20 mm sand bed to elucidate whether the presence of the potential catalysts could enhance tar cracking further. Calcined dolomite is already established as an efficient catalyst for tar destruction in fluidised bed gasification (Weerachanchai et al., 2009, Sutton et al., 2001, Gil et al., 1999). Therefore as limestone and dolomite are chemically similar, widely available and cheap, it was decided to investigate the tar cracking capabilities of both materials (in their calcined forms). The beds were comprised of a 10 mm bed of either 20 wt.% dolomite and 80 wt.% sand, or 20 wt.% limestone and 80 wt.% sand positioned between two 5 mm sand beds to ensure efficient preheating of the gases entering the bed. These beds from here on will be referred to as the 20% LS bed and the 20% Dol bed. The effect of dolomite loading at 973 K was also investigated where the 10 mm portion of the bed contained either 10 wt.%, 20 wt.% or 40 wt.% dolomite. The beds consist mainly of sand since sand has a high thermal capacity and therefore ensures the bed temperature is maintained at the experimental temperature. The beds were pre-heated to 1173 K for 300 s prior to starting the 1st stage pyrolysis temperature program to ensure the dolomite and limestone were fully calcined/activated form.

The presence of both the 20 % LS and 20 % Dol beds in the 2nd stage caused further reductions in the amounts of tar exiting the reactor (fig. 3.16 (a)). The effects were most pronounced at 973 K and 1073 K although this was most likely because at 1173 K 97 % of the pyrolysis tars were thermally cracked as was observed in the analogous experiments with an empty 2nd stage. When the 2nd stage contained the 20 % LS bed, tar yields were 25 %, 43 % and 20 % lower than those from the reactor with an empty 2nd stage at 973 K, 1073 K and 1173 K respectively. The 20 % Dol bed seemed to be slightly more effective and caused tar reductions of 35 %, 47 % and 40 % at 973 K, 1073 K and 1173 K respectively. Increasing the dolomite loading in the bed from 20 wt.% to 40 wt.% had no further effect (fig. 3.16 (b)).

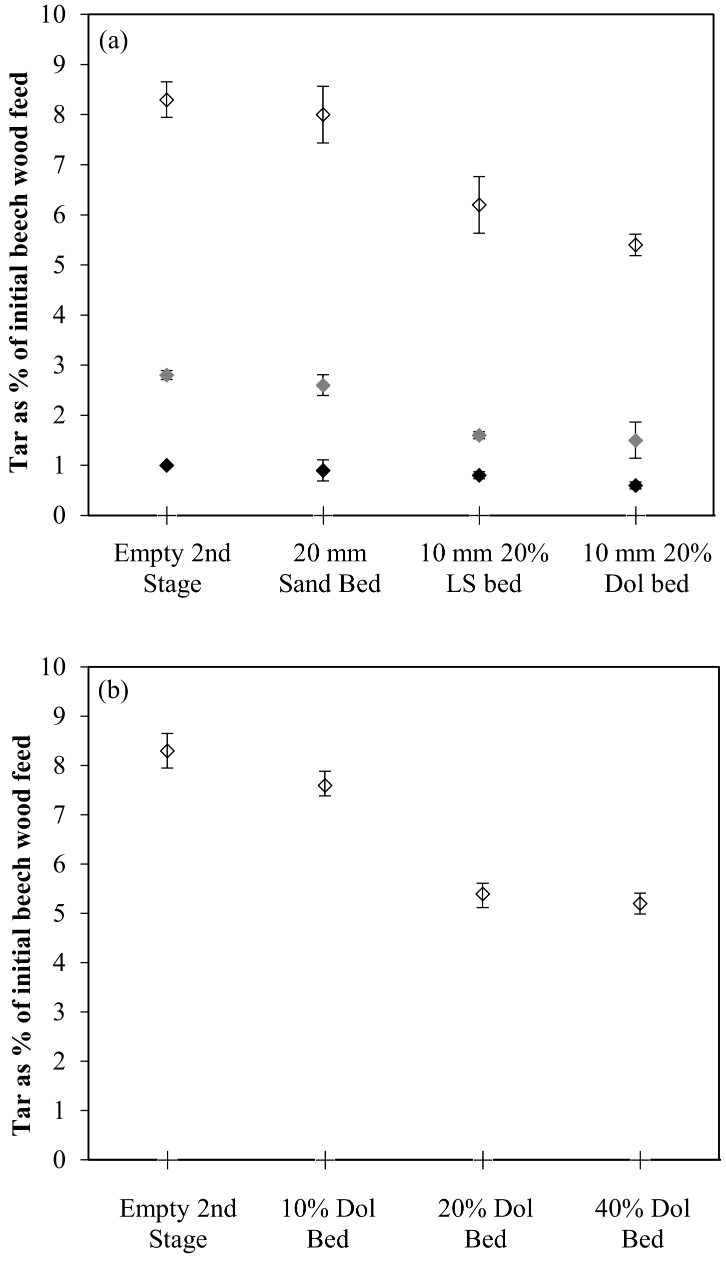

Figure 3.16 (a-b): Tar recovered as a function of 2nd stage bed type.

<u>Experimental Parameters</u>: ***1st stage***: **Feed** = Beech wood (1.000 g, 106-150 μm), **carrier gas** = He, **inlet pressure** = 2.2 bar$_a$, **superficial velocity** = 0.1 m s^{-1}, **heating rate** = 1 K s^{-1}, **hold temperature** = 773 K, **hold time** = 1173 K; ***2nd stage***: **inlet pressure** = 2.1 bar$_a$, **superficial velocity** = 0.25 m s^{-1}, **temperature** = ◇ 973 K, ◆ 1073 K, ◆ 900 °C.

The tars generated in the presence of the different beds were analysed further using SEC. The SEC chromatograms of the tars are provided in figure 3.17 (a-c). There is little difference between the SEC chromatograms of the tars generated in the reactor packed with the different beds at 973 K (fig. 3.17 (a)). This suggests that the tar cracking activity of the limestone and dolomite at this temperature is indescriminate. However there are differences in the chromatograms of the tars generated in the presence of the different beds at 1073 K and 1173 K.

At 1073 K, the excluded peaks in the chromatogram of the tars generated in the presence of the 20% LS and 20% Dol beds are more intense whilst the retained peaks are less intense than the corresponding peaks in the chromatograms of the tars generated in the 2-stage reactor with an empty 2nd stage and a 2nd stage packed with a 20 mm bed figure 3.17 (b)). This indicates that the presence of the calcined limestone and dolomite at 1073 K enhanced the cracking of the lower molecular weight fraction of the tars. Furthermore the retained peak in the chromatogram of the tars generated in the presence of the 20% LS bed has two maxima corresponding to tar species with average molecular masses of 242 u and 395 u. The retention times of these two peaks are both longer than the the retained peaks in the chromatograms of the tars generated in the presence of the 20 mm sand bed, the 20% Dol bed and no 2nd stage bed. In these cases, the retained peaks all elute at the same time corresponding to an average molecular mass of 412 u. This suggests that the presence of limestone at 1073 K enhanced the cracking of the heavier tar species in the lower molecular weight tar fraction. It would therefore appear that the tar cracking activities of the limestone and dolomite at 1073 K are slightly different.

SEC analysis of the tars exposed to the different 2nd stage beds at 1173 K also revealed some differences depite there being only very small differences in the tar yields (fig. 3.17 (b)). An additional small peak in the chromatograms of the tars exposed to the different beds appeared at elution times of 18-19 minutes corresponding to the elution of a tar component with an average molecular mass of 1010-1360 u. There are also some differences in the elution times, intensities and ratio of peak areas suggesting that the addition of the different beds has had some influence on the tar cracking reaction pathway despite the fact that introducing the beds had little effect on reducing the overall tar yield at 1173 K.

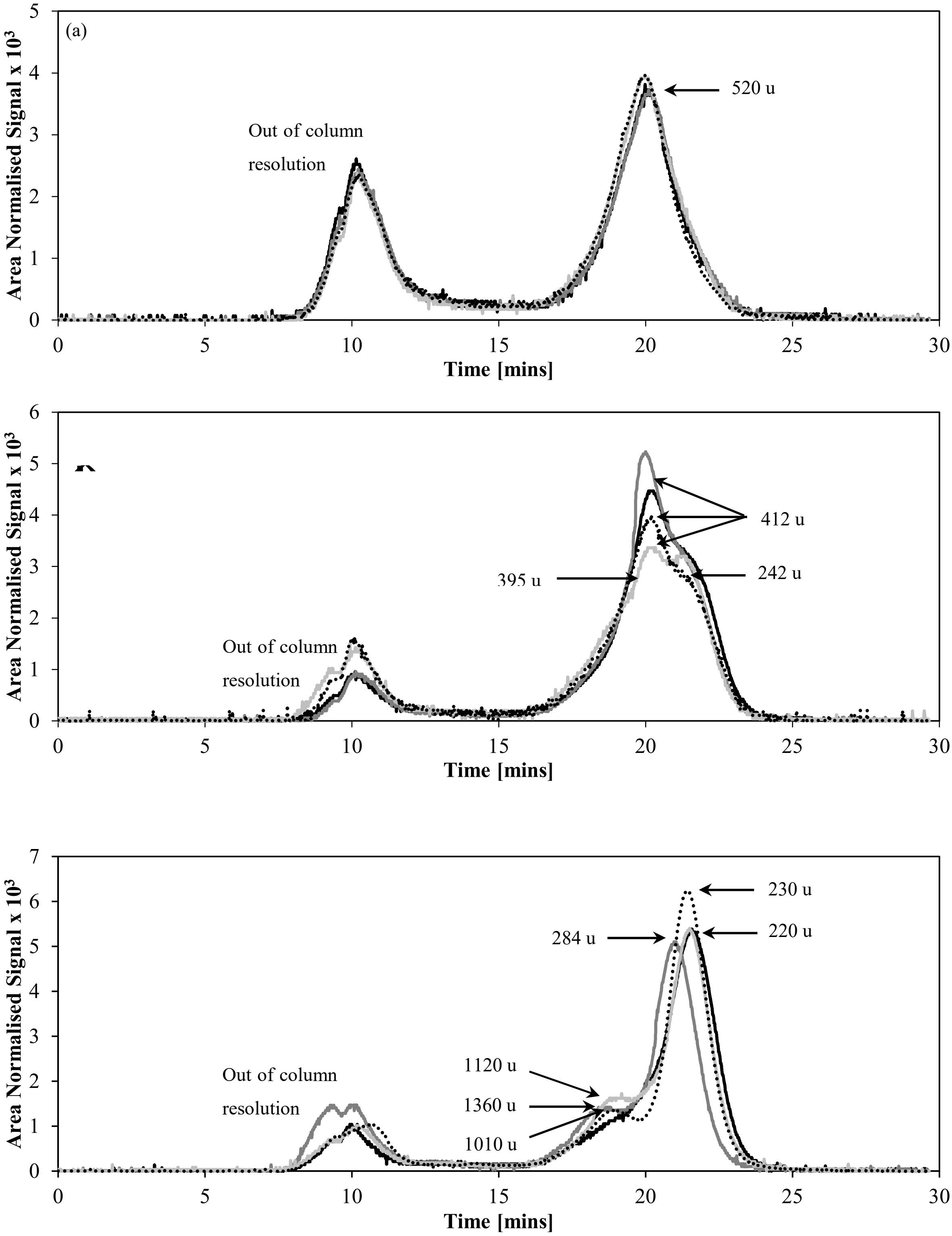

Figure 3.17: SEC chromatograms of tars recovered with various beds in the 2^{nd} stage at (a) 973 K, (b) 1073 K, (c) 1173 K. **Experimental Parameters**: ***1^{st} stage***: **Feed** = Beech wood (1.000 g, 106-150 μm), **carrier gas** = He, **inlet pressure** = 2.2 bar_a, **superficial velocity** = 0.1 m s^{-1}, **heating rate** = 1 K s^{-1}, **hold temperature** = 773 K, **hold time** = 1173 K; ***2^{nd} stage***: **inlet pressure** = 2.1 bar_a, **superficial velocity** = 0.25 m s^{-1}, **temperature** = variable, **bed type**: N/A —— ; 20 mm sand bed —— ; 20% LS bed —— ; 20% Dol bed

The findings from the gas analysis also suggest there may be subtle differences in the tar cracking activities of calcined limestone and dolomite. Although the addition of the different beds (including the 10% and 40% Dol beds not shown, see appendices A) did not affect CO and CH_4 production (fig. 3.18 (a-b)), CO_2 production was significantly enhanced by the addition of the 20% LS and 20% Dol beds (fig. 3.18 (c)). The presence of the 20% LS bed increased CO_2 production by 26%, 38% and 73%, whilst calcined dolomite enhanced CO_2 production by 56%, 78% and 74% at 973 K, 1073 K and 1173 K respectively. Increasing the dolomite loading in the dolomite bed from 10 wt.% to 20 wt.% and 40 wt.% at 700 ˚C also caused respective increases in the amount of CO_2 detected. It should be noted that CO_2 production in the presence of the 20% LS bed increased with increasing temperature, however when the temperature of the 20% Dol bed was increased from 1073 K and 1173 K, CO_2 production decreased slightly. Since both the dolomite and limestone are completely calcined before the the pyrolysis experiments were started, the increased production of CO_2 must be a consequence of enhanced tar cracking by the calcined limestone and dolomite in the beds. This is not necessarily desirable if the purpose of the process is to produce a fuel gas. The decrease in the CO_2 yield observed when the temperautre of the 20% dol bed was increased from 1073 K to 1173 K was possibly due to the onset of gasification reations between CO_2, tars and/or carbon deposits on the surface of the calcined dolimte, sand or reactor walls.

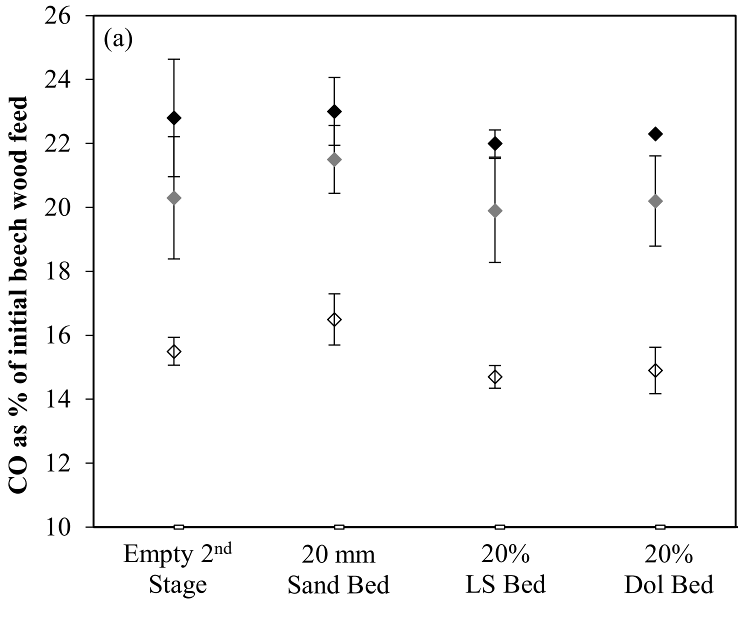

Figure 3.18: (a) CO production as a function if the different beds.

<u>Experimental Parameters</u>: ***1st stage***: **Feed** = beech wood (1.000 g, 106-150 μm), **carrier gas** = He, **inlet pressure** = 2.2 bar$_a$, **superficial velocity** = 0.1 m s^{-1}, **heating rate** = 1 K s^{-1}, **hold temperature** = 773 K, **hold time** = 900 s. ***2nd Stage***: **inlet pressure** = 2.1 bar$_a$, **superficial velocity** 0.25 m s^{-1}, **bed** = Variable, **temperature** = ◇ 973 K, ◆ 1073 K, ◆ 1173 K

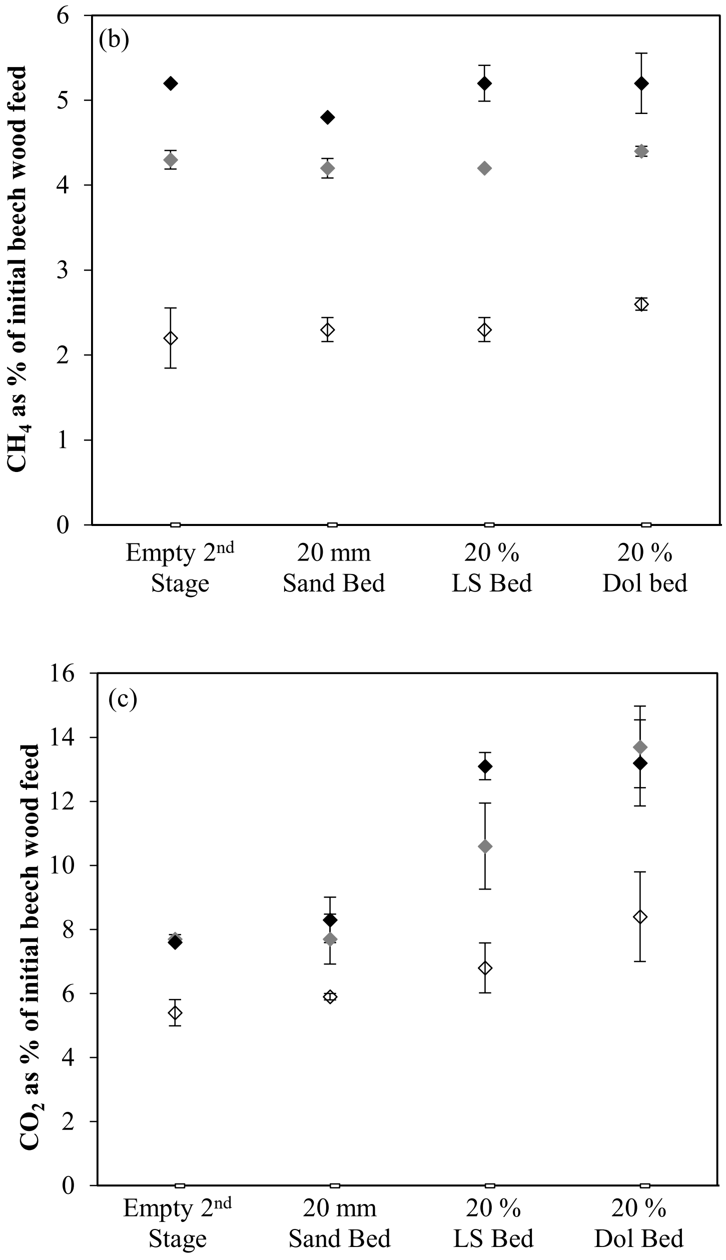

Figure 3.18: (b) CH_4 and (c) CO_2 production as a function if the different beds.
<u>**Experimental Parameters**</u>: ***1st stage***: **Feed** = beech wood (1.000 g, 106-150 μm), **carrier gas** = He, **inlet pressure** = 2.2 bar_a, **superficial velocity** = 0.1 m s^{-1}, **heating rate** = 1 K s^{-1}, **hold temperature** = 773 K, **hold time** = 900 s. ***2nd Stage***: **inlet pressure** = 2.1 bar_a, **superficial velocity** 0.25 m s^{-1}, **bed** = Variable, **temperature** = ◇ 973 K, ◆ 1073 K, ◆ 1173 K

Thermogravimetric analysis (TGA) was used to determine the extent of coke formation on the calcined limestone and dolomite particles as a function of 2nd stage temperature. The analyses also enabled determination of the extents of hydration and carbonation. Figure 3.19 (a-b) shows the TGA weight loss curves for the limestone and dolomite particles used in the 20% LS and 20% Dol beds used at 973 K, 1073 K and 1173 K. TGA analysis was also performed on the sand from the 20 mm sand beds and the sand component of the 20% LS and 20% Dol bed, however no weight loss was observed.

Each of the weight loss curves in figure 3.19 (a-b) have four weight loss regions. The first weight loss region (i) is small (between 0.24-0.63 %) and occurs after ~ 20 minutes. This is caused by the loss of unbound moisture from the sample at 373-383 K. The second weight loss (ii) is due to calcination of $Ca(OH)_2$ and $Mg(OH)_2$ species to CaO or MgO and H_2O at ~ 670 K. CaO and MgO hydrate rapidly in air at ambient temperatures. In this investigation, hydration of the calcined limestone and dolomite occurred after the experiments were completed whilst the beds were being removed from the reactor and weighed. Despite limiting the time in which the samples were exposed to the air and storing the samples in a dessicator in airtight vials, hydration levels were between 5 % and 9 % (table 3.9) It is important to limit hydration of the calcined limestone and dolomite samples to as low a level as possible as hydration causes structural and surface area transformations which may effect charactisation of the sample.

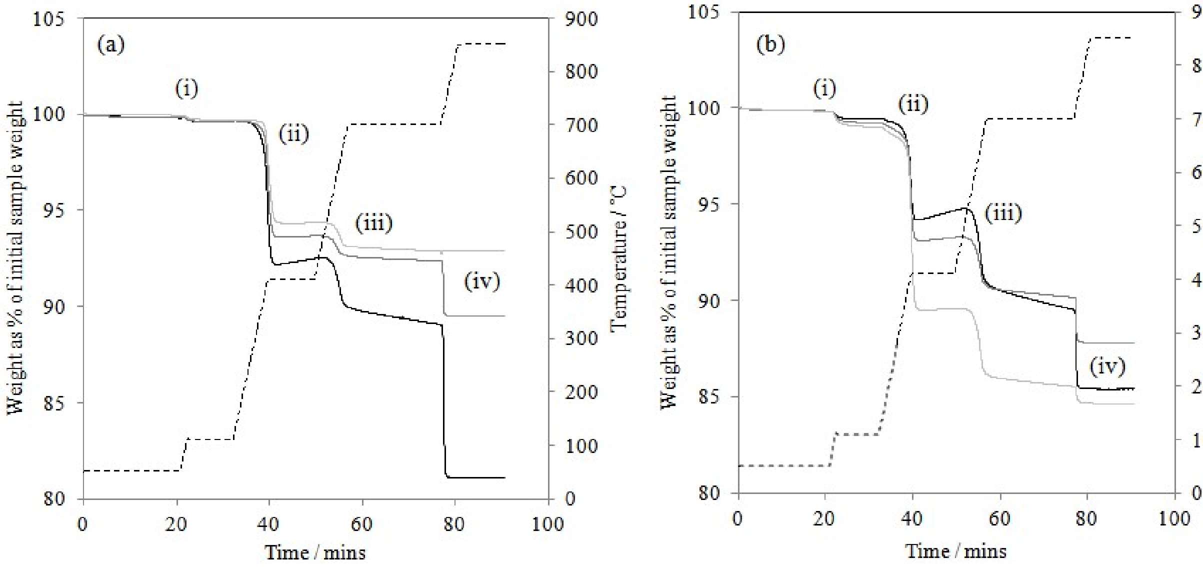

Figure 3.19: Weight loss curves determined by thermogravimetric analysis of (a) the limestone and (b) the dolomite particles used in the (a) 20 % LS and (b) 20% Dol beds at 2nd stage temperatures of 973 K, —— 1073 K and —— 1173 K.

The third weight loss region (iii) began when the temperature of the sample reached 773 K. At this temperature and in a nitrogen atmosphere, any $CaCO_3$ calcined to CaO releasing CO_2. It can be seen from figure 3.19 (a-c) and table 3.9 that the extents to which the limestone and dolomite particles were carbonated was low, between 2 % and 5 %. Although only a very small proportion of the samples were carbonated, this was not expected as at 2nd stage experimental temperatures of between 973-1173 K and in inert conditions, thermodynamics dictate that the calcined form (CaO or $Ca_{0.65}Mg_{0.35}O$) is favoured. Therefore it is assumed that the observed carbonation occured during handling via the $Ca(OH)_2$ intermediate which reacts rapidly with atmospheric CO_2.

The final weight loss (iv) occured when the TGA furnace purge gas was switched from nitrogen to air. This caused the coke deposits on the surface of the particles to combust, releasing CO_2. It is clear that increasing the temperature of the 2nd stage reduced coking of both the limestone and dolomite particles (fig.4.6 (a,b), table 4.3). At the investigated 2nd stage temperatures, coke formation is predominantly caused by decomposition of tars on the surface of the limestone or dolomite particles (Mendiara et al., 2011). The decrease in coke formation with increasing 2nd stage temperature is most likely due to the fact that at higher temperatures, more tar is cracked before it reaches the section of the bed containing the calcined limestone (or calcined dolmite). Furthermore, the TGA results indicate that whilst calcined limestone was more susceptible to coking than the calcined dolomite at 973 K, the reverse was true at 1173 K.

Table 3.9: A summary of how hydrated, carbonated and coked the limestone and dolomite particles from the 20% LS and 20% Dol beds were after the pyrolysis experiments at 973 K, 1073 K and 1173 K. Determined from the TGA weight loss curves in figure 4.6.

	2nd Stage Temperature	**973 K**	**1073 K**	**1173 K**
Hydration as % of inital sample weight	**Limestone**	8 %	6 %	5 %
	Dolomite	5 %	6 %	9 %
Carbonation as % of the $CaO/CaCO_3$ or $Ca_{0.65}M_{0.35}O/Ca_{0.65}M_{0.35}CO_3$ in the carbonated form	**Limestone**	4 %	2 %	2 %
	Dolomite	5 %	3 %	5 %
Coking as % of dehydrated and calcined sample weight	**Limestone**	10 %	3 %	0 %
	Dolomite	6 %	3 %	2 %

BET and SEM analyses were also used to determine how the structure of the limestone and dolomite particles changed with 2nd stage operating temperature (table 3.10 and fig. 3.20).

Table 3.10: BET surface areas and BJH average pore sizes for the limestone and dolomite particels retrieved from the 20% LS and 20% Dol beds.

2nd Stage Temperature	973 K	1073 K	1173 K
Calcined limestone BET Surface Area [$m^2\ g^{-1}$]	11.59	8.82	4.78
Calcined limestone BJH Average Pore Size [nm]	16.01	20.94	34.68
Calcined dolomite BET Surface Area [$m^2\ g^{-1}$]	23.45	18.62	11.86
Calcined dolomite BJH Average Pore Size [nm]	12.68	13.33	23.27

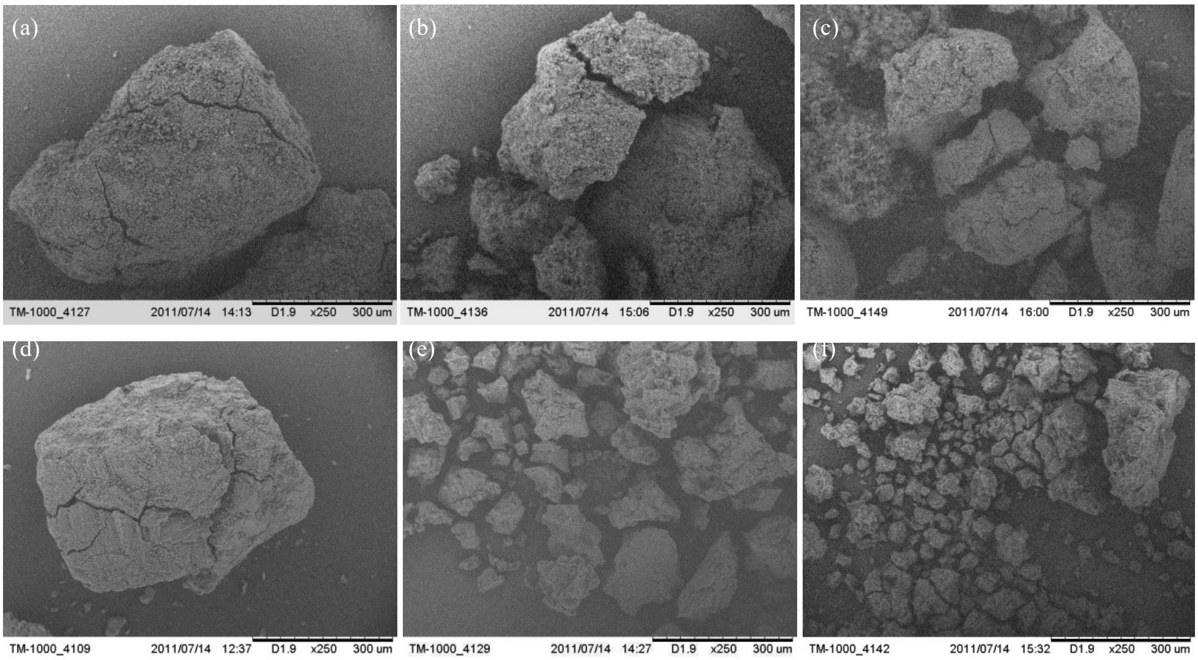

Figure 3.20: SEM images of the calcined limestone (a – c) and calcined dolomite particles (d – f) retrieved from the 2nd stage beds after pyrolysis experiments at 973 K (a,d); 1073 K (b,d) and 1173 K (c,f).
Experimental Parameters: ***1st stage***: **feed** = beech wood (1.000g, 106-150 μm), **carrier gas** = He, **inlet pressure** = 2.2 bar_a, **superficial velocity** = 0.1 m s^{-1}, **heating rate** = 1 K s^{-1}, **hold temperature** = 973 K, **hold time** = 900 s. ***2nd stage***: **inlet pressure** = 2.1 bar_a, **superficial velocity** 0.25 $m.s^{-1}$, **bed type** = variable, **temperature** = variable.

BET analysis revealed that the surface area of the calcined dolomite is significantly larger than the calcined limestone at all the invstigated temperatures (table 3.10). The larger reactive surface area of the dolomite may explain the higher tar cracking activity of the 20% Dol bed compared to the 20% LS bed. Increasing the temperature enhanced particle sintering which resulted in the observed loss of surface area and corresponding increase in the average pore size diameter for both the calcined limestone and calcined dolomite particles. Increasing the temperature of the 2nd stage also caused the particles to fracture and fragment (fig. 3.20). Fragmentation of the calcined dolomite particle was more severe than the calcined limestone particle. The larger proponsity of the calcined dolomite to fragment may be the reason for the larger surface area observed for the calcined dolomite compared with the calcined limestone and its slightly greater tar cracking effect. The lack of structural integrity would present problems for use as in fluidised bed situation where fragmentation and attrition results in the production of fines that would elutriate from the bed.

3.4 Summary and Conclusions

In the first section of this work, four different types of biomass or wastes were pyrolysed in a lab-scale fixed-bed reactor at 773 K. The distribution and nature of the pyrolysis products were determined and analysed. The product distributions of the three more conventional lignocellulosic biomass varieties produced similar product distributions in terms of their total volatile and char yields although the Thai rice husk produced 40 wt.% less tars than the Brazilian variant. The difference in tar yields was attributed to the higher concentration of potassium present in the Thai rice husk compared with the Brazilian variant and the beech wood. The product distributions and nature of the tars produced from the pyrolysis of BW and BRH appeared to be very similar despite the differences in the O/C ratios, ash content (particularly the inert ash component content), surface area and porosity of the resultant char, indicating that these factors have less influence on the pyrolysis behaviour compared with the concentration of certain catalytically active ash constituents such as potassium.

Pyrolysis of the textile industry solid residue produced the most char and the least amount of volatiles which was attributed to its high ash content and small pores. Small pores impede the release of volatiles from the char matrix while the high ash content provides a larger, potentially catalytically active surface on which secondary tar polymerisation and char forming reactions can take place. The textile industry residue pyrolysis also produced a tar comprised of lower molecular sized components compared with the other tars. It is possible that the smaller pores of the TIR acted to enhanced tar cracking, directing the formation of lower molecular weight tar components. However, the differences observed in the product distribution and nature of the TIR pyrolysis products may have also been a result of compositional differences between the TIR and the more conventional lignocellulosic biomass varieties and related differences in the thermochemical breakdown pathways.

The resultant pyrolysis chars were further analysed to assess their relative reactivates in air at 773 K and CO_2 at 1173 K. The BW and TRH chars demonstrated the highest reactivities in the air reactivity tests. These resultant char demonstrated the lowest BET surface areas but largest average pore sizes in the macroporous region. These findings agree with previous studies that found char oxidation occurs predominantly through the growth and extension of the macroporous network due to its favourable mass transfer characteristics and higher concentration of active sites on the pore surfaces. The high concentration of potassium was also likely to have influenced the high oxidative reactivity of the TRH char compared with the BRH char.

The chars exhibited different reactivities in the CO_2 gasification reactivity tests at 1173 K. The reactivity of the chars appeared to correlate well with the concentration of Ca and Mg present in the char. Macroporosity and a high ratio ash to organic content is also likely to have led to enhanced CO_2 gasification reactivity. The chars containing high levels of silica in combination with alkali metals demonstrated significantly lower reactivities which were attributed to the formation of molten alkali silicate phases that are likely to have deactivated the catalytic effect of the alkali metal and blocked access to the pores reducing the available reactive surface area.

When considering the different biomass feedstocks as fuels for a gasification process, these results indicate that beech wood would be the most suitable gasifier feed of the four biomass varieties tested in this study. Beech wood produced the largest amount of volatiles containing the highest proportions of the combustible gases (CO and CH_4). It also produces the least amount of char, which demonstrated a reasonably high reactivity with both air and CO_2. The large amount of tars initially released in pyrolysis of the beech wood would be largely cracked and reformed in subsequent high temperature gasification and combustion reactions but may present some problems as biomass varieties that release larger amounts of tars during pyrolysis tend to produce gases with a higher tar content when gasified. It was for this reason that beech wood was chosen as the fuel for the second part of the study, investigating the effect of elevated temperatures and solids with potential catalytic activity on the tar yield.

Pyrolysis of the two rice husks released similar quantities of volatiles to the beech wood and less tar, however they both had high ash contents and produced chars with low reactivities. If our hypotheses are correct and it is the formation of an ash coating on the surface of the chars inhibiting the reactivity of the chars at the higher temperatures, then it would suggest a gasifier design based on a fluidised-bed reactor would be the optimal system for processing these feedstocks. The abrasive nature of a fluidised bed would act to atrit away the surface of the char exposing new surfaces that can undergo reactions thus enhancing the observed reactivity; although the low fusion temperature that is typical of biomass ash may cause defluidisation of the bed material. Despite the apparent poor performance of these materials, exploitation of this potential energy source is made particularly attractive by the fact that these are a waste product produced in substantial quantities.

TIR initially appeared to be the least feasible fuel for gasification. It released the least amount of volatiles and the largest amount of char. The char also exhibited the lowest reactivity at 773 K with air. However at 1173 K, the reactivity of the textile industry residue char with CO_2 was significantly higher than any of the other biomass varieties tested in this study. This shows that higher temperatures are necessary for optimal gasification of this feedstock. The high ash content also indicates that a fluidised bed reactor may be most suitable for processing this material particularly if using a larger particle size. Whilst still not the most attractive of feedstocks on account of its low gasifiable organic content, gasification may provide the most efficient method of extracting the energy from this waste feedstock into a convenient fuel gas. This gas (along with the useful heat produced in the gasification process) could then be used to supplement on-site fuel, heat and power use whilst reducing the size of the waste stream and associated costs of disposal.

In the second section of this work, the fixed-bed reactor in its two-stage configuration was utilised to investigate the effect of temperature, surface area and presence of potential catalytically active materials on the pyrolysis product distribution of a beech wood biomass fuel. Under the pyrolysis conditions used in this study, 32.2 % of the biomass mass was converted to primary tars, 22.8 % to char, 4.8 % to CO_2, 2.9 % to CO and 0.4 % to CH_4. 36.9 % of the initial biomass was converted to unidentified pyrolysis vapours.

Subjecting the tars to higher temperatures caused a significant reduction in the amount of tars collected. It was found that by operating the 2nd stage 973 K, 1073 K and 1173 K, it was possible to eliminate 74 %, 92 % and 97 % of the tar generated during pyrolysis of the beech wood fuel in the 1st stage. The reduced tar yields were accompanied by a significant rise in the amount of combustible gases (CO and CH_4) produced. At 1173 K, 22.2 % of the initial biomass mass was converted to CO and 5.2 % to CH_4. Increasing the surface area in the 2nd stage by inserting sand beds had no additional effect on the product distribution.

The presence of sand beds containing calcined limestone or dolomite further enhanced tar cracking in the 2nd stage. The effects were most pronounced at 1073 K and 1173 K where the presence of the 20 % LS bed reduced tars by 25 % and 43 % compared with tar yields from the reactor with an empty 2nd stage at 973 K and 1073 K. The 20 % Dol bed was slightly more effective and caused tar reductions of 35 % and 47 % at 973 K and 1073 K respectively. The greater reactivity of calcined dolomite was attributed to its higher surface area. An increase in the CO_2 yield was observed at all temperatures when the 2nd stage contained the calcined limestone and dolomite beds; however CO and CH_4 yields were unaffected. TGA analysis showed that both the calcined limestone and dolomite particles were affected by coking. At 973 K, the calcined limestone was more susceptible to coking than the calcined dolomite, whilst the reverse was true at 1173 K. The extent of coking for both particles decreased with increasing temperature. Increasing the temperature also enhanced sintering which significantly reduced the surface area of the particles.

Increasing the calcined dolomite loading in the bed at 973 K had no additional effect on the tar yield.

Chapter 4

Biomass Pyrolysis and Commissioning of the New 2-Stage Fixed Bed Reactor

4.1 Introduction

Based on the experience gained performing the experiments with the original single and two-stage fixed-bed reactor reported in chapter 3, it was decided that a new upgraded reactor was necessary to carry out experiments involving chemical-looping combustion with solid fuels. This chapter discusses the limitations with the original fixed bed reactor and provides a description of how the new, upgraded reactor was designed and implemented to overcome these issues. Results from the biomass pyrolysis commissioning experiments are also presented and compared with analogous results obtained in the original fixed bed reactor. The effect of heating rate (slow and fast), biomass sample size and system pressure on the pyrolysis product distribution and characteristics were measured and discussed.

4.2 Experimental

A number of limitations were identified with the original 2-stage fixed-bed reactor design and operating procedure used in the preliminary tar production and tar cracking investigations reported in chapter 3. To overcome these problems, modifications were made to the reactor design and a new up-graded 2-stage reactor was constructed. A discussion of the limitations with the existing reactor design is provided in the description of the modified reactor design provided below (section 4.2.1).

4.2.1 Modified two-stage fixed bed reactor description

The new fixed-bed reactor could be operated in either a single stage (with 1 bed) or two stage configuration (with 2 beds) (fig 4.1). The reactor body was constructed from 1” NB Incoloy 800HT pipe. The 1st stage reactor body was 350 mm in length and unlike the original 2-stage fixed bed design, the 2nd stage reactor body was constructed from single length of Incoloy pipe (600 mm). The welded flange connections along with the 2nd-stage gas inlet built into the flange connection were omitted from the modified reactor design in favour of a more robust reactor design that could be operated at significantly higher pressures of up to 20-30 bar_a and temperatures up to 1273 K (compared with < 3 bar_a and 1273 K). The connections between the reactor body, gas supply system and tar trap utilised Swagelok pressure fittings. In addition to providing a vastly improved pressure rating, the Swagelok pressure fittings were also much easier and less time consuming to seal than the flange connections.

The reactor could be used for investigations involving solid or gaseous fuels. With minor modifications it would also be possible to feed liquid fuels. A wider reactor diameter was chosen to allow solid fuels to be fed in either a batch-wise or semi-continuous manner. The ability to feed solid fuels in this way enables samples to be fed into the reactor after it has been heated to the experimental setpoint allowing for much quicker heating rates to be achieved that are more consistent with the heating rates of commercial, large-scale combustion/ gasification/ pyrolysis reactor systems. In the work described in this chapter and chapter 6, fuel was fed using the small batch feeder. A feeder designed for continuous solid fuel feeding was also tried but was not able to feed reproducible quantities of biomass and was therefore omitted from this work package. The continuous feeder was able to feed coal continuously (see appendix B, section B.1 for more details).

Gases were introduced through a T-piece at the top of the reactor. Depending on the operating conditions and gases used, the fuel could be pyrolysed, gasified or combusted in the 1st stage generating a fuel or exhaust gas which can be directly analysed (single-stage experiments) or further reacted in the 2nd stage (two-stage experiments). Ash and residual char was retained by the sintered quartz disk (bed support) in the first stage and the evolved gases and volatiles were swept downstream into the tar trap or 2nd stage. By operating the reactor in a two-stage configuration, it was possible to load a bed of reactive solid particles into the 2nd stage such as oxygen carriers for investigations into chemical-looping combustion (CLC); tar cracking catalysts; or CO_2 sorbents for CO_2 capture or sorbent enhanced reforming (SER) investigations. The effects of different reactive particles on the fuel/exhaust gases generated in the 1st stage could be determined by comparing results from single stage experiments with results from two stage experiments as with the previous design.

Inert quartz tubes incorporating sintered quartz disks, which act as the bed supports, were designed to line the inside of the reactor preventing undesirable reactions between gaseous reactants and products with the Incoloy 800HT reactor walls. A high temperature polymer seal was positioned at the top of the quartz tube to prevent gas bypass. A bespoke design spring situated at the base of the quartz tube provides the force required for sealing and acted to compensate for any change in reactor length which may have occurred due to thermal expansion.

Mass flow controllers (Bronkhorst High-Tech B.V.) were used to control and monitor the flow rate and composition of the gas entering the reactor allowing for fast and accurate gas switching. The pressure was controlled and monitored by a pressure controller and pneumatic valve (Bronkhorst High-Tech

B.V.) at the exit of the tar trap. The pressure controller and pneumatic valve had a pressure range of 1-30 bar_a. A steam generation system was also designed (as shown in fig. 4.1) and tested but time constraints and problems maintaining stable steam concentrations during solid fuel feeding meant that the steam generation system was not used in the work discussed in this thesis. A brief description of the steam generation and results from the steam generator commissioning can be found in appendix B, section B.2.

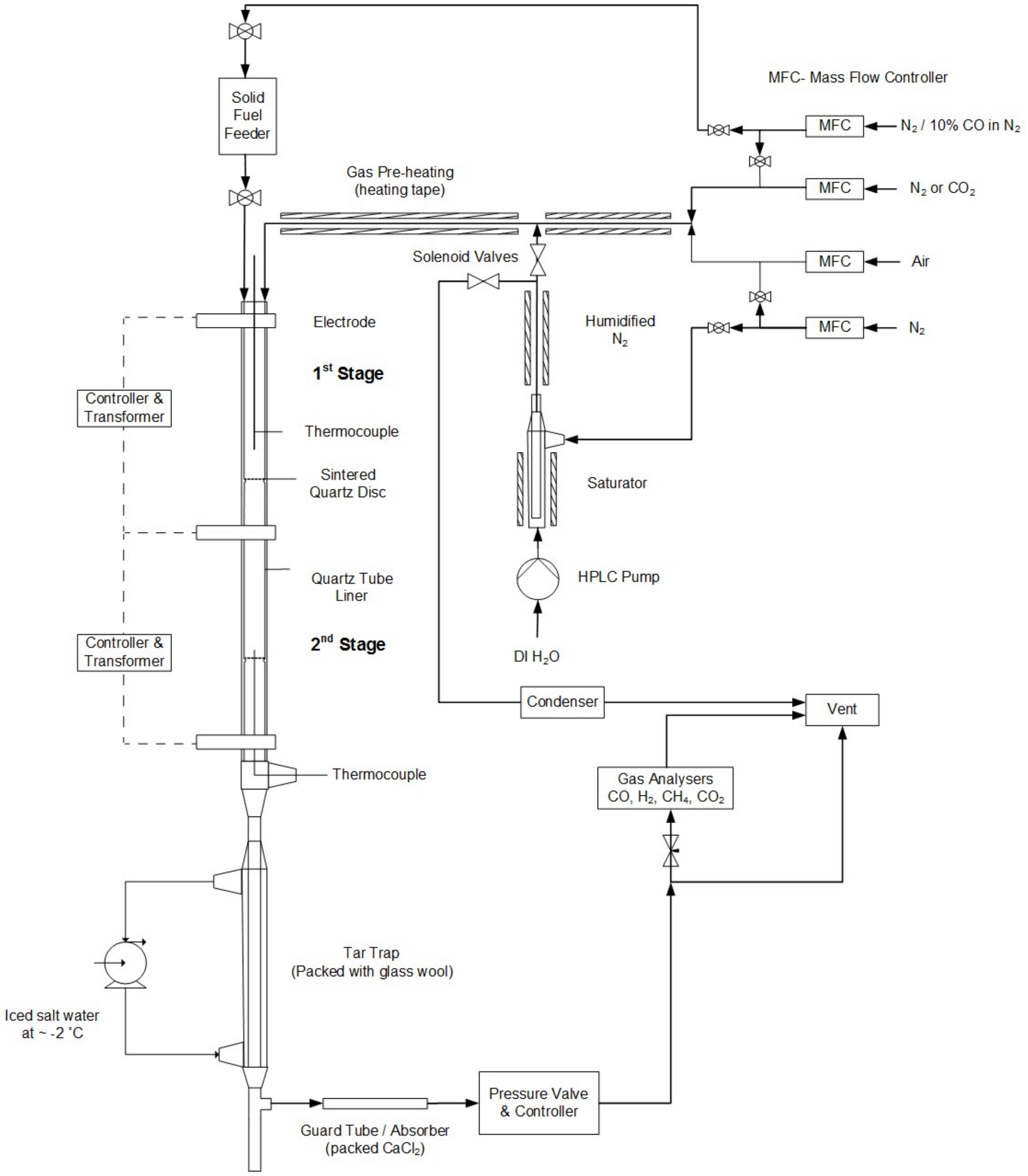

Figure 4.1: Schematic of the experimental set up for CLC experiments using the 2-stage fixed-bed reactor.

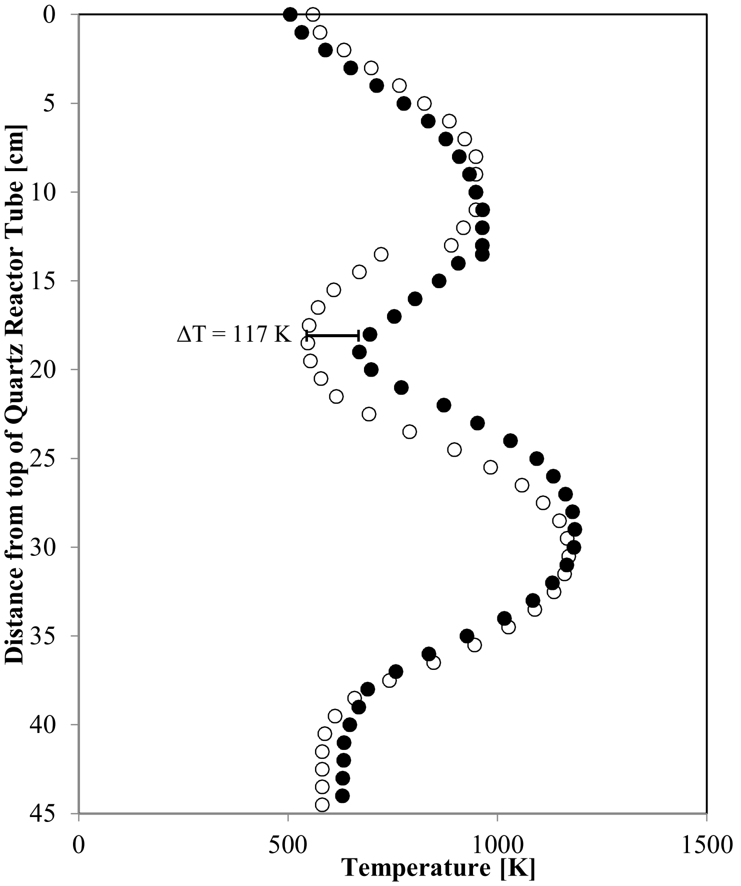

Figure 4.2: Temperature profile of two-stage reactor (1st stage T = 773 K; 2nd stage T = 1173 K) heated using the original 4 electrode setup (○) and new 3 electrode setup with a central bridging electrode (●).

The tar trap has an annular heat-exchanger design consisting of a 1000 mm stainless steel (½” OD) inner tube with a 1” OD outer tube connected around the outside of the ½” tube via 2 x 1” T-piece Swagelok connections. The gas exited the reactor through the internal ½” tube. The trap was cooled by pumping water (chilled to ~ -2 ˚C with ice and salt) around the annulus between outer wall of the internal ½” tube and internal wall of the external 1” tube as illustrated in the schematic provided in figure 4.1. The exit was loosely packed with ~ 6 g of glass wool to increase the internal surface area ensuring efficient trapping of the tars vapours in the form of aerosol droplets. The tar trap design described here was the product of a design process described in appendix B, section B.3.

The concentrations of CO_2, CO and CH_4 in the gas stream exiting the reactor are measured using online infrared analysers. The measurement of H_2 is also possible using an online thermal conductivity analyser.

A newly designed control program written in Agilent Vee made it possible to automate the whole process including fuel feeding, temperature control and switching, gas flow rate control and switching, pressure control and data monitoring and collection. All relevant information including measurements of the temperatures at different points in the reactor, flow rates, the system pressure and the signals from the gas analysers were logged every second and saved to a designated text file.

4.2.2 Materials

A single biomass variety, beech wood, was used for the biomass pyrolysis single-stage reactor commissioning work presented in this chapter. Biomass samples were prepared in the same manner as described in section 3.3.2. Samples were first ground in a high-shear cutting mill followed by sieving to obtain a size fraction of 106-150 µm. The ground and sieved biomass samples were then dried in small batches in an air-circulating oven at 308 K (35 °C) for 16 hours to remove the free moisture. The ultimate and proximate analysis can be found in table 3.1.

4.2.3 Operating Conditions

A standard set of conditions were developed and used when operating the new, upgraded fixed-bed reactor in either its single stage or 2-stage configuration (summarised in table 4.1). The work discussed in this chapter predominantly involved investigating the behaviour of different biomass varieties under fast pyrolysis conditions in the single-stage reactor. These experiments involved pre-heating the reactor to the experimental set point (773 K) and shooting the biomass sample (0.100-1.000 g) into the reactor from a pressurised 50 ml double-ended sample cylinder (pressurised to 0.5 bar above the reactor pressure) (Figure 5.1). Prior to feeding the loaded sample cylinder was purged for 5 minutes with a 10 ml s^{-1} flow of N_2 to displace any air (or O_2) that could interact with the sample and skew the results.

After the sample was fed, the reactor was held at the set point temperature for 300-600 s to ensure complete pyrolysis of the sample was achieved. A flow of N_2 with a superficial velocity of 0.25 m s^{-1} (60 ml_N s^{-1} at 500 ˚C) was introduced through the top of the reactor to sweep evolving volatiles from the sample bed downstream to the tar trap. During fuel feeding, 20 ml_N s^{-1} of flow was diverted to the feeder for sweeping the biomass particles from the sample feeder into the reactor. A superficial velocity of 0.25 m s^{-1} was found to be optimal.

Slow pyrolysis experiments were carried out in a similar manner to the method used in the original fixed bed reactor experiments (described in section 3.2.3). Biomass samples were pre-loaded into the single-stage reactor. The reactor was then heated from ambient to 773 K at a controlled heating rate of

1 K s^{-1}. The reactor was then held at the set point temperature for a further 900 s. The gas flow rate and system pressure were the same as those used for the slow pyrolysis experiments in the upgraded reactor (table 4.1).

Following the isothermal pyrolysis phase, the heating was either switched off and the reactor allowed to cool, or the gas inlet composition was switched to 10 vol.% O_2 (balance N_2). Switching the gas composition to 10 vol.% O_2 caused the organic content of the char bed to combust. The introduction of this char combustion step after the pyrolysis step was part of a new method for determining the char yield (discussed below in section 4.2.4).

Table 4.1: Summary of experimental operating parameters for the upgraded single-stage fixed-bed reactor.

Operating Conditions	1st Stage
Feedstock	Beech wood
Feed weight	0.100-1.000 g
Feed particle size	106-150 μm
Temperature	773 K
Heating Rate	Slow (1 K s^{-1}) or Fast (> 100 K s^{-1})*
Hold Time	600 s
Pressure	1.5 bar_a
Carrier Gas	Nitrogen
Flow Rate (Superficial Velocity)	60 ml_N s^{-1} (0.25 m s^{-1})

* Fast pyrolysis achieved by pressure feeding sample into reactor once the experimental set point temperature had been reached.

4.2.4 Product Recovery

Obtaining a repeatable and precise char yield was more difficult in the new upgraded fixed bed reactor as some of the char particles could not be removed from inside the quartz reactor tube due to electrostatic interactions. This was particularly problematic when smaller sample sizes were investigated (< 0.5 g) as a larger proportion of the total char would become stuck in this way. To overcome this issue, an alternative method was used to determine the char yields. The new method involved running at least two experiments: one where the inlet gas composition was switched to 10 vol.% air (balance N_2) after the isothermal pyrolysis phase causing the char bed to combust; the other involved ending the experiment after the isothermal pyrolysis step such that the residual char could be recovered. The char yield could then be determined by comparing the carbon content of the gas produced during the burn-off phase of the char bed in the first experiment with the carbon content of the char retrieved in the second experiment without the burn-off step (determined via elemental CHN analysis) (eq. 4.1-4.2).

$$C_{char,g} = Q_{Out,293K} \, . Ar_C \left(\frac{x_{CO_2}}{Mr_{CO_2}} + \frac{x_{CO}}{Mr_{CO}} + \frac{x_{CH_4}}{Mr_{CH_4}} \right) \qquad \text{(Equation 4.1)}$$

$$W_{char} = C_{char,g} \cdot \left(Ar_C \, . x_{C,char} \right) \qquad \text{(Equation 4.2)}$$

$C_{char,g}$ is the carbon content of the char (in wt.%) as determined from the concentrations of CO_2, CO and CH_4 measured at the outlet of the reactor; $Q_{Out,293K}$ is the total flow rate at the outlet of the reactor at 293 K and 1 bar_a (temperature and pressure of the gas analysers); Ar_C is the atomic mass of carbon; x_i is the mole fraction of gaseous species i in the gas stream exiting the reactor; Mr_i is the relative molecular mass of gaseous species i; W_{char} the total calculated weight of char (including ash); $x_{C,char}$ is the mole fraction of C in the char where $Ar_C \, . x_{C,char}$ is the mass fraction of C in the char as determined from elemental CHN analysis of the char.

The method used for recovering the tars from the reactor and determining the tar yield was the same as that described in section 3.2.5 except that the main solvent removal step (on the rotary evaporator) was carried out under vacuum and at a lower temperature of 0.337 bar_a and 333 K respectively compared with the conditions of 1.01 bar_a and 353 K used in chapter 3. These milder new conditions were chosen in an attempt to limit any potential polymerisation and any other interactions that may take place during solvent removal. In addition, a N_2 purged circulating oven was used for removing the residual solvent from the tars instead of an air circulating oven.

4.2.5 Gaseous Product Detection

The real-time concentrations of CO_2, CO and CH_4 and CO in the gas exiting the reactor were measured using an online multigas ADC analyser that was connected after the pressure control valve (table 4.3). A constant purge of 500 ml min^{-1} was maintained to the gas analyser to ensure the flow remained in the calibrated range for the analysers and the calculated response time measurements for the system remained valid. The remaining gas and gas exiting the analyser train was directed to a propane burner positioned in a nearby fume cupboard where any combustible gases were safely burnt off before being vented. A Hi-Tech K1500 thermal conductivity H_2 analyser was also installed however H_2 was not detected in the outlet gas from any of the pyrolysis experiments discussed in this chapter.

Table 4.3 Summary of the gas analyser set up used in this work.

Gas	**Analyser Type**	**Analyser Manufacturer and Model**	**Detection range [%]**	**Accuracy [% of measured value]**	**90 % response time* [s]**
CO_2	Infra-red	ADC MGA 3000	0-50	+/- 1 %	2.4
CO	Infra-red	ADC MGA 3000	0-50	+/- 1 %	2.4
CH_4	Infra-red	ADC MGA 3000	0-50	+/- 1 %	2.6
H_2	Thermal Conductivity	Hi-Tech K1500	0-25	+/- 1 %	5.3

* Response times quoted here are for the analyser only and do not include contributions from the reactor or trap.

4.3 Results & Discussion

4.3.1 Comparison of beech wood pyrolysis in the new upgraded and pre-existing single-stage fixed-bed reactors

Results

The tar yield from the slow pyrolysis of beech wood (1.000 g) in the new upgraded reactor was 27 % higher (46.2 wt.%) than the yield obtained after slow pyrolysis in the original pre-existing fixed bed reactor (36.3 wt.%) (fig. 4.3). The char yield was slightly lower at 19.0 wt.% compared with the char yield obtained from the equivalent slow pyrolysis experiment in the original reactor of 22.6 wt.%. Yields of the gaseous species detected in the reactor outlet gas were similar although the yield of CO from the slow pyrolysis experiment in the upgraded reactor was slightly higher (fig. 4.3).

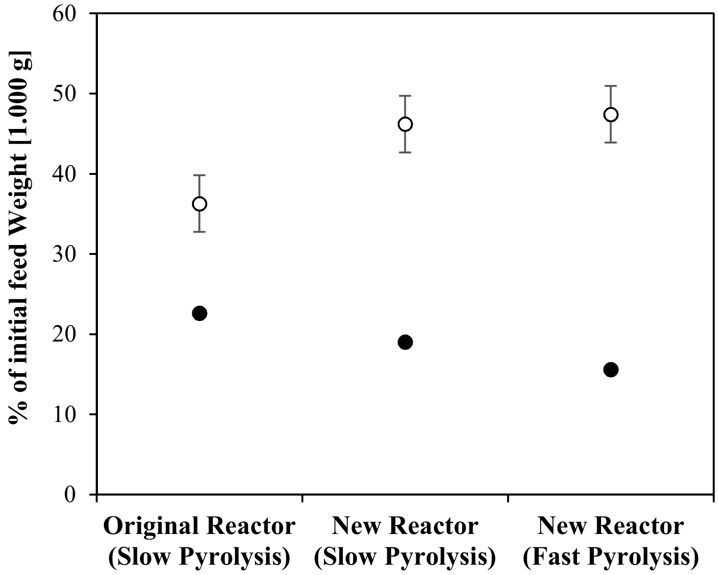

Figure 4.3: Comparison of the tar and char yields from the slow pyrolysis of beech wood in the original single-stage reactor (discussed in chapter 3) with the yields obtained from the slow and fast pyrolysis experiments in the new, upgraded reactor. Tar (●). char (○).

<u>Experimental Parameters:</u> ***1st stage (original reactor)**:* **Feed** = beech wood (1.000g, 106-150 µm), **carrier gas** = He, **superficial velocity** = 0.1 m s^{-1}, **inlet pressure** = 2.2 bar_a, **heating rate** = 1 K s^{-1}, **hold temperature** = 773 K, **hold time** = 900 s.

***1st stage (new reactor)**:* **Feed** = beech wood (106-150 µm), **feed weight** = 1.000 g, **carrier gas** = N_2, **controlled system pressure** = 1.5 bar_a, **superficial velocity** = 0.25 m s^{-1}, **heating rate** = 1 K s^{-1} (slow) or > 100 K s^{-1} (fast), **temperature** = 773 K, **hold time** = (900 s (slow pyrolysis), 600 s (fast pyrolysis)).

The differences between the product distributions of the slow pyrolysis and fast pyrolysis of 1 g of beech wood in the upgraded fixed fed reactor were less pronounced. The tar yields were very similar at 46.2 wt.% and 47.4 wt.% for the slow and fast pyrolysis experiments respectively. The char yield from the fast pyrolysis experiments was slightly lower (15.6 wt.%) than the char yield obtained from the slow pyrolysis experiment (19.0 wt.%). Care should be taken when interpreting these results as it was not possible to determine an error range for the char yields (due to a lack of experimental data points) making it difficult to determine whether these differences are significant or whether they lie within the error ranges. A lower char yield was to be expected as fast pyrolysis is known to produce a higher volatile and lower char yields than slow pyrolysis (Kandiyoti et al., 2006); however it was also expected that the lower char yield in the case of the slow pyrolysis would be accompanied by a more significant increase in the tar yield.

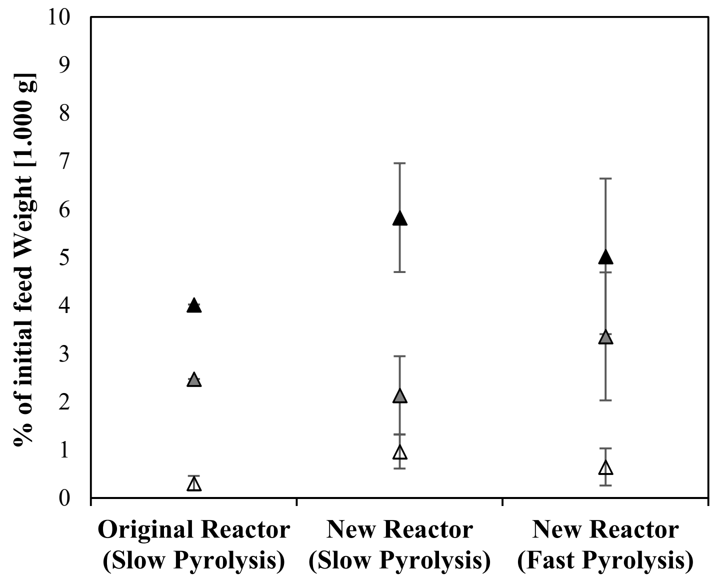

Figure 4.4: Comparison of the gas yields from the slow pyrolysis of 1 g of beech wood in the original, pre-existing single-stage reactor (discussed in chapter 3) with the yields obtained from the slow and fast pyrolysis experiments in the new, upgraded reactor. CO_2 (▲), CO (▲) and CH_4 (△).

Experimental Parameters: ***1st stage (original reactor)*:** **Feed** = beech wood (1.000 g, 106-150 μm), **feed weight** = 1.000 g, **carrier gas** = He, **superficial velocity** = 0.1 m s^{-1}, **inlet pressure** = 2.2 bar_a, **heating rate** = 1 K s^{-1}, **hold temperature** = 773 K, **hold time** = 900 s.

***1st stage (new reactor)*:** **Feed** = beech wood (1.000 g,106-150 μm), **carrier gas** = N_2, **controlled system pressure** = 1.5 bar_a, **superficial velocity** = 0.25 m s^{-1}, **heating rate** = 1 K s^{-1} (slow) or > 100 K s^{-1} (fast), **temperature** = 773 K, **hold time** = (900 s (slow pyrolysis), 600 s (fast pyrolysis)).

Inspection of the rate of gas production for the slow pyrolysis of beech wood (1.000 g) in the original and upgraded fixed bed reactors shows very similar behaviour (fig. 4.4). The onset of pyrolysis happened at approximately 500 K and was close to completion as the temperature set point of 773 K was reached (based on the CO and CO_2 measurements). The maximum rate of CO release appears to have occurred at similar temperatures of ~580 K for pyrolysis in the original reactor and ~500 K for pyrolysis in the new upgraded reactor.

Small differences in the CH_4 release can be observed in figure 4.5. CH_4 release appears to have begun at a lower temperature of ~470 K during the pyrolysis experiment in the new reactor and at a higher temperature of 550 K in the original reactor. CH_4 release also appeared to have been higher in the pyrolysis experiment in the upgraded reactor with release taking place over a longer time period. Despite the differences, the maximum rate of CH_4 release was measured at roughly the same temperature of ~650 K. In both experiments, total CH_4 production was very low (< 1 wt.% of the total biomass input) such that the measured CH_4 concentration in the outlet gases was also very low (< 0.8 vol.% and < 0.2 vol.% for the pyrolysis in the original and new reactor respectively) and close to the detection limits of the analysers. Therefore the errors in the measurements were high (relative errors of 48 % and 41 % for total CH_4 release in the original and new reactors respectively) diminishing the significance of these differences.

A benefit of the new upgraded reactor is that it is now possible to measure the rate of CO_2 release, which was not possible in the original reactor setup due to use of liquid nitrogen as the coolant for the tar trap. CO_2 release appeared to have started at the same temperature as CO release but continued for a longer time period than CO release contributing to the higher total yield of CO_2. The rate of CO_2 release also passed through a maximum at a higher temperature of ~640 K compared with the CO release.

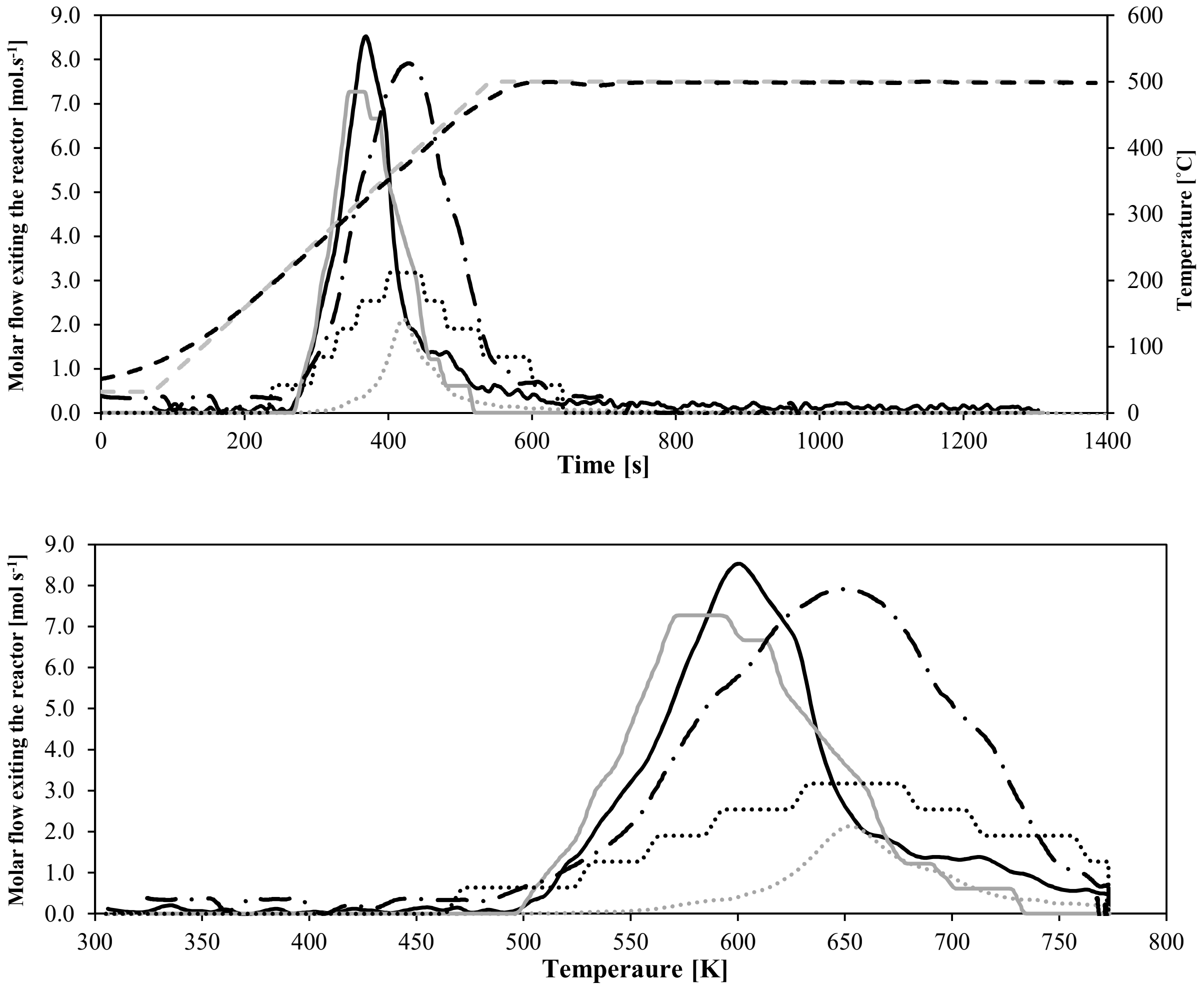

Figure 4.5: Comparison of the production of the different gaseous species (CO_2, CO, and CH_4) measured in the outlet gases during the slow pyrolysis of beech wood (1.000 g) in the original fixed-bed reactor (grey lines) and upgraded fixed bed reactor (black lines) as a function of (a) time and (b) temperature. CO (——); CH_4 (·········); CO_2 (— · -) and bed temperature (- - -).
Experimental Parameters: ***1st stage (original reactor)***: **Feed** = beech wood (1.000 g,106-150 μm), **feed weight** = 1.000 g, **carrier gas** = He, **superficial velocity** = 0.1 m s^{-1}, **inlet pressure** = 2.2 bar_a, **heating rate** = 1 K s^{-1}, **hold temperature** = 773 K, **hold time** = 900 s.

1st stage (new reactor): **Feed** = beech wood (106-150 μm), **feed weight** = 1.000 g, **carrier gas** = N_2, **controlled system pressure** = 1.5 bar_a, **superficial velocity** = 0.25 m s^{-1}, **heating rate** = 1 K s^{-1}, **temperature** = 773 K, **hold time** = 600 s.

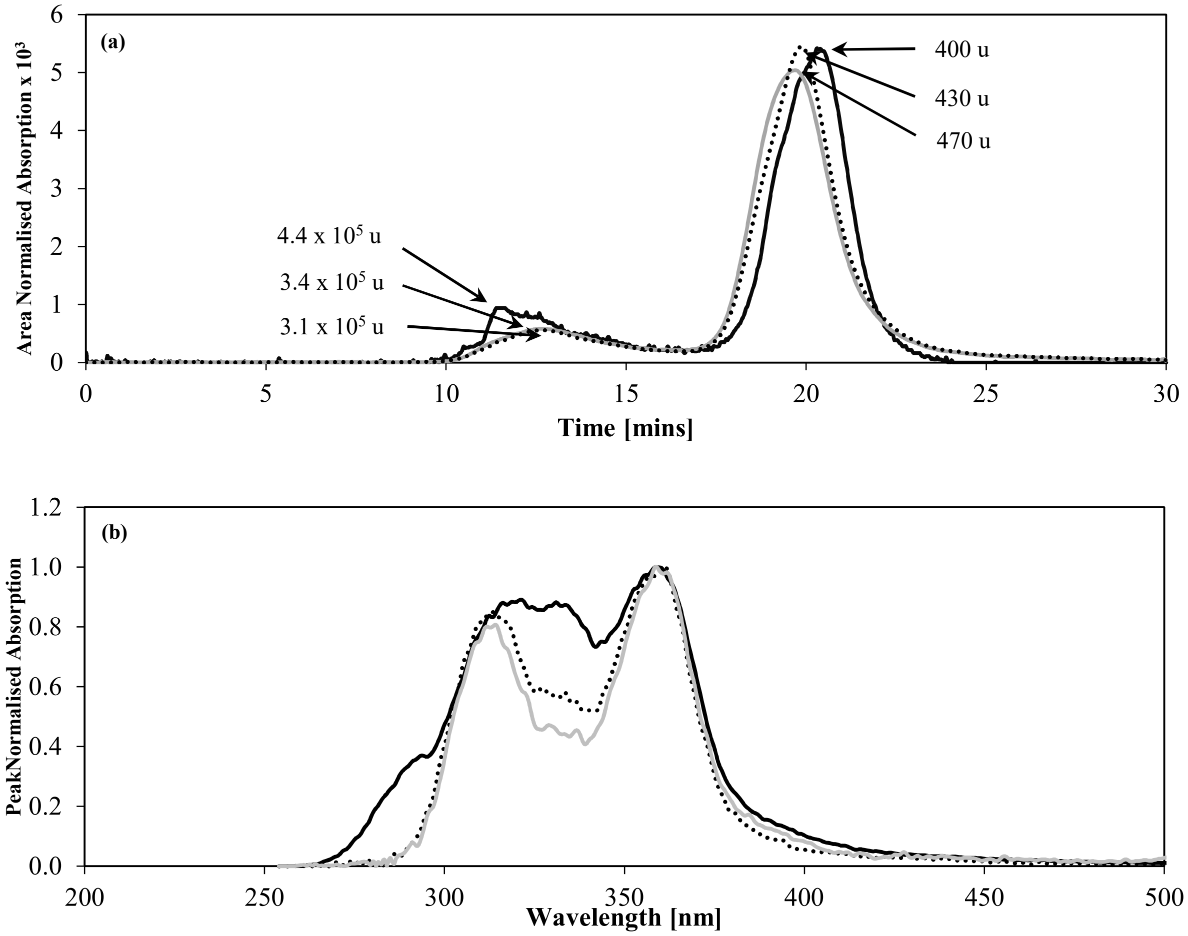

Figure 4.6: (a) SEC and (b) UVF analysis of the tars recovered from the slow pyrolysis of 1 g of beech wood in the original, pre-existing single-stage reactor (discussed in chapter 3) with the yields obtained from the slow and fast pyrolysis experiments in the new, upgraded reactor.

<u>**Experimental Parameters:**</u> ***1st stage (original reactor)***: **Feed** = beech wood (1.000 g,106-150 μm), **feed weight** = 1.000 g, **carrier gas** = He, **superficial velocity** = 0.1 m s^{-1}, **inlet pressure** = 2.2 bar_a, **heating rate** = 1 K s^{-1}, **hold temperature** = 773 K, **hold time** = 900 s.

1st stage (new reactor): **Feed** = beech wood (106-150 μm), **feed weight** = 1.000 g, **carrier gas** = N_2, **controlled system pressure** = 1.5 bar_a, **superficial velocity** = 0.25 m s^{-1}, **heating rate** = 1 K s^{-1}, **temperature** = 773 K, **hold time** = 600 s.

Slow pyrolysis in the original reactor (━━━); slow pyrolysis in the upgraded reactor (───); fast pyrolysis in the upgraded reactor (········).

The tar samples obtained after the slow and fast pyrolysis experiment in the two fixed-bed reactors exhibited the characteristic bimodal size distribution (fig. 4.6 (a)). The tar sample obtained after slow pyrolysis in the original reactor appeared to have a slightly larger proportion of the heavier tar fraction (characterised by the retained peak in the SEC chromatogram) compared with the tar samples generated in the upgraded reactor. The peak of the excluded peak (corresponding to the elution of the lighter tar species) appeared at the longest elution time indicating that the lighter fraction of the tars produced in the original reactor had a marginally lower average molecular mass of ~ 400 u than both the tar samples produced in the slow and fast pyrolysis experiment in the upgraded reactor.

The tars produced from the slow and fast beech wood pyrolysis in the upgraded reactor contained similar proportions of the heavier tar fraction, however there were some differences between the retained peaks in the SEC chromatograms (fig. 4.6 (a)). The retained peak of the tars produced from the slow pyrolysis of beech wood was broader and less intense, with a maximum at a slightly shorter elution time than the retained peak in the SEC chromatogram for the tars produced from the fast pyrolysis experiments. The average molecular masses of the lighter tar fractions (determined from the elution times of the excluded peak maxima) were 470 u and 430 u for the slow and fast pyrolysis experiments respectively.

There are some distinct differences in the UVF spectra of the tars derived from the slow pyrolysis experiments in the different reactors (fig. 4.6 (b)). The lower wavelength peak in the UVF spectra of the tars generated in the original reactor appears to be much broader exhibiting a maxima between 310-330 nm whereas the lower wavelength peak in the tars from the upgraded reactor is narrower with a maxima at ~ 315 nm. The region of low intensity between the two peaks is also more intense and there is a more intense region of absorption between 270-300 nm (before the low wavelength peak) in the UVF spectra of the tars produced in the original reactor compared with the tars produced during slow pyrolysis in the upgraded reactor.

The UVF spectra of the tars produced from the fast and slow pyrolysis experiments in the upgraded reactor are less pronounced (fig. 4.6 (b)). The less intense region between the two peaks is slightly more intense in the spectrum for the tars produced from the fast pyrolysis experiment but are otherwise very similar in appearance.

Discussion

A direct comparison of the results from the slow pyrolysis experiments in the original and upgraded reactor is not possible owing to the numerous differences in the reactor construct and operating parameters used (discussed in section 4.2.1). However some theories and explanations for the observed trends in the data are proposed below.

A possible explanation for differences observed in the pyrolysis product distributions (*i.e.* lower tar yield), SEC chromatograms and UVF spectra of the slow pyrolysis tars from the different reactors could be that the primary pyrolysis products underwent more severe secondary cracking of the primary pyrolysis products in the original reactor compared with the upgraded reactor. Cracking of the tar species as they evolve could potentially take place on the surface of the chars or on the reactor walls. The upgraded reactor was designed to incorporate a quartz tube internal liner to prevent contact between the hot, potentially catalytically active Incoloy 800HT reactor walls and the evolving volatiles. The higher superficial velocity used for the experiments in the upgraded reactor meant that the average residence time of the evolving volatiles in the sample bed was less than in the new, upgraded reactor, reducing the chance of secondary cracking reactions taking place on the surface of the chars.

Based on the results from the UVF analysis, it would appear that the more conjugated tar species of the lighter tar fraction (characterised by the higher wavelength peak in the UVF spectra) of the tars produced in the original reactor underwent more severe cracking into smaller less conjugated tar compounds. This theory would explain the broader peak at the lower wavelength in the UVF spectra and the lower average molecular mass of the lighter tar fraction as indicated by the longer elution time of the retained peak in the SEC chromatogram. The larger proportion of the heavier tar fraction (characterised by the retained peak in the SEC chromatogram) in the tars produced in the original reactor could be a result of the higher molecular mass tars being more refractory in nature leading to more pronounced cracking of the lighter tar fraction relative to the heavier tar fraction.

The differences in the product distributions and SEC and UVF analyses of the tars produced via slow and fast pyrolysis in the upgraded reactor are a little more difficult to explain. Fast pyrolysis of biomass typically produces more tar and less char than biomass pyrolysed at lower heating rates (Kandiyoti et al., 2006). Higher heating rates result in a more rapid build-up of pressure within the char particle aiding vapour release and reducing the average contact time between the evolving vapours and internal charring surfaces of the particle on which char forming and tar cracking interactions can take place. However, whilst the char yield from the fast pyrolysis experiments was slightly lower than the yield obtained from the slow pyrolysis experiments, little difference in the tar yield was observed.

Higher heating rates are also expected to result in tars with a higher average molecular mass and higher proportion of the heavier tar fraction (characterised by the excluded peak in the SEC chromatogram) since tars undergo less cracking and the more destructive nature of fast pyrolysis leads to the ejection of large fragments from the biomass structure (Kandiyoti et al., 2006, Somrang, 2012). These large fragments can then become entrained in the carrier gas as aerosol droplets, exiting the reactor before being decomposed. Some possible explanations for the deviation in the measured results from the expected trends are proposed below:

(i) Whilst significant efforts have been made to reduce secondary interactions that take place within the upgraded reactor, there is still likely to be substantial secondary interactions taking place on the hot surfaces of the reactor walls downstream of the sample bed, and on the surfaces of the sand and quartz frit that make up the sample bed support.

(ii) The inventory of biomass shot into the reactor in the fast pyrolysis experiments was relatively large (1.000 g) such that there is still likely to be secondary tar cracking interaction taking place between the evolving tar vapours and the charring biomass particles before the vapours exit the bed.

(iii) The heating rate experienced by the char particles in the fast pyrolysis experiments has not yet been quantified/calculated. It is therefore not possible to determine the extent of the difference in heating rates of the slow and fast pyrolysis experiments and whether the difference was large enough to effect the overall pyrolytic decomposition mechanism. The temperature measured in the sand bed, on which the biomass sample was fired onto, dropped by ~ 40 K when the biomass sample was introduced (Figure 4.9). This temperature drop was caused by the onset of pyrolysis (highly endothermic process) upstream of the sand bed cooling the gas stream as it passes through the pyrolysing sample. Sand has a high heat capacity and therefore retains heat well, however it is likely that the temperature difference between the pyrolysing char particles and the surrounding gases (and sand bed) was likely to have been much greater which would infer that the actual temperature at which pyrolysis was taking place (particularly during the early stages) was much lower than the measured bed temperature.

Further work is necessary to quantify/calculate the heating rates experienced by the biomass particles during the fast pyrolysis experiments.

4.3.2 The effect of sample feed mass on the fast pyrolysis product distribution of beech wood

In an attempt to overcome some of the potential issues associated with the relatively large biomass sample size of 1 g, and the proposed deleterious effect that the large sample size is likely to have had on the heating rate, a set of experiments was undertaken to investigate the effect of sample size on the fast pyrolysis behaviour of the beech wood feed. It was proposed that smaller biomass sample sizes would aid heating rates due to the lower energy demand required for heating the samples to the temperature set point. Furthermore, the use of smaller samples would also help to limit secondary interactions since the size of the sample bed that forms would be smaller reducing the residence time of the evolving volatiles within the bed.

Results

The product distributions obtained from the fast pyrolysis of different quantities of beech wood between 0.1-1 g were fairly similar exhibiting no discernible trends (figs. 4.7-4.8). Tar yields were between 43-47 wt.% and char yields varied between 15-20 wt.%. The variation observed in the gas yields (CO_2, CO and CH_4) was all within the experimental error.

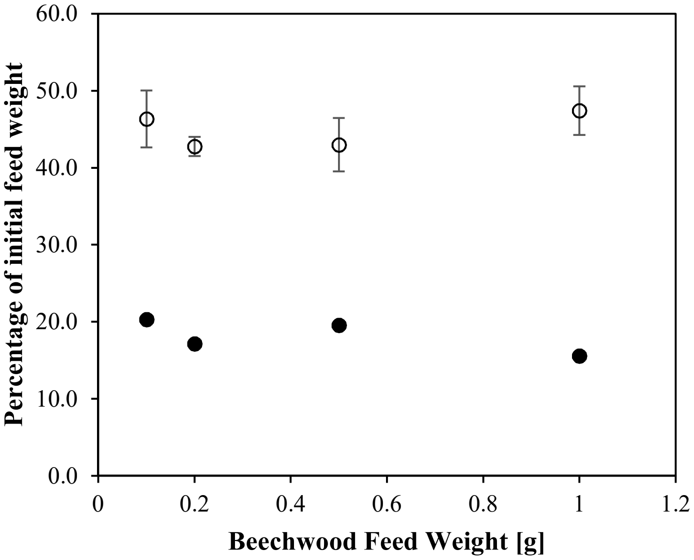

Figure 4.7: Tar and char yields as a function of sample feed weight from the fast pyrolysis of beech wood.

Experimental Parameters: ***1st stage***: **Feed** = beech wood (1.000 g,106-150 µm), **carrier gas** = N_2, **controlled system pressure** = 1.5 bar_a, **superficial velocity** = 0.25 ms^{-1}, **temperature** = 773 K, **hold time** = 600 s. Tar (●), char (○).

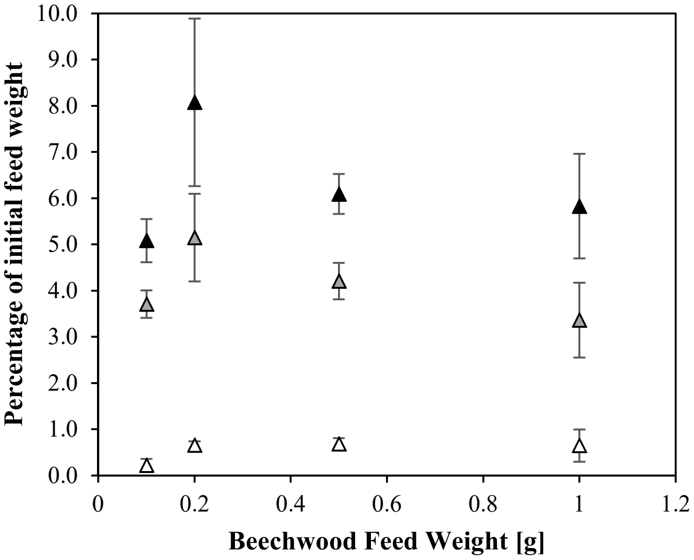

Figure 4.8: Gas yields as a function of sample feed weight from the fast pyrolysis of beech wood.

Experimental Parameters: ***1st stage***: **Feed** = beech wood (1.000 g,106-150 µm), **carrier gas** = N_2, **controlled system pressure** = 1.5 bar_a, **superficial velocity** = 0.25 ms^{-1}, **temperature** = 773 K, **hold time** = 600 s. CO_2 (▲), CO (▲) and CH_4 (△).

(a)

(b)

(c)

(d)

Figure 4.9: Comparison of (a) the 1st stage bed temperature profiles and the production of the different gaseous species (b) CO_2, (c) CO, and (d) CH_4) measured in the outlet gases during the fast pyrolysis of beech wood (0.100-1.000 g) in the upgraded fixed bed reactor.

<u>**Experimental Parameters:**</u> ***1st stage***: **Feed** = beech wood (106-150 μm), **feed weight** = variable, **carrier gas** = N_2, **controlled system pressure** = 1.5 bar_a, **superficial velocity** = 0.25 ms^{-1}, **temperature** = 773 K, **hold time** = 600 s. **Beech wood loading:** 0.100 g (——); 0.2 g (——), 0.5 g (– – –), 1.000 g (·········).

The concentration profiles of the gaseous products CO_2, CO and CH_4 measured in the gas stream exiting the reactor show that the maximum release of each of the gases was achieved imediately after the biomass was fed into the reactor (fig. 4.9). Gas release then declines over the proceeding 20-400 s depending on the mass of sample fed. This observation indicates that the heating rate experienced by the biomass would have been relatively fast causing the rapid onset of pyrolysis as the biomass came into contact with the hot sand bed in the reactor.

Increasing the mass of sample increased both the maximum concentration of each of the gases measured in the outlet gases and the time period over which the gases were detected. The time period over which the gases were detected increased from ~ 25 s to ~ 400 s based on the measured CH_4 release (or to 200 s baed on the CO and CO_2 release) when the sample size was increased from 0.1 g to 1 g. This indicates that the time period in which pyrolysis was taking place was also extended with increasing sample mass. The implications of these observations are discussed in more detail below.

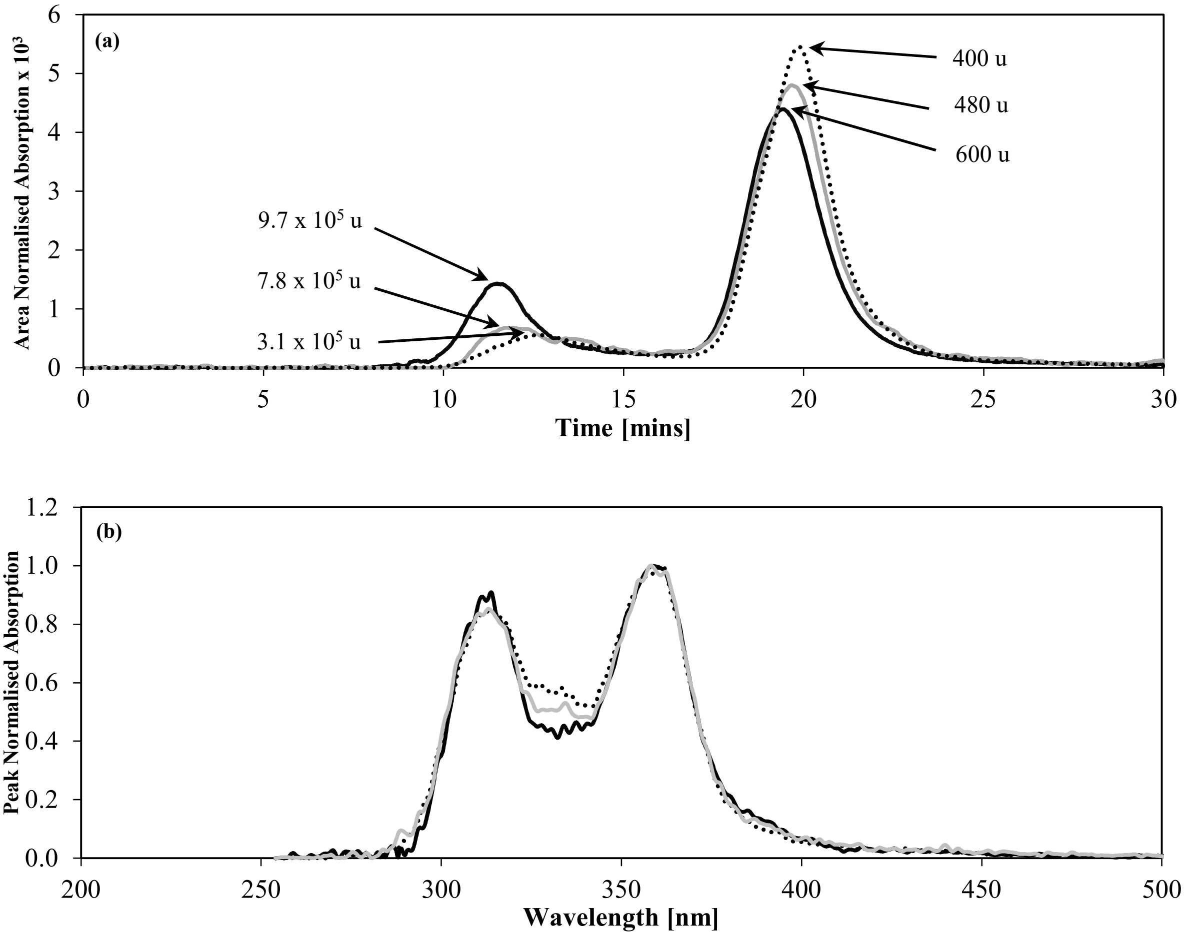

Figure 4.10: (a) SEC and (b) UVF analyses of the tars recovered from the fast pyrolysis of different weights of beech wood in the single stage reactor.

Experimental Parameters: ***1st stage***: **Feed** = beech wood (106-150 μm), **feed weight** = variable, **carrier gas** = N_2, **controlled system pressure** = 1.5 bar_a, **superficial velocity** = 0.25 ms^{-1}, **temperature** = 773 K, **hold time** = 600 s. 0.1 g(━━━); 0.5 g (━━━); 1 g(········).

The SEC chromatograms of the tars recovered after the fast pyrolysis of beech wood with varying sample sizes shows a substantial shift in the molecular size distribution from the lower molecular mass size fraction (retained peak) to the higher molecular mass fraction (excluded peak) with decreasing sample size (fig. 4.10(a)). The average molecular mass of both size fractions (calculated from the elution times of the peak maxima) also increased from 400 u to 600 u and 3.1 x 10^5 u to 9.7 x 10^5 u for the lower and higher molecular mass fractions respectively.

The UVF spectra of the tars obtained from the fast pyrolysis of beech wood with varying sample sizes are very similar showing two distinct peaks at ~ 315 nm and ~ 360 nm respectively separated by a region of lower absorption intensity (fig. 4.10(b)). The only differences between the peak normalised spectra is that the intensity of the region between the two peaks increases with increasing sample loading.

Discussion

Whilst no discernable effect of biomass sample size (0.1-1.0 g) on the product distribution of the fast pyrolysis experiments was observed, varying the sample size did seem to effect the pyrolysis behaviour (as illustrated by figure 4.9) and the nature of the recovered tars (fig. 4.10).

Increasing the sample mass increased the time period over which the gases (CO_2, CO and CH_4) were detected in the outlet gas after the biomass sample was fed, inferring that the time period in which pyrolysis took place was also increased (fig. 4.9). The observed increase in pyrolysis time with increasing sample mass could be due to the more severe temperature drop (as illustrated by fig. 4.9(a)) and its consequential effect on the heating rate of the sample.

The larger sample sizes are also likely to have behaved more like a packed bed once fired into the reactor, with large temperature (and heating rate) differences between the sample that was in contact with the hot surfaces of the sand and reactor walls, and the sample that was contained (and therefore insulated by the reacting particles on the outer surfaces of the bed) within the main bulk of the biomass sample. The average pathway of the evolving volatiles would have also been more tortuous compared with the smaller biomass sample sizes (due to the larger sample bed that forms), which may have impeded vapour release from the bed contributing to the detection of gases over a longer time period.

The char beds that formed in the experiments with the smallest sample size of 0.1 g were far more dispersed across the surface of the sand indicating that conductive heat transfer from the sand and reactor walls would have been better resulting in faster and more uniform heating rates. The residence time and less tortuous average pathway of the volatiles within the charring sample bed (or lack therof) would have been substantially reduced infering a more rapid release of the volatiles and reduced secondary interactions. This theory is supported by the results of the SEC and UVF analyses.

SEC analysis showed that decreasing the sample mass shifted the molecular size distribution in favour of the higher molecular mass tar species characterised by the excluded peaks in the SEC chromatogram (fig. 4.10(a)). The average molecular mass of both the higher and lower molecular mass fractions were also shifted to a higher average mlecular mass with decreasing molecualr mass. These findings indicate that more of the larger but less stable tar species created during the ejection of the large structural fragments under fast pyrolysis conditions survived and were recovered in the tar product; supporting the earlier proposed theory that decreasing the sample size helped to reduce secondary tar cracking interactions between the primary tar species and charring biomass solids. The higher intensity of the low intensity region in the UVF spectra may be a result of enhanced cracking of the higher and more conjugated lower molecular mass tar fractions into secodary (and tertiarry) tar products with a more varied range of conjugation extents (fig. 4.10(b)).

4.3.3 The effect of system pressure on the fast pyrolysis product distribution of beech wood

Since the upgraded reactor was designed to allow pressurised operation, a few experiments were carried out investigating the effect of pressure between 1.5-5 bar_a on the fast pyrolysis of 0.1 g of beech wood.

Results

Increasing the system pressure at which the beech wood feed was pyrolysed resulted in a decrease in both the tar and char yields (fig. 4.11). The tar yield decreased from 46.3wt.% to 41.0 wt.% and the char yield decreased from 20.3wt.% to 12.5 wt.% when the system pressure was increased from 1.5 bar_a to 5 bar_a. Distinguishing trends in the gas (CO_2, CO and CH_4) yields is slightly more difficult owing to the large relative errors in the measurements (fig. 4.12). The CO yield appeared to increase slightly from ~ 3 wt.% to ~ 6 wt.% with increasing pressure whereas the CO_2 yield was relatively stable when the pressure increased from 1.5 bar_a to 3 bar_a but then dropped from 5.7 wt.% to 3.0 wt.% when the pressure was increased to 5 bar_a.

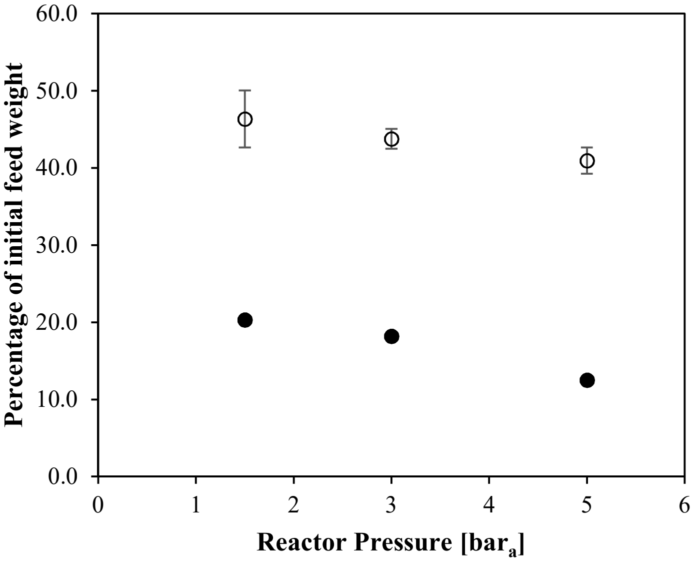

Figure 4.11: Tar and char yields as a function of system pressure from the fast pyrolysis of beech wood.
Experimental Parameters: ***1st stage***: **Feed** = beech wood (0.100 g, 106-150 μm), **carrier gas** = N_2, **controlled system pressure** = variable, **superficial velocity** = 0.25 m s^{-1}, **temperature** = 773 K, **hold time** = 600 s. Tar (○), char (●).

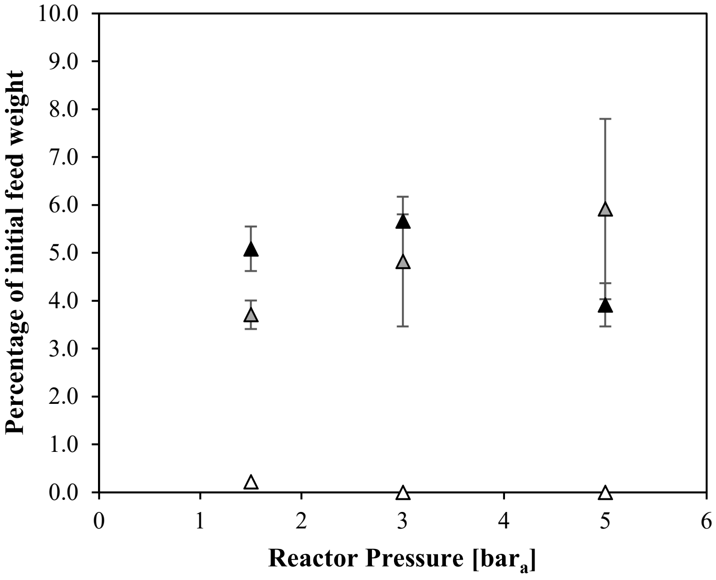

Figure 4.12: Gas yields as a function of system pressure from the fast pyrolysis of beech wood.
Experimental Parameters: ***1st stage***: **Feed** = beech wood (0.100 g, 106-150 µm), **carrier gas** = N_2, **controlled system pressure** = variable, **superficial velocity** = 0.25 m s^{-1}, **temperature** = 773 K, **hold time** = 600 s. Tar (○), char (●).

SEC analysis of the tars recovered after fast pyrolysis of the beech wood feed at 1.5 bar$_a$ and 3 bar$_a$ produced very similar chromatograms (fig. 4.13(a)). Both tar samples had similar proportions of the higher and lower molecular mass fractions represented by the excluded and retained peaks respectively. There were more notable differences in the SEC chromatogram of the tars produced from the fast pyrolysis of beech wood at 5 bar$_a$ and the tars produced at 1.5 bar$_a$ and 3 bar$_a$. The SEC chromatogram of the tars produced at 5 bar$_a$ had a larger proportion of the lower molecular mass fraction relative to the higher molecular mass fraction than the tars produced at the lower pressures. The average mass of the higher molecular mass fraction was also shifted to a lower molecular mass of ~ 5.2 x 10^5 u and the average molecular mass of the lighter tar fraction was shifted to a higher molecular mass of ~ 710 u (compared with 9.6-9.7 x10^5 u and 560-600 u for the higher and lower molecular mass fractions of the tars produced at the lower pressures).

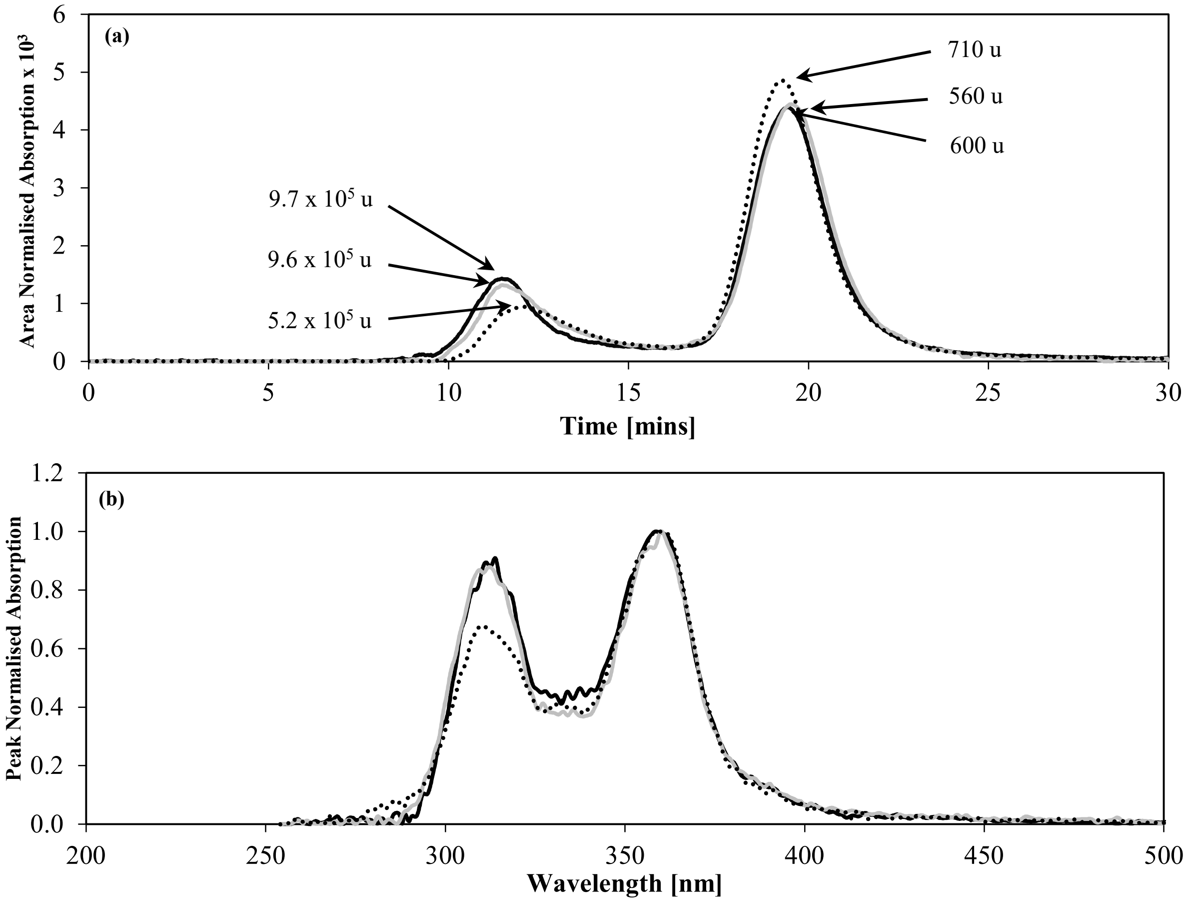

Figure 4.13: (a) SEC and (b) UVF analyses of the tars recovered from the fast pyrolysis of different amounts of beech wood in the single stage reactor operated at different pressures (1.5-5 bar_a).

Experimental Parameters: ***1st stage***: **Feed** = beech wood (0.100 g, 106-150 μm), **carrier gas** = N_2, **controlled system pressure** = variable, **superficial velocity** = 0.25 m s^{-1}, **temperature** = 773 K, **hold time** = 600 s. 1.5 bar_a (▬▬); 3 bar_a (──); 5 bar_a (········).

The UVF analyses of the tars show similar trends to the SEC chromatograms (fig. 4.13(b)). The UVF spectra of the tars produced at 1.5 bar_a and 3 bar_a are almost identical with two peaks of similar absorption intensity at ~ 315 nm and ~ 360 nm separated by a region of lower absorption intensity. The UVF spectra of the tars produced at 5 bar_a was slightly different. The peak corresponding to absorption at the lower wavelength of ~ 315 nm in the peak normalised UVF spectra was less intense than the equivalent peaks in the UVF spectra of the tars produced at 1.5 bar_a and 3 bar_a.

Discussion

Increasing the pressure of pyrolysis typically results in higher char yields and lower yields of tars and other volatiles/gases (Guell, 1993, Kandiyoti et al., 2006). In the experiments reported here, increasing the pressure caused a small decrease in the tar yield (as expected) but also appeared to cause a decrease in the char yield (not expected). The rate at which volatiles exit a pyrolysing biomass particle is proportional to the pressure differential caused by the pressure build up within the particle as a result of the melting and vapourisation of the biomass structure, and the system pressure outside the particle. Increasing the pressure of the system reduces the pressure differential thus decreasing the average rate at which volatiles exit the particle and increasing the average residence time of the volatiles within the charring particle. The increased residence time of the pyrolysis vapours in the pyrolysing particle is likely to have led to increased secondary cracking of the less stable, larger molecular weight primary tar vapours resulting in a decrease in the molecular size distribution of the recovered tar as indicated by SEC analysis.

The unexpected decrease in the char yield may be a result of the onset of small amounts of gasification reactions taking place between the char surface and CO_2, evolving tar vapours, light hydrocarobns and other undetected volatile species at the higher pressures leading to slightly enhanced CO yields and lower CO_2 yields.

The results of the SEC indicate that increasing the pressure between 3 bar_a and 5 bar_a resulted in the enhanced cracking of some of the less stable, higher molecular weight tar components into lighter tar components. The enhanced cracking of the higher molecular mass fraction also caused an increase in the average molecular mass of the lower molecular mass fraction from 560-600 u (in the case of the tars recovered after pyrolysis at 1.5 bar_a and 3 bar_a) to 700 u. UVF analysis indicates that the lower molecular mass fraction of the tars produced at 5 bara contained a higher proportion of the more conjugated tar components (that absorb and fluoresce UV radiation at the higher wavelength of ~ 360 nm) relative to the less conjugated tar components (that fluoresce at the lower wavelength of ~ 315 nm).

4.4 Conclusions

A new, upgraded two-stage fixed bed reactor was designed and constructed. The new fixed-bed reactor allows for more flexible operation compared with the existing reactor used in chapter 3, offering the ability to study processes at pressures of 1-30 bar_a and temperature up to 1273 K. A new solid feeding system was also designed and installed allowing for multiple batches of solid fuel to be fed into the reactor during an experiment. The solid feeding system allowed for biomass pyrolysis to be studied under fast pyrolysis conditions *i.e.* fast heating rates that were more consistent with sorts of heating rates biomass is exposed to in commercial, large-scale combustion/ gasification/ pyrolysis reactor systems. Changes made to the tar trap and tar trap cooling system meant that the effects of CO_2 and steam could be studied where previously their use would have led to the formation of blockages within the liquid N_2 cooled tar trap. An internal quartz reactor assembly was also designed to line the internal surfaces of the reactor to limit secondary tar cracking interactions that could take place on the potentially catalytically active walls of the Incoloy 800HT pressure vessel.

The tar yield obtained after the slow pyrolysis (1 K s^{-1}, 773 K) of 1 g beech wood in the upgraded reactor was 27 wt.% higher than the yield obtained from analogous experiments in the original fixed bed reactor. This represents a substantial improvement in the tar yield and was attributed to reduced secondary tar cracking on the reactor walls within the upgraded reactor and validates the choice of using a quartz reactor assembly to line the internal surfaces of the Incoloy 800HT outer vessel. The increased tar yield was accompanied by a much smaller decrease in the char yield which was to be expected given that the residence time of the evolving volatiles within the charring sample bed would have been reduced (inferring less time in which secondary char forming interaction can take place) due to the wider reactor diameter (shorter sample bed height) and higher superficial velocity used.

Fast pyrolysis (> 100 K s^{-1}, 773 K) of 1 g of beech wood produced slightly lower char and CO_2 yields and slightly improved CO yields but no discernible differences were observed in the tar yield compared with the slow pyrolysis product distribution. Fast pyrolysis processes are known to produce higher tar yields and lower char yields than equivalent slow pyrolysis processes. It was theorised that the large sample size fed into the reactor caused a substantial cooling effect due to the onset of the highly endothermic pyrolysis process which impeded heating rates. Secondary tar cracking interactions were also expected to be significant owing to the relatively large sample bed presenting a large charring surface on which these interactions could take place.

Changing the biomass sample size between 0.1g and 1 g did not appear to have any significant effect on the fast pyrolysis product distribution. However, analysis of the tars via SEC revealed that the molecular weight distribution of the tars shifted in favour of the higher molecular weight fraction. Tars produced from the fast pyrolysis of biomass are expected to consist of a greater proportion of higher molecular mass fragments due to the destructive nature of fast pyrolysis resulting in the ejection of large fragments of undecomposed and partially decomposed structural fragments. The observed shift in molecular size distribution of the recovered tars with decreasing sample size was thought to be the result of faster and more uniform heating rates due to improved heat transfer between the sand and reactor walls and the more dispersed biomass particles; and fewer tar cracking interactions as a result of the reduced contact between the pyrolysis vapours and charring solids.

Increasing the system pressure between 1.5 bar_a and 5 bar_a resulted in small decreases in both the tar and char yields. The decrease in tar yield was to be expected given that increased pressures impede the release of volatiles from the particle. The time in which the evolving volatiles were exposed to the internal surfaces of the charring particles is therefore increased, increasing the chance of secondary tar cracking and char forming reactions taking place. The slight decrease in char yield may be a result of the onset of small amounts of gasification between the char surface and CO_2, tar vapours, light hydrocarbons and other undetected gaseous species at the higher pressures leading to slightly enhanced CO yields and lower CO_2 yields. Further work is necessary to test this theory and investigate the effect of pressure on the fast pyrolysis process over a wider range of pressures.

Chapter 5

The Development of Wet Granulation Production Methods and a Rigorous Testing Protocol for Fe-Based CLC Oxygen Carrier Materials

5.1 Introduction

The oxygen carrier material is the salient feature of a CLC process and as such, the majority of CLC research has focused on their development. More than 900 different oxygen carrier materials have been developed and studied at the laboratory scale (Lyngfelt and Mattisson, 2011). There are a number of very good review articles that give in-depth accounts of oxygen carrier development over the years, providing insightful discussions into the importance of the oxygen carrier properties on the design of an optimal CLC process (Lyngfelt and Mattisson, 2011, Adánez et al., 2012, Hossain and de Lasa, 2008).

Early research in the field of oxygen carrier development focused almost exclusively on the oxides of four main metals: Ni, Fe, Mn and Cu. More recently, research focus has diversified with significant interest diverted towards the development of mixed-metal oxides (Rydén et al., 2014, Lambert et al., 2010, Ryden et al., 2008); low-cost oxygen carrier materials derived from naturally occurring ores and metal oxide containing industrial solid waste (Leion et al., 2009c, Arjmand et al., 2014, Ryden et al., 2009, Ortiz et al., 2011, Jerndal et al., 2011); and metal oxides with the ability to release gaseous oxygen in the fuel reactor (Chemical-Looping with Oxygen Uncoupling, CLOU) (Adánez-Rubio et al., 2011, Abad et al., 2012, Imtiaz et al., 2013).

A large number of techniques for the synthesis and preparation of oxygen carrier materials have been developed and documented in the literature (Lyngfelt, 2011, Guo et al., 2014, Mei et al., 2014, Dueso et al., 2015, Sarshar et al., 2012, Erri and Varma, 2007, Song et al., 2013, Kierzkowska et al., 2010, Mattisson et al., 2004). Many of these techniques offer oxygen carrier materials with highly desirable characteristics such as improved thermal and mechanical stabilities, high surface areas and well controlled porous structures, however the scalability of these production methods is often limited. Factors limiting the scalability of an oxygen carrier production method include: the complexity and/or number of process steps involved; the requirement of lots of different types of reactants; and the use of expensive and/or hazardous precursor or additive materials (Fan, 2011).

The research presented in this chapter focuses on the development and optimisation of simple and scalable fabrication techniques (based on wet granulation) for the production of cheap iron oxide based oxygen carrier materials for use with gasified biomass or coal. It is especially important that oxygen carriers for CLC processes utilising gasified solid fuels be produced at a low-cost due to the deleterious effects that solid fuel contaminants such as tar vapours, sulfur-containing gases, alkali-compound vapours, chlorine and ash are expected to have on the lifetime of the oxygen carrier.

This chapter provides detailed preparation procedures for Fe-based oxygen carriers using a number of mechanical mixing wet granulation techniques. The synthesised OC particles were subjected to rigorous testing using a range of analytical methods to assess their physical and chemical properties and determine their suitability for use in large-scale chemical-looping systems. The reduction kinetics (the rate limiting step in the CLC of gaseous fuels) for the reduction of Fe_2O_3 to Fe_3O_4 with CO (major component of fuel gas produced from the gasification of solid fuels) according to equation 5.1 were assessed for the OC particles consisting of pure Fe_2O_3 and 60 wt.% Fe_2O_3 supported with 40 wt.% Al_2O_3 using a thermogravimetric analyser (TGA). The aim of the work was to produce and investigate inexpensive particles of high reactivity and robust physical characteristics.

$$3\,Fe_2O_{3\,(s)} + CO_{(g)} \leftrightarrow 2\,Fe_3O_{4\,(s)} + CO_{2\,(g)} \qquad \Delta H^{\Theta}_{T=1023\,K} = -44.3\,kJ.mol^{-1} \qquad \text{(Equation 5.1)}$$

$$2\,Fe_3O_{4\,(s)} + \frac{1}{2}O_{2\,(g)} \leftrightarrow 3\,Fe_2O_{3\,(s)} \qquad \Delta H^{\Theta}_{T=1023\,K} = -238.4\,kJ.mol^{-1} \qquad \text{(Equation 5.2)}$$

5.2 Experimental

5.2.1 Particle Preparation

Three different fabrication methods based on mechanical mixing were trialled for producing the pure and supported iron oxide (Fe_2O_3) oxygen carrier particles investigated in this work. The following sections provide detailed descriptions of the fabrication techniques that were tried. A summary of the different particles that were prepared can be found in table 6.1.

Mechanical Mixing using a domestic food blender as a granulator (Method B)

Particles of iron oxide and alumina supported iron oxide were prepared by adding stoichiometric amounts of the precursor powders to achieve oxygen carriers with the desired iron oxide to support ratio to a domestic food blender. De-ionised water was added in a dropwise fashion to the powders as the powders were mechanically mixed via the high shear action of the blender until insipient wetness had been achieved and small agglomerates had formed. The agglomerates were removed from the blender and gently sieved to the desired size fractions (i.e. 150-212 μm, 212-300 μm, 300-425 μm, 425-500 μm and 500-710 μm). The powders that had not formed agglomerates were returned to the blender and the process was repeated until all the powder had been consumed to form agglomerates. The agglomerates were transferred to heat stable alumina crucibles before being sintered in a tube furnace under a flowing air atmosphere at 1173-1273 K (depending on the type of particle that was being sintered) for 4 hours. Once cooled the sintered particles were sieved again yielding oxygen carrier particles ready for testing.

Mechanical mixing and pelletisation using a lab-scale pharmaceutical particle pelletisation suite (Method E)

The pharmaceutical particle preparation suite (Caleva Solutions Ltd) consists of a high shear mini-mixer (50 g capacity), mini-screw extruder and a moving bowl spheronizer. Stoichiometric amounts of the precursor powders were loaded into the mini-mixer and dry mixed for 30 minutes at a controlled mixing speed of 40 rpm to ensure the powders were well mixed (this step was not necessary and omitted from the procedure when preparing pure iron oxide oxygen carrier particles). The mixing speed was then ramped up to 70 rpm and de-ionised water was added to the powders in a dropwise fashion over a 20 minute period until an extrudable paste had formed. The total amount of water added during this step varied slightly between batches and formulations and was determined initially through trial and error and then through an experience led approach. The paste was mixed for a further 10 minutes to ensure homogeneity before being transferred to the mini-extruder. The mini-screw extruder was operated at 75 rpm and fitted with an extrusion die consisting of 6 x 500 μm circular apertures such that extrusion of the paste yielded cylindrical extrudates with a uniform 500 μm diameter. The extrudates were then partially dried in a circulating air oven at 308 K (35 °C) for 10 minutes to reduce the tendency of the extrudates to agglomerate, whilst remaining malleable enough that they could be shaped into spheres (rather than attrit into fines) during the spheronisation process.

Prior to spheronisation, the extrudates were cut into smaller cylinders roughly 2 mm in length. The spheroniser consisted of a spinning textured disc inside a cylindrical drum. The void space below the spinning plate was pressurised with air to 3 bar_a to avoid particle attrition and loss of fines as a result of particles getting caught and crushed in the gap between the spinning plate and the drum walls. The spheroniser was operated at a speed of 900-1100 rpm for 20-60 s (depending on the formulation). Visual inspections of the particles were carried out every 20 s to ascertain the progress of the spheronisation process. The spherical particles retrieved from the spheroniser were then gently sieved to a size fraction of 150-710 μm before being sintered as outlined earlier in the description of method B.

Mechanical mixing and pelletisation using a sieve extrusion (Method S)

This method is identical to the procedure outlined in above (Method E) with the exception that a 425 μm sieve was used to perform the extrusion. In this case the paste was extruded through the sieve using a scraper. The post-extrusion drying step was carried out with the extrudates attached to the sieve. The reasoning behind this adaptation in the method is discussed in section 5.4.1.

5.2.2 Oxygen Carrier Nomenclature

A standard notation has been used to identify the different oxygen carriers that were prepared and investigated in this work.

XFe**Y**Al(**Z**)

where **X** is the Fe_2O_3 loading in wt.%, **Y** is the Al_2O_3 loading in wt.% and **Z** is a series of letters identifying the type of production method used or the Al_2O_3 precursor used in the particle formulation.

(B)*- fabricated via method (B)

(E)*- fabricated via method (E)

(S) *+- fabricated via method (S)

(SAC)- fabricated via method S using an α-Al_2O_3 (Corundum) powder (Sigma Aldrich, 10 μm powder)

(SAB)- fabricated via method S using an $Al(OH)_3$ (Bayerite) powder (Sigma Aldrich)

(SPN)- fabricated via method S using an Al(OH)O powder (Sasol Pural NF, $d_{50} = 15$ μm)

(SPS)- fabricated via method S using an Al(OH)O powder (Sasol Pural SCF 55, 83 % < 25 μm)

* The 60Fe40Al particles prepared via the different methods were all synthesised from the same Al_2O_3 precursor α-Al_2O_3 (Corundum) powder (Sigma Aldrich, 10 μm powder).

+ The 60Fe40Al(S) and 60Fe40Al(SAC) are formulated using the same method and the same precursor material except the 60Fe40Al(SAC) OC particles were sintered at a higher temperature of 1273 K in an attempt to improve the strength of the particles.

5.2.3 Particle Characterisation

The as-synthesised OC particles were subjected to a rigorous testing protocol using a range of analytical methods to assess their physical and chemical properties, and suitability for use in large-scale systems.

Verification of the Fe_2O_3 loading was carried out by measuring the weight loss of small aliquots (~5 mg) of the OC particles in a TGA (TA measurement TGA Q5000) under a reducing atmosphere of 10 vol.% H_2, balance N_2 at 1223 K. Samples were exposed to these conditions for a period of 30 minutes to ensure complete reduction of the Fe_2O_3 component of the original particle to metal Fe (*i.e.* Fe^0). Each measurement was typically carried out in triplicate. The validity of the TGA approach for determining the Fe_2O_3 content of the oxygen carrier particles was checked via XRF analysis (Bruker AXS S4 Explorer).

N_2-adsorption analysis (Micrometrics, Tristar 3000) was carried out to determine the BET surface area and BJH pore size distributions for the meso-porous region (d_p = 2-50 nm) and small macropores up to ~200 nm in diameter (abstract A, section A.1-A.3). The size distribution and volume of pores in the region d_p = 0.2-10 μm was measured using mercury porisimetry (Micrometrics Autopore IV) (abstract A, section A.4). The skeletal density of the particles (required for the determination of the envelope density) was measured via helium adsorption analysis (Micrometrics, Accupyc 1330).

Visualisation of the surface morphology of the particles was conducted using a Hitachi S3400 SEM with 20 kV of accelerating voltage under high vacuum.

Determination of physical (or mechanical) 'strength' of the particles is particularly important when designing oxygen carrier particles for CLC processes based on a fluidised bed design. A Lloyd EZ50 Material Testing Instrument was used to measure the force required to fracture a single particle (referred to as a 'single particle' crushing strength test). The fracturing force was normalised by dividing through by the average cross-sectional area of the spherical particle to give a crushing strength in the form of a pressure (*i.e.* units of Pa). Particles of size fraction 300-425 μm were used and tests were repeated 30 times for each particle. The single particle crushing strength test provides an easy method for comparing the relative physical rigidity of the different particles prepared via different methods or using different formulations. It should be noted however that these crushing strength tests are limited as they do not provide a true representation of the physical (and chemical) stresses that a particle will undergo in an actual large-scale CLC process in an interconnected fluidised bed.

5.2.4 Thermogravimetric Reactivity Investigations

Thermogravimetric Analyser (TGA) Setup

Preliminary investigations into the reactivity of the different iron oxide based oxygen carrier particles was carried out using a Thermogravimetric Analyser (TA measurement TGA Q5000) (fig. 5.1). Chemical-looping conditions were simulated by exposing small amounts of sample to alternating reducing (3 vol.% CO/ 15 vol.% CO_2 in N_2) and oxidising (4 vol.% O_2 in N_2) conditions at temperatures ranging between 773-1223 K. The reactor was purged with N_2 for 2 minutes between reduction and oxidation phases to avoid mixing of the reducing and oxidising gases that could interfere with the collection of accurate kinetic measurements. The sample weight was measured and recorded by the TGA software every 0.5 s during the redox reactions.

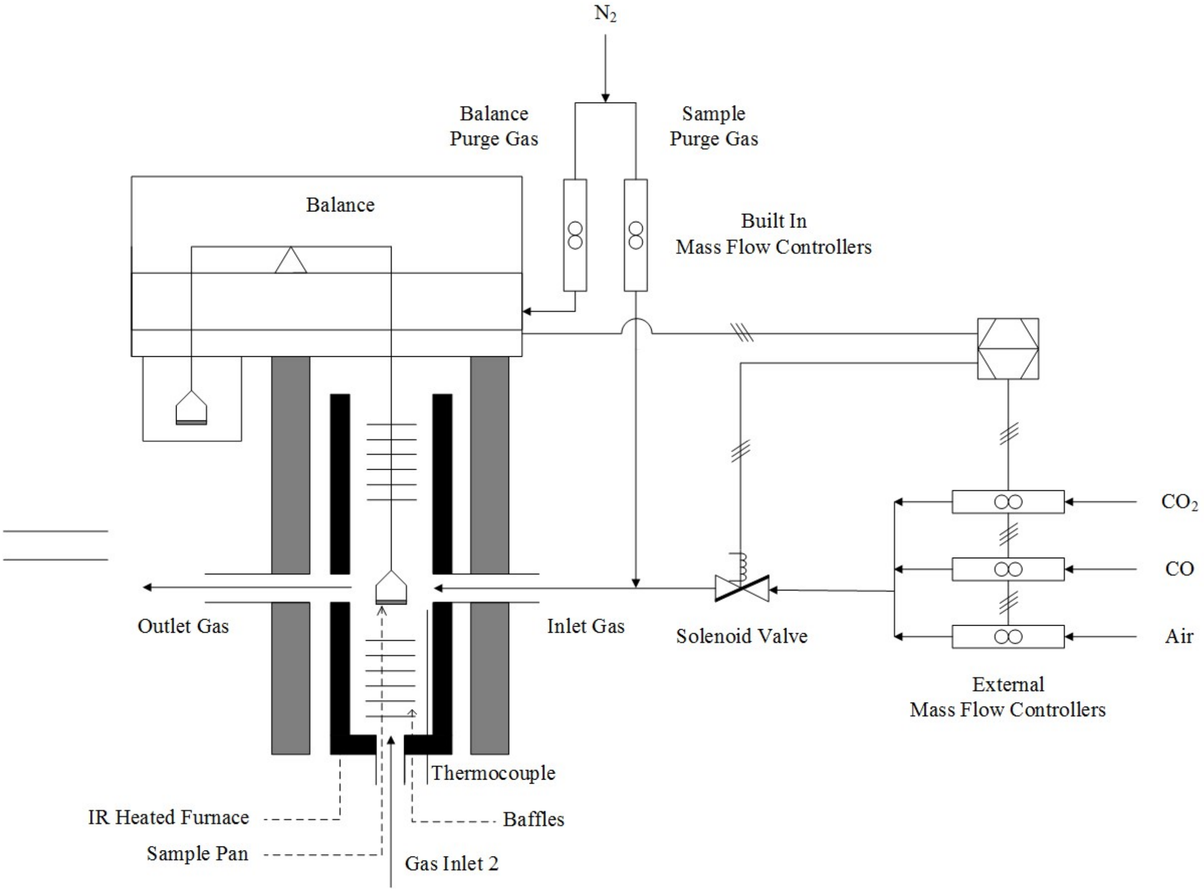

Figure 5.1. Schematic of the thermogravimetric analyser setup used for measuring the reduction kinetics of the different iron oxide OC particles.

Gas was supplied from BOC gas cylinders of (i) pure CO_2 (> 99.9 % purity), (ii) 10.1 vol.% CO, balance N_2 and (iii) pure N_2 (> 99.998 % purity); (iv) laboratory air was also supplied. Since multiple gas streams needed to be mixed to achieve the target gas compositions and flow rates for the reduction and oxidation phases, an external gas blending setup was developed and installed. The external gas blending setup was comprised of three PID mass flow controllers (Brooks Smart Mass Flow Controller, MODEL 5850S) which were used to control the flow of gas streams (i),(ii) and (iv). The PID controller enabled accurate mass flow measurement and set point regulation with accuracy of ± 0.7 % of the flow rate for a range of 4 ml/min up to 200 ml min^{-1}). The flow of (iii) was controlled by one of the TGA's inbuilt mass flow controllers (MFC).

The external MFCs were connected to the computer via a RS-485 multi-channel P.C. system and controlled via a computer program, written in-house using Agilent Vee 9.0 as the software platform. Synchronisation of the TGA with the external MFC control program was achieved by connecting a USB data acquisition (DAQ) module (Measurement Computing, USB-1208FS) to the TGA via an external ‘event’ switch in the back of the TGA that was originally designed for controlling an external gas switching valve and calibrated rotameter (TA measurement) add-on setup (this add-on only allowed for the blending of two gas streams as opposed to a maximum of four in the case of the new setup). The position of the external ‘event’ switch (i.e. ‘on’ or ‘off’) could be controlled from the TGA control software and allowed for information relating to the phase position (beginning or end of the oxidation or reduction phase), cycle number and run number to be relayed to the external MFC control program through a pre-determined combination of ‘on’ and ‘off’ signals.

The gases supplied through the external gas mixing setup were mixed with the N_2 sample purge via a 3-way solenoid valve and specially designed ¼” T-fitting with gas mixing chamber (Bronkhorst High-Tech B.V.). The incorporation of the 3-way valve into the setup allowed the setpoints of the external MFCs to be set and stabilised during the purge prior to the gas switch. This had the effect of minimising the response times associated with gas switching such that the gas switch was as close as possible to a perfect step function.

The reducing conditions (3 vol.% CO/ 15 vol.% CO_2 in N_2) were selected to control reduction of Fe_2O_3 to Fe_3O_4 across the entire temperature range studied based on the assumption that thermodynamic equilibrium was established i.e. $P_{CO2}/P_{CO} = K_{eq} = 0.2$ (fig. 5.2). The reduction of iron oxide from Fe_2O_3 to Fe_3O_4 is widely considered to be the most useful reduction step for chemical-looping applications (Adánez et al., 2012). Further reduction of Fe-based OCs to Fe^{II} and Fe^{0} oxidation states has been found unfeasible in all but a few chemical-looping situations due to slow reduction kinetics and thermodynamic constraints limiting the conversion efficiencies of both CO and CH_4 based fuels (Jerndal et al., 2006). The oxidation of Fe_3O_4 to Fe_2O_3 is very fast and highly exothermic. An O_2 concentration of 4 vol.% for the oxidation phase was chosen to limit deviation from isothermal conditions that complicates the determination of kinetic parameters. The formation of hot spots within the particle as a consequence of localised exotherms may also lead to morphological changes due to sintering and fracturing.

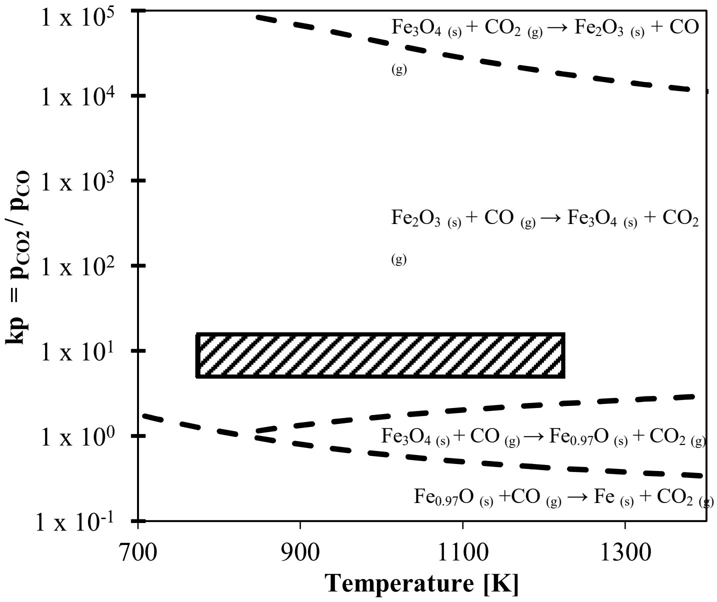

Figure 5.2. Equilibrium diagram for the reaction of Fe_2O_3 with CO produced using factsage (a thermodynamic modelling software) that calculates equilibrium constants based on a minimisation of Gibbs free energy approach. The hatched box represents the area in which the conditions selected for this study reside.

5.3 Kinetic Theory

The reduction of Fe_2O_3 to Fe_3O_4 (but also further to $Fe_{0.97}O$ and Fe^0) by CO proceeds via the following potentially rate-controlling (or rate-limiting) reaction steps (A-E):

(A) Mass transport of CO from the bulk gas phase to the exterior of the solid particle;
(B) Diffusion of CO through the internal pore structure of the iron-based OC particle;
(C) Chemical reaction of CO with Fe_2O_3 at the surface;
(D) Diffusion of the gaseous product, CO_2, through the internal pore structure of the particle;
(E) Mass transport of the CO_2 product from the exterior of the particle into the bulk gas phase.

With this type of reaction where mass transport and chemical reaction between the gaseous reactant and porous solid matrix takes place simultaneously, a concentration gradient is established such that the interior surfaces of the porous Fe-based OC particle is exposed to a lower concentration of CO compared with the surfaces closer to the exterior of the particle. Where the reaction is not zero order with respect to the concentration of CO, this means that different parts of the particle will react at different rates depending on the position within the particle such that under isothermal conditions, the observed rate measured across the whole particle will almost always be lower than the intrinsic rate of reaction without mass transfer limitations (Bird, 2002). Whilst significant efforts can be made to remove mass transport effects when designing experiments for the determination of kinetic information (discussed in the context of this work in section 5.4.3), it is not always possible to completely eradicate for all conditions. The effectiveness of the porous solid reactant (or porous catalyst) is thus described by the difference between the observed and intrinsic rates of reaction under isothermal conditions with the effectiveness factor, η, being the ratio of these values. However, it is possible to calculate the intrinsic rate from the observed rate of reaction by applying a relatively simple algorithm that includes terms that quantitatively describe the different mass transfer effects that ultimately determine the effectiveness of a particle (Satterfield, 1970).

To simplify the mathematical analysis and calculation of the intrinsic kinetic information, the following assumptions are made of the reaction system (1-5):

(1) The porous solid particle is spherical in shape.

(2) The geometry of the porous structure is constant throughout the particle such that diffusional flux of the gas species within the porous matrix can be described by Fick's first law and an invariant effective diffusivity coefficient, D_{eff} (eq. 5.3).

$$N_{CO} = -D_{eff}\left(\frac{dc_{CO}}{dr}\right) \qquad \text{(Equation 5.3)}$$

Where N_{CO} is the flux of CO within the pores of the particle, $D_{eff,CO}$ is the effective diffusivity coefficient for CO in the pores of the particle, c_{CO} is the concentration of CO and r is the radial position within the spherical porous particle.

(3) The reaction system is isothermal.

(4) The rate of reaction is first order and irreversible (eq. 5.4);

$$r' = -k_i\, c_{CO} \qquad \text{(Equation 5.4)}$$

Where r' is the rate of reaction of CO with Fe_2O_3, and k_i is the intrinsic rate constant for the reaction.

(5) Pseudo-steady state conditions.

5.3.1 Deriving the mathematical algorithm to describe the effects of intra-particle mass transport on the observed rate of a chemical reaction

The assumptions outlined above allow the intrinsic kinetic information of the system to be calculated by only considering the material balance (eq. 5.5-5.6) over a differential shell of thickness Δr and radius r within a spherical iron oxide particle of radium R as illustrated in figure 5.3.

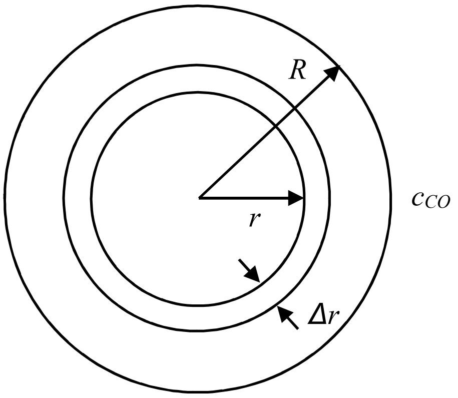

Figure 5.3. Schematic of model for the porous spherical solid pellet reaction system considering simultaneous diffusion and reaction (Satterfield, 1970).

$$\begin{bmatrix}\text{Rate of diffusion}\\ \text{inward at}\\ r = r + \Delta r\end{bmatrix} - \begin{bmatrix}\text{Rate of}\\ \text{diffusion inward}\\ \text{at } r = r\end{bmatrix} = \begin{bmatrix}\text{Rate of}\\ \text{reaction in}\\ \text{shell of thickness } \Delta r\end{bmatrix} \qquad \text{(Equation 5.5)}$$

or,

$$N_{CO,r}|_{r} \cdot 4\pi r^{2} - N_{CO,r}|_{r+\Delta r} \cdot 4\pi (r + \Delta r)^{2} = r' \cdot 4\pi r^{2} \Delta r \qquad \text{(Equation 5.6)}$$

$N_{CO,r}|_{r}$ and $N_{CO,r}|_{r+\Delta r}$ are the molar fluxes of CO flowing in the r direction at a distance of r and r + Δr repectively from the centre of the porous spherical particle. By dividing equation 5.6 through by 4πΔr and letting Δr → 0 equation 5.6 becomes equation 5.7

$$\lim_{\Delta r \to 0} \frac{r^{2} N_{CO,r}|_{r} - r^{2} N_{CO,r}|_{r+\Delta r}}{\Delta r} = r^{2} r' \qquad \text{(Equation 5.7)}$$

Substituting in equation 5.3 and equation 5.4, equation 5.7 becomes equation 5.8:

$$D_{eff,CO} \frac{1}{r^{2}} \frac{d}{dr} \left(r^{2} \frac{dc_{CO}}{dr} \right) = k_{i} c_{CO}^{\ n} \qquad \text{(Equation 5.8)}$$

It is now possible to solve equation 5.8 (in the form of a second order differential equation and applying the exponential definitions for hyperbolic functions) for the boundary conditions: of $c_{CO} = c_{CO,S}$ =constant at r = R (*i.e.* at the exterior surface of the porous spherical particle) and c_{CO} at r = 0 (at the centre of the particle) is finite such that $dc_{CO}/d\mathrm{r} = 0$, to give equation 5.9.

$$\frac{c_{CO}}{c_{CO,S}} = \left(\frac{R}{r}\right) \frac{\sinh\left(r \sqrt{\frac{k_{i} c_{CO}^{n-1}}{D_{eff,CO}}} \right)}{\sinh\left(R \sqrt{\frac{k_{i} c_{CO}^{n-1}}{D_{eff,CO}}} \right)} \qquad \text{(Equation 5.9)}$$

To simplify the expression given in equation 5.9, it is convenient to introduce the dimensionless quantity known as the Thiele diffusion modulus (Φ) (eq. 5.10):

$$\Phi = R\sqrt{\frac{k_i c_{CO}^{n-1}}{D_{eff,CO}}} \qquad \text{(Equation 5.10)}$$

Note that for a first order reaction (*i.e.* where n=1), this expression simplifies to:$\Phi = R\sqrt{k_i/D_{eff}}$

The Thiele diffusion modulus is an important parameter that describes the relationship between the intrinsic rate of reaction and the rate of diffusion and therefore the relative contribution each of these quantities make towards the overall observed rate of reaction between gas (or liquid) phase reactants and a porous solid reactant (or within a porous solid catalyst).

The assumption of pseudo-steady state infers that the overall (observed) rate of reaction is equal to the mass transfer of CO into the porous spherical particle at r = R such that:

$$r' = 4\pi R^2 D_{eff}\left(-\frac{dc_{CO}}{dr}\right)_{r=R} \qquad \text{(Equation 5.11)}$$

Combining (Equation 5.9) and (Equation 5.11), it is possible to derive (Equation 5.12) that allows for the calculation of the observed rate of reaction in terms of the concentration profile described by equation 5.9.

$$r' = 4\Phi\pi R D_{eff} c_{CO,s}\left(\coth\Phi - \frac{1}{\Phi}\right) \qquad \text{(Equation 5.12)}$$

As mentioned earlier, the effectiveness factor (*η*) is the ratio of the observed rate of reaction and the intrinsic rate of reaction without mass transfer limitations. The effectiveness factor for a porous spherical particle can therefore be defined as:

$$\eta = \frac{4\Phi\pi R D_{eff} c_{CO,s}\left(\coth\Phi - \frac{1}{\Phi}\right)}{\frac{4}{3}\pi R^3 k_i c_{CO,s}}$$ (Equation 5.13)

For a first-order reaction, equation 5.13 can be simplified to (eq. 5.14):

$$\eta = \frac{3}{\Phi^2}(\Phi\coth\Phi - 1)$$ (Equation 5.14)

5.3.2 Deriving a mathematical algorithm to describe the relationship between the bulk and surface concentration of CO

As with the rate at which the CO enters the porous spherical particle, the pseudo-steady state assumption also infers that the rate at which the CO diffuses through the gas film surrounding the particle is equal to the rate of chemical reaction within the particle (Bird, 2002). This means that r' α ($c_{CO,in}$ – $c_{CO,s}$) *i.e.* the difference between the CO concentration in the bulk phase (or the inlet concentration, $c_{CO,in}$, as is the case for a differential reactor) and the surface concentration of CO at the exterior surface of the particle. The observed rate of reaction (in terms of $\mathrm{mol.\,s^{-1}g_{Fe_2O_3}^{-1}}$) for a first-order, irreversible reaction in a spherical porous particle can therefore be given by:

$$r' = \frac{4\pi R^2 k_{g,CO}(c_{CO,in} - c_{CO,s})}{\frac{4\pi R^3}{3}\rho_{Fe_2O_3}}$$ (Equation 5.15)

and

$$r' = \frac{\eta k_i c_{CO,s}}{\rho_{Fe_2O_3}}$$ (Equation 5.16)

Here, $k_{g,CO}$ is the external mass transfer coefficient for the bulk gas phase and $\rho_{Fe_2O_3}$ is the envelope density of the Fe_2O_3 component of the particle. Using the convenient definition of the observed reaction rate in terms of the intrinsic rate constant and effectiveness factor provided by equation 5.16, it is possible derive a term for $c_{CO,s}$ that can be substituted into equation 5.15. Further rearrangement enables the derivation of a term for the overall observed rate in terms of the known bulk (or inlet) CO concentration and an overall observed rate constant, k_o in units of s^{-1}.

$$r' = \frac{k_o}{\rho_{Fe_2O_3}} c_{CO,in} \qquad \text{(Equation 5.17)}$$

Where

$$\frac{1}{k_o} = \frac{R}{3k_{g,CO}} + \frac{1}{\eta k_i} \qquad \text{(Equation 5.18)}$$

The intrinsic rate constant, k_i, and effectiveness factor, η, can now be solved iteratively from the observed rate, r', and observed rate constant, k_o, by converging the effectiveness factor calculated using equation 5.14 and equation 5.18 with an initial input of $\eta = 1$.

Calculation of the mass transfer coefficients

The effective diffusivity, D_{eff}, of CO within the pores of the oxygen carrier particle was calculated by estimating the bulk, gas phase diffusion coefficient, D_b, and the Knudsen diffusion coefficient D_K for using equation 5.19.

$$\frac{1}{D_{eff}} = \frac{\varepsilon_{Fe_2O_3}}{\tau} (\frac{1}{D_K} + \frac{1}{D_b}) \qquad \text{(Equation 5.19)}$$

Here, $\varepsilon_{Fe_2O_3}$is the volume of pores associated with the Fe_2O_3 component of the oxygen carrier and τ is a fitted tortuosity factor that takes into consideration the effect of the torturous path on D_{eff}. Incorporating τ into the D_{eff} term compensates for the fact that in reality, the pores within the particle are not straight and cylindrical as assumed by the Knudsen diffusitiy coefficient calculation equation 5.21. Tortuosity factors for commercial catalyst pellets typically range between 2 to 6 (Satterfield, 1970). In this work, the tortuosity factor is determined (or fitted) empirically from kinetic measurements for different sized oxygen carrier particles reacted under the same conditions.

The bulk gas phase diffusion coefficient, D_b, was estimated for a binary gas mixture consisting of CO and N_2 using Chapman-Enskog kinetic theory and the Lennard-Jones potential function for intramolecular forces (eq. 5.20).

$$D_b = 0.001858 \times \frac{\sqrt{T^3 \left(\frac{1}{M_{r,1}} + \frac{1}{M_{r,2}}\right)^{1/2}}}{P\sigma_{1,2}^2 \Omega^{(1,1)*}} \qquad \text{(Equation 5.20)}$$

T refers to the absolute temperature in K; M_1 and M_2 are the average molecular weights of the two gas species (*i.e.* CO and N_2); P is the pressure in atm; $\Omega^{(1,1)*}$ is the collision integral which in turn, is a function of $kT/\varepsilon_{1,2}$ (dimensionless temperature); and $\varepsilon_{1,2}$ and $\sigma_{1,2}$ are force constants in the Lennard-Jones potential function. The effects of CO_2 on D_b, were omitted as it is a non-polar gas of similar size to N_2 and CO. Incorporating terms that describe the additional interactions involving CO_2 introduces a great deal more complexity into the calculations for what is likely to offer only a small to negligible improvement.

Knudsen diffusion is a process that takes place in small pores where the average pore diameter is significantly less than the mean free path. Here, collisions between the gas species and solid pore walls have a greater influence on the overall diffusion process than collisions between gas species. The contribution of Knudsen diffusion towards the overall 'effective' diffusivity is accounted for by the Knudsen Diffusion coefficient, D_K. The calculation used to derive D_K is for a straight, cylindrical pore is given by (eq. 5.21).

$$D_K = 97 r_e \sqrt{\frac{T}{M_{r,CO}}} = 194 \frac{\varepsilon_{Fe_2O_3}}{S_g \rho_{Fe_2O_3}} \sqrt{\frac{T}{M_{r,CO}}} \qquad \text{(Equation 5.21)}$$

Where r_e is the pore radius in cm (determined by MIP and assumed to be round and straight) and S_g is the surface area ($cm^2\ g^{-1}$) of the oxygen carrier particle.

The external, bulk phase mass transfer coefficient, k_g, was estimated using equation 5.22.

$$k_g = D_b Sh/d_p \qquad \text{(Equation 5.22)}$$

where

$$Sh = 0.91 Re^{0.49} Sc^{0.33} \qquad \text{(Equation 5.23)}$$

$$Re = \rho_g U D_H/\mu \qquad \text{(Equation 5.24)}$$

$$Sc = \mu/(\rho_g D_b) \qquad \text{(Equation 5.25)}$$

D_b is the bulk, gas phase diffusion coefficient defined earlier in equation 5.20, Sh is the Sherwood number and d_p is the diameter of the particle. The Sherwood number was calculated using a semi-empirical correlation given in equation 5.23 where Re is the Reynold's number and Sc is the Schmidt number given by equation 5.25. The Reynold's number was approximated for the TGA chamber by assuming the flow of N_2 through a circular channel that is equal in diameter to the height of the TGA pan *i.e.* 11 mm equation 5.24. U is the superficial velocity of the gas, ρ_g is the density of the gas and μ is the dynamic viscosity of N_2.

5.3.3 TGA Data Analysis and Evaluation

The weight and temperature profiles recorded by the TGA for a single redox cycle of a typical CLC experiment are presented in figure 5.4. The exact experimental data shown is for the 3rd cycle of a CLC experiment involving a 100FeS (5 mg, 150-212 μm) oxygen carrier at 623 K. Each CLC cycle was comprised of 4 distinct stages (labelled (i)-(iv) in figure 5.4 (a)).

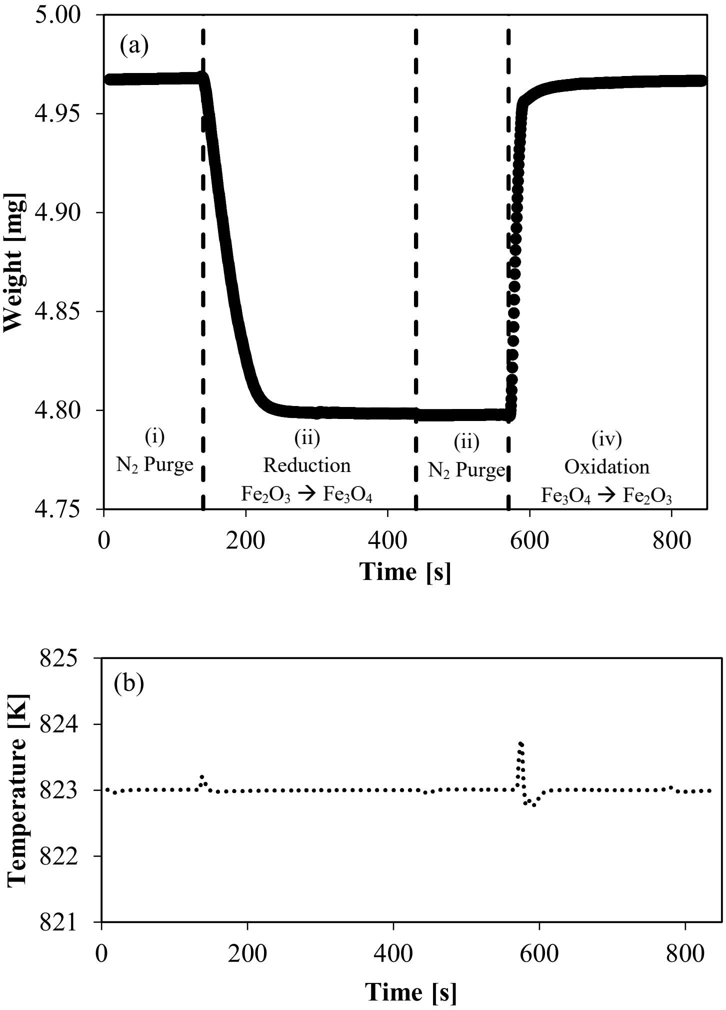

Figure 5.4. Typical TGA (a) weight profile and (b) temperature profile for the 3rd redox cycle of a simulated CLC experiment involving a 100FeS oxygen carrier (5 mg, 150-212 μm) at 823 K and total flow rate of 80 ml min^{-1} with a 5 minute reduction period in 3 vol.% CO, 15 vol.% CO_2, balance N_2 and 5 minute oxidation period in 4 vol.% O_2, balance N_2, separated by 2 minute 100 vol.% N_2 purge steps.

The first stage (i) was a 2 minute N_2 purge step designed to purge residual reactive gases from the previous oxidation phase out of the reaction chamber before the reduction phase begins. The second phase (ii) was the reduction step where the inlet gas was switched from 100 vol.% N_2 to a gas mixture of 3 vol.% CO, 15 vol.% CO_2, balance N_2. During this phase, the Fe_2O_3 is reduced by CO forming

Fe_3O_4 and CO_2 resulting in the weight loss observed in figure 5.4 (a). In the example provided in figure 5.4 (a), the reduction appears to be complete (i.e. the weight profile plateaus) after approximately 120 s of the inlet gas being switched; however the total time chosen for the reduction step was 5 minutes so that enough time was provided to ensure complete reduction for all oxygen carriers and conditions tested. The reduction step was followed by a second N_2 purge step (ii) which in turn was followed by the oxidation step. The oxidation step involved switching the gas inlet from 100 vol.% N_2 to a mixture of 4 vol.% O_2, balance N_2. Here, the Fe_3O_4 was oxidised back to Fe_2O_3 by the O_2 resulting in the observed weight gain. As expected, the oxidation of Fe_3O_4 to Fe_2O_3 was much faster than the reduction of Fe_2O_3 to Fe_3O_4 reaching completion approximately 60 s after the inlet gas was switched to the oxidising gas. A total time of 5 minutes was also used for the oxidation period for the same reason as was explained for the reduction period.

The temperature profile of the TGA reproduced in figure 5.4 (b), shows that there were some small temperature fluctuations in the chamber which coincide with, and are therefore most likely caused by, gas switching. However, these temperature fluctuations were small (< 1 K in magnitude) indicating that the reaction chamber was isothermal during the reaction.

To obtain overall rates of reaction *r'* (in $\mathrm{mol.\,s^{-1}\,g_{\mathit{Fe_2O_3}}^{-1}}$), the reduction (weight loss) and oxidation (weight gain) periods of the weight profile were differentiated with respect to time and divided through by the initial mass of Fe_2O_3. The rate profile with respect to time and conversion for the reduction phase of the weight profile shown in figure 5.4 (a) are presented in figure 5.5 (a) and (b). The conversion of the Fe_2O_3 (X) component of the oxygen carrier was calculated using equation 5.26.

$$X = 1 - \frac{M_{Ox} - M}{M_{Ox} - M_{Red}} \qquad \text{(Equation 5.26)}$$

M is the instantaneous mass at t=t, M_{Ox} is the mass of the oxygen carrier (or Fe_2O_3 component of the oxygen carrier) in its fully oxidised form (obtained as the initial mass in the weight profile presented in figure 5.4 (a)) and M_{Red} is the mass of the oxygen carrier in its fully reduced form which is calculated using equation 5.27 for the reduction of Fe_2O_3 to Fe_3O_4.

$$M_{Red} = \frac{M_{Ox} \cdot M_{r\,Fe_3O_4}}{M_{r\,Fe_2O_3}} \cdot \frac{2}{3} \qquad \text{(Equation 5.27)}$$

Where $M_{r\,Fe_3O_4}$ is the relative molecular mass of Fe_3O_4; $M_{r\,Fe_2O_3}$ is the relative molecular mass of Fe_2O_3 and 2/3 is the ratio of the stoichiometric coefficients for the reduction of Fe_2O_3 to Fe_3O_4 (eq. 5.1).

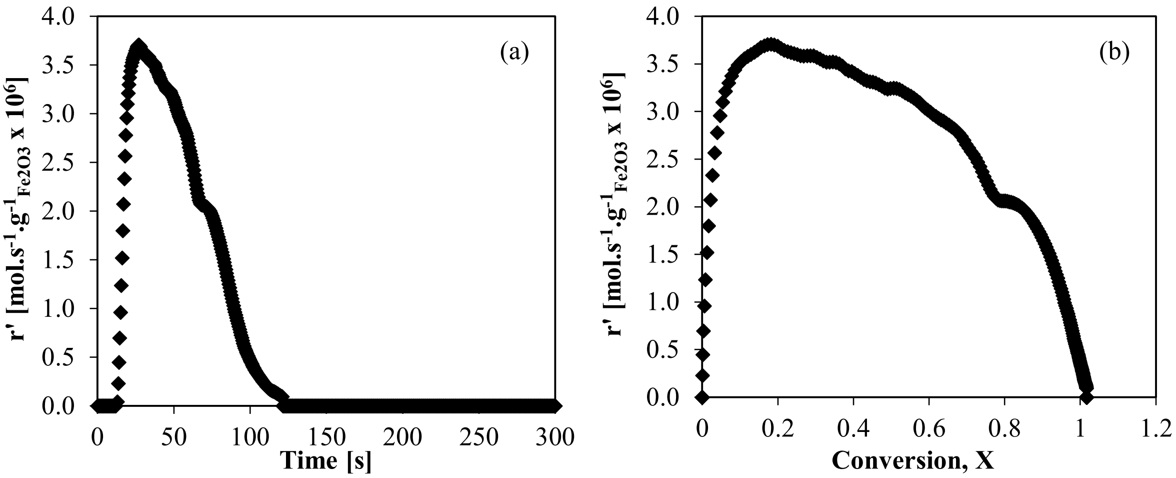

Figure 5.5. Rate change as a function of (a) time and (b) conversion for the reduction of Fe_2O_3 to Fe_3O_4 for a typical TGA simulated CLC experiment. **Experimental parameters: Reactor:** TGA; **Oxygen Carrier**: 100Fe(S) (5 mg, 150-212 μm); **Reaction:** $Fe_2O_3 \rightarrow Fe_3O_4$; **Temperature**: 823 K; **Reducing gas composition**: 3 vol.% CO, 15 vol.% CO_2, balance N_2; **Oxidising gas composition**: 4 vol.% O_2, balance N_2; **Total Flow Rate**: 80 ml min^{-1}; **Cycle Number**: 3.

When comparing the reactivities of different oxygen carriers at a range of different conditions, it is convenient to express the rate of reduction as a single value for a specific set of conditions. The single value rate of reduction that is typically reported is the rate at zero conversion *i.e.* at $X = 0$ as this should be the point in the conversion that exhibits the highest reactivity (in the absence of mass transfer limitation and assuming pseudo-steady state conditions are immediately achieved). The particle at zero conversion is also the point in its conversion at which the measured physical parameters selected for the model are most true (e.g. surface area, porosity, mass of Fe_2O_3 *etc.*).

Two methods were originally trialled for estimating the rate at zero conversion. The first method (i) was used by Bohn (2010), who fitted a linear line of best fit (the linear fit method) to the linear portion of the rate vs. conversion plot (which in the case of the example provided in figure 5.5(b) is the portion $0.2 < X < 0.7$) and extrapolated back to $X = 0$ (as illustrated in figure 5.1 and labelled method (i)). This method assumes that all the reactive surface area is accessible to the gas at the beginning of the reaction and that the reaction mechanism is surface reaction controlled. The rate therefore decays linearly with increasing conversion (or decreasing reactive surface).

The second method (ii) was applied by Zhang (2014) who used the maximum rate as the initial rate of reduction at zero conversion (hereon referred to as the maximum rate method and illustrated in figure 5.1). Zhang (2014) was able to measure the rate of reduction down to much lower conversions ($X \rightarrow 0$) than Bohn (2010) and showed that the method of using the peak rate of reduction (ii) was a better approximation of the initial rate than the linear fit initial rate approximation (ii). Zhang (2014) found that the linear fit method tended to 'overestimate' the initial rate by around 10 % based on the grain model they developed to describe their experimental data and suggested reaction mechanism. Here, the peak rate method (ii) was used to predict the maximum initial rate at zero conversion during the preliminary experimental design and particle model validation phase of this work. However, another method (based on the linear fit method and described in section 5.4.4) was adopted to report the initial rate constant values for the main content of this chapter based on the findings from the preliminary experimental design and particle model validation work (sections 5.4.5 and 5.4.6).

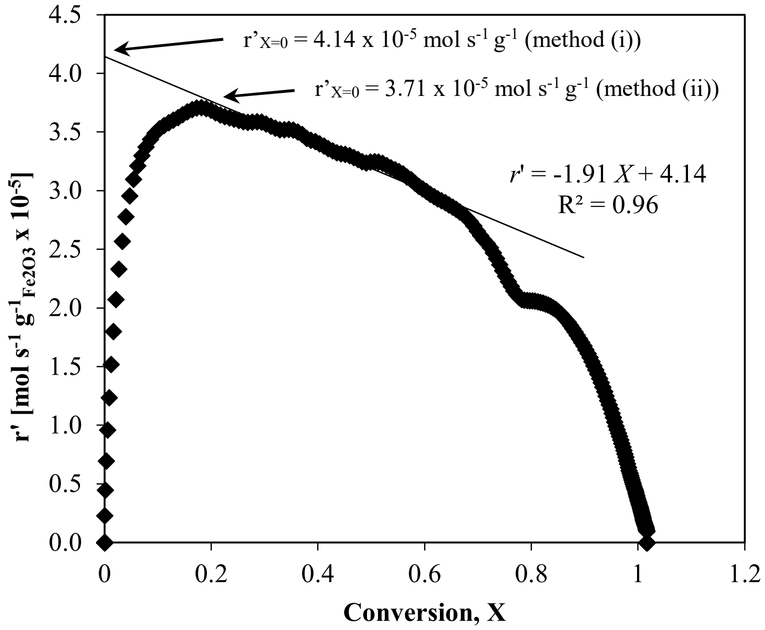

Figure 5.6. Example of two methods (i) 'the linear fit method' and (ii) 'the maximum rate method' that can be applied for the determination of the initial rate of reduction from the rate as a function of conversion plot. **Experimental parameters: Reactor:** TGA; **Oxygen Carrier**: 100FeS (5 mg, 150-212 μm); **Reaction:** $Fe_2O_3 \rightarrow Fe_3O_4$; **Temperature**: 823 K; **Reducing gas composition**: 3 vol.% CO, 15 vol.% CO_2, balance N_2; **Oxidising gas composition**: 4 vol.% O_2, balance N_2; **Total Flow Rate**: 80 ml min^{-1}; **Cycle Number**: 3.

5.4 Results and Discussion

5.4.1 Particle formulation

Wet granulation via the incipient wetness fabrication technique (*i.e.* method B) is an established approach that has been used in a number of previous CLC studies involving iron-base oxygen carriers at Imperial College and the University of Cambridge. A major issue with this approach is that it creates a significant quantity of air borne fines which represents both a significant health risk to other lab users and leads to significant contamination of the lab in which the particle fabrication is performed. This represents the primary motivation behind the development of an alternative preparation method that both reduced the health and contamination issues and produced uniform spherical Fe_2O_3 oxygen carrier particles with a well-controlled particle size. Table 5.1 provides a summary of the different fabrication method process parameters and yields of particles obtained.

Table 5.1. Summary of the important process parameters for the preparation of the 100Fe and 60Fe40Al particles prepared via the different methods (B, E and S).

	100Fe(B)*	**100Fe(E)**	**100Fe(S)**	**60Fe40Al(B)**	**60Fe40Al(E)**	**60Fe40Al(S)**
Fe_2O_3 loading [g]	-	30	30	120	18	18
Al_2O_3 loading [g]	-	0	0	80	12	12
DI water [ml]	-	5.0	6.5	31.0	7.5	8.0
Mixing speed [rpm]	-	75	75	-	75	75
Mixing time (dry powders) [min]	-	-	-	30	30	30
Mixing time (after water addition) [min]	-	20	20	-	20	20
Extrusion speed [rpm]	-	60	-	-	60	-
Intermediate dry temperature [K]	-	308	308	-	308	308
Intermediate dry time [min]	-	30	30	-	30	30
Speronisation speed [rpm]	-	900	900	-	900	900
Speheronisation time [s]	-	20-60	20-60	-	20-60	20-60
Spheroniser void space pressure [bar$_g$]	-	2.0	2.0	-	2.0	2.0
Sintering temperature [K]	1173	1173	1173	1173	1173	1173
Sintering time [hour]	4	4	4	4	4	4
Yield (150-710 µm) [wt.%]	**-**	**41.2**	**68.6**	**95.1**	**37.1**	**62.5**

* 100Fe(B) particles were left over from a previous project. Limited data was available relating to the preparation parameters used but the user who prepared these particles consulted on the preparation of the analogous 60Fe40Al(B) particles.

The first alternative method that was trialled (method E) involved the use of a mechanical extruder to control the extrudate and resulting particle size. A significant problem with this approach was that the friction caused by the extrusion process caused the barrel to overheat leading to blockage formation due to the rapid drying of the paste in the barrel. As a consequence very low particle yields were obtained via this method. In an attempt to overcome this issue vegetable oil and a polyacrylate dispersant (designed to reduce the viscosity of the paste) were added in small quantities (1 ml and 0.1-0.3 g respectively) during the preparation of different batches of the 100Fe(E). Neither approach worked. The low miscibility of oil and water lead to a phase separation within the paste such that a paste consisting of the solid powders in oil extruded first followed by the aqueous paste. The polyacrylate dispersant had a far more dramatic effect on the viscosity of the paste than expected such that the extrudates were very 'loose' in nature and did not hold their shape. Based on these results the method was further adapted swapping the mechanical extrusion process for a process utilising a sieve and scraper. Much improved yields were obtained in this way. It was therefore decided to use this approach to produce the 60Fe40Al particles prepared from different Al_2O_3 precursors.

5.4.2 Particle Characterisation

Thermogravimetric weight loss analysis of the fresh, as-synthesised 60Fe40Al OC particles was carried out with 5 mg of sample in 5 vol.% H_2 (balance N_2) at 1223 K over a 2 hour period to determine the Fe_2O_3 loading in the OC particles (and whether the target input Fe_2O_3 loading was achieved in the synthesised product). Conditions were chosen to ensure complete reduction of the Fe_2O_3 content to Fe^0. The Fe_2O_3 loading could then be calculated from the ratio of the observed weight loss of oxygen to the theoretical weight loss of oxygen for a sample of 100 wt.% Fe_2O_3 OC particles of the same initial weight. Each test was repeated 3 times to determine variations within the sample which is given by the error range. Larger samples of the 60Fe40Al OC particles (~ 2 g) prepared using the different fabrication methods (B, E and S) were analysed using XRF to assess the suitability of the TGA-based compositional analysis approach for Fe_2O_3-based OC particles. The results are summarised in table 5.2.

Table 5.2. Summary of input and measured actual Fe_2O_3 loadings for the oxygen carrier particles synthesised and studied in this chapter. Fe_2O_3 loadings were determined by measuring the weight loss of the OC particles in a TGA at 1223 K in 5 vol.% H_2 (blance N_2) over a 2 hour period.

Oxygen Carrier Particle	Input $M_{(Fe2O3)}$ [wt.%]	TGA Measured M_{Fe2O3} [wt.%]	XRF Measured M_{Fe2O3} [wt.%]
60Fe40Al(S)	60	58.8 ± 0.9	59.2
60Fe40Al(E)	60	59.6 ± 0.6	60.1
60Fe40Al (B)	60	60.1 ± 2.1	59.1
60Fe40Al (SAC)	60	58.9 ± 1.8	–
60Fe40Al (SAB)	60	59.0 ± 0.3	–
60Fe40Al (SPN)	60	61.5 ± 0.7	–
60Fe40Al (SPS)	60	59.9 ± 1.4	–

In all cases, the actual measured Fe_2O_3 loadings of the OC particles were within 2 % of the target input Fe_2O_3 (table 5.2). The measurement error/compositional variation within the sample were also low (< 3%). XRD analysis of the samples confirmed the suitability of the TGA compositional analysis approach giving Fe_2O_3 loadings within 2 % of the loadings determined from the TGA approach and all within the error range of the TGA measurement.

N_2 adsorption analysis was used to determine the surface areas (BET theory), pore size distributions and volume of meso- (2-50 nm) and small macro- pores in the pore size region up to ~200 nm (BJH theory). Method E produced the 100Fe OC particle with the largest surface area followed by method S and then method B (table 5.3). The 100Fe(S) OC particle had the largest volume of pores within the porous region detectable with N_2 adsorption analysis (2-200 nm) with an average pore size of 105 nm. The 100Fe(B) had a slightly lower volume of meso- and small macro-pores with an average pore size of 72 nm whilst the 100Fe(E) particles appeared to have the least volume of pores within this pore size region and smallest average pore size. Comparison of the pore size distributions of the 100Fe particles (fig. 5.7 (a)) revealed that the 100Fe(E) particles had a pore size distribution that was shifted towards a larger pore size and close to the upper detection limit of the instrument such that it could not be fully resolved with this analysis. The addition of 40 wt.% α-alumina (corundum) shifted the pore size distribution towards a larger pore size such that in all cases, the pore size distributions could not be resolved by BJH N_2-adsorption analysis (fig. 5.7 (b)).

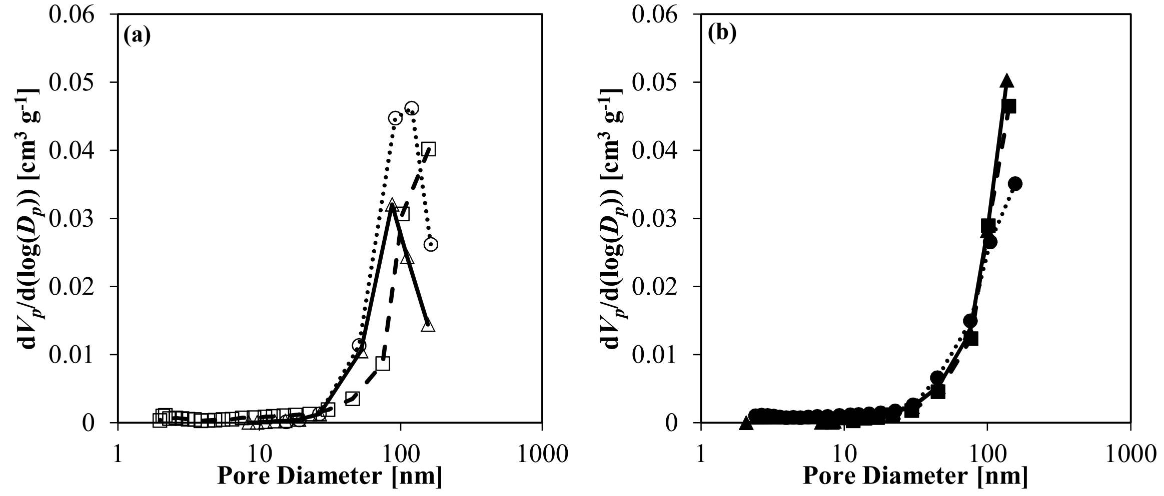

Figure 5.7. Pore size distributions determined by BJH N_2-adsorption analysis of the fresh (a) 100 wt.% Fe_2O_3 (100Fe) (open symbols) and (b) 60 wt.% Fe_2O_3/40 wt.% Al_2O_3 (60Fe40Al) (solid symbols) OC particles prepared via the different preparation methods: method B (△); method E (□); and method S (⊙).

The 60Fe40Al OC particles fabricated using the alumina precursors $Al(OH)_3$ (60Fe40Al(SAB)) and AlO(OH) (60Fe40Al(SPS) and 60Fe40Al(SPN)) produced oxygen carriers with dramatically different porous structures (in the 2-200 nm porous region) to the 60Fe40Al OC particles that were produced using the α-Al_2O_3 (corundum) additive (table 5.1). The use of $Al(OH)_3$ as the alumina precursor (60Fe40Al(SAB)) increased the volume of meso- and small macro-pores substantially to ~ 0.2 cm^3 g^{-1} compared with the 100Fe and 60Fe40Al OC particles fabricated from the α-Al_2O_3 precursors which demonstrated pore volumes of 0.01-0.02 cm^3 g^{-1}. The use of the AlO(OH) precursors also created 60Fe40Al OCs with a larger volume of meso- and small macro-pores of 0.08-0.09 cm^3 g^{-1}. A comparison of the pore size distributions of the different OCs produced from the different alumina precursors reveals that the use of $Al(OH)_3$ created a large volume of pores over a wide range of pore sizes (~ 5-130 nm) with a maximum volume of pores at ~ 30 nm which correlates well with the calculated average pore diameter of 28 nm (using the $D_{p,av} = 4V_p/S_g$ rule that assumes the porous structure is comprised of uniform rigid cylindrical pores). The OCs produced from the AlO(OH) alumina precursors were found to have similar bi-modal pore size distribution with distinct porous regions in the meso-porous region between ~2-20 nm and a second porous region created by larger pores of approximately 50-150 nm in diameter. The calculated average pore sizes were ~ 20 nm for both the 60Fe40Al(SPN) and 60Fe40Al(SPS) OC particles.

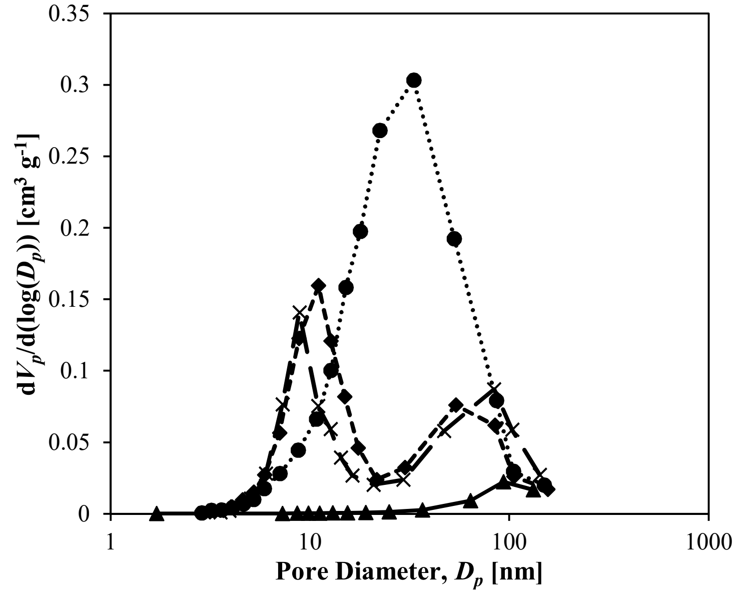

Figure 5.8. Pore size distributions determined by BJH N_2-adsorption analysis of the fresh 60 wt.% Fe_2O_3/40 wt.% Al_2O_3 OC particles prepared from the different alumina precursors: 60Fe40Al(SAC) (—▲—); 60Fe40Al(SAB) (···●···);60Fe40Al(SPN) (--◆--); and 60Fe40Al(SPS) (—×—).

Table 5.3. Summary of BET/BJH- N_2 adsorption and MIP measurements obtained for the different Fe_2O_3-based OC particles prepared in this study.

	100Fe(B)	**100Fe(E)**	**100Fe(S)**	**60Fe(B)**	**60Fe(E)**	**60Fe(S)**	**60Fe(SAC)**	**60Fe(SAB)**	**60Fe(SPN)**	**60Fe(SPS)**
Surface Area [m^2 g^{-1}]	0.79	1.26	1.06	1.32	1.16	1.35	0.90	28.96	18.04	15.78
Cumulative pore vol. (BJH) [cm^3 g^{-1}]	0.012	0.011	0.019	0.015	0.016	0.013	0.009	0.213	0.091	0.081
Average Pore diameter ($4V_p/S_g$) (BJH) [nm]	98	72	105	80	80	38	73	28	18	19
Cumulative Volume of pores (MIP) [cm^3 g^{-1}]*	0.06 (0.22)	0.23 (0.55)	0.15 (0.40)	0.08 (0.38)	0.20 (0.53)	0.12 (0.38)	0.09 (0.25)	0.47 (1.00)	0.17 (0.53)	0.16 (0.53)
Average pore diameter ($4V_p/S_g$) (MIP) [nm]*	291 (1104)	714 (1758)	551 (1495)	255 (1143)	684 (1844)	325 (989)	403 (1130)	65 (138)	37 (117)	41 (134)
Skeletal density x10^{-6} [g m^{-3}]$^+$	5.65	3.00	4.00	9.01	2.65	3.45	5.35	4.83	5.01	5.01
Porosity*	0.24 (0.55)	0.40 (0.62)	0.37 (0.61)	0.43 (0.77)	0.34 (0.59)	0.30 (0.56)	0.33 (0.58)	0.69 (0.83)	0.45 (0.73)	0.45 (0.73)
Envelope density x 10^{-6} [g m^{-3}]*	4.27 (2.53)	1.79 (1.13)	2.52 (1.55)	5.13 (2.05)	1.74 (1.10)	2.42 (1.50)	3.61 (2.27)	1.48 (0.83)	2.74 (1.37)	2.76 (1.37)

* MIP measurements outside of the brackets are calculated for pore sizes of 0.05-10 μm.

* MIP measurements inside brackets are calculated for pore sizes 0.05-100 μm

$^+$ Skeletal density was measured using He adsorption analysis.

Analysis of the porous region outside the resolution of N_2-adsorption analysis was achieved using mercury intrusion porosimetry (MIP). Since this technique is not able to distinguish between inter-particle porosity and interstitial porosity (void space created between the particles due to the way in which they were packed in the sample tube); two arbitrary porosity cut-off pore sizes were set for analysis of the MIP results (table 5.3). The conservative (low) cut-off pore size was 0.9 µm (equivalent to 10 % of R) and the upper cut-off pore size was 90 µm (equivalent to R).

The pore size distributions provided by MIP (fig. 5.9) shows that all of the OCs had a bimodal pore size distribution with two distinct porous regions created by a set of small pores between ~ 5-1000 nm in diameter (that were either fully or partially resolved by the N_2-adsorption BJH analysis) and a porous region created by set of larger pores of between 1 x 10^4-9 x 10^4 nm in diameter. The trends in the smaller set of pores were reasonably consistent with the findings from the N_2-adsorption analysis. The 100Fe(E) OC particles had the largest pore volume and largest average pore size followed by the 100Fe(S) OC particles. In both cases, the porosity created by the smaller set of pores spanned a relative large distribution of pore sizes between ~100-1000 nm in diameter. The 100Fe(B) OC particles had the smallest volume of pores in the porous region created by the smaller set of pores. The distribution of the smaller set of pores was also much more narrow compared with the 100Fe(E) and 100Fe(S) OC particles, spanning pore sizes of ~100-350 nm in diameter.

As with the smaller set of pores, the larger macro-porosity (1 x 10^4- 9 x 10^4 nm) observed in the MIP pore size distribution of the 100Fe(E) OC particles was created by slightly larger pores than the 100Fe(S) OC particles exhibiting a maximum pore volume at a pore size of ~ 6.1 x 10^4 nm compared with 4.5 x 10^4 for the 100Fe(S) particles. The 100Fe(B) appeared to have the largest set of macro-pores that were shifted towards the upper pore size cut-off limit of 9 x10^4 nm.

The MIP pore size distribution for the 60Fe40Al OCs produced using the different methods showed that the addition of 40 wt.% α-Al_2O_3 skewed the distribution of smaller pores (5-1000 nm in diameter) in favour of a larger average pore size compared with the equivalent 100Fe OC particles (fig. 5.9). The addition of 40 wt.% α-Al_2O_3 also effected the porosity created by the larger macro-pores particularly in the case of the 60Fe40Al(B) OC particles shifting the larger pores to a pore size distribution with a smaller average pore size that was within the resolution of the analysis. The total pore volume was slightly lower in the 60Fe40Al(E) and 60Fe40Al(S) particles but larger in the case of the 60Fe40Al(B) compared with the equivalent 100Fe particles prepared via the same production methods.

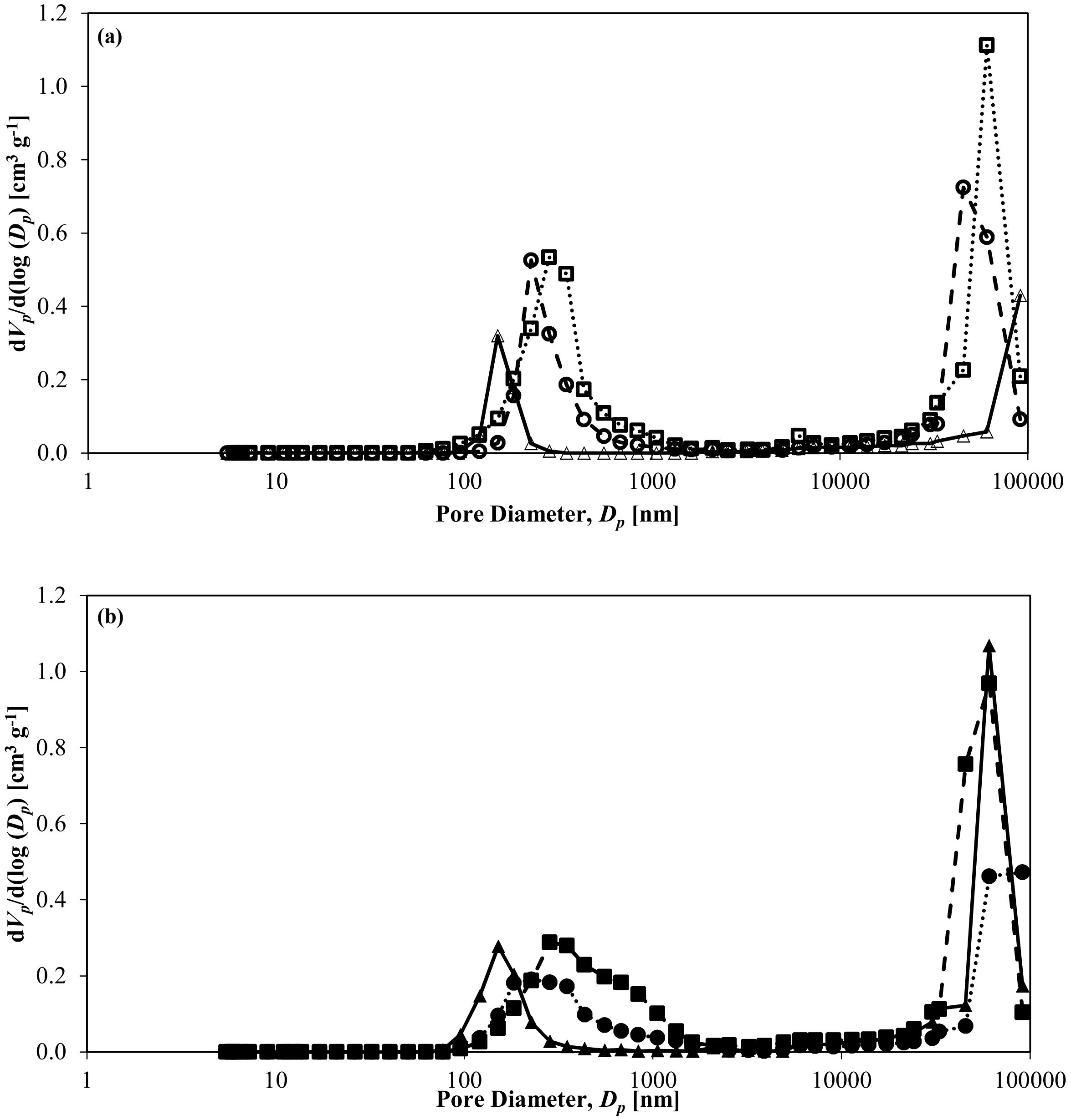

Figure 5.9. Pore size distributions determined by MIP analysis of the fresh (a) 100 wt.% Fe_2O_3 (100Fe) (open symbols) and (b) 60 wt.% Fe_2O_3/40 wt.% Al_2O_3 (60Fe40Al) OC particles (closed symbols) prepared via the different preparation methods: method B (—△—); method E (···□···); and method S (– ● –).

Similar trends to those presented in the BJH pore size distribution results were observed in the MIP pore size distributions of the 60Fe40Al OC particles synthesised from the different Al_2O_3 precursors (fig. 5.10). In all cases, the precursors that reacted/decomposed to form Al_2O_3 during the sintering process created OC particles with a far larger volume of meso-porosity and lower average pore size in the porous region between 5-1000 nm, compared with the 60Fe40Al particles prepared using the α-Al_2O_3. The MIP results also revealed that the 60Fe40Al(SAB) OC particles had the largest volume of pores in both porous regions created by pores spanning 5-1000 nm and 1 x 10^4-9 x 10^4 nm in diameter.

The MIP pore size distribution also show the bi-modal pore size distribution of pores exhibited by the 60Fe40Al(SPN) and 60Fe40Al(SPS) particles in the smaller pore size region 5-1000 nm as observed by BJH. Interestingly the MIP results reveal that whilst the volume of pores in the 60Fe40Al(SPN) and 60Fe40Al(SPS) OC particles are similar, the second set of pores (in the porous region 5-1000 nm) spans a much wider distribution of pore sizes between ~50-1000 nm whilst the equivalent set of pores in the 60Fe40Al(SPS) OC particles had a similar porous volume across a narrower range of pore sizes between ~50-150 nm in diameter. The porosity of the 60Fe40Al(SPN) and 60Fe40Al(SPS) created by the larger pores between 1 x 10^4-9 x 10^4 nm in diameter are very similar with average pore diameters of ~ 6 x 10^4 nm.

The porous structural differences observed between the 60Fe40Al(S) and 60Fe40Al(SAC) (prepared using the same method and from the same precursors) was a result of the different sintering temperature used. The 60Fe40Al(SAC) particles were sintered at a higher temperature of 1293 K compared with 1173 K. The use of higher temperatures is known to enhance thermal sintering processes that result in reduced surface areas, pore widening and a loss of porosity as was observed here (Adanez et al., 2004, Mattisson et al., 2004).

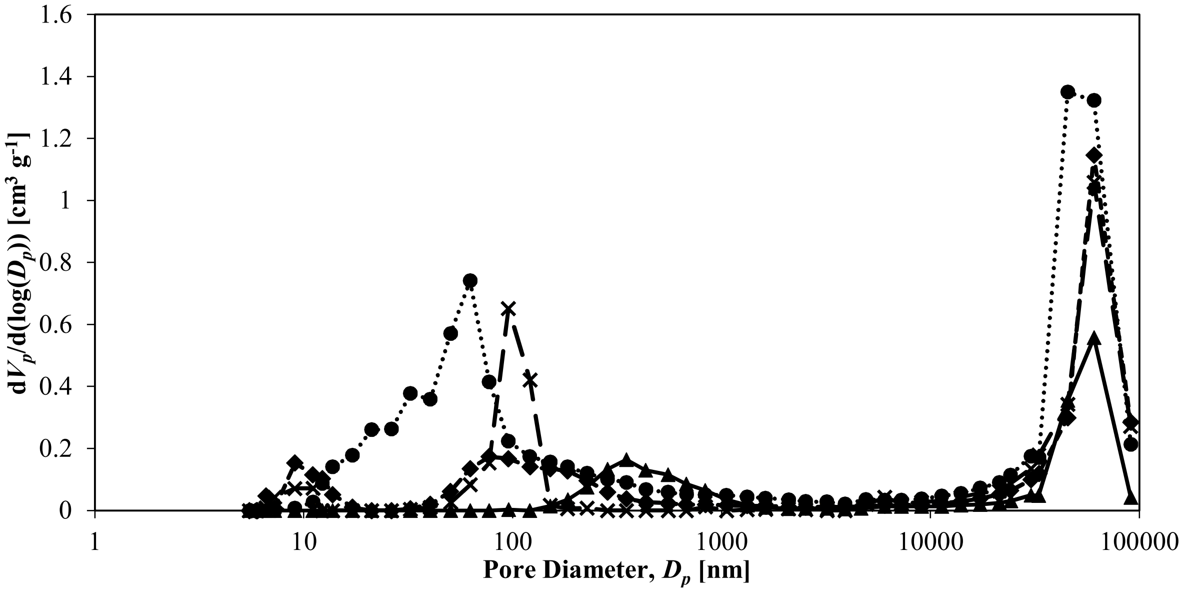

Figure 5.10. Pore size distributions determined by MIP analysis of the fresh 60 wt.% Fe_2O_3/40 wt.% Al_2O_3 (60Fe40Al) OC particles prepared from the different Al_2O_3-precursors. 60Fe40Al(SAC) (—▲—); 60Fe40Al(SAC) (···●···); 60Fe40Al(SPN) (--◆--); and 60Fe40Al(SPS) (—×—).

The chemical phase composition of the fresh 60Fe40Al OC particles was studied using XRD (X'Pert Pro PANalytical, CuKα, 40kV and 40mA). In all the patterns provided in figure 5.11, the peaks associated with the crystalline α-Fe_2O_3 phase are clearly visible. Another set of peaks associated with the crystalline α-Al_2O_3 phase was also visible in the 60Fe40Al(S) pattern. However, there were no visible peaks associated with the aluminium containing phases in the 60Fe40Al(SAB), 60Fe40Al(SPN), and 60Fe40Al(SPS) XRD patterns. A possible explanation for this observation (or lack thereof) is that iron containing phases strongly fluoresce when irradiated by CuKα X-rays which results in diffraction patterns with very high intensity and noisy baselines. If the alumina phases present in the 60Fe40Al(SAB), 60Fe40Al(SPN) and 60Fe40Al(SPS) were amorphous (wide, low intensity peaks) as observed for the pure Al_2O_3 particles produced from $Al(OH)_3$ shown in figure 5.12, it is likely that the diffraction pattern was swamped by the high intensity, noisy background of the Fe_2O_3 phase such that it could not be differentiated from the background noise.

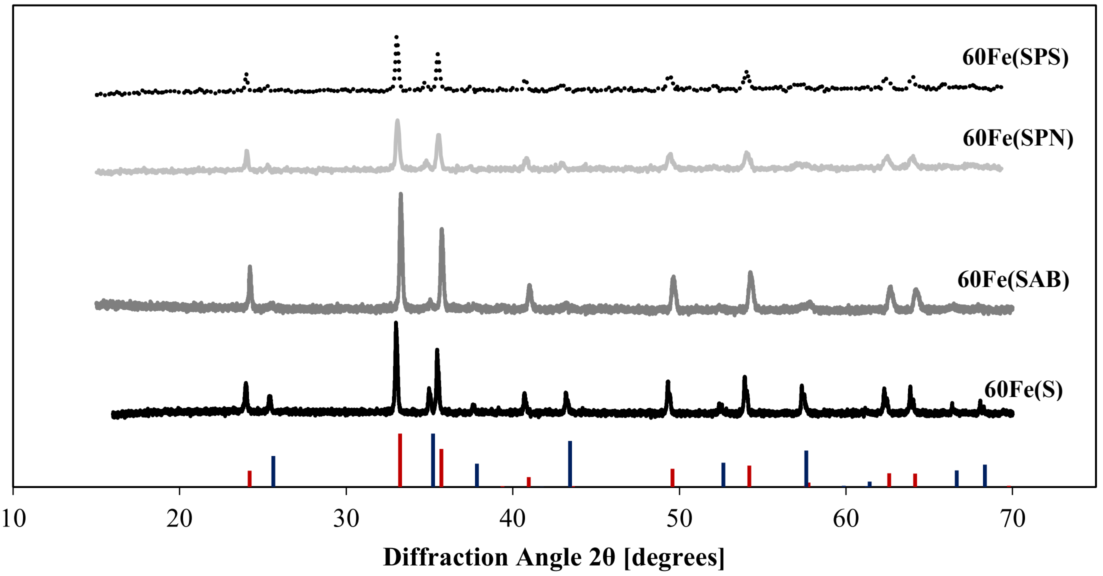

Figure 5.11. XRD patterns (with arbitrary intensity y-axis) for the fresh OC particles (post sintering) and reference XRD patterns for α-Fe_2O_3 (hematite) (——) and α-Fe_2O_3 Al_2O_3 (corundum) (——).

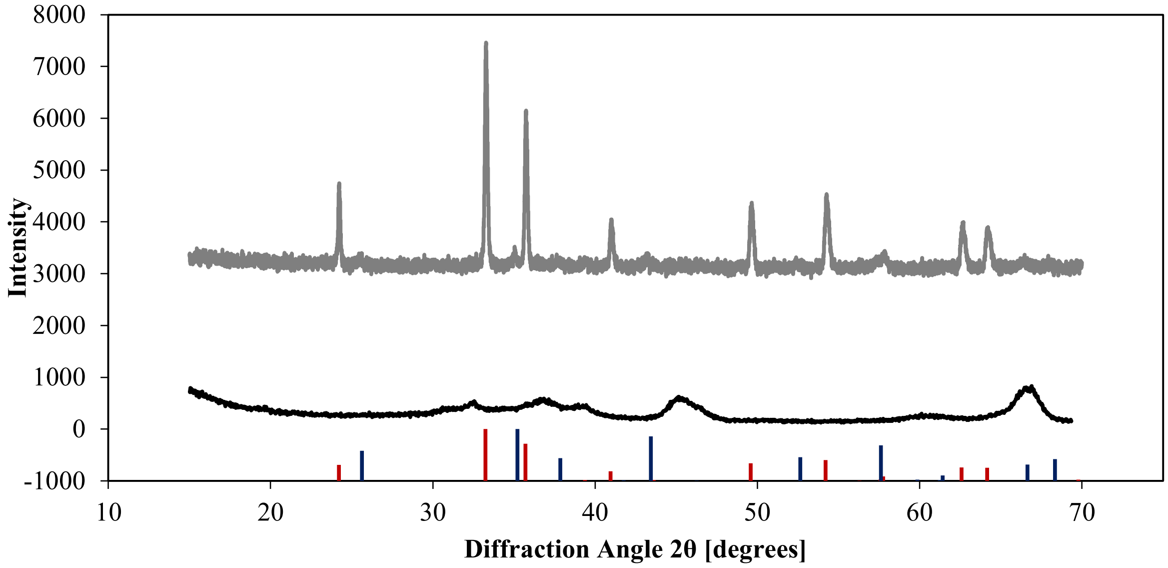

Figure 5.12. XRD patterns (with true intensity y-axis) for the fresh 60F40Al(SAB) OC particle (——) and pure Al_2O_3 particles prepared from the $Al(OH)_3$ alumina precursor (——). Reference XRD patterns for α-Fe_2O_3 (hematite) (——) and α-Fe_2O_3 Al_2O_3 (corundum) (——).

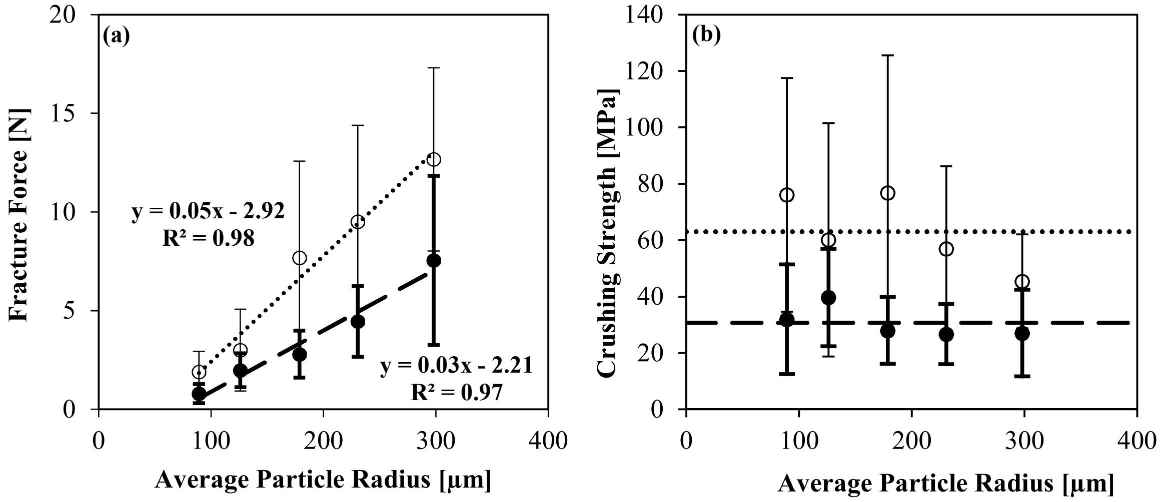

Figure 5.13. Summary of single particle crushing strength tests for different size fractions of 100Fe(S) (open symbols) and 60Fe(SAC) (closed symbols) expressed as (a) force (in N) required fracture a single OC particle and (b) the crushing strength expressed as (MPa) where the fracture force was divided through by the average cross-sectional area of the particle Each test was repeated 30 times to obtain error ranges (standard deviation) that reflect the behaviour of the sample as a whole.

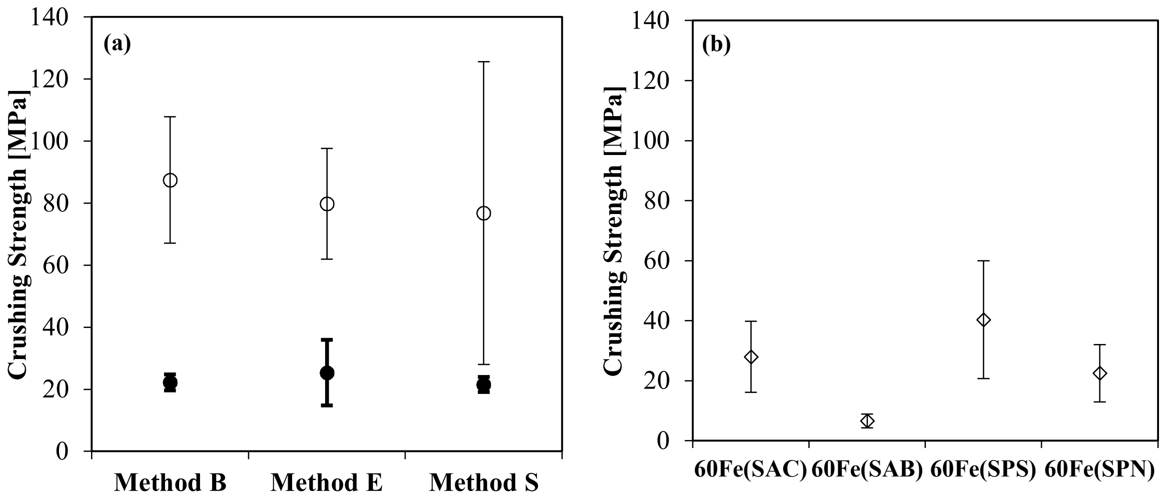

Figure 5.14. Summary of single particle (300-425 μm) crushing strength tests for (a) the 100Fe (○) and 60Fe40Al (●) OC particles and (b) 60Fe40Al OC particles prepared from different alumina precursor materials.

The crushing strength of the fresh OC particles was determined by measuring the force required to fracture the particles using a Lloyd EZ50 Material Testing Instrument. An initial set of experiments was carried out to investigate the effect of particle size on the 'strength' of the 100Fe(S) and 60Fe40Al(S) OC particles. As illustrated in figure 5.13(a) the force required to fracture the particles decreased linearly with particle size. The crushing force was normalised by dividing through by the average cross-sectional area of the particle to provide a crushing strength in the form of a pressure (MPa) (fig. 5.13(b)).

A second set of experiments was then carried out to investigate the effect of preparation technique and formulation on the crushing strength of the different OC particles in the size range 300-425 μm (fig. 5.14(a)). The 100Fe OC particles demonstrated a significantly larger crushing strengths (average strengths between 77-87 MPa) compared with the equivalent 60Fe40Al OC particles (21-25 MPa) prepared by the different methods, however it was not possible to comment on possible small differences in the crushing strengths as a result of preparation technique due to the large standard deviation in the measurement (RSD ~ 40-50%).

There were small differences in the crushing strengths of the 60Fe40Al particles prepared from the different Al_2O_3 precursors (fig. 5.14(b)). The 60Fe40Al(SPN) was the most robust demonstrating the highest average crushing strength of ~ 40 MPa. The 60Fe40Al(SAC) exhibited the second highest crushing strength of ~ 28 MPa followed by the 60Fe40Al(SPS) particle (~ 23 MPa). The 60Fe40Al(SAB) was the weakest particle exhibiting a crushing strength of ~ 7 MPa.

As expected, the most porous OC particle (i.e. 60Fe40Al(SAB)) demonstrated the lowest crushing strength. Increasing the sintering temperature was found to improve the crushing strength as illustrated by the higher crushing strength exhibited by the 60Fe40Al(SAC) particle sintered at 1272 K compared with the 60Fe40Al(S) particle sintered at 1173 K. The difference in crushing strengths exhibited by the 60Fe40Al(SPN) and 60Fe40Al(SPS) was unexpected given that the particles were prepared from different variants of the same Al_2O_3 precursor (AlO(OH)) and shared very similar porous structures. It should be noted that the significance of these differences are questionable as the errors are similar in magnitude to the differences in crushing strengths.

Scanning electron microscopy was used to visualise the particle shape and surface morphology of the different OC particles. Figure 5.15 (a-c) shows low magnification (300 x) images of some the 100Fe OC particles (300-425 μm) prepared via the different methods (B, E and S). The 100Fe(B) had the most irregular shape but was still relatively spherical. Methods E and S produced more consistently spherical particles as a consequence of the spheronisation step in the preparation method.

The surface morphologies of the 100Fe(S), 60Fe40Al(S) and 60Fe40Al(SAB) particles were observed at a higher magnification of x2000. Observation of the surface of the 100Fe(S) OC revealed that the particle was made up of small grains (roughly 0.5- 3 μm in diameter). Pores and channel openings on the surface appear to be small < 3 μm and are formed between the sintered Fe_2O_3 grains. Alumina is clearly visible in both the 60Fe40Al(S) and 60Fe40l(SAB) OC particles (larger darker grains in figure 5.15 (e-f), confirmed by in-situ EDS analysis). The alumina in the 60Fe40Al(S) is present as relatively large grains of ~ 10 μm in diameter and appear to be embedded within the Fe_2O_3 granular matrix. The alumina phase of the 60Fe40Al(SAB) also appears to be formed of relatively large grains (relative the Fe_2O_3 phase) although the alumina phase appears to have been better intermixed with the Fe_2O_3 phase with the Fe_2O_3 phase appearing to exist as more of a dispersed phase over a larger alumina granular phase. There also seems to be a lot more, wider pore openings on the surface of the 60Fe40Al(SAB) supporting the findings from MIP analysis.

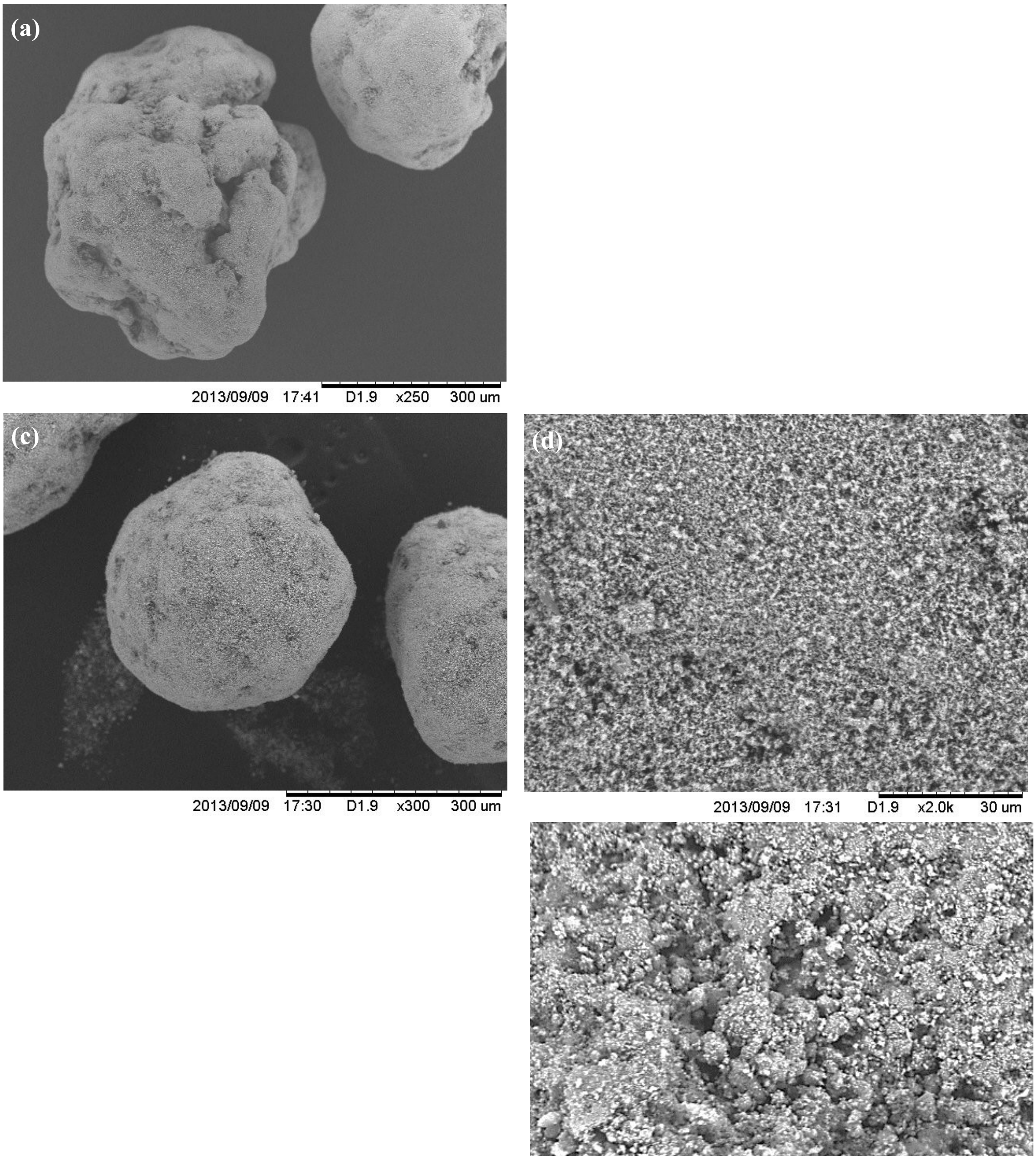

Figure 5.15. SEM showing the shape of the different OC particles (300-425 µm) prepared via the different methods: (a) method B; (b) method E and (c) method S; and the surface morphologies for (e) 100Fe(S) OC particle; (f) 60Fe40Al(S) OC particle and (e) 60Fe40Al(SAB) OC particle.

5.4.3 TGA Simulated CLC Experimental Design

To obtain accurate kinetic information, it is necessary to operate the TGA under conditions approaching those of an ideal differential reactor. If this is to be achieved, conditions must be chosen to minimise, or preferably remove heat and mass transfer effects that can lead to the measurement of an observed rate of reaction, r', that is (in most cases) lower than the intrinsic rate of reaction. Heat and mass transfer limitations can manifest as temperature and concentration gradients both within the particles and externally to the particles (Bird, 2002). Concentration gradients can form externally to the particle if (i) the rate of reaction (i.e. the rate of which the reactive gas is consumed) is of a similar magnitude to or less than the rate of which the gas is supplied to the reactor or (ii) if the sample mass is large such that the sample behaves more like a packed bed (i.e. the reactive gas has to diffuse past the particles on the surface of the bed and is thus partially consumed by the surface particles to reach the particles in the centre of the bed that are not directly exposed to the flowing gas) as opposed to a collection of individual particles that are all reacting independently with the same concentration of reactive gas.

A preliminary set of experiments was carried out to evaluate the effect of different experimental parameters including cycle number, flow rate, sample mass and particle size on the observed rate of reduction. The desired outcome of these experiments was to establish a set of standard experimental parameters by which all prospective oxygen carrier materials synthesised as part of this project could be tested. A summary of the standard set of experimental conditions used for the first two sets of experiments reported in this section is provided in table 5.4 with a description as to how these conditions were chosen provided below.

Table 5.4. Summary of initial standard experimental parameters for the TGA simulated CLC experiments.

Parameter	Parameter Value
Sample Mass [mg]	2 ± 0.2
Particle size [μm]	150-212*
Temperature [K]	773-1223 (increasing at 50 K increments)
Pressure [bar$_a$]	1.01
Total Flow Rate [mlN/s]	80
Reducing gas	3 vol.% CO, 15 vol.% CO_2, balance N_2^+
Oxidising gas	4 vol.% O_2, balance N_2
Reduction period duration [min]	5
Oxidation period duration [min]	5
N_2 purge period duration [min]	2

* Other size fractions were used for experimental determination of τ (300-425 μm and 500-710 μm)

$^+$ The concentration of CO was varied between 1-5 vol.% for the experimental determination of the reaction order (section 5.4.4).

The Effect of Cycle Number

To investigate how the observed rate of reaction changes with cycle number, two 10 redox cycle CLC experiments were performed in the TGA with a 100FeS oxygen carrier particle at 823 K and 973 K (fig. 5.16).

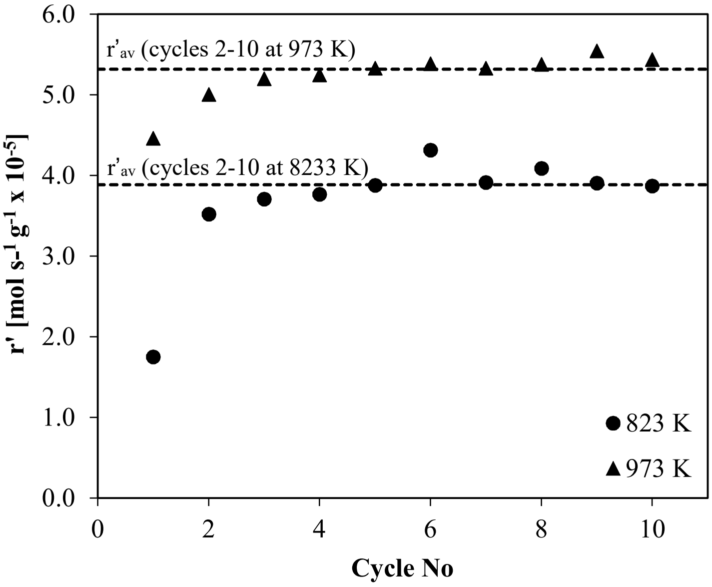

Figure 5.16. The evolution of the rate of reduction as a function of cycle number at 823K and 973 K. **Experimental parameters: Reactor:** TGA; **Oxygen Carrier**: 100FeS (5 mg, 150-212 μm); **Reaction:** $Fe_2O_3 \rightarrow Fe_3O_4$; **Temperature**: Variable; **Reducing gas composition**: 3 vol.% CO, 15 vol.% CO_2, balance N_2; **Oxidising gas composition**: 4 vol.% O_2, balance N_2; **Total Flow Rate**: 80 ml min^{-1}; **Total Cycle Number**: 10. ● 823 K; ▲ 973 K.

At both temperatures, the observed rate of reduction for the first cycle was significantly lower than the observed rates for the following cycles 2-10 with the rate reaching a relatively stable value by the 3rd cycle. This behaviour is typical of Fe-based oxygen carrier and has been reported on many occasions in the literature (Zhang, 2014, Bohn, 2010, Mattisson et al., 2004). The reason for this behaviour is thought to be a result of morphological changes *i.e.* pore development and the formation of small fractures at the weak locations in the solid matrix due to chemical and thermal stresses in the first cycle, exposing a larger reactive surface area. The initial rate (r') and rate profiles as a function of conversion (fig. 5.17) appear to stabilise after the first cycle indicating that the morphology also stabilises after the initial morphological changes that take place during the first cycle reduction. As a consequence, it was decided to run each experiment for a total of 3 cycles and use the rate data for the 3rd cycle for the kinetic analysis.

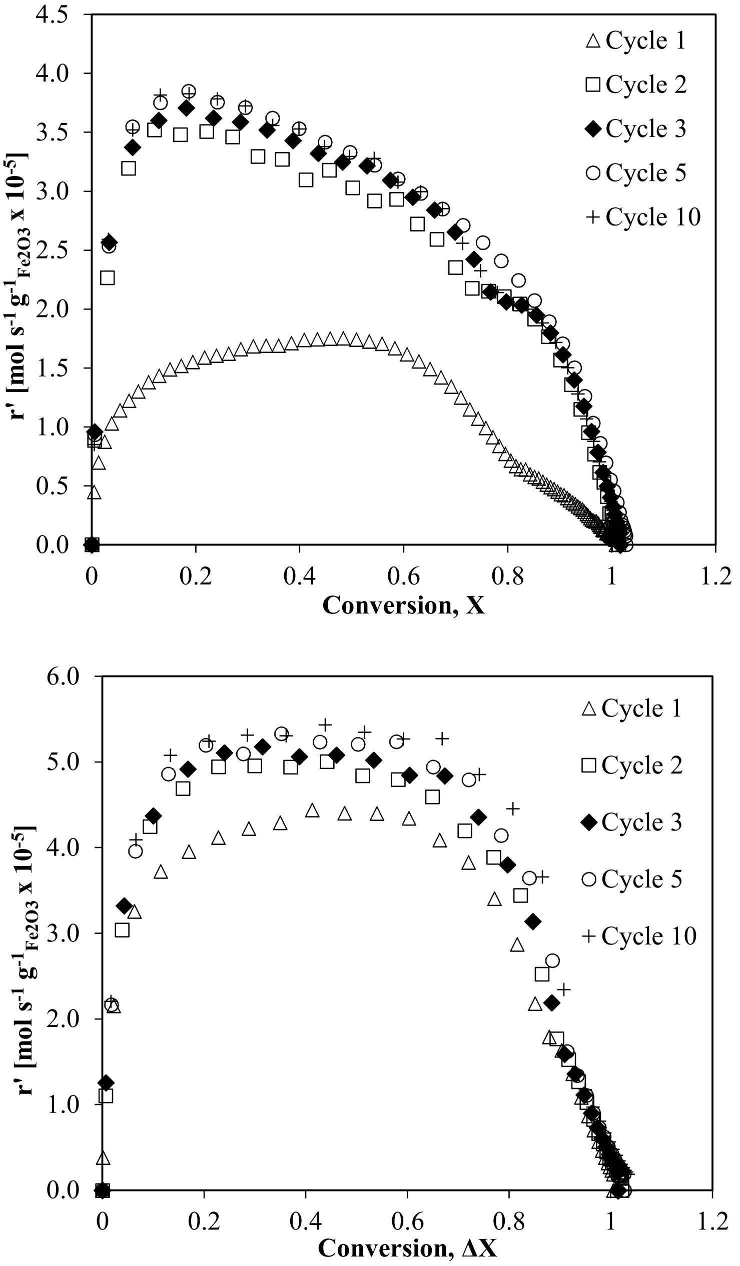

Figure 5.17. Rate of reduction as a function of conversion for different reduction cycle numbers at (a) 823 K and (b) 973 K. **Experimental parameters: Reactor:** TGA; **Oxygen Carrier**: 100FeS (5 mg, 150-212 µm); **Reaction:** Fe_2O_3 → Fe_3O_4; **Temperature**: Variable; **Reducing gas composition**: 3 vol.% CO, 15 vol.% CO_2, balance N_2; **Oxidising gas composition**: 4 vol.% O_2, balance N_2; **Total Flow Rate**: 80 ml min^{-1}; **Total Cycle Number**: 10. △ cycle 1; □ cycle 2; ◆ cycle 3; + cycle 5; ○ cycle 10.

Efforts to Eliminate Inter-particle and Intra-particle Mass Transport Effects

The mass transfer effects associated with total mass of sample and particle size fraction were investigated for the reduction of a 100FeS oxygen carrier at 823 K with 3 vol.% CO, 15 vol.% CO_2, balance N_2. First the mass of 100FeS oxygen carrier particles (150-212 μm) loaded into the TGA was varied between 2 and 7 mg (fig. 5.18(a)). A second set of experiments was then conducted to determine the effect of the particle size for the size fractions 150-212 μm; 212-300 μm; 300-425 μm; 425-500 μm and 500-710 μm (fig. 5.18(b)).

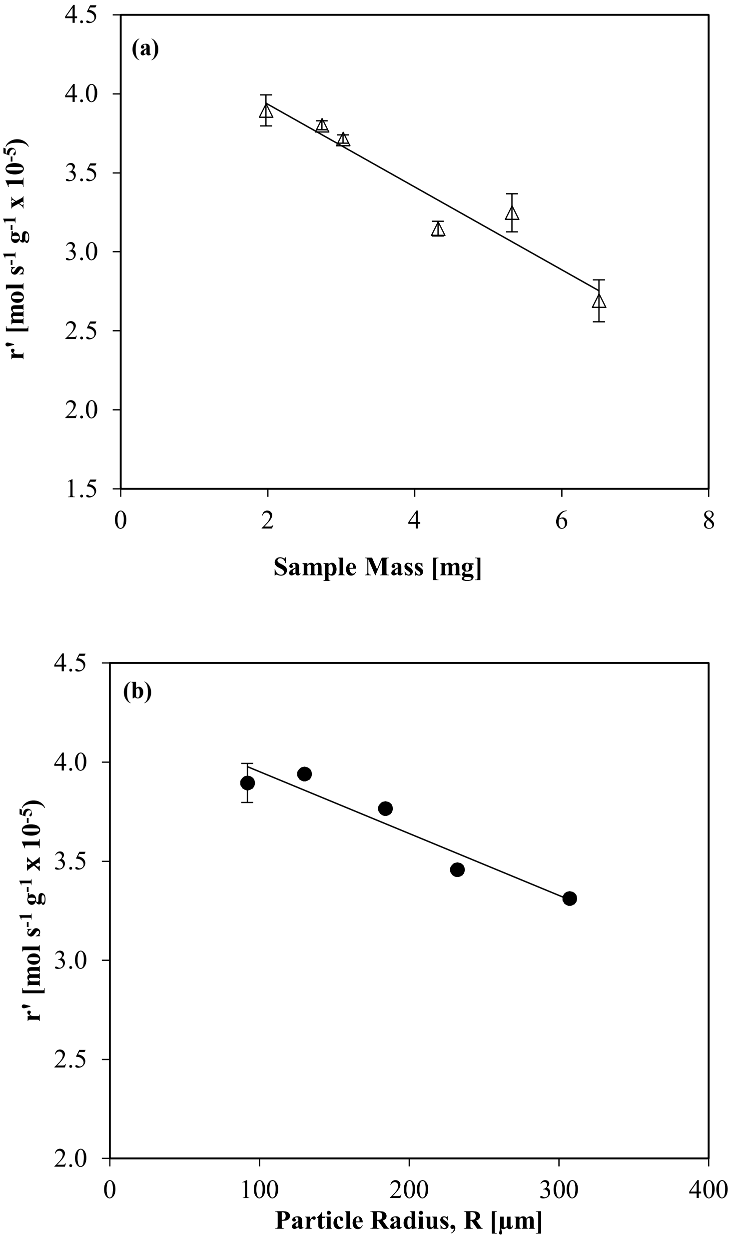

Figure 5.18. Observed rate of 3rd cycle reduction as a function of (a) total sample mass loaded into the TGA pan and (b) particle radius. **Experimental parameters**: **Reactor:** TGA; **Oxygen Carrier**: 100FeS; **Sample Mass:** variable;) **Particle Size Fraction:** variable; **Reaction:** $Fe_2O_3 \rightarrow Fe_3O_4$; **Temperature**: 823 K; **Reducing gas composition**: 3 vol.% CO, 15 vol.% CO_2, balance N_2; **Oxidising gas composition**: 4 vol.% O_2, balance N_2; **Total Flow Rate**: 80 ml/min; **Total Cycle Number**: 3.

Both increasing the mass of sample loaded into the TGA (fig. 5.18(a)) and increasing particle size (fig. 5.18(b)) had deleterious effects on the observed rate of reduction. Increasing the mass of sample from ~2 mg to ~7 mg had a greater effect on the observed rate of reduction causing a decrease in the observed rate by 30 % compared with a decrease of 15 % when the particle size was increased from 150-212 μm to 500-710 μm. The decreasing trend in r' was observed for all sample masses tested indicating that even at very small sample mass loadings of 2 mg, there may be some inter-particle mass transfer effects. Smaller sample masses (< 2 mg) have been trialled but produced noisy TGA weight profiles that were difficult to de-convolute. The smaller particle size fractions of 150-212 μm and 212-300 μm produced similar observed rates with the decreasing trend in rate observed for particle sizes > 300 μm. These findings are consistent with previous kinetic studies into the reactivity of pure Fe_2O_3 oxygen carriers and indicate that intra-particle mass transfer effects can be eliminated for particle sizes < 300 μm at the conditions tested. It was therefore decided that a standard sample mass of 2 mg and particle size of 150-212 μm would be adopted for the kinetic analysis reported in this chapter.

The total flow rate of the inlet gas was also varied between 50-200 ml_N min^{-1}, however flow rates > 80 ml_N min^{-1} produced noisy weight profiles particularly during the gas switch which complicated the determination of the initial and maximum rates. A simple calculation of the molar flow rate of CO into the reaction chamber (3 vol.% CO, 80 ml_N min^{-1} total flow rate) and the molar consumption by the reaction at temperatures between 823-923 K revealed that the drop in CO concentration as a consequence of the reaction was < 7 %. Whilst this is not an insignificant deviation from an ideal reactor situation, the deviation was still relatively small and it was decided to adopt 80 ml_N min^{-1} as the standard flow rate for the experiments presented in this chapter.

A set of preliminary experiments using 100Fe(S) oxygen carrier particles for the temperature range 823-973 K was carried out to compare kinetic measurements for the simulated CLC in the TGA, with reference case observed kinetic measurements carried out in a spouted fluidised bed reactors (Zhang, 2014). For comparison, the observed rate constants were expressed in Arrhenius form (*i.e.* $k_o = A_o e^{-E_{a,obs}/RT}$), to derive the observed activation energy ($E_{a,obs}$, in $kJ.mol^{-1}$). Arrhenius plots of ln(k_o) as a function of $10^3/RT$ (where R is the ideal gas constant, T is the absolute temperature in K and A_o is the pre-exponential factor *i.e.* $k_{o\,(T \to 0\,K)}$) (fig. 5.19) were constructed such that the $E_{a,obs}$ and ln(A_o) values could be easily extracted from the gradient and y-axis intercept of the linear least squares fit line of the Arrhenius plots respectively.

As evident from figure 5.19, the k_o values and $E_{a,obs}$ (calculated using the maximum observed rate) for the TGA experiments were substantially lower than the reference case. The calculated $E_{a,obs}$ for the TGA experiments was 27.6 kJ mol^{-1} compared to 50.8 kJ mol^{-1}. Two possible explanations for this behaviour were proposed: (i) the reaction was limited by mass transfer externally to the particle (indicated by the fact that $E_{a,obs} \approx -(1\ to\ 2)/R$ where R is the average radius of the spherical particle) and/or; (ii) the assumption that the inlet CO concentration could be modelled as a step function was false.

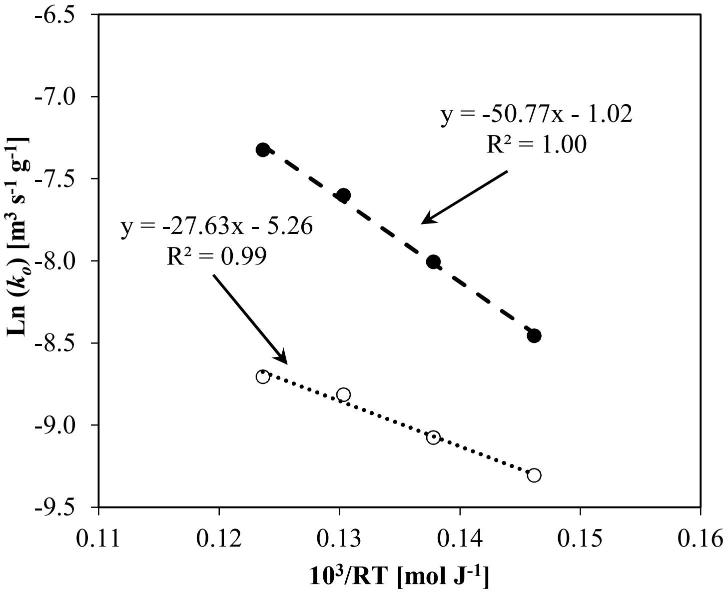

Figure 5.19. Arrhenius plot for the observed rate constants determined for the reduction of 100Fe oxygen carrier particles (Fe2O3 → Fe3O4) at 823-972 K in the TGA (open symbols) and reference case spouted bed reactor (solid symbols). The gradient of the plots is equal to the apparent activation energy, $E_{a,obs}$, and the y axis intercept gives the natural logarithm of the pre-exponential factor (i.e. k_o as T→0K).

The material balance calculation (discussed above) revealed that the molar flow of CO into the reactor $\gg$ molar consumption of CO by the reaction for the temperature range 823-973 K indicating that local depletion of reactants was unlikely to be the cause of the low $E_{a,obs}$ on its own. A more likely reason for the values of k_o and $E_{a,obs}$ calculated here is that the 'real' gas switch at the beginning of the reduction phase did not behave as step-function and that there was a lag period in which the CO concentration was rising to the set point.

Comparing the k_o values as a function of conversion revealed that the maximum rate constant was reached at a much lower conversion in the reference case *i.e.* X = 0.02-0.1 (T = 823-973 K) compared with X = 0.2-0.4 for the rate constants determined from the TGA experiments. As it has been assumed here (and demonstrated elsewhere in the literature (Zhang (2014), Bohn (2010)) that the effective diffusivity within a 100 wt.% Fe_2O_3 particle remains relatively constant throughout the reaction as it undergoes reduction to Fe_3O_4, this observation supports the hypothesis that the actual CO concentration profile deviated from a step function. The observed rate of reaction during the initial stages of the reaction would have increased as a function of the rising CO concentration resulting in an observed maximum rate of reaction at a point in time where the CO concentration stabilised at the set point. If this was the case, the assumption that the inlet concentration of CO was equal to the set point CO concentration during this 'lag period' would have led to the calculation of lower rate constant values during the initial stages (immediately proceeding the gas switch), culminating in the observation of a maximum rate at a higher conversion.

This potential error in the calculated rate constants during the initial stages of the reaction, may have also been exacerbated with increasing temperature resulting in the low value of $E_{a,obs}$ derived here. The increased rate of reaction with increasing temperature could have led to a temporary period during the initial section of the lag period (when the CO concentration was low) where the reaction was limited by transfer of reactant into the TGA (*i.e.* molar rate of consumption of CO ≈ the temporal molar flow of CO into the reaction chamber). The rate of consumption of reactants entering the TGA, and therefore time and conversion that the reaction transitions out of the external mass transfer limited regime would also increase with temperature resulting in a larger error or discrepancy between the true maximum reaction controlled rate constant that would have been observed in the absence of external mass transfer limitations and the actually observed maximum rate constant.

To test whether the validity of the initial assumption that the CO concentration profile in the reactor could be modelled as a step function, a mass spectrometer (Aston Analytical) was connected to the outlet of the TGA reaction chamber. Measuring the concentration of CO in the presence of N_2 using a mass spectrometer is very difficult as they have the same molecular masses. To overcome this issue, a cylinder of 10 vol.% CO_2 was used in place of a 10 vol.% CO cylinder and diluted down using N_2 to simulate the concentration profile during the gas switch from 100 vol.% N_2 to 3 vol.% CO in N_2 (fig. 5.20).

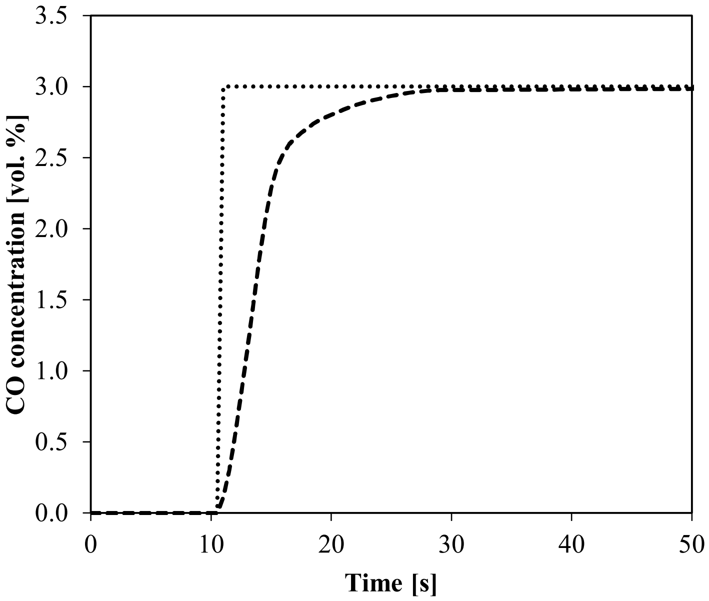

Figure 5.20. Comparison of the predicted CO concentration profile in the TGA reaction chamber with respect to time during the gas switch at the beginning of the reduction phase of a simulated CLC experiment determined from (i) mass spectrometer measurements (using 3 vol.% CO2 as a tracer for 3 vol.% CO) at the outlet of the TGA reaction chamber (- - -); and (ii) assuming the CO concentration during the gas switch could be modelled as a step function (⋯⋯). **Experimental parameters: Reactor:** TGA; **Oxygen Carrier**: N/A; **Temperature**: 293 K; **Inlet gas composition**: 100 vol.% N_2 → 3 vol.% CO_2, balance N_2; **Total Flow Rate**: 80 ml min^{-1}.

Assuming the mass spectrometer measurements for the gas switch (N_2 → 3 vol.% CO_2, balance N_2) could be used to accurately predict the concentration of CO during the gas switch at the beginning of the reduction phase (i.e. N_2 → 3 vol.% CO, 15 vol.% CO_2 balance N_2); figure 5.20 shows that the CO concentration profile clearly deviates from the initial assumption that it could be modelled as a step function, requiring ~ 12 s to reach 95 % of the set point inlet CO concentration. To account for the actual concentration response within the furnace at the beginning of the reduction period, the rate constant values were recalculated using the CO concentration profile predicted from the mass spectrometer measurements for the 100 vol.% N_2 → 3 vol.% CO_2 gas switch (fig. 5.21).

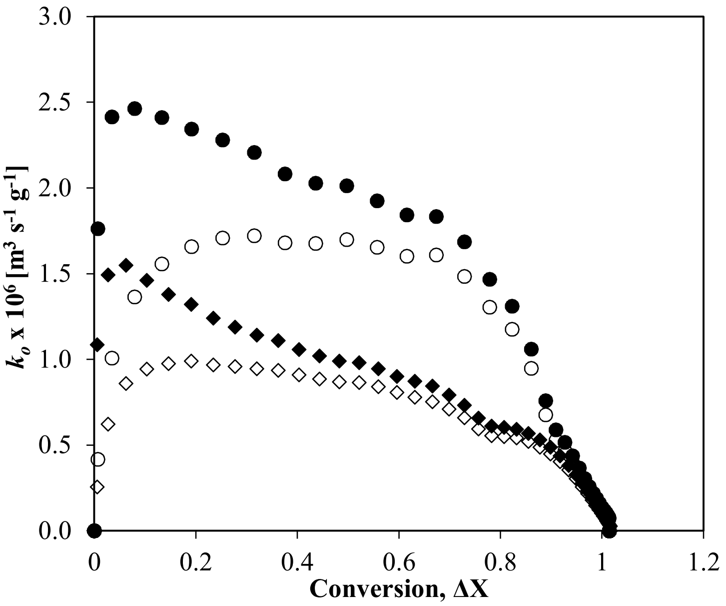

Figure 5.21. Comparison of the observed rate constant values as a function of 100Fe conversion calculated assuming the concentration of CO (with respect to time) could be modelled as a step function (open symbols) and assuming the CO concentration profile could be predicted using mass spectrometer measurements for the gas switch 100% N_2 → 10 vol.% CO_2, balance N_2 (closed symbols) at 823 K ◇ and 973 K ○. **Experimental parameters: Reactor:** TGA; **Oxygen Carrier**: 100Fe(S); **Sample Mass:** 2 mg; **Particle Size Fraction:** 150-212 μm; **Reaction:** $Fe_2O_3 \rightarrow Fe_3O_4$; **Temperature**: 823 K; **Reducing gas composition**: 3 vol.% CO, 15 vol.% CO_2, balance N_2; **Oxidising gas composition**: 4 vol.% O_2, balance N_2; **Total Flow Rate**: 80 ml min^{-1}; **Total Cycle Number**: 3.

Recalculation of the rate constants using the CO concentration profile predicted from the mass spectrometer measurements resulted in a dramatic increase in the rate constant values, particularly during the initial stages at conversions < 0.3 (fig. 5.21). The maximum rate constant values are now reached at conversions of < 0.1 and the k_o profile as a function of conversion are also in close agreement to those measured in the reference case using the spouted fluidised bed reactor (fig. 5.22).

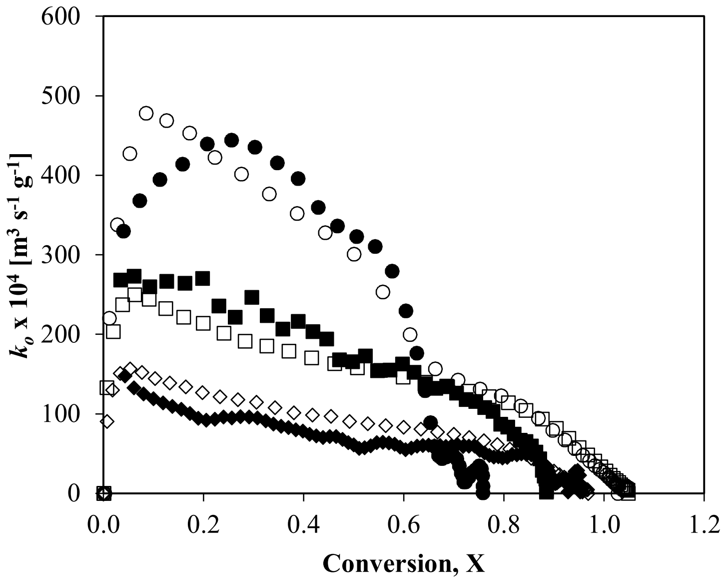

Figure 5.22. Observed rate constant, k_o profiles as a function of conversion for the 3rd cycle reduction ($Fe_2O_3 \rightarrow Fe_3O_4$) of 100Fe particles measured using a TGA (open symbols) and in the reference case spouted fluidised bed (closed symbols) at 773 K □; 823 K ◇ and 923 K ○. (N.B. rate constants are expressed in s^{-1}, *i.e.* per unit volume, due to the substantial difference in the surface area and envelope density measurements of the 100Fe particles used for the TGA and reference case spouted bed experimental investigations.

Based on the results obtained after correcting the rate constant profiles as a function of conversion to take into consideration the true concentration profile in the TGA reaction chamber (with respect to time), it was decided that the current method for estimating the rate at zero conversion was no longer appropriate. Three new methods were trialled and compared with the intrinsic rate constant, k_i values and activation energy $E_{a,i}$ obtained in the analogous reference case spouted bed experimental investigation and the original maximum r' method (ii) used previously. The new methods that were trialled included: (iii) using the rate constant in the corrected rate constant profile at the conversion for which the maximum rate was attained (hereon referred to as 'the corrected maximum r' method'); (iv) using the maximum rate constant value in the corrected rate constant profile (hereon referred to as 'the maximum k method'); and (v) a slight adaptation of the linear fit method, where a line of best fit was fitted to the linear section of the concentration corrected k_o vs conversion plot (typically in the conversion range of $X = 0.2$-0.6 where k appears to decay linearly with conversion) and extrapolating back to $X = 0$ (hereon referred to as 'the corrected linear fit method'). Each of these methods are illustrated in figure 5.23. A comparison of the Arrhenius plots generated from the rate constants estimated using the different methods (ii-v) is provided in figure 5.24 along with the Arrhenius plot generated from the intrinsic rate constants obtained from the analogous reference case spouted fluidised bed experimental study. Table 5.5 summarises the observed and intrinsic activation energies and pre-exponential constants obtained from the Arrhenius plots in figure 5.24.

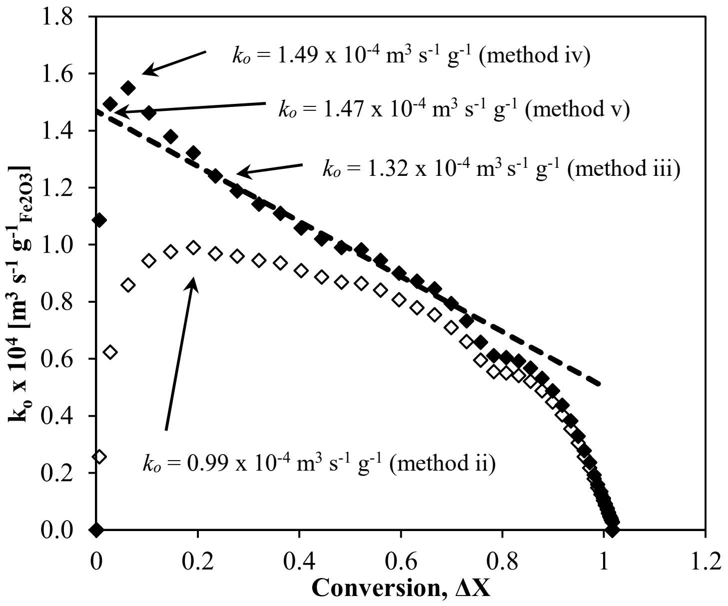

Figure 5.23. Example of the four different methods that were trialled for estimating the initial observed rate constant at zero conversion using the original and CO concentration response corrected rate constant vs conversion plots. The four methods that were trialled include: methods: (ii) the original maximum rate method; (iii) the corrected maximum rate method; (iv) the maximum rate constant method; and (v) the corrected linear fit method. **Experimental parameters: Reactor:** TGA; **Oxygen Carrier**: 100Fe(S) (5 mg, 150-212 μm); **Reaction:** Fe_2O_3 → Fe_3O_4**;** **Temperature**: 823 K; **Reducing gas composition**: 3 vol.% CO, 15 vol.% CO_2, balance N_2; **Oxidising gas composition**: 4 vol.% O_2, balance N_2 **Total Flow Rate**: 80 ml min^{-1}; **Cycle Number**: 3.

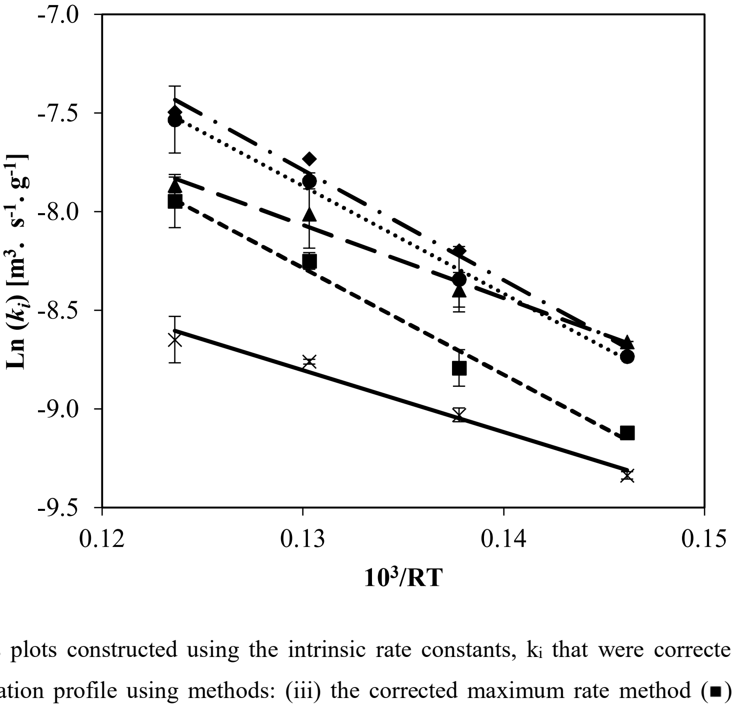

Figure 5.24. Arrhenius plots constructed using the intrinsic rate constants, k_i that were corrected for the experimentally measured CO concentration profile using methods: (iii) the corrected maximum rate method (■); (iv) the maximum rate constant method (▲); and (v) the corrected linear fit method (●).The Arrhenius plots for the original k_o values (calculated using the original maximum rate method (ii) that assumed the CO concentration profile proceeding the gas switch could be modelled as a step function) (×); and the Arrhenius plot constructed from the intrinsic rate constants k_i determined in the reference spouted fluidised bed experimental campaign (♦') are also included for comparison.

Table 5.5. Summary of the observed and intrinsic activation energies (Ea) and pre-exponential factors (Ao) derived from the Arrhenius plots of rate constants (Figure 6.24) estimated using the different methods outlined in Figure 6.23 for the temperature range 823-973 K.

Rate Constant, *k* at $X = 0$ Estimation Method		**E_a [kJ mol^{-1}]**	**ln(A_o) [m^3 s^{-1} g^{-1}]**	**ln(A_o) [s^{-1}]**	**R^2**
Method (ii)	k_o	27.63	-5.26	-19.55	0.99
(Original maximum *r'*)	**k_i**	**31.34**	**-4.73**	**-19.01**	**0.98**
Method (iii)	k_o	46.87	-2.29	-16.58	0.97
(Corrected maximum *r'*)	**k_i**	**54.08**	**-1.26**	**-15.54**	**0.99**
Method (iv)	k_o	32.83	-3.91	-18.20	0.98
(Corrected maximum *k*)	**k_i**	**36.92**	**-3.27**	**-17.55**	**0.98**
Method (v)	k_o	47.02	-1.88	-16.17	0.99
(Corrected linear fit)	**k_i**	**54.60**	**-0.77**	**-15.06**	**0.99**
Reference Case	k_o	50.91	-1.00	-15.29	1.00
	k_i	**55.82**	-0.53	**-14.82**	**0.99**

Figure 5.24 and table 5.5 show that using method (iii) (*i.e.* selecting the rate constant in the corrected rate vs conversion profile at the conversion for which the maximum rate was attained) to estimate the initial rate constant offers a much improved estimation of the effect of temperature (*i.e.* the E_a) on the rate of reaction. However, the lag period in the CO concentration profile reaching the set point meant that the maximum rate was observed at a higher conversion where the concentration normalised rate (*i.e.* the rate constant) had already started to deteriorate. As a consequence, the estimated rate constants at all temperatures were roughly 50% lower than those measured in the reference case giving a much lower pre-exponential factor.

Estimating the overall initial rate constant using method (iv) (*i.e.* the maximum rate constant method) provided a much improved estimation of the rate constants obtained in the reference case at the lowest temperature of 823 K. However, this method provided a poor estimation of the effect of temperature on the rate constant giving a similar activation energy value to the E_a, calculated using the rate constants derived from the original estimation method (ii) (table 5.5). For the temperature range that has been investigated so far, the maximum rate constant (in the corrected rate constant vs conversion plot) was reached at very low conversions < 0.06 when the concentration of CO was rising to the set point. A possible explanation for the worsening rate constant estimations with increasing temperature provided by method (iv) is that the observed rate during the initial stages of the reaction (when the CO concentration is low and rising to the set point) becomes increasingly limited by local depletion of reactants caused by the faster rate of reaction. There is also likely to be substantial error in the calculation of the rate constant during the initial stages of the reaction when the CO concentration is highly transient. This method was therefore deemed unsuitable.

The final method (v) (the corrected linear fit method) provided the most consistent estimates for the rate constants and E_a with the analogous reference case investigation in the spouted fluidised bed reactor. The calculated intrinsic activation energy and pre-exponential constant were within the experimental error calculated in the reference case. This method used rate constant data calculated for the conversion range of between $\sim X = 0.2\text{-}0.6$ where the concentration was more stable and after the initial stages where mass transfer limitations may have impeded the observed rate. This method was deemed most suitable and used for all future estimations of rate constants at $X = 0$. It should be noted that as with the original linear fit method (i) for estimating the k_o at $X = 0$, this method assumes that the reaction is surface reaction controlled with all of the reactive surface area exposed at the beginning of the reaction such that the rate (and rate constant) decays linearly with increasing conversion (or decreasing reactive surface).

5.4.4 Particle Model Assumption Validation

There are a number of assumptions (outlined previously in section 5.3 (1-5)) that have to be made in order to derive the intrinsic kinetic information from the observed kinetic data using the simple gas-solid reaction in a porous particle model with simultaneous reaction and mass transport. The following section provides descriptions of how some of the assumptions were empirically or theoretically tested. The numbering of the sections below is consistent with the numbering by which the assumptions were ordered in section 5.3.

(1) The particle is spherical in shape

The assumption that the oxygen carrier particles were spherical is possibly the easiest to test as it can be done through visual inspection of the low magnification SEM images of the different oxygen carriers prepared in this work (fig. 5.15). Inspection of the SEM images of the different 100Fe and 60Fe40Al oxygen carrier particles prepared via the different methods shows that the spherical particle assumption is best for the oxygen carrier particles prepared via method ’S’, however it is acceptable for all the oxygen carrier particles prepared via the different methods in this study.

(3) The reaction system is isothermal

As mentioned previously in section 5.3.3, the temperature control of the TGA reaction chamber during the simulated CLC experiments was very accurate to the temperature set point with a precision of < ± 0.1 K (fig. 5.4(b)) indicating that the reaction chamber can be considered isothermal during the experiment.

To determine whether the isothermal assumption also holds true for the particle, an order of magnitude estimation of the Biot number (N_{Bi}) for a single spherical 100Fe particle of $R = 307$ µm (*i.e.* the largest particle size fraction used in this study 500-710 µm) in an isothermal fluid was calculated using equation 5.28.

$$N_{Bi} = \frac{hR}{3\lambda_e} \qquad \text{(Equation 5.28)}$$

Where h is the convective heat transfer coefficient of the fluid (either 3 vol.% CO, 15 vol.% CO_2, balance N_2, or 4 vol.% O_2 balance N_2), λ_e is the thermal conductivity of the solid (i.e. Fe_2O_3) and R/3 is the characteristic length for a sphere. The Biot number is a dimensionless number used in transient heat transfer analysis that gives the ratio of the internal conductive resistance to heat transfer within the solid particle and external convective resistance to heat transfer of the fluid at the surface of the particle. Here a value of 0.5 W m^{-1} K^{-1} was chosen as the average effective thermal conductivity of the particle (λ_e) based on the work of (Takegoshi et al., 1984) for a partially reduced Fe_2O_3 particle. The convective heat transfer coefficient of the fluid (h) was calculated from the Nussult number (Nu) calculation (eq. 5.29). Nu is another dimensionless number that gives the ratio of the convective and conductive heat transfer across the boundary of a solid particle in a fluid. Here, the limiting value for heat transfer from spheres at low Reynold's numbers (Re) of Nu=2 was used. This was considered a reasonable estimate of Nu given that the calculated value of Re was less than 1 for all conditions studied (table 5.6).

$$Nu = \frac{hd_p}{\lambda_{mix}} \qquad \text{(Equation 5.29)}$$

Where d_p is the diameter of the particle and λ_{mix} is the thermal conductivity of the fluid (calculated using the Chapman-Enskog model).

The Biot number estimations for the temperature range 773-1223 K revealed that in all cases $N_{Bi} < 0.06$. Since the condition of $N_{Bi} < 0.1$ is true, the particle can be considered as isothermal and can therefore be modelled using a simple lumped-capacitance model for transient heat transfer. Based on this assumption, it is possible to construct a simple heat balance to determine the extent of any temperature gradients that form within the particle as it reacts (eq. 5.30).

$$r' \Delta H^{\ominus}_{T_b} \frac{4}{3} \pi R^3 = h 4 \pi R^2 (T - T_b) \qquad \text{(Equation 5.30)}$$

Where *T* is the temperature of the particle, T_b is the temperature of the bulk fluid and $\Delta H^{\ominus}_{T_b}$ is the enthalpy of reaction at $T=T_b$. A summary of the calculated values for $(T - T_b)$ is presented in table 5.6 and shows that for all reduction conditions, the temperature gradients were < 5 K. This was not the case during oxidation.

Table 5.6. Parameters used for calculating the Biot number, N_{Bi}, for a spherical Fe_2O_3 particle (500-710 μm) during the reduction part of the simulated CLC cycle (3 vol.% CO, 15 vol.% CO_2, balance N_2).

T [K]	λ_{CO} **x 10²** [W m⁻¹ K⁻¹]	λ_{CO_2} **x 10²** [W m⁻¹ K⁻¹]	λ_{N_2} **x 10²** [W m⁻¹ K⁻¹]	λ_{mix} **x 10²** [W m⁻¹ K⁻¹]	h [W m⁻¹ K⁻¹]	λ_e [W m⁻¹ K⁻¹]	N_{Bi}
723	5.39	4.84	5.34	5.26	176.47	0.5	0.035
773	5.70	5.16	5.70	5.61	188.29	0.5	0.037
823	6.00	5.48	6.10	5.99	201.22	0.5	0.040
873	6.30	5.80	6.50	6.37	213.99	0.5	0.042
923	6.60	6.11	6.88	6.73	225.98	0.5	0.045
973	6.89	6.41	7.26	7.10	238.27	0.5	0.047
1023	7.24	6.71	7.64	7.46	250.54	0.5	0.050
1073	7.58	7.00	8.01	7.81	262.19	0.5	0.052
1123	8.12	7.28	8.37	8.17	274.18	0.5	0.054
1173	8.46	7.56	8.74	8.52	285.87	0.5	0.057
1223	8.87	7.83	9.11	8.87	297.68	0.5	0.059

(4) The rate of reaction is first order and irreversible

The full rate expression for the reduction of Fe_2O_3 to Fe_3O_4 by CO considering the reverse reaction is provided in equation 5.31.

$$r' = k\left(c_{CO} - \frac{c_{CO_2}}{K_p}\right)^n \quad \text{(Equation 5.31)}$$

Where k is the rate constant, $c_{CO_2}$is the concentration of CO_2 and K_p is the equilibrium constant. As illustrated by figure 5.x, the equilibrium constant for the reverse reaction i.e. $Fe_3O_4 \rightarrow Fe_2O_3$ is very large (i.e. > 1×10^4) for all conditions studied such that $K_p \gg c_{CO_2}$ and $\frac{c_{CO_2}}{K_p} \approx 0$. The rate expression can therefore be simplified to equation 5.32.

$$r' = k\,(c_{CO})^n \quad \text{(Equation 5.32)}$$

The rate expression given in equation 5.32 and assumption that the rate of reaction was first order with respect to the concentration of CO was tested by varying the inlet concentration of CO between 1-5 vol.% with a fixed CO_2 inlet concentration of 15 vol.%. at 823 K. Figure 5.25 presents the relationships between the maximum rates (r') and the inlet concentration of CO in logarithmic form for 100Fe and 60Fe40Al oxygen carriers prepared by the different methods (B, E and S). A strong linear relationship between r' and [CO] was observed for all the oxygen carriers tested here (*i.e.* $R^2 \geq 0.97$) confirming that r' can be expressed as a simple power function of the concentration of CO (*i.e.* equation 5.32). Plotting the initial rate, r', and inlet concentrations in their logarithmic forms also makes it is possible to derive the order of reaction from the gradient of the lines of best fit i.e. $ln\,(r') = ln(k_{C_{CO}\rightarrow 0}) + nln(c_{CO})$ (where $ln(k_{C_{CO}\rightarrow 0})$ refers to the theoretical value of k' as [CO] →0. The gradients of all the lines of best fit in figure 5.25 were between 0.86 and 1.10 indicating that the assumption that the reduction is first order with respect to the concentration of CO (*i.e.* n=1) was reasonable. The effectiveness factor in all cases were found to be > 0.97 for the temperature range studied.

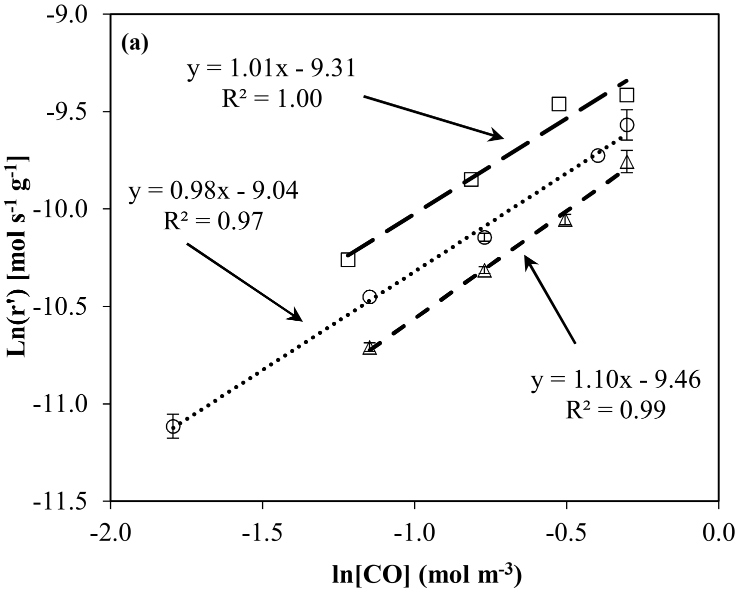

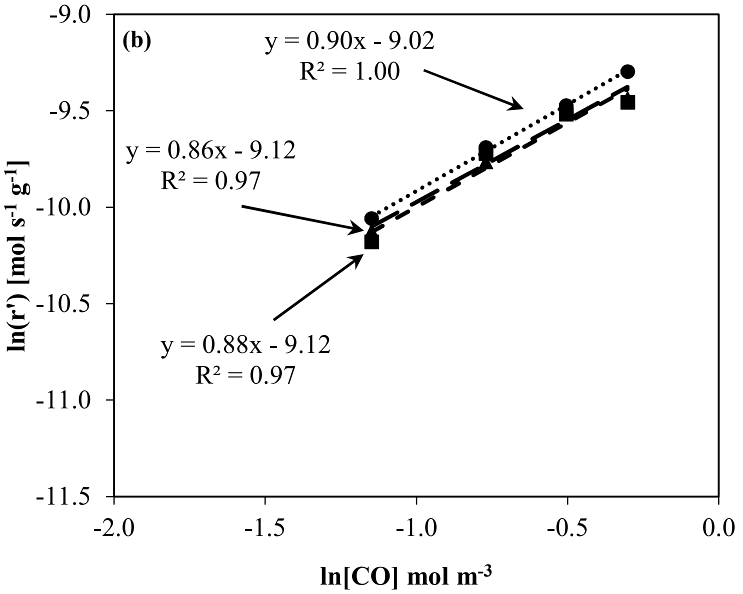

Figure 5.25. Dependence of initial rate (r') on the inlet concentration of CO (1-5 vol.%) for (a) 100Fe oxygen carrier particles and (b) 60Fe40Al oxygen carrier particles prepared via the different methods (B, E and S): 100Fe(S) ○; 100Fe(E) □; 100Fe(B) △ with the filled symbols in (b) representing the analogous 60Fe40Al particles.

Experimental parameters: **Reactor:** TGA; **Oxygen Carrier**: Variable; **Sample Mass:** 2 mg; **Particle Size Fraction:** 150-212 μm; **Reaction:** $Fe_2O_3 \rightarrow Fe_3O_4$**; Temperature**: 823 K; **Reducing gas composition**: 1-5 vol.% CO, 15 vol.% CO_2, balance N_2; **Oxidising gas composition**: 4 vol.% O_2, balance N_2; **Total Flow Rate**: 80 ml min^{-1}; **Cycle Number**: 3.

5.4.5 Effect of Fabrication Technique and the addition of 40 wt.% Al_2O_3 as a support on the reduction kinetics of Fe_2O_3 to Fe_3O_4

The reduction kinetics ($Fe_2O_3 \rightarrow Fe_3O_4$) for pure iron oxide (100Fe) and 60wt.% Fe_2O_3 supported with 40 wt.% Al_2O_3 (60Fe40Al) OC particles, prepared via the three different methods (B, E and S described in section 5.2.1) were investigated in the TGA with 3 vol.% CO, 15 vol.% CO_2, balance N_2 at temperatures ranging from 773-973 K. The Arrhenius plots (fig. 5.26 (a-b)) show that the fabrication technique had a dramatic influence on the reactivity of the pure iron oxide oxygen carrier particles. The 100Fe(E) OC particles (prepared using the extruder to control the particle size) were significantly more reactive than the equivalent oxygen carrier particles prepared via methods S and B. The intrinsic rate constants k_i (per unit mass *i.e.* in units of $m^3\ s^{-1}\ g^{-1}$) for the 100Fe(E) particles were between 3 and 4 times larger than the intrinsic rate constants measured for the 100Fe(B) and 100Fe(S) particles at all the temperatures studied. The 100Fe(E) OC particles also exhibited the highest activation energy of 63 ± 16 kJ mol^{-1} although it was within the error range of the 100Fe(S) OC particles where the intrinsic activation energy was found to be 59 ± 8 kJ mol^{-1}. The 100Fe(B) OC particles demonstrated the second highest reactivity at the lower temperature range, but displayed the lowest activation energy such that the reactivity approached that of the 100Fe(S) OC particles as the temperature approached 973 K.

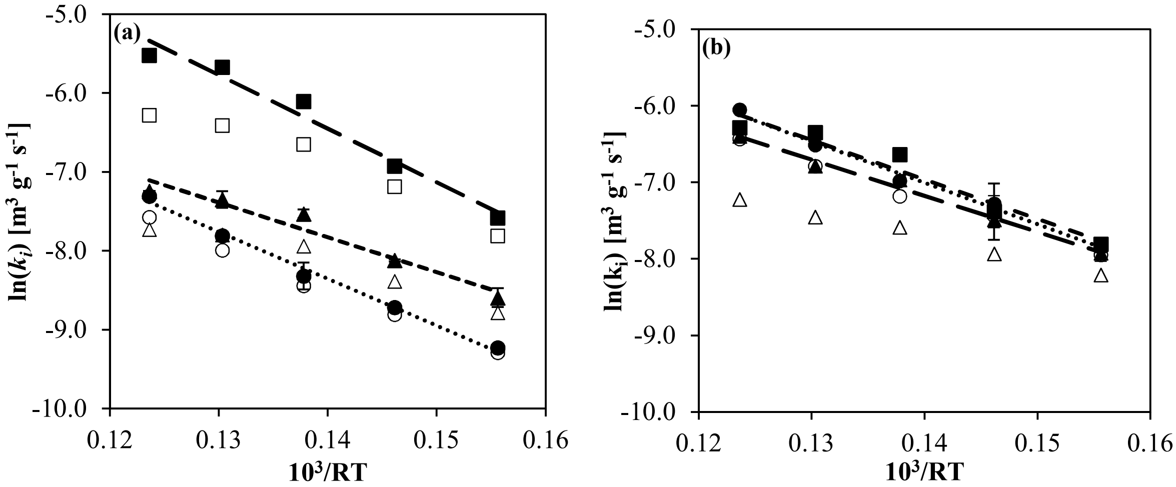

Figure 5.26. Arrhenius plot for the overall rate constants, k_o (open symbols) and intrinsic rate constants, k_i (solid symbols) for the reduction of (a) 100 wt.% Fe_2O_3 oxygen carrier particles and (b) 60 wt.% Fe_2O_3 supported with 40wt.% Al_2O_3 oxygen carrier particles prepared via the different fabrication methods: method B (△); method E (□); and method S (○). **Experimental parameters: Reactor:** TGA; **Oxygen Carrier**: Variable; **Sample Mass:** 2 mg; **Particle Size Fraction:** 150-212 μm; **Reaction:** $Fe_2O_3 \rightarrow Fe_3O_4$; **Temperature**: 773-973 K; **Reducing gas composition**: 3 vol.% CO, 15 vol.% CO_2, balance N_2; **Oxidising gas composition**: 4 vol.% O_2, balance N_2; **Total Flow Rate**: 80 ml min^{-1}; **Cycle Number**: 3.

Table 5.7. Summary of the overall and intrinsic activation energies (E_a) and pre-exponential factors (A_o) derived from the Arrhenius plots of rate constants (fig. 6.26) for the reduction of 100Fe and 60Fe40Al oxygen carrier particles ($Fe_2O_3 \rightarrow Fe_3O_4$) prepared via the different methods (B,E and S) at 773-973 K. R^2 is the coefficient of determination for the line of best fit used to determine the E_a and ln(A_o) from the Arhenius plots (fig. 6.26) via least squares linear regression analysis. Errors for the E_a (Arrhenius plot gradient) and ln(A_o) (Arrhenius plot intercept) were derived using a student statistical t-test (STUDENT, 1908) with a 90 % confidence interval.

Oxygen Carrier Particle		**E_a [kJ mol^{-1}]**	**ln(A_o) [m^3 g^{-1} s^{-1}]**	**ln(A_o) [s^{-1}]**	**R^2**
100Fe(B)	$\boldsymbol{k_i}$	41 ± 10	−2.2 ± 0.3	−16.9 ± 0.3	0.95
	k_o	34 ± 7	−3.4 ± 0.3	−18.4 ± 0.3	0.94
100Fe(E)	$\boldsymbol{k_i}$	63 ± 16	2.4 ± 0.6	−11.6 ± 0.6	0.96
	k_o	48 ± 13	−0.1 ± 0.5	−15.2 ± 0.5	0.96
100Fe(S)	$\boldsymbol{k_i}$	59 ± 8	0.4 ± 0.3	−13.9 ± 0.3	0.99
	k_o	53 ± 7	−0.6 ± 0.3	−15.6 ± 0.2	0.98
60Fe40Al(B)	$\boldsymbol{k_i}$	40 ± 7	−1.8 ± 0.3	−15.3 ± 0.3	0.99
	k_o	31 ± 6	−3.4 ± 0.3	−16.8 ± 0.3	0.99
60Fe40Al(E)	$\boldsymbol{k_i}$	46 ± 19	−0.6 ± 0.8	−14.7 ± 0.8	0.94
	k_o	41 ± 16	−1.3 ± 0.7	−15.4 ± 0.7	0.94
60Fe40Al(S)	$\boldsymbol{k_i}$	54 ± 6	0.6 ± 0.3	−13.4 ± 0.3	0.98
	k_o	46 ± 6	−0.8 ± 0.3	−14.8 ± 0.3	0.98

The addition of 40wt.% Al_2O_3 improved the reactivity of the OC particles prepared via methods S and B (per unit mass of Fe_2O_3) across all the temperatures studied (fig. 5.26, table 5.7). The opposite trend was observed for the 60Fe(E) particles, which were found to be less reactive than the equivalent 100Fe(E) particles, particularly at the higher temperatures due to the lower E_a derived for the 60Fe(E) OC of 46 ± 19 kJ mol^{-1} compared with 63 ± 16 kJ mol^{-1}. The addition of 40 wt.% Al_2O_3 appeared to reduce the influence of the preparation technique on the reactivity of the OC particles compared with the trends observed for 100Fe OC particles. In all cases the calculated intrinsic activation energies for the reduction of Fe_2O_3 to Fe_3O_4 were slightly lower than the activation energies calculated for their 100Fe counterparts (produced via the same method).

The intrinsic activation energies for the reduction of the 100Fe particles prepared via the different fabrication methods correlates well with the surface area and volume of pores measured via MIP. The higher intrinsic rate constant measured for the 100Fe(B) compared with the more porous and higher surface area 100Fe(S) (particularly at the lower temperature range) is unusual however it should be noted that the surface area and porosity measurements used here were determined for the fresh unreacted particle. It was not possible to perform any meaningful analysis of the sample after the experiments were completed due to the very small amount of sample that was used. It is well known that the oxygen carriers undergo significant morphological changes when they are reacted at high temperatures in a CLC process leading to dramatic changes in the surface area, porosity and pore size distribution. Some additional error in the kinetic information calculated here is therefore likely owing to discrepancies in the morphological measurements of the fresh unreacted particles used here and the actual morphological measurements of the reacted particles that could not be quantified in this study.

It should also be noted that the tortuosity factor used to determine the intrinsic rate constants were determined by varying the size fraction (150-212 μm, 300-425 μm and 500-710 μm) of the 100Fe(S) and 60Fe(S) OC particles only. The derived tortuosity factor for the 100Fe(S) and 60Fe(S) OC particles were then applied to determine the intrinsic rate constants for the other 100Fe and 60Fe particles respectively. Furthermore, the low temperature and relatively small particle size fractions used (< 710 μm) meant that the calculated effectiveness factors η across all particle size fractions was high (> 0.97 and > 0.99 for 100Fe(S) and 60Fe(S) OC particles respectively). The description of mass transfer effects provided by the experiments carried out here was therefore limited and almost certainly provided an under estimate of the tortuosity factor ($\tau = 0.5$ and $\tau = 5 \times 10^{-7}$ for 100Fe(S) and 60Fe(S) OC particles respectively) given that both values are < 1 which is the lower limit for what is physically possible (i.e. $\tau = 1$ for a straight cylindrical channel with no tortuosity). The unphysically low tortuosity factors calculated here were likely due to the fact that the effectiveness factors were high, and the tortuosity is the only parameter adjusted to make particles of different diameters have the same effective rate constant, the calculation is highly open to error.

As a consequence, it is not possible to comment in any great detail on the differences in the E_a and A_o reported here at this time. Further work is necessary to determine tortuosity factors for each type of particle individually across a wider range of particle size fractions and/or at higher temperatures where mass transfer effects are likely to contribute more significantly to the observed kinetic information.

5.4.6 Effect of elevated temperatures up to 1223 K on the reduction kinetics of Fe_2O_3 to Fe_3O_4 for the 100Fe(S) and 60Fe40Al(S) OC particles

Some additional experiments were carried out to assess the reduction kinetics (Fe_2O_3 to Fe_3O_4) of the 100Fe(S) and 60Fe40Al(S) OC particles at elevated temperatures of 973-1223 K that are more comparable to the sorts of temperatures the OC particles would be exposed to in a commercial CLC system. As illustrated in the Arrhenius plot presented in figure 5.27, the increasing linear trend in ln (k_i) with increasing temperatures is observed up to 1123 K for the 100Fe(S) OC particles and 1173 K for the 60Fe40Al(S) OC particles. Above these temperature limits the trend in the intrinsic rate constants reverses and starts to decrease with increasing temperature.

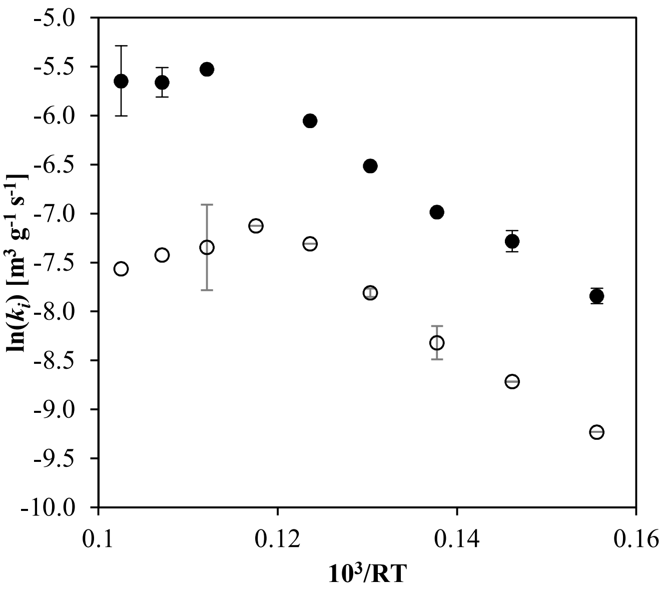

Figure 5.27. Arrhenius plot for intrinsic rate constants, k_i (solid symbols) for the reduction of 100 Fe(S) oxygen carrier particles (open symbols) and 60Fe40Al(S) oxygen carrier particles (closed symbols). **Experimental parameters: Reactor:** TGA; **Oxygen Carrier**: Variable; **Sample Mass:** 2 mg; **Particle Size Fraction:** 150-212 µm; **Reaction:** $Fe_2O_3 \rightarrow Fe_3O_4$**;** **Temperature**: 773-1023 K; **Reducing gas composition**: 3 vol.% CO, 15 vol.% CO_2, balance N_2; **Oxidising gas composition**: 4 vol.% O_2, balance N_2; **Total Flow Rate**: 80 ml min^{-1}; **Cycle Number**: 3.

The decreasing trend in the intrinsic rate constant with increasing temperature above 1073-1123 K and 1173 K for the 100Fe(S) and 60Fe40Al(S) OC particles respectively is most likely due to enhanced thermal sintering at the higher temperatures. Thermal sintering is the thermal softening and coalescing of the iron oxide grains which results in a loss of fine surface structure and total surface area; loss of porosity; and pore growth causing a shift in the pore size distribution from smaller pores (micro- and meso-pores) to larger macro-pores. Sintering processes are enhanced by the morphological changes that the particle undergoes as it reacts (reactive sintering). Sintering becomes more prominent at temperatures above the Tammann temperature of the material, defined as the temperature at which the mobility and reactivity of molecules within a solid matrix becomes appreciable and is approximately equal to half the absolute melting temperature of the material (Ertl et al., 2008). The Tammann temperatures for Fe_2O_3, Fe_3O_4 and Al_2O_3 are ~ 920 K, ~935 K and ~1173 K (calculated using $T_{Tammann} = 0.5T_m$ where T_m is the melting point of the metal oxide). The temperature at which the intrinsic rate constants start to decrease with increasing temperature for the reduction of the 100Fe(S) particle is above the $T_{Tammann}$ of both Fe_2O_3 and Fe_3O_4.

The improved thermal stability of the 60Fe40Al(S) particle relative to the 100Fe(S) oxygen particle is most likely due to Al_2O_3 grains acting as a barrier/spacer between the Fe_2O_3/Fe_3O_4 grains limiting the sintering processes and therefore helping to maintain the surface area and porous morphology of the

OC particle. Al_2O_3 is also more thermally stable than the Fe_2O_3 and Fe_3O_4 with a $T_{Tammann}$ of ~ 1173 K inferring that significant sintering of the Al_2O_3 phase is unlikely at the temperature range studied here.

5.4.7 The influence of Al_2O_3 precursor on the reactivity of the reactivity of a 60 wt.% Fe_2O_3/ 40 wt.% Al_2O_3 oxygen carrier material

It is clear from initial inspection of the Arrhenius plot of the different 60Fe40Al OC particles investigated in this study that the Al_2O_3 precursor material had a dramatic effect of the intrinsic reduction kinetics (fig. 5.28). The 60Fe40Al(SPN) and 60Fe40Al(SPS) OC materials were the most reactive at the lower temperature range but the effect of temperature on the measured and intrinsic kinetics was low giving very low activation energies of 15 ± 4 kJ mol^{-1} and 18 ± 5 kJ mol^{-1}. The similarities in the reduction kinetics demonstrated by the 60Fe40Al(SPN) and 60Fe40Al(SPS) was to be expected given that the Al_2O_3 precursor materials were similar (both versions of Al(OH)O) and the fresh particles were morphologically very similar exhibiting very similar surface areas, porosities and pore size distributions (table 5.3). In both cases, there was some deviation from the linear trend observed in the Arrhenius plots but unlike the trends observed for the 100Fe(S) and 60Fe40Al(S) OC materials, there was no noticeable deterioration in the reduction kinetics at the higher temperature as a result of thermal sintering.

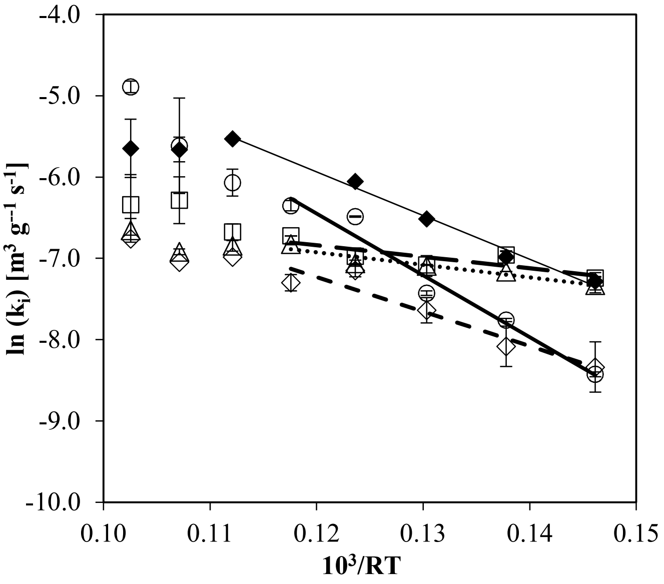

Figure 5.28. Arrhenius plot of intrinsic rate constants, k_i for the reduction of the different 60Fe40Al oxygen carrier materials prepared using the different Al_2O_3 precursors: 60Fe40Al(SAC) (◇); 60Fe40Al(SAB) (○); 60Fe40Al(SPN) (△); 60Fe40Al(SPS) (□); and 60Fe40Al(S) (◆). **Experimental parameters: Reactor:** TGA; **Oxygen Carrier**: Variable; **Sample Mass:** 2 mg; **Particle Size Fraction:** 150-212 µm; **Reaction:** $Fe_2O_3 \rightarrow Fe_3O_4$**;** **Temperature**: 823-1173 K; **Reducing gas composition**: 3 vol.% CO, 15 vol.% CO_2, balance N_2; **Oxidising gas composition**: 4 vol.% O_2, balance N_2; **Total Flow Rate**: 80 ml min^{-1}; **Cycle Number**: 3.

The 60Fe40Al(SAB) was the least reactive at the lower temperature but demonstrated the highest activation energy such that it was the most reactive (highest rate constants) at temperatures > 973 K (not including the 60Fe40Al(S) which was prepared using a lower sintering temperature such that direct comparison is not possible). The 60Fe40Al(SAB) OC material also demonstrated the highest thermal stability with the rate constants observing a roughly linearly increasing temperature across the entire temperature range studied up to 1123 K.

The 60Fe40Al(SAC) was the least reactive of the OC materials investigated here at the lower temperature range. However, the more substantial effect of temperature on the reduction kinetics ($E_{a,i}$ = 43 ± 4 kJ mol^{-1}) compared with the 60Fe40Al(SPN) and 60Fe40Al(SPS) OC materials, meant that the kinetic measurements approached those obtained for the 60Fe40Al(SPN) and 60Fe40Al(SPS) OC materials at the higher temperature region > 1073 K. The 60Fe40Al(SAC) exhibited a substantially lower reactivity compared with the 60Fe40Al(S) OC material (*i.e.* the same material but sintered at 1173 K compared with 1273 K). This behaviour is most likely due to the lower available surface area on which reactions could take place and lower porosity of the 60Fe40Al(SAC). The lower surface area and porosity was most likely caused by the greater extent of sintering that took place during the sintering step of the preparation at the higher temperature of 1273 K.

Based on morphological measurements of the fresh OC materials, one would expect that the 60Fe40Al(SAB) OC material to exhibit the highest reactivity due to its highest surface area and highest porosity. Whilst this is true at the higher temperature range, it was not the case at the lower temperature range < 973 K. Trends in the order of reactivities and intrinsic activation energies of the other OC materials are also difficult to identity and explain showing no clear trend between the measured morphological measurements. As mentioned previously, the analysis presented here is limited by the fact that morphological measurements of the reacted material could not be obtained. It is therefore possible that the morphological trends observed for the fresh, unreacted materials were different for the reacted materials.

At temperatures < 973-1023 K the Arrhenius relationships for the 60Fe40Al OC materials deviates slightly from the linear trend observed at the lower temperatures 823-973 K. However unlike the 100Fe(S) OC particles, there is no significant deterioration in the OC reactivity with increasing temperature. In fact the effect of temperature on the intrinsic rate constants appears to have increased in the case of the 60Fe40Al(SAB) and 60Fe40Al(SPS) OC materials giving rise to respectively higher intrinsic activation energies of 123 kJ.mol^{-1} and 36 kJ.mol^{-1} for the temperature range 1073-1173 K compared with 75 kJ.mol^{-1} and 14 kJ.mol^{-1} for the lower temperature range 823-1023 K.

Table 5.8. Summary of the overall and intrinsic activation energies (E_a) and pre-exponential factors (A_o) derived from the Arrhenius plots of rate constants (fig. 5.28) for the reduction of 100Fe and 60Fe40Al oxygen carrier particles ($Fe_2O_3 \rightarrow Fe_3O_4$) prepared from the different Al_2O_3 precursor materials at 823-1073 K. R^2 is the coefficient of determination for the line of best fit used to determine the E_a and ln(A_o) from the Arhenius plots (fig. 5.28) via least squares linear regression analysis. Errors for the E_a (Arrhenius plot gradient) and ln(A_o) (Arrhenius plot intercept) were derived using a student statistical t-test (STUDENT, 1908) with a 90 % confidence interval.

Oxygen Carrier Particle		**E_a [kJ.mol^{-1}]**	**ln(A_o) [m^3.g^{-1}.s^{-1}]**	**ln(A_o) [s^{-1}]**	**R^2**
60Fe40Al(SAC)	k_i	43 ± 9	-0.7 ± 0.4	-15.3 ± 0.4	0.97
	k_o	42 ± 8	-1.3 ± 0.4	-15.9 ± 0.4	0.98
60Fe40Al(SAB)	k_i	72 ± 8	2.1 ± 0.4	-12.5 ± 0.4	0.97
	k_o	67 ± 7	1.4 ± 0.4	-13.2 ± 0.4	0.97
60Fe40Al(SPN)	k_i	15 ± 4	-5.2 ± 0.3	-19.8 ± 0.3	0.93
	k_o	14 ± 3	-5.4 ± 0.3	-20.0 ± 0.3	0.94
60Fe40Al(SPS)	k_i	18 ± 5	-4.7 ± 0.3	-19.3 ± 0.	0.92
	k_o	17 ± 4	-5.0 ± 0.2	-19.6 ± 0.2	0.93
60Fe40Al(S)*	k_i	54 ± 9	0.5 ± 0.6	-14.1 ± 0.6	0.99
	k_o	43 ± 8	-1.2 ± 0.5	-15.8 ± 0.5	0.99
100Fe(S)$^+$	k_i	59 ± 5	-0.1 ± 0.3	-14.7 ± 0.3	0.99
	k_o	51 ± 4	-1.3 ± 0.2	-15.9 ± 0.2	0.99

*The kinetic values for the 60Fe40Al(S) OC particles presented in this table have been re-calculated for temperature range 823-1023 K so that comparisons can be made with the other the kinetic information for the other 60Fe40Al particles presented in this table.

$^+$ The kinetic values for the 100Fe(S) oxygen carrier has also been recalculated for the temperature range 823-1023 K. A lower upper temperature limit was used for the 100Fe(S) particle due to the onset of sintering that significantly affected the measured rate constant at the 1173 K causing substantial deviation from the linear trend observed in the Arrhenius plot.

The deviation in the Arrhenius relationships at temperatures < 823-973 K was accompanied by an increase in the final conversion extent (ΔX) for the reduction of Fe_2O_3 to Fe_3O_4 with increasing temperature (fig. 5.29)). Final conversion extents were greater than the theoretical maximum (for Fe_2O_3 to Fe_3O_4) across the entire temperature range studied but at the lower temperature range of 823-973 K the final conversion measurements remained stable at $\Delta X = 1\text{-}1.1$. At temperatures above 973 K, the final conversions reached by the 60Fe40Al OCs increased with increasing temperature to $\Delta X = 1.4\text{-}1.7$.

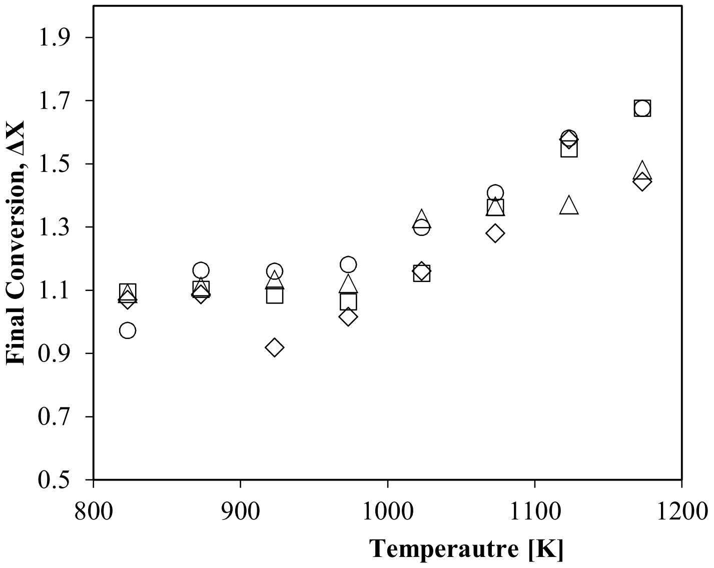

Figure 5.29. Plot of final conversion as a function of experimental temperature for the reduction of the different 60Fe40Al oxygen carrier particles prepared from the different Al_2O_3 precursor materials. 60Fe40Al(SAC) (◇); 60Fe40Al(SAB) (○); 60Fe40Al(SPN) (△) and 60Fe40Al(SPS) (□). <u>**Experimental parameters**</u>: **Reactor:** TGA; **Oxygen Carrier**: Variable; **Sample Mass:** 2 mg; **Particle Size Fraction:** 150-212 μm; **Reaction:** $Fe_2O_3 \rightarrow Fe_3O_4$; **Temperature**: 823-1173 K; **Reducing gas composition**: 3 vol.% CO, 15 vol.% CO_2, balance N_2; **Oxidising gas composition**: 4 vol.% O_2, balance N_2; **Total Flow Rate**: 80 ml min^{-1}; **Cycle Number**: 3.

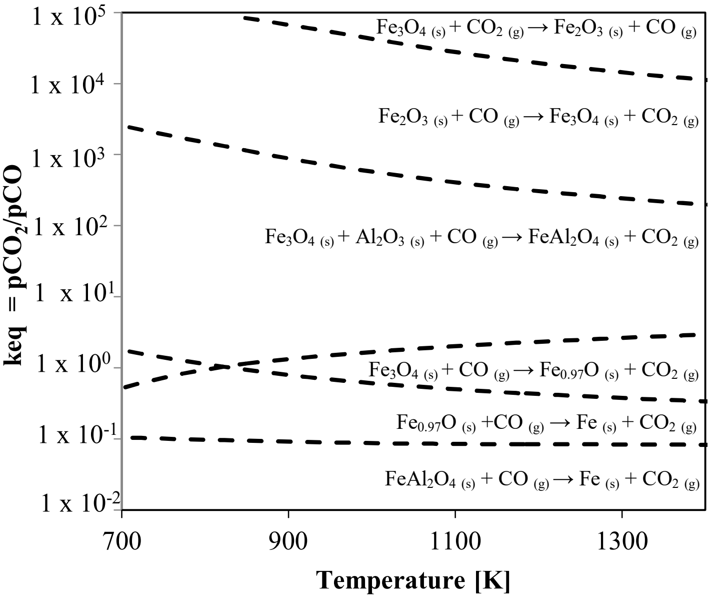

Figure 5.30. Equilibrium diagram for the reaction of Fe_2O_3 with CO in the presence of Al_2O_3. The data was calculated using Factsage (a thermodynamic modelling software) that calculates equilibrium constants based on a minimisation of Gibbs free energy approach.

A likely explanation for the observed change in the Arrhenius relationship and conversion extents is that the presence of Al_2O_3 facilitated the reduction of Fe_3O_4 further to Fe^{II} through the formation of the $FeAl_2O_4$ spinel phase. Figure 5.30 illustrates that the formation of $FeAl_2O_4$ spinel phase is thermodynamically possible across the entire range of conditions used in this study. The reaction of Fe_3O_4 with Al_2O_3 and CO involves a solid state reaction which is likely to have been inhibited by slow reaction kinetics at the lower temperature range. However, as the temperature was increased above 973 K (*i.e.* above the Fe_3O_4 $T_{Tammann}$ of 935 K), the mobility of the Fe ions becomes more pronounced leading to substantial improvements in the rate of $FeAl_2O_4$ formation with increasing temperature, contributing to the increasing trend in conversion extent with increasing temperature above 973 K. It was also interesting that the OC materials that exhibited the largest conversion extents (i.e. 60Fe40Al(SAB)) and 60Fe40Al(SPS)) also demonstrated the highest reactivity at temperatures > 973 K. These findings indicate that the formation of $FeAl_2O_4$ spinel phase was favourable, helping to preserve and possibly even enhance the reactivates of the OC materials at the higher temperatures. Furthermore, reduction of Fe_2O_3 to FeO (in the form of $FeAl_2O_4$) considerably increases the oxygen carrying capacity of the material by a factor of three.

5.5 Conclusions

A range of pure Fe_2O_3 and 40 wt.% Al_2O_3 supported Fe_2O_3 (60 wt.%) oxygen carrier materials were prepared via three variants on a wet granulation process. The synthesised OC materials were subjected to a rigorous testing protocol to assess their physical and chemical properties. A particle model based on the concept of effectiveness factor was used to calculate the intrinsic kinetic information from the kinetic measurements obtained in the TGA. The intrinsic kinetic information calculated from the kinetic measurements obtained from the TGA were in very close agreement with the intrinsic kinetic data calculated from measurements obtained from a reference case small fluidised bed reactor. Activation energies for a pure iron oxide materials tested in the TGA and the reference case fluidised bed reactor were 59 ± 8 kJ mol^{-1} and 55 ± 13 kJ mol^{-1} respectively.

The fabrication technique was found to have a significant effect on the morphological properties (surface area, porosity, pore size distribution) and reactivity of the OC particles particularly in the case of the pure iron oxide OC materials. Pure iron oxide OC particles prepared using method E was the most reactive across the temperature range studied (773-973 K). The pure iron oxide particle prepared via method S was the least reactive particle at the lower end of the temperature range but exhibited a higher activation energy such that its reactivity at 973 K was similar to that of the pure iron oxide OC prepared via method B. The trend in activation energies and reactivity at 973 K roughly correlated with the surface area and volume of pores between $5\text{-}10^4$ nm in diameter as measured by MIP.

The addition of 40 wt.% α-Al_2O_3 as a support for the Fe_2O_3 OC caused a shift in the pore size distribution to a slightly larger pore size but the surface areas and total volume of pores in the pore size range $5\text{-}10^5$ µm were slightly lower compared with the pure iron oxide OC materials prepared via the same method. The crushing strength of the material was also reduced by the addition of Al_2O_3 but all particles tested in this study exhibited adequate mechanical strength for use in large scale circulating fluidised bed systems.

Despite the lower surface area and total volume of pores, the α-Al_2O_3 supported iron oxide OC materials prepared via methods B and S were more reactive than the equivalent pure iron oxide materials. The reactivity of the α-Al_2O_3 supported iron oxide OC material prepared via method E was slightly lower than its pure iron oxide counterpart. The effect of fabrication technique on the 40 wt.% Al_2O_3 supported Fe_2O_3 was much less than observed for the pure iron oxide OC materials. Activation energies for the reduction of Fe_2O_3 to Fe_3O_4 in the supported iron oxide materials were slightly lower than the activation energies calculated for the equivalent pure iron oxide materials but were within the calculated error ranges.

The Al_2O_3 precursor material used to prepare a 40 wt.% Al_2O_3 supported iron oxide OC material also influenced the morphology and reactivity of the OC material. The use of an $Al(OH)_3$ alumina precursor created an OC particle with a substantially larger surface area and volume of pores. The use of Al(OH)O also improved the surface area and volume of pores relative to the α-Al_2O_3 supported Fe_2O_3 OC particle but to a lesser extent compared with the particle prepared from the $Al(OH)_3$ precursor. There was significant variation in the activation energies calculated for the Al_2O_3 supported Fe_2O_3 OC materials prepared from the different Al_2O_3 precursors. The Al_2O_3 supported Fe_2O_3 prepared from the $Al(OH)_3$ precursor exhibited highest activation energy of 72 ± 8 kJ mol^{-1} calculated from the rate constants obtained over the temperature range 823-1023 K. The activation energies determined for the materials prepared from the Al(OH)O were substantially lower at 15 ± 4 kJ mol^{-1} and 18 ± 5 kJ mol^{-1}. The activation energy for the Al_2O_3 supported Fe_2O_3 prepared from the α-Al_2O_3 precursor was 43 ± 9 kJ mol^{-1}. There was no obvious correlation between the reactivities and activation energies for the different Al_2O_3 supported Fe_2O_3 particles and the respective morphological measurements taken for the fresh unreacted particles. Further work is necessary to establish how the morphology of the different particles changes during the reaction to establish whether there were correlations between the measured reactivities and the morphologies of the reacted OC materials. It is also possible that interactions with the Al_2O_3 support may also have had an effect on the reactivities of the supported OC materials.

Investigation of the reactivity of the different OC materials at temperatures > 973 K revealed that the addition of Al_2O_3 improved the thermal stability of the OC material compared with the pure iron oxide OC material. The supported iron oxide materials also achieved final conversions greater than the maximum theoretical conversion for the reduction of Fe_2O_3 to Fe_3O_4. Conversion extents for all of the Al_2O_3 supported Fe_2O_3 OC materials were relatively constant and were between 1.0 and 1.1 but increased with increasing temperature above ~ 973 K up to 1.4-1.7 at 173 K. A related deviation in the linear trend observed in the Arrhenius relationship was also observed above 973 K. This behaviour was attributed to the further reduction of Fe_3O_4 to $FeAl_2O_4$ which involved a solid state reaction and became more pronounced above the Tammann temperature of Fe_3O_4. In the case of the Al_2O_3 material prepared from the $Al(OH)_3$ precursor material and one of the Al(OH)O precursor materials tested in this work, the calculated activation energies were higher for the higher temperature range of 973-1173 K compared with the activation energies measured at the lower temperature range of 823-973 K. If the proposed theory is correct, it would indicate that the formation of $FeAl_2O_4$ is beneficial acting to enhance the thermal stability, reactivity and oxygen transfer capacity of the iron oxide based oxygen carrier material.

Chapter 6

Investigations into the Effects of Volatile Biomass Pyrolysis Products on the Performance of Fe-based CLC Oxygen Carrier Materials

6.1 Introduction

The development of a CLC process utilising biomass is of particular interest as it has the potential to result in negative CO_2 emissions *i.e.* a net removal of CO_2 from the atmosphere. Most CLC research has focused on gaseous fuels and extended pilot scale trials have demonstrated the feasibility of natural gas CLC for large scale power generation (Lyngfelt, 2011). CLC using solid fuels or gasified solid fuels is more complex and less well understood as larger amounts of contaminants are introduced into the system such as light hydrocarbons, tar vapours, alkali compound vapours, sulfur and nitrogen containing species and ash. The presence of these impurities could be of significant detriment to the reactivity and lifetime of the OC and overall process efficiency, however back in 2009-2010 when this research project was conceived; very little research had been published in this area. Tar formation is of particular concern as it is difficult to combust and can lead to reduced fuel conversion efficiencies (Mendiara *et al*., 2011). In addition, decomposition of the tars on the surface of the OC can result in severe coking and temporary deactivation. Coking of the OC also limits the overall CO_2 capture efficiency of the process as regeneration of the OC in air produces CO_2 which cannot be captured (Corbella *et al.,* 2005).

Over the past few years, the use of biomass as a fuel for CLC has steadily gained interest. A few research groups have now tested the use of biomass in interconnected dual fluidized bed CLC systems with in-situ gasification of the biomass(Shen et al., 2009, Thunman et al., 2013). Mendiara et al. (2013) studied the CLC of sawdust in a 500 kW_{th} interconnected fluidised bed CLC unit with hematite as the oxygen carrier. They managed to achieve carbon capture efficiencies of > 95 % at temperatures between 880-915 ˚C using both steam and CO_2 as the gasifying agent in the fuel reactor. The tar content of the gas stream exiting the fuel reactor was found to be between 1.38 and 0.2 g/Nm^3 which was deemed above pipeline entry specifications such that additional gas conditions steps would be required. Despite this, the tar destruction efficiency of the CLC process using hematite as the OC material was found to be approximately 5 times greater than the efficiency reported for a sawdust gasification experiment run in a fluidised bed reactor using an Fe/olivine tar cracking catalyst. The authors attribute the improved tar cracking efficiency of the CLC process to the ability of the hematite to react with tars rather than solely acting as a catalyst. Analysis of the light tar species was achieved via online GC equipped with a TCD detector. The main component of the tars was found to be napthalenes.

The majority of research interest involving biomass and chemical-looping has been directed at the development of a bio-syngas upgrading/tar removal system based on the chemical-looping concept (Huang et al., 2013, Luo et al., 2013, Keller et al., 2014). Larsson et al. (2014) studied the use of ilmenite as a tar cracking 'catalyst'[3] for the upgrading of a bio-syngas produced from gasification of a woody biomass. The upgrading process was carried out in the 2-4 MW_{th} interconnected fluized bed system at Chalmers University of Technology, Sweden. The authors found that adding small amounts of ilmenite to a solids inventory of sand reduced to tar yield by ~ 50 wt.% but at the detriment of the chemical conversion efficiency of the gasification process. The cold gas efficiency was reduced by 10 percentage points when 12 wt.% ilmenite was added into the process. A similar earlier study in the same reactor found that ilmenite was less effective resulting in a reduction in the amount of tars exiting the process of 35 % for a residence time of 0.4-0.5 s with a raw gas feed containing 30 g/Nm^3 of tar (Lind et al., 2011). The resulting (detectable) tar species were found to consist of predominantly of stable ring structures such as benzenes and napthalenes.

Lind et al. (2013) compared the tar cracking capabilities of ilmenite and a synthetic Al_2O_3 supported NiO OC material in a CLR process. They found that the Ni-based OC material was superior resulting in a 95 % reduction in the tar content of the outlet gas compared with 60 % for the ilmentite catalyst at 880 ˚C and 850 ˚C respectively. Both materials were affected by small amounts of carbon deposition but no lasting effects on the reactivity after regeneration in the air reactor were observed. Carbon deposition was kept low (< 0.25 %) by maintaining a high solid circulation rate between the fuel and air reactors.

The work carried out to date involving the use of biomass as a fuel for CLC processes indicates that further work is necessary to improve the process/ tar cracking capabilities of the OC material to reduce the amount of tars exiting the process in line with CO_2 pipeline entry specifications and improve overall process efficiency. This chapter presents findings from preliminary investigations into the effect of tars produced from biomass pyrolysis on the performance of two iron-based CLC oxygen carrier materials (a pure Fe_2O_3 OC and 60 wt.% Fe_2O_3 supported with 40 wt.% Al_2O_3 OC). This work makes use of a newly constructed two-stage fixed-bed reactor that has been specifically designed for studying the interactions between pyrolysis tars and oxygen carrier materials for CLC processes.

---

[3] The authors refer to Ilmenite as a catalyst which is not technically correct as it reacts with the tar species transferring oxygen from the air reactor to fuel reactor and needs periodically regenerating.

6.2 Experimental

6.2.1 Materials

Beech wood was the sole biomass variety used in the study into the effect of tars on the CLC process described in this chapter. Biomass samples were prepared in the same manner as described in section 3.2.2. Samples were first ground in a high-shear cutting mill followed by sieving to obtain a size fraction of 106-150 µm. The ground and sieved biomass samples were then dried in small batches in an air-circulating oven at 308 K (35 °C) for 16 hours to remove the free moisture. The ultimate and proximate analysis can be found in table 3.1.

Two different types of iron oxide based oxygen carrier materials were investigated in this chapter: a 100 wt.% Fe_2O_3 (100Fe(S)) and a 60 wt.% Fe_2O_3 supported with 40 wt.% Al_2O_3 (60Fe40Al(SAB)). Detailed preparation procedures and results from preliminary testing are provided in chapter 5, sections 5.2.1 and 5.4. A particle size fraction of 300-425 µm was used for both OC materials.

6.2.2 Operating Conditions

The experimental investigation discussed in this chapter employed the new upgraded fixed bed reactor described in chapter 4, section 4.2 (fig. 4.1) in both its single and two-stage configuration. A description of the operating procedure for each of the different types of experiments carried out in the single- and two-stage reactor is provided below.

Single Stage Experimental Procedure

The effect of tars on the CLC process was studied under three different gaseous environments (rationale discussed below): 100 vol.% N_2; 15 vol.% CO_2, balance N_2; and 3 vol.% CO, 15 vol.% CO_2, balance N_2. Single stage experiments were carried out to establish the effect of the different gaseous environment on the primary product distribution and nature of the liquid products (tars) obtained from the fast pyrolysis of 0.1 g of beech wood at 773 K. The idea here being that the results from the single stage experiments would provide a baseline by which results from the 2-stage experiments could be compared. A detailed operating procedure for the fast pyrolysis experiments in the upgraded single stage reactor was provided earlier in section 4.2.3. A summary of the conditions used for the single stage experiments described in this chapter is provided in table 6.1.

For the experiments involving the fast pyrolysis of the beech wood in 15 vol.% CO_2 (balance N_2) and 3 vol.% CO, 15 vol.% CO_2 (balance N_2), two cold blank cycle with a simulated biomass feed were performed before heating the reactor to establish a baseline concentration profile that could be used for data analysis and determining the final pyrolysis product distribution. A certified, pre-mixed gas mixture of 15 vol.% CO_2 (BOC) was used for purging the biomass sample cylinder and pressure feeding the biomass into the reactor (instead of N_2) to minimise disruptions in the CO_2 concentration profile. A total flow rate of 60 ml_N s^{-1} was used, which was equivalent to a superficial velocity of 0.25 m s^{-1} through the reactor at 773 K respectively. Gas was supplied from BOC gas cylinders of (i) pure CO_2, (ii) 10 vol.% CO, balance N_2 and (iii) pure N_2; (iv) laboratory air was also supplied.

The timings of the biomass feed for the pyrolysis experiments under conditions of 15 vol.% CO_2 (balance N_2) and 3 vol.% CO, 15 vol.% CO_2 balance N_2 were the same as those used for the two-stage CLC experiments with biomass addition discussed below in section 6.3.3. The beech wood was fed into the reactor 150 s after the CO_2 was switched on (30 s after the CO was switched on).

Table 6.1: Summary of experimental operating parameters for the upgraded single-stage fixed-bed reactor.

Operating Conditions		**1st Stage**
Feedstock		Beech wood
Feed weight		0.100 g
Feed particle size		106-150 μm
Temperature		773 K
Heating Rate		Slow (1 K s^{-1}) or Fast (> 100 K s^{-1})*
Hold Time		600 s
Pressure		1.5 bar_a
Carrier Gas	**Condition 1:**	100 vol.% N_2
	Condition 2:	15 vol.% CO_2, 85 vol.% N_2
	Condition 3:	3 vol.% CO, 15 vol.% CO_2, 82 vol.% N_2
Flow Rate (Superficial Velocity)		60 ml_N s^{-1} (0.25 m s^{-1})

* Fast pyrolysis achieved by pressure feeding sample into reactor once the experimental set point temperature had been reached.

Two-stage Reactor Experimental Procedure

The two-stage fixed-bed reactor used for the experiments described in this chapter was previously introduced in chapter 4, section 4.2.1 (fig 4.1). To establish the effect of tar on the performance of the different OC materials studied in this work, three different types of two-stage pyrolysis experiments were carried out.

(1) Pyrolysis experiments with an empty 2nd stage or 2nd stage loaded with a small bed of sand. These experiments were performed to establish the effect of elevated temperature (973 K) and presence of inert surface area on the distribution and nature of products obtained from the pyrolysis of beech wood in the 1st stage.

(2) Chemical-looping combustion experiments without biomass pyrolysis in the first stage. These experiments were carried out to establish a base line performance of the oxygen carrier material without exposure to the tars and other beech wood pyrolysis products.

(3) Chemical-looping combustion experiments with biomass pyrolysis in the first-stage for investigations into the effect of tars and the other volatile pyrolysis products on the performance of the oxygen carrier material, and distribution and nature of the products.

(1) Two-stage experiments with an empty 2nd stage or sand bed in the 2nd stage

A standard set of operating conditions were developed and used for all experiments carried out in the 2-stage fixed-bed reactor. 2.8 g of sand (500-700 μm) was loaded into the first stage to provide a small inert bed (5 mm in height) that the 1st stage bed thermocouple could be submerged in. Sand has a high thermal capacity and provided a stable heat sink that allowed for stable and precise measurement and control of the 1st stage bed temperature. For experiments involving an empty 2nd stage, only the outer quartz reactor liner was inserted into the reactor *i.e.* the 2nd stage quartz tube insert (for supporting the 2nd stage bed) was not used. For the investigations into the effects of additional inert surface area on the pyrolysis product distribution, 0.75 g of sand (300-425 μm) was added into the 2nd stage and supported in place with the 2nd stage quartz tube insert bed support. A thin layer of quartz wool was placed over the top of the 2nd stage bed support to block any gaps between the outer quartz reactor tube and inner quartz tube bed support preventing sand (or OC particles) from falling into the gap which could lead to loss of material from the bed.

Once the reactor was assembled, a cold calibration was performed using a certified calibration gas mixture (29.9 vol.% CO_2, 9.7 % CO, 10.1 % CH_4, balance N_2) supplied by BOC. For experiments where pyrolysis was carried out in either 15 vol.% CO_2, balance N_2 or 3 vol.% CO, 15 vol.% CO_2 balance N_2; two cold blank cycles with a simulated biomass feed were performed as described in the above section.

As with the single-stage experiments, a total flow rate of 60 ml.s^{-1} was used for all of the two-stage experiments discussed in this chapter which was equivalent to superficial velocities of 0.25 m.s^{-1} and 0.40 m.s^{-1} through the 1st and 2nd stages at 773 K and 973 K respectively.

The reactor was then heated up to the experimental temperatures of 773 K and 973 K for the 1st and 2nd stages respectively. Once the reactor had reached a stable set point temperatures, the cooling system for the tar trap. The trap was allowed to cool for 15 minutes before starting an experiment. The experimental procedure from this point on was the same as outlined in section 4.x and 6.x.

(2) Chemical-looping experiments without biomass addition

Loading of the oxygen carrier into the 2nd stage was the same as outlined for the two-stage experiments with a 2nd stage bed of sand. An oxygen carrier inventory of 0.75 g (d_p = 300-425 μm) was used which represented the minimum amount of the 100Fe(S) OC material required to provide a uniformly distributed layer of OC particles of ~ 0.5 mm in depth (*i.e.* 1-2 particles in height). Larger sample sizes (2-6 g) were also trialled during the reactor commissioning phase but caused fracturing of the quartz tubes due to the stress imposed by the thermal and reactive expansion and shrinkage of the particles.

After the reactor was assembled, a cold calibration was carried out as was standard for all the fixed-bed experiments described in this thesis. Before the reactor was heated to the experimental temperature set points, two simulated CLC cycles were carried out. Under cold conditions, no reaction between the gases and the OC material loaded into the second stage would take place such that the measured outlet concentration was equal to the inlet concentration. The gas concentration profiles obtained under cold conditions could therefore be used as baselines for determining the quantity and rate of CO_2 production and CO consumption by the reaction at the experimental temperature set points (as outlined in the above section). The reactor was then heated to the experimental temperature set points (1st stage T = 773 K, 2nd stage T = 973 K).

Analogous CLC conditions to those used in chapter 5 for assessing the reactivity of the different OC materials were used for the CLC experiments carried out in the two-stage fixed-bed reactor. The simulated CLC experiments involved exposing the oxygen carrier material loaded in the 2nd stage to alternating reducing (3 vol.% CO/ 15 vol.% CO_2 in N_2) and oxidising (4 vol.% O_2 in N_2) conditions at 973 K.

The reduction phase of the CLC experiment involved first switching the gas composition from 100 vol.% N_2 to 15 vol.% CO_2 (balance N_2). The concentration was allowed to stabilise for 120 s before adding in the CO (i.e. switching the gas composition to 3 vol.% CO, 15 vol.% CO_2 (balance N_2)). As discussed previously in chapter 5, the gas composition for the reduction phase of the CLC experiments was chosen to limit the reduction of Fe_2O_3 to Fe_3O_4 based on the assumption that thermodynamic equilibrium was established i.e. $P_{CO2}/P_{CO} = K_{eq} = 3$ (chapter 5, section 5.2.4). The staggered introduction of the CO_2 and CO flows into the reactor at the beginning of the reduction phase was designed to ensure that a stable CO_2 concentration was obtained before switching on the CO such that the P_{CO2}/P_{CO} in the system never dropped below ~ 1.6, which would allow the further reduction to $Fe_{0.97}O$ at 973 K. The OC material was exposed to the reducing conditions for a total of 300 s (after the CO addition) to ensure complete reduction of Fe_2O_3 to Fe_3O_4.

Oxidation of the reduced OC material was achieved by exposing the OC material to 4 vol.% O_2 (balance N_2). The oxidation of Fe_3O_4 to Fe_2O_3 is very fast and highly exothermic. These conditions were chosen for the oxidation phase of the CLC experiment to limit deviation from isothermal conditions and prevent the formation of hot spots within the particle and bed that may lead to morphological changes due to sintering and fracturing. The oxidation period lasted 300 s to ensure complete oxidation of the Fe_3O_4 to Fe_2O_3. The reactor was purged with N_2 for 2 minutes between reduction and oxidation phases to avoid mixing of the reducing and oxidising gases. 5 redox cycles were carried out in total. A summary of operating parameters used for the 5 cycle CLC experiments in the upgraded 2-stage fixed-bed reactor is provided in table 6.2.

Table 6.2: Summary of experimental operating parameters for the 5 cycle simulated CLC experiments carried out in the upgraded 2-stage fixed bed reactor.

Operating Parameter	Operating Conditions
Temperature (1st / 2nd Stage)	773 K / 973 K
Oxygen Carrier (2nd Stage)	100Fe(S) (0.750 g, 300-425μm) 60Fe40Al(SAB) (0.750 g, 300-425μm)
Reducing Gas	3vol.% CO/ 15 vol.% CO_2 (300 s)
Oxidising Gas	4 vol.% O_2 / N_2 (300 s)
Purge Period	100 vol.% N_2 (120 s)
Total No. Cycles	5
Flow Rate / (Superficial Velocity 1st / 2nd Stage)	60 $ml_N\ s^{-1}$ (0.25 $m\ s^{-1}$/ 0.40 $m\ s^{-1}$)
Pressure	1.5 bar_a

(3) Chemical-looping experiments with biomass addition

Setting up of the reactor for CLC experiments involving biomass pyrolysis in the first stage was the same as that outlined above for CLC experiments without biomass addition. Following completion of the two cold CLC cycles, a third cold cycle was performed in which a blank biomass sample was fed into the reactor (*i.e.* simulated biomass feed with an empty feed sample cylinder) under the conditions used for cycles involving biomass addition. This third cold cycle was carried out to determine the effect of the pressurised gas introduced during the biomass feeding on the concentration profiles. The concentration profiles produced here provided the baseline for the cycles in which the OC materials were exposed to the biomass pyrolysis vapours and gases. The third cold cycle could be omitted when the biomass was fed into the reactor under 100 vol.% pyrolysis conditions as the zero base line could be used for processing the data determining the product yields.

Following completion of the cold base line CLC cycles, the reactor was heated up to the experimental set points (1st stage T = 773 K, 2nd stage T = 973 K) and allowed to stabilise. Once the experimental temperature had been reached, the tar trap cooling system was switched on and the biomass sample (beech wood, 0.1 g, 106-150 µm) was loaded into the feeder and purged to remove air from the cylinder.

Prior to feeding the biomass, two simulated CLC cycles with gaseous reduction (3 vol.% CO, 15 vol.% CO_2, balance N_2) were performed (as outlined above in the description of CLC experiments without biomass addition) to: (a) activate the OC material (cycle 1); and (b) obtain an initial reactivity/performance measurement for the OC material (cycle 2) before it was exposed to the volatile pyrolysis products produced during the biomass pyrolysis.

The effect of the volatiles produced from biomass pyrolysis was measured under three different gaseous environments: (i) 100 vol.% N_2; (ii) 15 vol.% CO_2, balance N_2; and (iii) 3 vol.% CO, 15 vol.% CO_2, balance N_2. For experiments involving conditions (i) and (ii), experiments were carried out both before a gaseous reduction (pre-red) and after a gaseous reduction (post-red) to investigate how the oxidation state of the OC material effected (a) the performance of the OC material after exposure to the volatile pyrolysis products and (b) the resulting product distribution.

The different gaseous environments were chosen to establish whether the behaviour of the OC and the oxidation states that it could access would influence the product distribution and/or performance of the OC materials after exposure to the pyrolysis products as outlined below:

(i) **Biomass fed under pure N_2**- no limitation on the final oxidation state was imposed such that in theory, the OC material could be reduced further than Fe_3O_4.

(ii) **Biomass fed under 15 vol.% CO_2**- the addition of 15 vol.% CO_2 controlled the final reduction state to Fe_3O_4. When the biomass pyrolysis was carried out before the gaseous reduction, reduction of Fe_2O_3 to Fe_3O_4 was possible as a result of interactions with the biomass pyrolysis products. However, feeding biomass under conditions of 15 vol.% CO_2 after the OC material had been reduced meant that the OC material could not be reduced further. Therefore, the only interactions that could have taken place would have been surface mediated/catalysed reactions between the volatile pyrolysis products.

(iii) **Biomass fed under 3 vol.% CO, 15 vol.% CO_2**- biomass was added during a gaseous reduction cycle to establish the effect of exposing the pyrolysis products to a partially reacted OC material.

For experiments where the biomass is fed under 15 vol.% CO_2, balance N_2, or 3 vol.% CO, 15 vol.% CO_2, balance N_2, the biomass was fed 150 s after the CO_2 flow was switched on (30 s after the CO was switched on). These timings were chosen to ensure that the OC material would be in a partially reduced form (but not fully reduced) for the CLC experiments where the biomass is pyrolysed under the conditions used for the gaseous reduction (i.e. 3 vol.% CO. 15 vol.% CO_2 (balance N_2)). Once the biomass had been fed, the conditions in the reactor were maintained for 300 s to allow pyrolysis and subsequent interactions between the volatile pyrolysis products and OC material in the 2nd stage to reach completion.

Experiments were either ended immediately after the biomass addition phase to allow for retrieval of the OC material directly after exposure to the pyrolysis vapours; or continued such that another 2 complete cycles (gaseous reduction with 3 vol.% CO, 15 vol.% CO_2, balance N_2) were completed with the aim of establishing whether exposure to the volatile pyrolysis products effected the reactivity of the OC material in subsequent redox cycles. A summary of the operating parameters used for the CLC experiments in the upgraded 2-stage fixed-bed reactor with biomass pyrolysis carried out in the first stage is provided in table 6.3.

Table 6.3: Summary of experimental operating parameters for the simulated CLC experiments carried out in the upgraded 2-stage fixed bed reactor with biomass pyrolysis carried out in the first stage during the 3rd cycle.

Operating Conditions	**1st Stage**	**2nd Stage**
Biomass feedstock	Beech wood (0.100 g, d_p = 106-150 μm)	N/A
Oxygen carrier	N/A	100Fe(S) 60Fe40Al(SAB) (0.750 g, 300-425μm)
Temperature	773 K	973 K
Pressure	1.5 bar_a	
Flow Rate (Sup. Vel. 1st stage / 2nd stage)	60 $\text{ml}_N\ \text{s}^{-1}$ (0.25 m s^{-1}, 0.40 m s^{-1})	
Reducing Gas	3vol.% CO / 15 vol.% CO_2 / N_2 Bal. (300 s)	
Oxidising Gas	4 vol.% O_2 / N_2 Bal. (300 s)	
Purge Period	100 vol.% N_2 (120 s)	
Total Number of Cycles	5 (or 3 ended after the biomass pyrolysis phase)	
Biomass pyrolysis Cycle No.	3	
Conditions of biomass pyrolysis	100 vol.% N_2 Pre-Red [a] 100 vol.% N_2 Post-Red [b] 15 vol.% CO_2 Pre-Red 15 vol.% CO_2 Post-Red 3 vol.% CO,15 vol.% CO_2 In-Red [c]	

---

[a] Pre-Red refers to experiments where the biomass pyrolysis phase is carried out before a gaseous reduction phase.

[b] Post-Red refers to experiments where the biomass pyrolysis phase is carried out after a gaseous reduction phase.

[c] In-Red refers to experiments where the biomass pyrolysis phase is carried during a gaseous reduction phase.

6.2.3 Product Recovery and Characterisation

The procedure for recovering the tars from the reactor and tar trap was the same as that described previously in chapter 4, section 4.2.4. SEC, UVF and elemental (CHN) analysis (described in chapter 3, section 3.2.6) was used to characterise the tars produced in the experiments discussed in this chapter. The concentration of CO_2, CO and CH_4 in the reactor outlet gas were measured and recorded using an online multigas ADC analyser (chapter 4, section 4.2.5).

N_2-adsorption analysis (Micrometrics, Tristar 3000) was carried out to determine the BET surface area and BJH pore size distributions of the fresh, unreacted and reacted OC materials for the pore size range 2-200 nm (abstract A, section A.1-A.3). The size distribution and volume of pores in the pore size range 5-10000 nm was achieved using mercury porosimetry (Micrometrics Autopore IV) (abstract A, section A.4). Elemental (CHN) analysis was used to measure carbon deposition on the surface of the OC particles recovered from the reactor after exposure to the volatile beech wood pyrolysis products.

Visualisation of the surface morphology of the particles was conducted using a Hitachi S3400 SEM with 20 kV of accelerating voltage under high vacuum. Some additional images were also taken using an optical light microscope with webcam facility to observe the reacted particles at a lower magnification.

6.2.4 Data Processing

CLC Experiments with gaseous reduction by CO

The concentrations of CO and CO_2 measured in the reactor outlet for an entire 5 cycle CLC experiment in the upgraded 2-stage fixed-bed reactor are shown in figure 6.1. The feature labelled (i) is the initial cold calibration that was used to check the calibration values of the analyser. The features labelled (ii) are the two redox cycles that were carried out before the reactor was heated to obtain concentration profiles for a redox cycle without the reduction reaction taking place. The concentration profiles measured here were equivalent to the concentration profile at the inlet. The features labelled (iii) are the 5 experimental CLC cycles at the experimental set point (973 K) with the reduction reaction between the OC material and CO taking place.

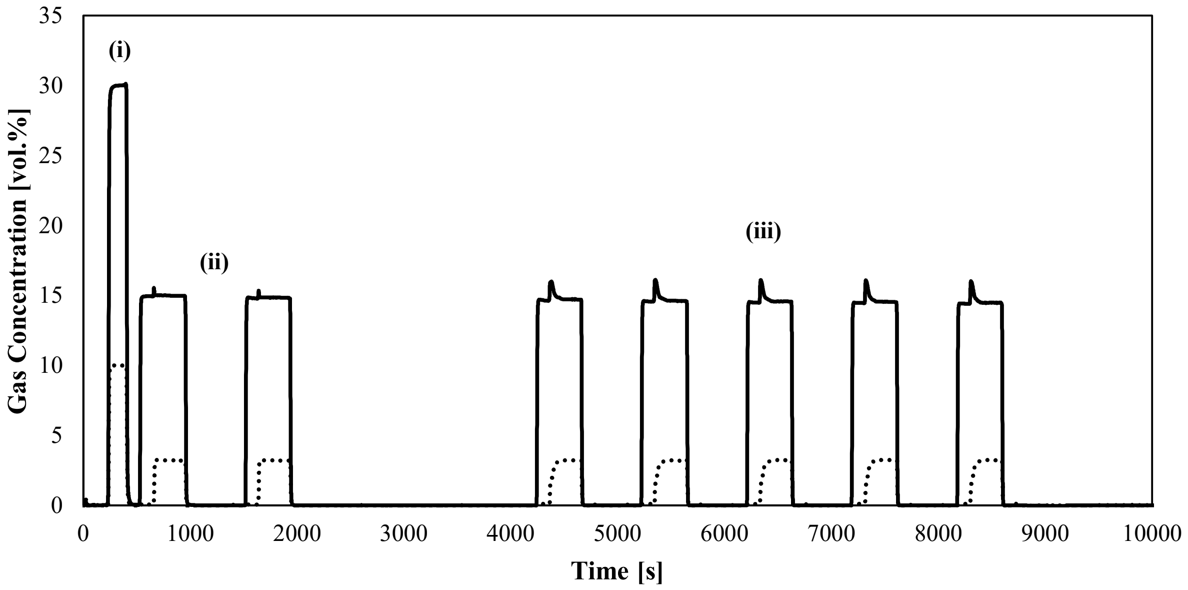

Figure 6.1. Concentration profile for an entire 5 cycle simulated CLC experiment in the upgraded 2-stage fixed bed reactor involving a 100Fe(S) oxygen carrier with gaseous reduction by 3 vol.% CO, 15 vol.% CO_2 only. CO_2 (——); CO (·········). **Experimental parameters:** ***1st stage***: **Feed** = N/A, **Temperature** = 773 K, **Flow rate** = 60 $ml_N\ s^{-1}$ (0.25 $m\ s^{-1}$); ***2nd stage***: **Oxygen Carrier**: 100Fe(S) (5 mg, 150-212 μm); **Reaction**: $Fe_2O_3 \rightarrow Fe_3O_4$; **Temperature**: 973 K; **Reducing gas composition**: 3 vol.% CO, 15 vol.% CO_2, balance N_2; **Oxidising gas composition**: 4 vol.% O_2, balance N_2; **Reduction time**: 300 s, **Oxidation time**: 300 s, **Purge period time**: 120 s, **Flow rate**: 60 $ml_N\ s^{-1}$ (0.40 $m\ s^{-1}$); **Total Number of Cycles**: 5.

A more detailed concentration profile for the third reduction cycle of the experiment shown in figure 7.1 is provided in figure 7.2 (b). The inlet concentration profiles produced during the cold reduction cycle have been overlaid to provide a comparison of how the concentrations of CO_2 and CO were affected by the reaction with the OC material. As expected, the concentration of CO_2 and CO measured in the outlet of the reactor differed to the inlet concentration profiles. Compared with the baseline inlet concentration profiles, the CO concentration was lower whilst the CO_2 concentration was higher during the period after the CO flow was switched on indicating that the CO input was being converted to CO_2 by the reduction of Fe_2O_3 to Fe_3O_4. The differences between the inlet and outlet concentration profiles were greatest during the period immediately proceeding the point at which the CO flow was switched on but decayed with time. The outlet concentration profiles of both CO and CO_2 returned to the inlet concentrations (*i.e.* matched up with the concentration profile measured under cold conditions) approximately 60 s after the CO was switched on indicating that the reaction had reached completion.

The temperature profile presented in figure 6.2.a shows that the temperature within the OC bed was very stable with temperature fluctuations of < 5 K from the set point temperature indicating that the bed could be considered isothermal during the reaction period.

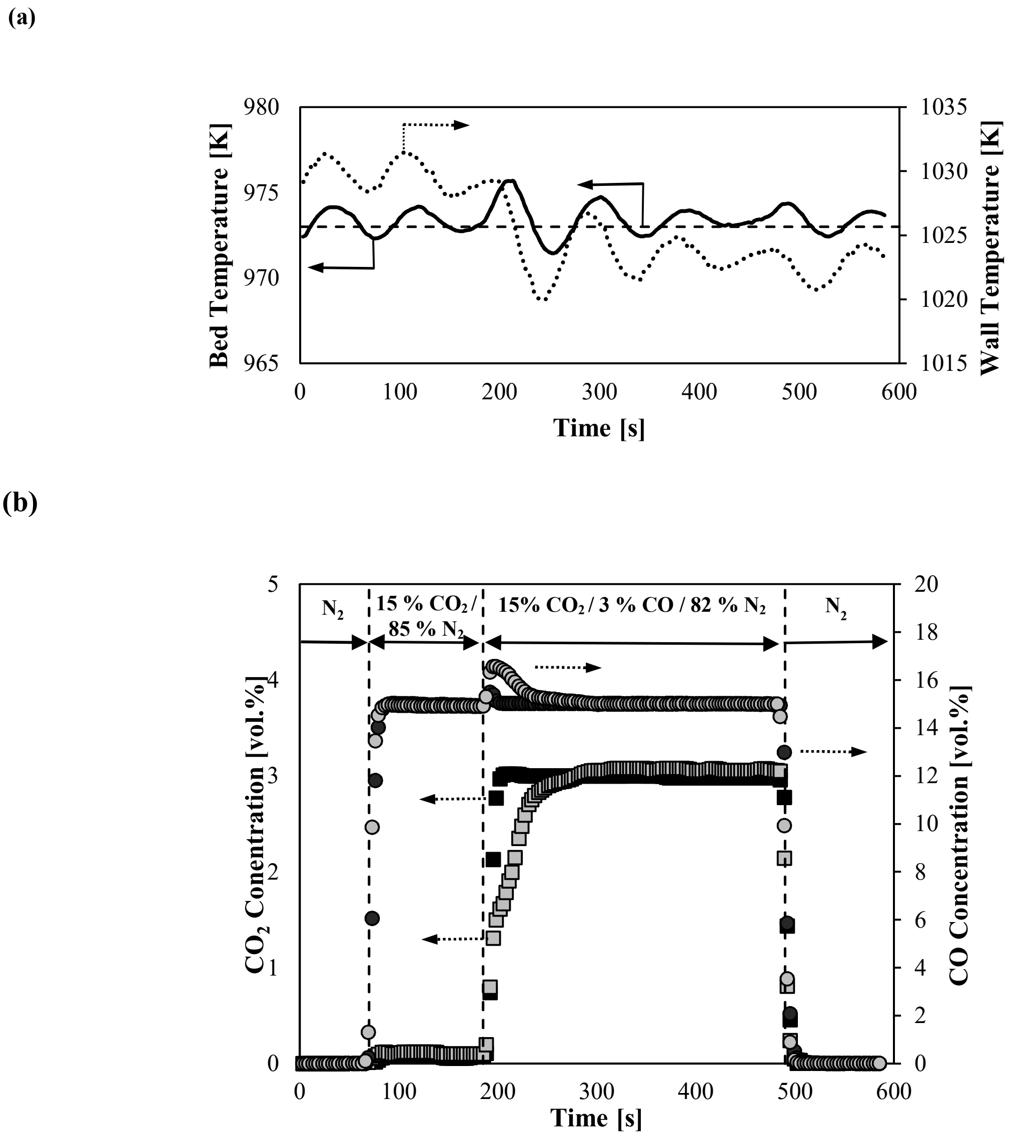

Figure 6.2. (a) Temperature profile and (b) CO_2 and CO concentration profiles in the inlet and outlet for the 3rd cycle of simulated CLC reduction phase in the upgraded 2-stage fixed bed reactor involving a 100Fe(S) oxygen carrier with gaseous reduction by 3 vol.% CO, 15 vol.% CO_2 only. CO_2 outlet (○); CO outlet (□); inlet concentrations (corresponding black symbols). **Experimental parameters:** ***1st stage***: **Feed** = N/A, **Temperature** = 773 K, **Flow rate** = 60 ml$_N$ s^{-1} (0.25 m s^{-1}); ***2nd stage*****: Oxygen Carrier**: 100Fe(S) (5 mg, 150-212 μm); **Reaction**: $Fe_2O_3 \rightarrow Fe_3O_4$; **Temperature**: 973 K; **Reducing gas composition**: 3 vol.% CO, 15 vol.% CO_2, balance N_2; **Oxidising gas composition**: 4 vol.% O_2, balance N_2; **Reduction time**: 300 s, **Oxidation time**: 300 s, **Purge period time**: 120 s, **Flow rate**: 60 ml$_N$ s^{-1} (0.40 m s^{-1}); **Total Number of Cycles**: 5.

To obtain information relating to the overall rates of reaction and Fe_2O_3 to Fe_3O_4 conversion, the difference between the inlet and outlet concentration during the reduction period were calculated using the inlet concentration (measured under cold conditions) as the baseline. The observed rate of reaction, r' (in mol s^{-1} g^{-1}) at a specific point in time could then be determined by multiplying the instantaneous difference between the inlet and outlet concentration (expressed as a mole fraction) by the total molar flow rate at the inlet[4] and then dividing through by the total mass of Fe_2O_3. The maximum observed rates were used for comparison of the reactivity of the different OC materials exposed to the biomass volatile pyrolysis products in this chapter.

The conversion of Fe_2O_3 to Fe_3O_4, X at a specific time was readily calculated from the rate measurements (fig. 6.3). Conversion, X was defined as the ratio between the cumulative molar flow (*i.e.* rate) of CO consumed (or CO_2 produced) and the theoretical values calculated for the complete conversion of Fe_2O_3 to Fe_3O_4 according the reaction stoichiometry.

It is interesting that the maximum conversions reached in the two-stage experiments were lower than those reported for the TGA reactivity studies at analogous conditions described in chapter 5. This was likely due to the higher measurement resolution of the thermogravimetric balance that was able to measure mass changes down to very low levels (i.e. when the reaction was nearing completion and residual rate had decayed to very low levels) compared with gas analysis measurements where the difference in concentrations caused by the residual rate of reaction at high conversions was likely to have been overshadowed by the noise in the signal.

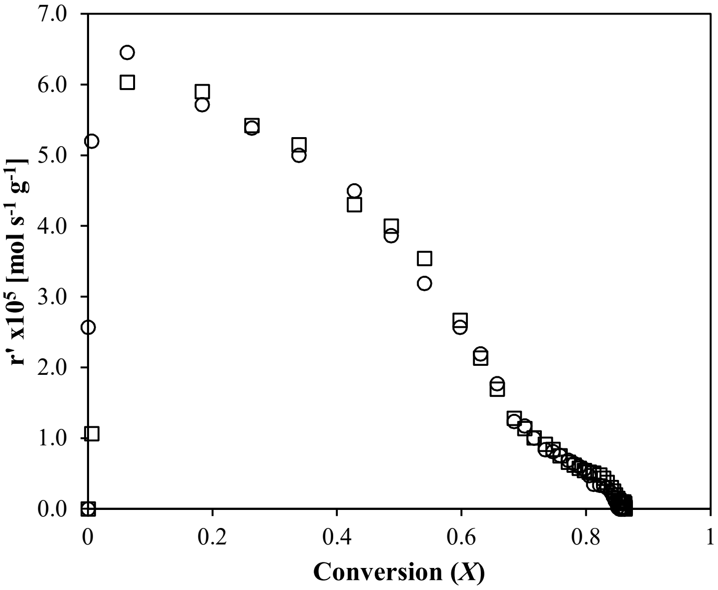

Figure 6.3. Variation in the rate of reaction as a function of Fe_2O_3 to Fe_3O_4 conversion calculated from the differences in the CO_2 and CO concentration profiles caused by the reaction presented in Figure 7.2 (b).

Experimental parameters: ***1st stage***: **Feed** = N/A, **Temperature** = 773 K, **Flow rate** = 60 ml_{nN} s^{-1} (0.25 m s^{-1}); ***2nd stage***: **Oxygen Carrier**: 100Fe(S) (5 mg, 150-212 μm); **Reaction**: $Fe_2O_3 \rightarrow Fe_3O_4$; **Temperature**: 973 K; **Reducing gas composition**: 3 vol.% CO, 15 vol.% CO_2, balance N_2; **Oxidising gas composition**: 4 vol.% O_2, balance N_2; **Reduction time**: 300 s, **Oxidation time**: 300 s, **Purge period time**: 120 s, **Flow rate**: 60 ml_N s^{-1} (0.40 m s^{-1}); **Total Number of Cycles**: 5.

---

[4] The total molar flow rate was not changed by the reaction as the number of moles of CO consumed by the reaction was equal to the moles of CO_2 produced by the reaction according to the reaction stoichiometry.

CLC Experiments with the addition of biomass

This section provides a description of how the outlet CO_2 and CO concentration measurements were processed to extract the yields of CO_2 and CO produced as a result of pyrolysis and subsequent interactions with the OC material for the most complicated scenario investigated in which the biomass was fed into the reactor and pyrolysed during a gaseous reduction cycle (gaseous environment of 3 vol.% CO, 15 vol.% CO_2, balance N_2). Figure 6.4 (b) presents the concentration profiles of CO and CO_2 in the inlet (determined from the cold redox cycle with a blank biomass feed) and outlet during the 3rd reduction cycle in which the biomass was pyrolysed in the 1st stage during a gaseous reduction phase. A more detailed view of the concentration profiles during the reaction with CO and volatile pyrolysis products is provided in figure 6.5. Small temperature drops can be observed in the temperature profiles of both the 1st and 2nd stage beds as a result of the biomass feed and onset of pyrolysis in the 1st stage and subsequent interactions with the volatile pyrolysis products in the 2nd stage (fig. 6.4 (a)). Both temperature drops were small and fluctuations in temperature away from the set point were less than 5 K for the entire reduction period indicating that the temperature in both reactor stages could be considered to be isothermal for the period in which the reactions were taking place.

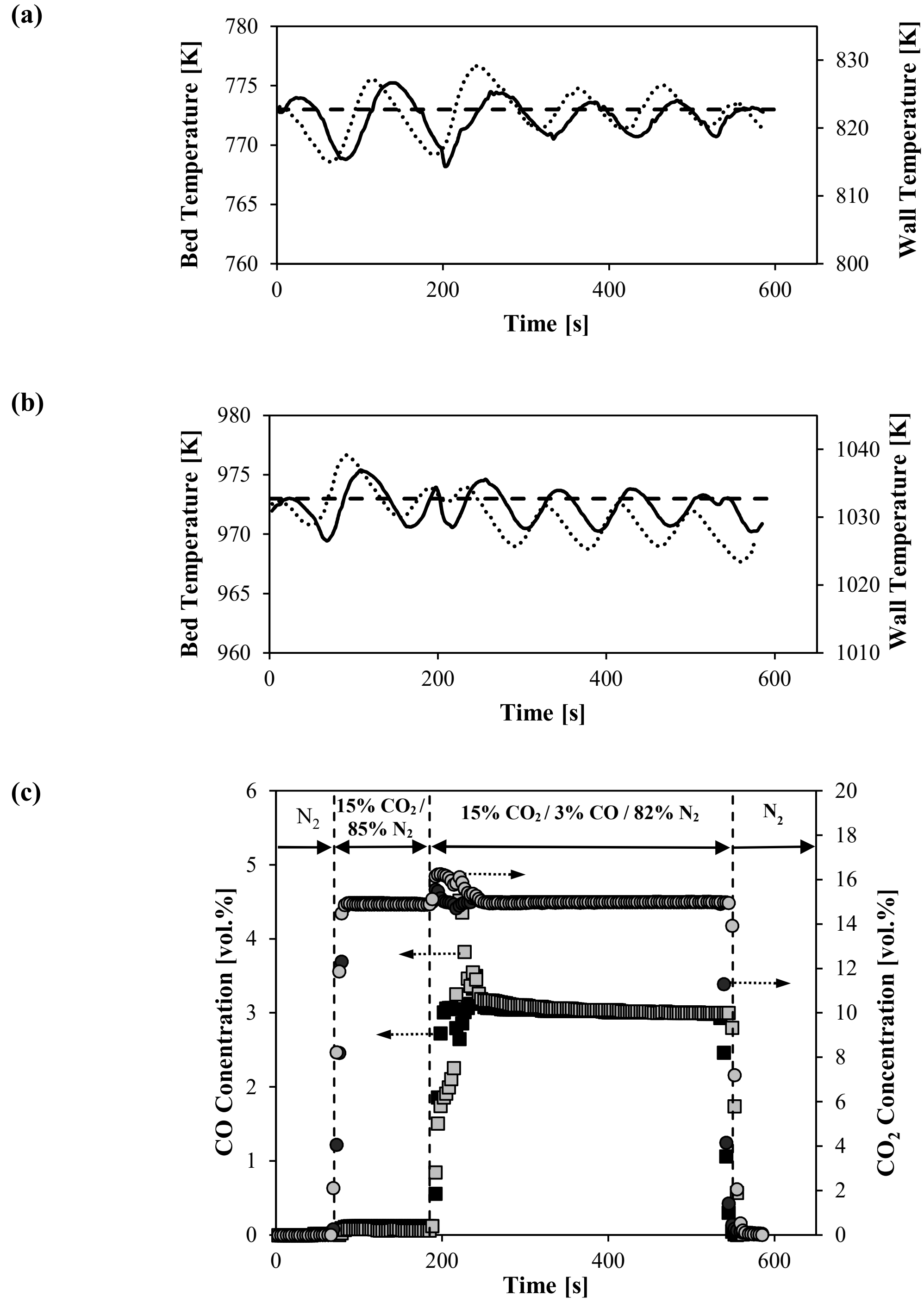

Figure 6.4. Temperature profiles for (a) 1st stage and (b) 2nd stage of the reactor and (c) CO_2 and CO concentration profiles in the inlet and outlet for the 3rd cycle of a simulated CLC reduction phase in the upgraded 2-stage fixed bed reactor involving a 100Fe(S) oxygen carrier with gaseous reduction by 3 vol.% CO, 15 vol.% CO_2 only. Bed temperature (——), bed set point temperature (– – –) and wall temperature (·········). CO_2 outlet (○); CO outlet (□); inlet concentrations (black symbols).

Experimental parameters: ***1st stage***: **Feed** = beech wood (0.100 g, 106-150 µm), **Temperature** = 773 K, **Flow rate** = 60 ml$_{nN}$ s^{-1} (0.25 m.s^{-1}), **Biomass feed conditions**: 3 vol.% CO, 15 vol.% CO_2, balance N_2; **Biomass feed cycle no.**: 3; ***2nd stage***: **Oxygen Carrier**: 100Fe(S) (5 mg, 150-212 µm); **Reaction**: $Fe_2O_3 \rightarrow Fe_3O_4$; **Temperature**: 973 K; **Reducing gas composition**: 3 vol.% CO, 15 vol.% CO_2, balance N_2; **Oxidising gas composition**: 4 vol.% O_2, balance N_2; **Reduction time**: 300 s, **Oxidation time**: 300 s, **Purge period time**: 120 s, **Flow rate**: 60 ml$_N$ s^{-1} (0.40 m s^{-1}); **Total Number of Cycles**: 5.

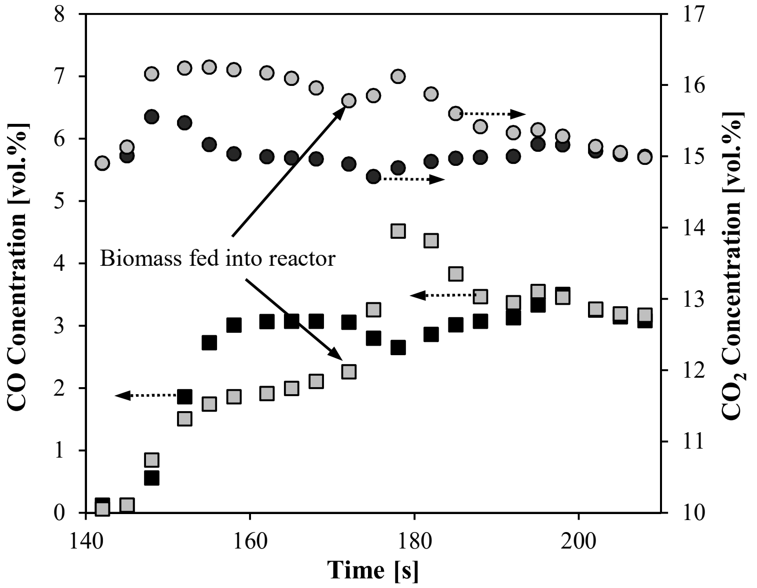

Figure 6.5. CO_2 and CO concentration profiles in the inlet and outlet of a simulated CLC reduction phase in the upgraded 2-stage fixed bed reactor as 0.75 g 100Fe(S) oxygen carrier is simultaneously reduced by 3 vol.% CO, 15 vol.% CO_2 and exposed to pyrolysis vapours produced during pyrolysis of 0.100 g of beech wood in the 1st stage of the reactor.

CO_2 outlet (○); CO outlet (□); inlet concentrations (black symbols).

Experimental parameters: ***1st stage***: **Feed** = beech wood (0.100 g, 106-150 μm), **Temperature** = 773 K, **Flow rate** = 60 $ml_N\ s^{-1}$ (0.25 $m\ s^{-1}$), **Biomass feed conditions**: 3 vol.% CO, 15 vol.% CO_2, balance N_2; **Biomass feed cycle no.**: 3; ***2nd stage***: **Oxygen Carrier**: 100Fe(S) (5 mg, 150-212 μm); **Reaction**: $Fe_2O_3 \rightarrow Fe_3O_4$; **Temperature**: 973 K; **Reducing gas composition**: 3 vol.% CO, 15 vol.% CO_2, balance N_2; **Oxidising gas composition**: 4 vol.% O_2, balance N_2; **Reduction time**: 300 s, **Oxidation time**: 300 s, **Purge period time**: 120 s, **Flow rate**: 60 $ml_N\ s^{-1}$ (0.40 $m\ s^{-1}$); **Total Number of Cycles**: 5.

The inlet concentration profiles were subtracted from the outlet concentration profiles as was the procedure for determining the rate of reduction from the outlet concentration profiles for cycles involving gaseous reduction with CO only. The calculated difference between the inlet and outlet concentrations of CO and CO_2 in this case was a result of both consumption of CO (added in the inlet) by the reaction with Fe_2O_3; and interactions involving either the consumption and/or production of CO_2 and CO between the OC material and the volatile pyrolysis products produced during the 1st stage beech wood pyrolysis. In order to estimate the yields of CO and CO_2 produced due to interactions with the volatile pyrolysis products, the profiles for the molar rate of production of CO_2 and CO with respect to time obtained from the 2nd cycle reduction phase involving gaseous reduction with CO only, were subtracted from the equivalent profiles obtained for the 3rd cycle with additional interactions with biomass pyrolysis products as illustrated in figure 6.6. The yields of CO and CO_2 could then be estimated by integrating (with respect to time) the resulting rate profile for the production CO and CO_2 due to interactions between the volatile pyrolysis products and OC material (fig. 6.7).

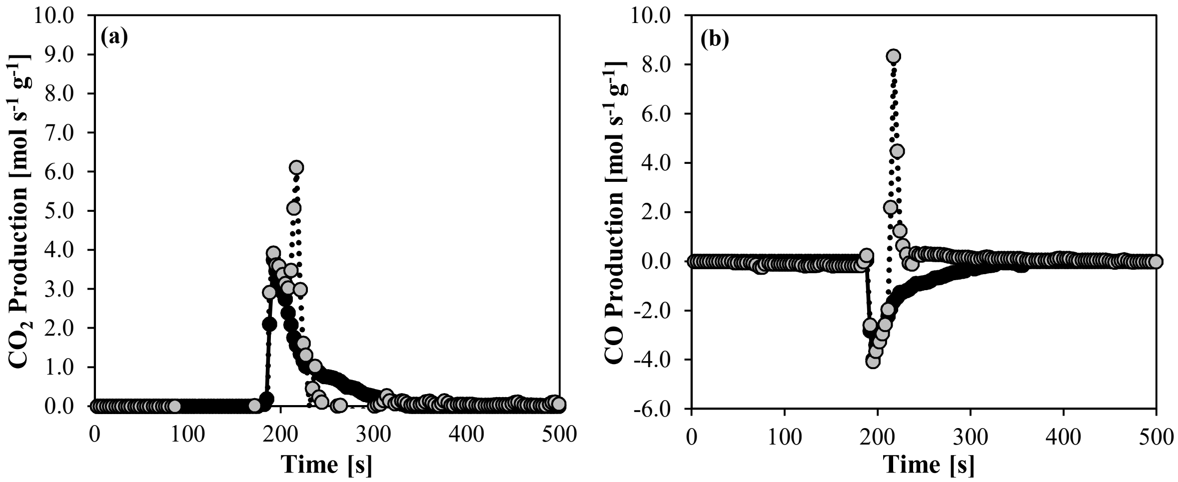

Figure 6.6. Rate of production of (a) CO and (b) CO_2 due to the combined reduction of a 100Fe(S) OC by CO introduced in the inlet gas and reactions between the OC material and volatile pyrolysis products produced from the pyrolysis of beech wood. CO_2 outlet (○); CO outlet (□); rate of production due to reduction with CO only obtained from the 2nd cycle reduction phase (black symbols). **Experimental parameters:** ***1st stage***: **Feed** = beech wood (0.100 g, 106-150 µm), **Temperature** = 773 K, **Hold time** = 300 s **Flow rate** = 60 ml_N s^{-1} (0.25 m s^{-1}), **Biomass feed conditions**: 3 vol.% CO, 15 vol.% CO_2, balance N_2; **Biomass feed cycle no.**: 3; ***2nd stage*: Oxygen Carrier**: 100Fe(S) (5 mg, 150-212 µm); **Reaction**: $Fe_2O_3 \rightarrow Fe_3O_4$; **Temperature**: 973 K; **Reducing gas composition**: 3 vol.% CO, 15 vol.% CO_2, balance N_2; **Oxidising gas composition**: 4 vol.% O_2, balance N_2; **Reduction time**: 300 s, **Oxidation time**: 300 s, **Purge period time**: 120 s, **Flow rate**: 60 ml_N s^{-1} (0.40 m. s^{-1}); **Total Number of Cycles**: 5.

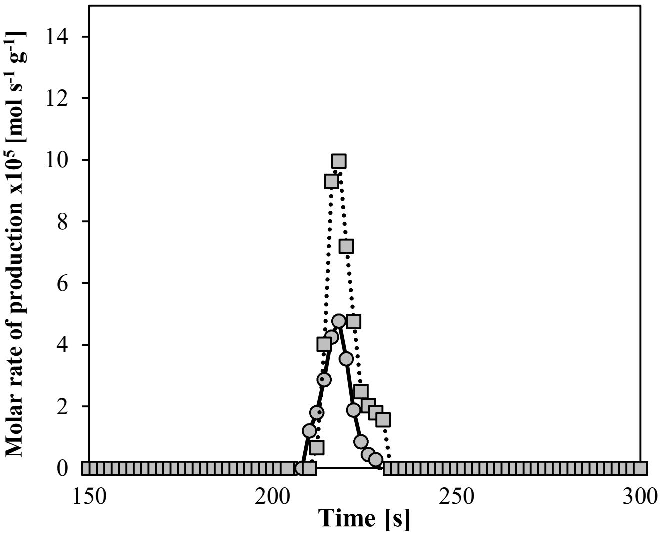

Figure 6.7. Rates of production of CO and CO_2 due reactions between the OC material and volatile pyrolysis products produced from the pyrolysis of beech wood with contributions from interactions between the OC and inlet CO removed.

CO_2 outlet (○); CO outlet (□). **Experimental parameters:** ***1st stage***: **Feed** = beech wood (0.100 g, 106-150 µm), **Temperature** = 773 K, **Hold time** = 300 s **Flow rate** = 60 ml_N s^{-1} (0.25 m s^{-1}), **Biomass feed conditions**: 3 vol.% CO, 15 vol.% CO_2, balance N_2; **Biomass feed cycle no.**: 3; ***2nd stage*: Oxygen Carrier**: 100Fe(S) (5 mg, 150-212 µm); **Reaction**: $Fe_2O_3 \rightarrow Fe_3O_4$**;** **Temperature**: 973 K; **Reducing gas composition**: 3 vol.% CO, 15 vol.% CO_2, balance N_2; **Oxidising gas composition**: 4 vol.% O_2, balance N_2; **Reduction time**: 300 s, **Oxidation time**: 300 s, **Purge period time**: 120 s, **Flow rate**: 60 ml_N s^{-1} (0.40 m s^{-1}); **Total Number of Cycles**: 5.

6.3 Results

6.3.1 Single Stage Pyrolysis under different gaseous environments

A set of single-stage experiments were carried out to establish how the composition of the gaseous environment under which the biomass would be pyrolysed in the 2-stage combined CLC and pyrolysis experiments effected the pyrolysis behaviour and primary product distribution. As illustrated in figure 6.8 (a) and (b), the composition of the gaseous environment had little influence on the overall pyrolysis product distribution. Tar yields were between 42.9 wt.% and 47.2 wt.%; variation was within the experimental error of the measurements. The CO_2 and CO yield were slightly higher for the pyrolysis experiments carried out in an atmosphere of 3 vol.% CO, 15 vol.% CO_2 although the difference is small and within the error ranges of the measurements.

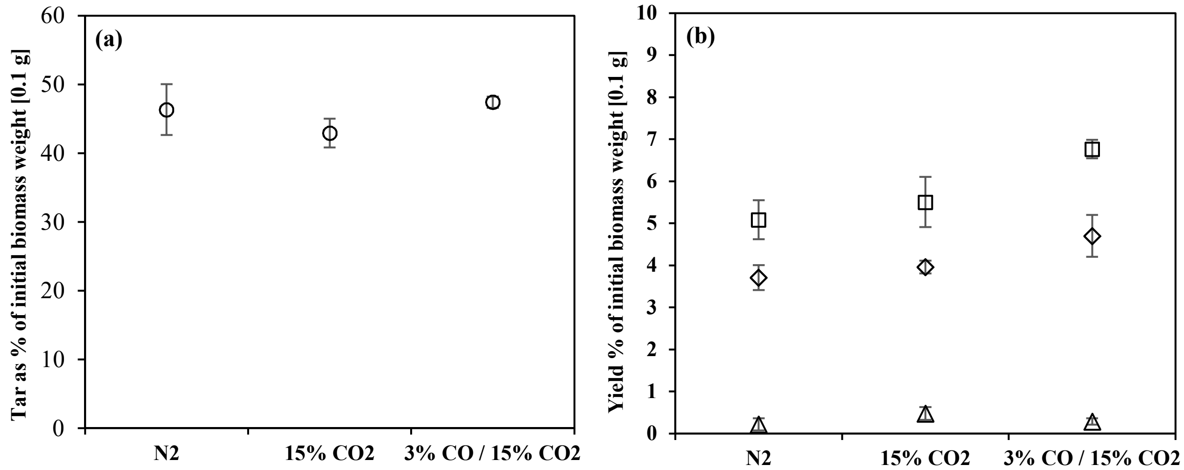

Figure 6.8. (a) Tar yields and (b) detectable gas yields produced from the fast pyrolysis of 0.100g of beech wood in different gaseous environments in the upgraded single stage reactor.

Experimental parameters*: 1st stage*: **Feed** = beech wood (106-150 µm), **Feed Weight** = variable, **Carrier gas** = variable, **Pressure** = 1.5 bar_a, **Flow rate** = 60 ml_N s^{-1} (0.25 m s^{-1}), **Temperature** = 773 K, **Hold time** = 300 s. Tar (○), CO_2 (□), CO (◇) and CH_4 (△).

There were small differences in the molecular mass distribution of the tars produced under the different gaseous environments as characterised by SEC (fig. 6.9 (a)). Both the tars produced from beech wood pyrolysis in 15 vol.% CO_2 (bal. N_2) and 3 vol.% CO, 15 vol.% CO_2 (bal. N_2) had a greater proportion of the higher molecular mass fraction (and lower proportion of the lower molecular mass fraction) compared with the tars produced during the beech wood pyrolysis in a N_2 atmosphere. The average molecular mass of the lower molecular weight fraction (estimated from the elution time of the retained peak maxima) were shifted to higher molecular masses the tars produced in a N_2 atmosphere.

The UVF spectra also show some small differences in the conjugation extents of the tar species that make up the lower molecular weight fraction of the tars produced in the different gaseous environments (fig. 6.9 (b)). The intensity of the lower wavelength peaks (at ~ 315 nm) of the pyrolysis tars produced in environments of 15 vol.% CO_2 (bal. N_2) and 3 vol.% CO, 15 vol.% CO_2 (bal. N_2) are slightly less than the equivalent peak in the spectrum of the tars produced under a N_2 atmosphere. This indicates that there was a slightly larger proportion of the more conjugated tar species in the pyrolysis tars produced in atmospheres containing CO_2 and/or CO. The more conjugated species are also likely to be heavier than the less conjugated tar species which fits with the findings of the SEC which saw a shift in the average molecular mass of the lower molecular mass tar fraction when pyrolysis was carried out in atmospheres containing CO_2 and/or CO.

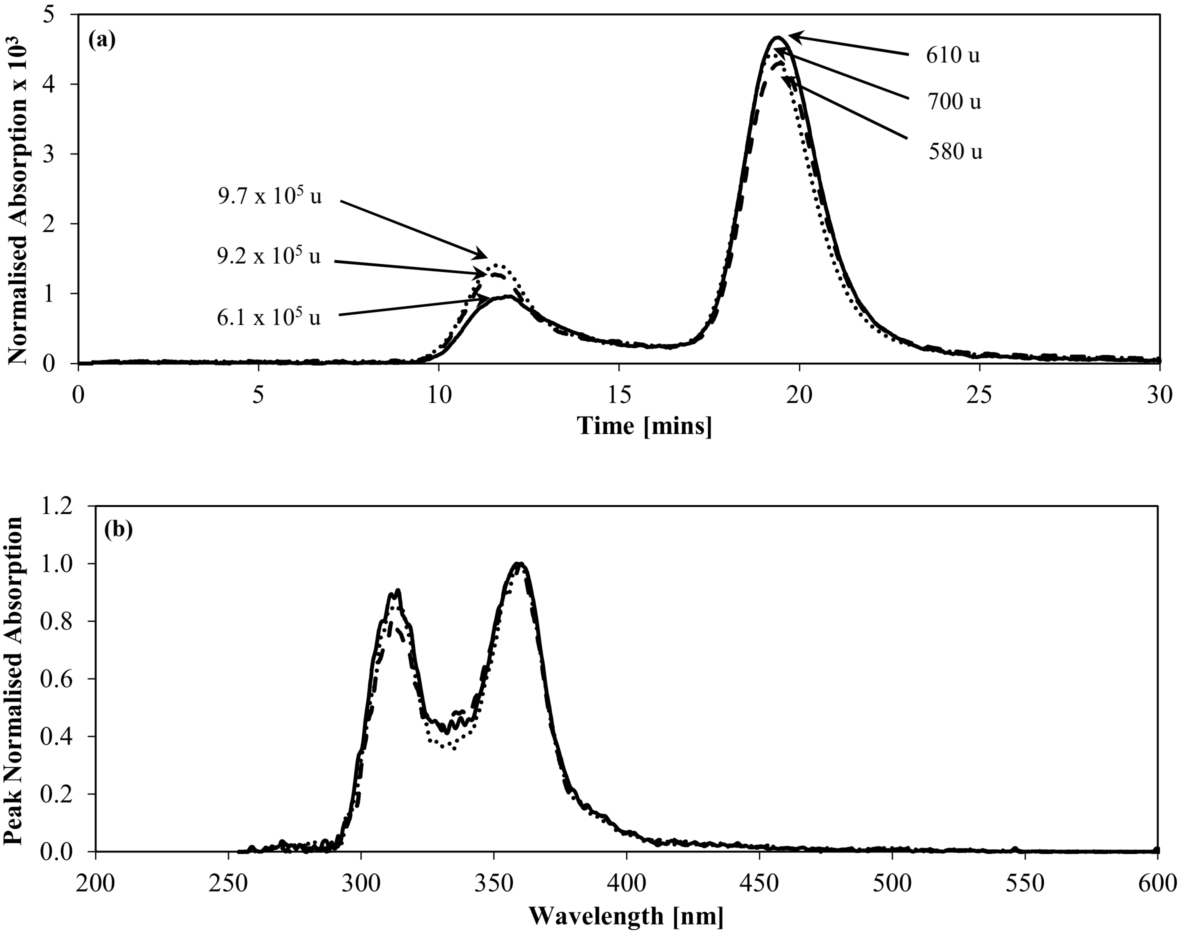

Figure 6.9 (a) SEC and (b) UVF analyses of the tars recovered from the fast pyrolysis of 0.10 g of beech wood in the single stage reactor under different gaseous environments. **Experimental Parameters:** ***1st stage***: **Feed** = beech wood (0.100 g, 106-150 μm), **Feed Weight** = variable, **Carrier gas** = variable, **Pressure** = 1.5 bar_a, **Flow rate** = 60 $ml_N\ s^{-1}$ (0.25 $m\ s^{-1}$), **Temperature** = 773 K, **Hold time** = 300 s. **Gaseous environment:** 100 vol.% N_2 (——), 15 vol.% CO_2 (bal. N_2) (– – –), and 3 vol.% CO, 15 vol.% CO_2 (bal. N_2) (·········).

Summary

The gaseous environment under which the fast pyrolysis of beech wood at 773 K was carried out had minimal effect on the recovered product distribution. This was to be expected as the temperature was much lower than that required for gasification reactions to take between the reactive gases (CO_2 and CO) at a fast enough rate to cause noticeable differences in the product distribution (Higman and van der Burgt, 2008). The small differences in the character of the tars (observed via SEC and UVF analysis) may be a result of an inhibiting effect of the CO_2 and CO in the inlet gas on the decomposition of some of the less stable larger molecular weight tar fraction into smaller tar species.

6.3.2 Two-Stage Pyrolysis Experiments at 973 K under different gaseous environments

The two-stage pyrolysis experiments presented in this section were designed to determine the effects of exposing the primary pyrolysis products produced in the first stage to elevated temperatures of 973 K and increased inert surface areas in the 2nd stage of the reactor. The results from these experiments were used as a baseline allowing for the identification of any additional affects the presence of an oxygen carrier material in the 2nd stage may have on the product distributions under the same conditions.

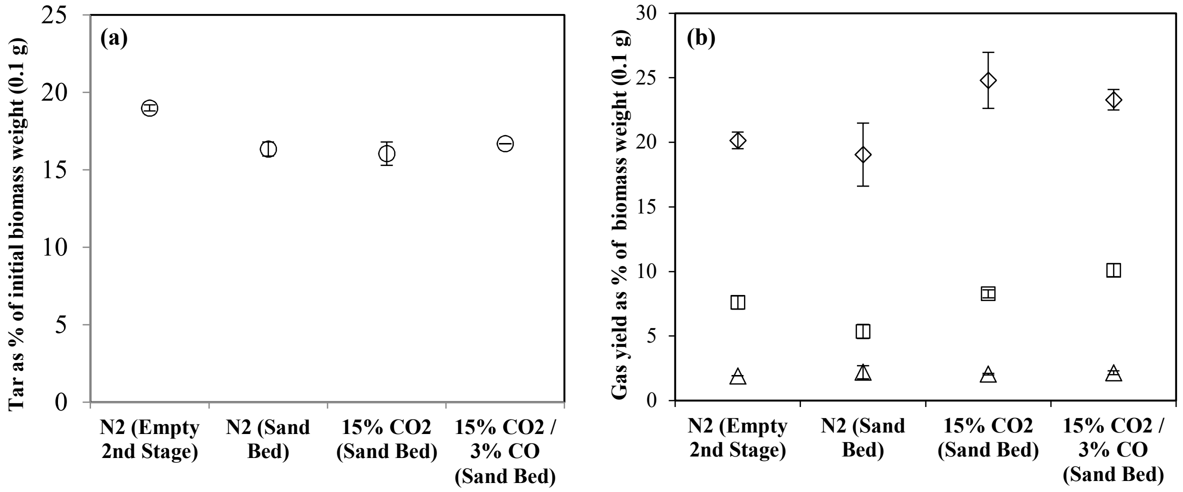

Figure 6.10. (a) Tar yields and (b) detectable gas yields produced from the fast pyrolysis of 0.100g of beech wood in different gaseous environments in the upgraded two-stage reactor with a 2nd stage sand bed at 973 K.

Experimental parameters: ***1st stage***: **Feed** = beech wood (0.100 g, 106-150 μm), **Temperature** = 773 K, **Hold time** = 300 s **Flow rate** = 60 ml$_N$ s^{-1} (0.25 m s^{-1}), **Pressure** = 1.5 bar$_a$. **Carrier gas** = variable; ***2nd stage***: **Bed type** = sand (0.75 g, 300-425 μm), **Temperature** = 973 K, **Flow rate** = 60 ml$_N$ s^{-1} (0.40 m s^{-1}). Tar (○), CO_2 (□), CO (◇) and CH_4 (△).

Exposure of the primary pyrolysis products produced in the first stage to the empty 2nd reactor stage at 973 K resulted in a substantial decrease in the tar yield from 46.3 wt.% to 19.0 wt.% representing a decrease in the tar yield of 59 % (fig. 6.10 (a)). The large decrease in tar yield was accompaied by a significant increase in the CO yield from 3.7 wt.% to 20.2 wt.%. Increases in the CO_2 and CH_4 were also observed but to a much lesser extent.

Adding the sand bed into the second stage at 973 K caused an additional albeit modest decrease in the tar yield of 13.4 % compared with the yield obtained from 2-stage pyrolysis experiment with an empty 2nd stage. A small decrease in the CO_2 yield was also observed but the yields of CO and CH_4 did not seem to be affected.

Varying the inlet gas composition had no additional effect on the tar yield; yields were within the experimental error of the yield obtained from the 2-stage pyrolysis experiment with a 2nd stage sand bed at 773 K under a N_2 atmosphere. The presence of CO_2 and CO in the carrier gas did however effect the product yields of CO_2 and CO (fig. 6.10 (b)). The CO_2 yield increased from 5.4 wt.% to 8.3 wt.% whereas the yield of CO increased from 19.1 wt.% to 24.8 wt.% when pyrolysis was carried out under an atmosphere containing 15 vol.% CO_2. The increase in the CO and CO_2 yields was most likely due to the onset of gasification reactions in the higher temperature 2nd stage between the CO_2 introduced in the carrier gas and some of the previously undetected products such as light hydrocarbon and carbon deposits that formed on the surfaces of the reactor walls and sand bed in the 2nd stage.

The yield of CO was slightly lower whilst the yield of CO_2 was slightly higher when CO was present in the carrier gas (*i.e.* 3 vol.% CO, 15 vol.% CO_2, bal. N_2) compared with the analogous experiment in an atmosphere of 15 vol.% CO_2. High surface concentrations of CO are known to inhibt the rates of char gasification by CO_2 (Liu and Niksa, 2004). The presence of CO is likely to have had a similar effect on the gasification of the other pyrolysis products explaining the slightly higher yield of CO_2 and lower yield of CO observed here compared with the equivalent yields obtained when only CO_2 (and N_2) was present in the carrier gas. The presence of CO in the carrier gas will have also affected the equilibirum position according to Le Chatelier's principle resulting in a less CO produced.

Summary

Subjecting the tars and other volatile pyrolysis products to elevated temperatures of 973 K caused a substantial reduction in the tar yield. The reduction in the tar yield was accompanied by a significant increase in the yield of CO and a smaller increase in the CO_2 yield. Introducing a bed of sand to increase the inert surface area within the 2nd stage caused a further modest reduction in the tar yield but did not seem to affect the yields of the detectable gases. The presence of 15 vol.% CO_2 in the carrier gas did not affect the tar yield but resulted in slightly improved yields of CO and CO_2 which was attributed to the onset of gasification reactions between the CO_2 in the carrier gas and undetected pyrolysis products such as light hydrocarbons and carbon deposits that formed on the surfaces within the 2nd stage. The presence of 3 vol.% CO in the carrier gas appeared to inhibit the extent of the gasification reactions.

6.3.3 The effects of the OC material on the volatile biomass pyrolysis products on the performance of a 100Fe(S) oxygen carrier material

Product Distribution

Exposure of the pyrolysis products to the bed of 100Fe(S) oxygen carrier material (0.75 g, 300-425 µm) in the second stage caused further reductions in the tar yields relative to the yields obtained under analogous conditions with an inert sand bed in the 2nd stage (fig. 6.11(a)). The reduction in tar yields were between 26.7 wt.% and 38.9 wt.%. The amount of tar recovered after exposure to the 100Fe(S) bed in both its oxidised and reduced forms under the different gaseous environments were between 10.1 wt.% and 11.8 wt.%. No distinguishable trend was observed between tar yield or reduction in tar yield, and the condition of the oxygen carrier (i.*e.* oxidation state) and gas inlet composition.

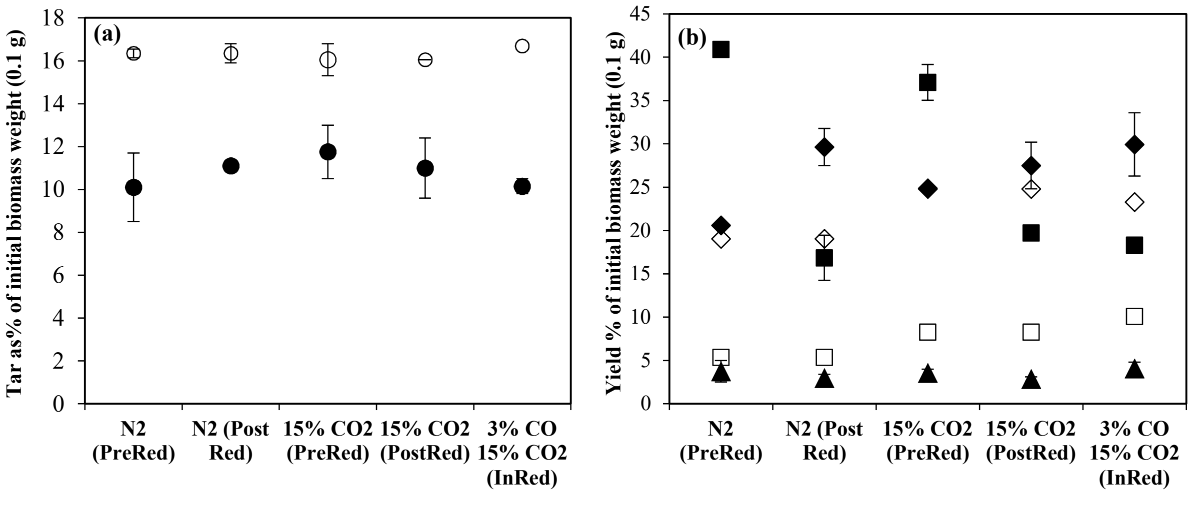

Figure 6.11. (a) Tar yields and (b) detectable gas yields from the different simulated CLC experiments in which the 100Fe(S) OC material is exposed to volatile pyrolysis products during the 3rd cycle reduction phase at 973 K.

Experimental parameters: **1st stage**: **Feed** = beech wood (0.100 g, 106-150 µm), **Temperature** = 773 K, **Flow rate** = 60 ml_N s^{-1} (0.25 m s^{-1}), **Pressure** = 1.5 bar_a, **Carrier gas** = variable, **Biomass feed cycle no.** = 3, ***2nd stage***: **Oxygen Carrier** = 100Fe(S) (5 mg, 150-212 µm); **Reaction** = $Fe_2O_3 \rightarrow Fe_3O_4$, **Oxidation State of OC** = variable, **Temperature** = 973 K, **Flow rate** = 60 ml_N s^{-1} (0.40 m s^{-1}), **Total Number of CLC Cycles** = 5. Tar (●); CO_2 (■); CO (◆) CH_4 (▲); open symbols are gas yields for analogous experiments with an inert sand bed in place of the oxygen carrier.

Inspection of the SEC results (fig. 6.12) shows that there were some subtle differences in the molecular mass distribution of the tar collected after exposure to the 100Fe(S) OC materials in their oxidised (Fe_2O_3, i.e. 'N2(PreRed)' conditions) and reduced forms (Fe_3O_4, i.e. 'N2(PostRed)' conditions). The tar recovered after exposure to the reduced OC materials (i.e. 'PostRed' conditions) appeared to comprise of a larger proportion of the higher molecular mass fraction (excluded peak) and less of the lower molecular mass fraction (retained peak) compared with the tar recovered after exposure to the oxidised OC materials ('PreRed' conditions). The same trends in the SEC analysis were observed for the tar recovered after analogous experiments in an atmosphere of 15 mol.% CO_2, balance N_2 (appendix C, fig. C.1). The SEC results indicate that the oxidation state of the OC material influences the mechanism by which tar compounds crack and/or reform in the system.

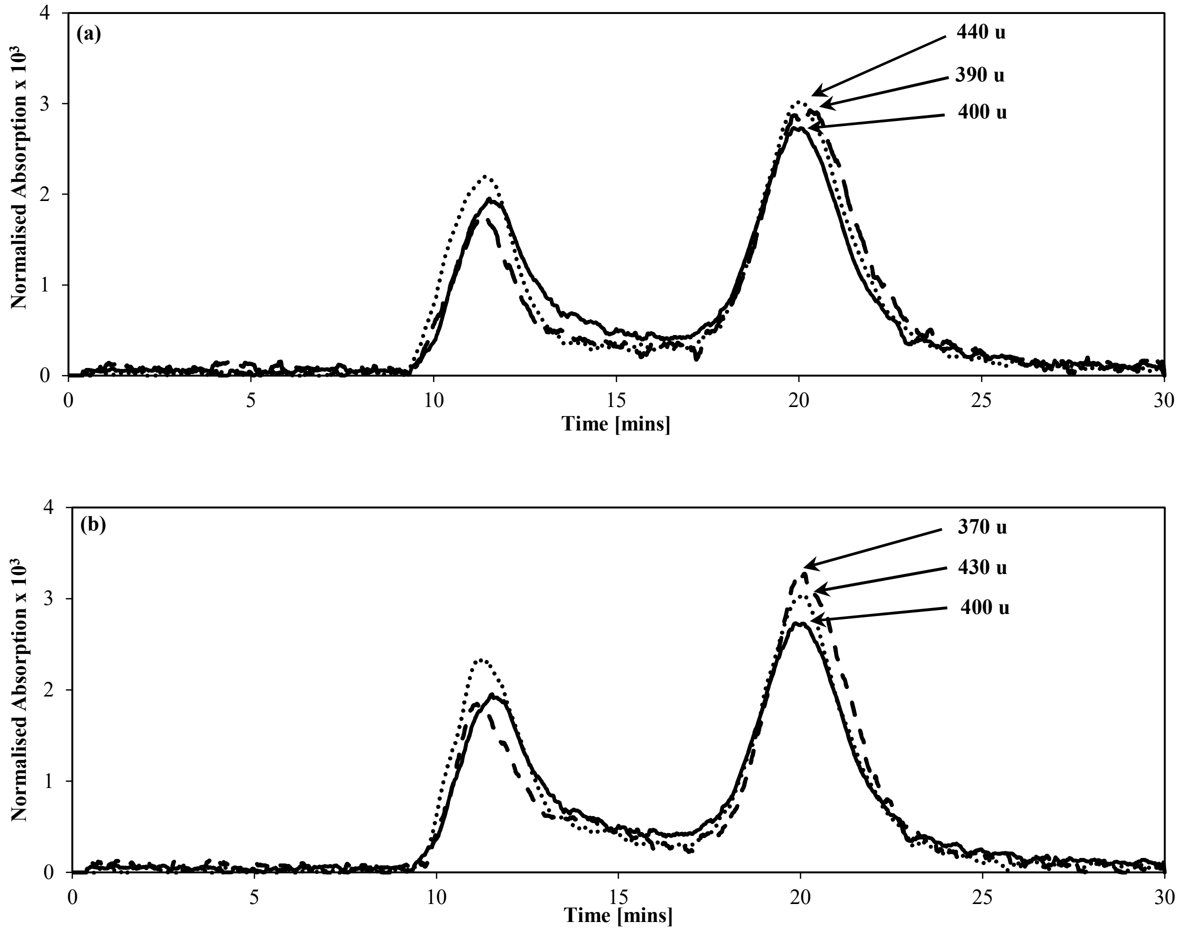

Figure 6.12. SEC analyses of the tars recovered from the fast pyrolysis of 0.10 g of beech wood in the two-stage reactor loaded with (a) the 100Fe(S) OC material and (b) 60Fe40Al(SAC) OC material in both their oxidised and reduced forms under a N_2 atmosphere. **Experimental parameters:** ***1^{st} stage***: **Feed** = beech wood (0.100 g, 106-150 μm); **Carrier gas** = N_2, **Pressure** = 1.5 bar$_a$, **Flow rate** = 60 ml$_N$ s^{-1} (0.25 m s^{-1}), **Temperature** = 773 K, **Hold time** = 300 s. **Biomass feed cycle no.** = 3, ***2^{nd} stage***: **Oxygen Carrier** = (a) 100Fe(S) and (b) 60Fe40Al(SAB) (0.75 g, 300-425 μm), **Reaction** = $Fe_2O_3 \rightarrow Fe_3O_4$, **Temperature** = 973 K, **Flow rate** = 60 ml$_N$ s^{-1} (0.40 m s^{-1}), **Total number of CLC cycles** = 5. Sand (——); 'PreRed' conditions (– – –); 'PostRed' conditions (·········).

There were no obvious differences between the UVF spectra of the tar collected after exposure to the 100Fe(S) OC material in its oxidised or reduced form (in a N_2 atmosphere) although the peaks were slightly broader and appeared at a slightly higher wavelength compared with the spectra of the tars collected after exposure to a bed of sand under the same conditions (fig. 6.13 (a)). Similar behaviour was observed in the spectra of the tar exposed to the 60Fe40Al(SAB) OC materials (fig. 6.13 (b)). The UVF spectra of the tar exposed to the 60Fe40Al(SAB) OC materials also show the emergence of a small peak at a wavelength of 385 nm. This observation indicates that interactions (whether that be cracking, reforming, polymerisation etc.) in the presence of the 60Fe40Al(SAB) OC materials resulted in the formation of a tar species with a relatively high extent of conjugation that was not formed when the tar was exposed to the 100Fe(S) OC material or a bed of sand. The small peak at the higher wavelength was more intense in the spectra of tar collected after exposure to the 60Fe40Al(SAB) OC material in its reduced form compared with the tar collected after exposure to the OC in its oxidised form. Similar trends were observed in the spectra of tars collected after analogous experiments carried out under an atmosphere of 15 mol.% CO_2, balance N_2 (appendix C, fig. C.2).

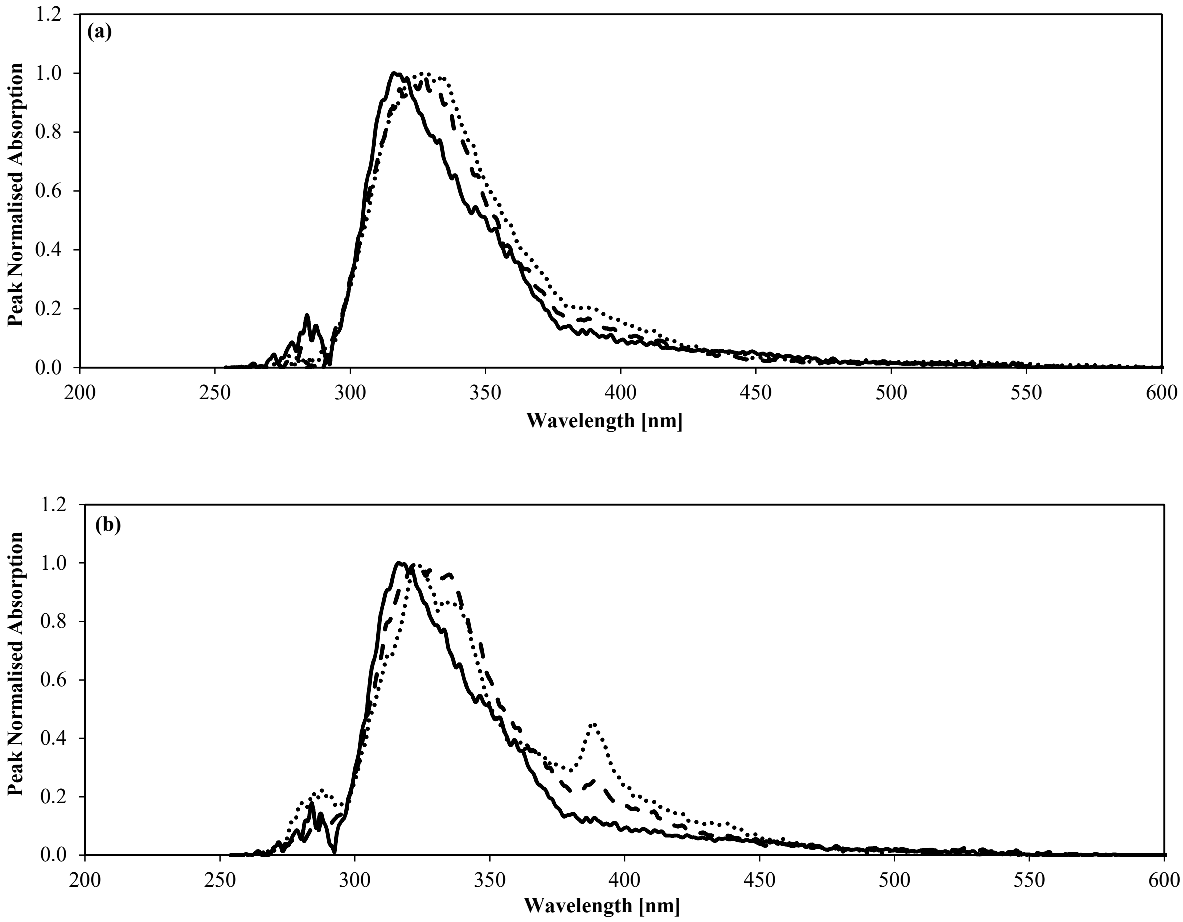

Figure 6.14. UVF spectra of the tars recovered from the fast pyrolysis of 0.10 g of beech wood in the two-stage reactor loaded with (a) the 100Fe(S) OC material and (b) 60Fe40Al(SAC) OC material in both their oxidised and reduced forms under a N_2 atmosphere. **Experimental parameters:** ***1st stage***: **Feed** = beech wood (0.100 g, 106-150 μm); **Carrier gas** = N_2, **Pressure** = 1.5 bar_a, **Flow rate** = 60 $ml_N\ s^{-1}$ (0.25 $m\ s^{-1}$), **Temperature** = 773 K, **Hold time** = 300 s. **Biomass feed cycle no.** = 3, ***2nd stage***: **Oxygen Carrier** = (a) 100Fe(S) and (b) 60Fe40Al(SAB) (0.75 g, 300-425 μm), **Oxidation state** = variable; **Reaction** = $Fe_2O_3 \rightarrow Fe_3O_4$, **Temperature** = 973 K, **Flow rate** = 60 $ml_N\ s^{-1}$ (0.40 $m\ s^{-1}$), **Total number of CLC cycles** = 5. Sand (——); 'PreRed' conditions (– – –); 'PostRed' conditions (·········).

The conditions under which the OC material was exposed to the volatile biomass pyrolysis products (*i.e.* oxidation state of the 100Fe(S) OC and carrier gas composition) had a significant effect on the CO_2 and CO yields (fig. 6.11(b)). The CO_2 yields were substantially larger when the OC material was exposed to the biomass pyrolysis products in its oxidised state (*i.e.* experiments denoted as N_2_Pre-Red and 15%CO_2_Pre-Red). The higher yield of CO_2 was the result of interactions between the volatile pyrolysis products and Fe_2O_3 resulting in the oxidation of the pyrolysis products to produce CO_2 (and possibly other oxygenated products) and reduction of Fe_2O_3 to Fe_3O_4 (and possibly further depending on the composition of the carrier gas).

The yield of CO_2 produced during the N_2_Pre-Red experiments were slightly higher at 40.9 wt.% compared with the 15%CO_2_Pre-Red experiments where the CO_2 yield was 37.1 wt.%. A similar but opposite trend was observed in the yields of CO. The input of 15 vol.% into the carrier gas imposed a thermodynamic constraint on to the iron-based OC system limiting reduction of Fe_2O_3 to Fe_3O_4, which in turn limited the oxygen transport capacity of the OC material. The difference in the CO_2 and CO yields was most likely due to the lower amount of oxygen that the Fe_2O_3 was able to transfer to the volatile pyrolysis products during the 15%CO_2_Pre-Red experiment (where reduction of the Fe_2O_3 OC material was limited) compared with the N_2_Pre-Red experiment (where reduction was not limited).

Exposure of the volatile pyrolysis products to the 100Fe(S) bed in its reduced form under atmospheres of 100 vol.% N_2 and 15 vol.% CO_2, 85 vol.% N_2, produced respectively similar CO_2 and CO yields. In both cases, the yields of CO_2 and CO were higher than the yields obtained from the equivalent experiments with an inert sand beds in the 2nd stage. The size of the increase in the CO and CO_2 yields was larger (particularly in the case of the CO yield) for the experiments carried out under a N_2 atmosphere compared with the experiments carried out in an atmosphere contained 15 vol.% CO_2.

The increase in the yields of CO_2 and CO during the N_2_Post-Red experiments compared with the N_2_Sand experiments was most likely due to reactions between the reduced 100Fe(S) OC material (Fe_3O_4) and volatile pyrolysis products resulting in the further reduction of Fe_3O_4 (to $Fe_{0.97}O$ and possibly Fe) and the oxidation of the pyrolysis products. The higher yield of CO and lower yield of CO_2 observed for the N_2_Post-Red experiments compared with the N_2_Pre-Red experiments will have been due to the lower amount of available oxygen and larger proportion of incomplete, partial oxidation/reduction reactions taking place between the volatile pyrolysis products and the 100Fe(S) OC material in its less reactive reduced forms (Fe_3O_4 and $Fe_{0.97}O$).

The smaller increase in the CO_2 and CO yields observed for the 15%CO_2_Post-Red experiments (relative to the 15%CO_2_Sand experiments) compared with the difference observed in the yields obtained from the experiments carried out in N_2 can only be a result of enhanced cracking/gasification of the pyrolysis products on the surface of the reduced 100Fe(S) (Fe_3O_4) OC. Further reduction and transfer of oxygen from the reduced 100Fe(S) OC material (Fe_3O_4) was prevented by the thermodynamic constraint imposed on the 100Fe(S) OC system by the inclusion of 15 vol.% CO_2 in the carrier gas. Despite the inability of the 100Fe(S) material to be reduced further, the yields of CO and CO_2 were comparable to those obtained during the N_2_Post-Red experiments. This was due to additional gasification reactions taking place between the pyrolysis products and the CO_2 present in the carrier gas; which also contributed to the higher yields of CO_2 and CO obtained during the 15%CO_2_Sand experiments compared with the N_2_Sand experiments.

The presence of the 100Fe(S) OC material did not affect the CH_4 yields which remained between 3.6-4.1 wt.% across all conditions studied.

The effect of pyrolysis product exposure on the reactivity of the 100Fe(S) OC

A few experiments were carried out where the an additional two cycles were completed with gaseous reduction (3 vol.% CO, 15 vol.% CO_2, bal. N_2) after the oxygen carrier material was exposed to the biomass pyrolysis products in the 3rd cycle. Figure 6.12 provides details relating the maximum rate of reduction observed during the reduction of $Fe_2O_3 \rightarrow Fe_3O_4$ as a function of cycle number.

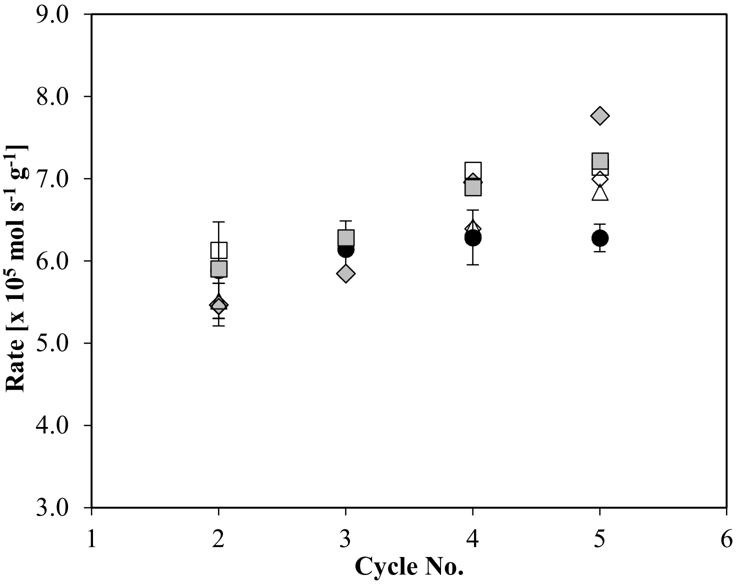

Figure 6.15. Maximum rate of reduction ($Fe_2O_3 \rightarrow Fe_3O_4$) with CO as a function of cycle number for the simulated CLC experiments in which the 100Fe(S) OC material was exposed to volatile pyrolysis products during the 3rd cycle reduction phase at 973 K. 5 cycle experiment with no exposure to pyrolysis products (●); 100%N2_PreRed (◇);100%N2_PostRed (◈); 15%CO2_PreRed (□);15%CO2_PostRed (▣); 3%CO15%CO2_InRed (△).

Experimental parameters: ***1st stage***: **Feed** = beech wood (0.100 g, 106-150 μm), **Temperature** = 773 K, **Flow rate** = 60 ml$_N$ s^{-1} (0.25 m.s^{-1}), **Pressure** = 1.5 bar$_a$, **Carrier gas**: variable; **Biomass feed cycle no.** = 3; ***2nd stage***: **Oxygen Carrier** = 100Fe(S) (0.75 g, 3000-425 μm), **Reaction** = $Fe_2O_3 \rightarrow Fe_3O_4$, **Temperature** = 973 K, **Flow rate** = 60 ml$_N$ s^{-1} (0.40 m s^{-1}), **Total Number of CLC Cycles** = 5.

The observed rate of reduction of the 100Fe(S) OC that was not exposed to the pyrolysis products in the 3rd cycle exhibited a fairly stable reactivity across all four cycles (2-5) presented in figure 6.12. There was a small increase in the observed rate between cycles 2 and 3 but the observed rate was constant from cycle 3 onwards at ~ 6.2 x 10^{-5} mol s^{-1} g^{-1}. The reactivity of the OC carriers exposed to the pyrolysis products appeared to increase with cycle number after exposure to the pyrolysis products in the 3rd cycle. The extent of the increase in the observed rate of reaction relative to the baseline reactivity where the OC was not exposed to pyrolysis products in the 3rd cycle seems to be slightly larger for the experiments where the OC material was exposed to the pyrolysis products in its reduced form. An initial hypothesis was that the increase in rate was a result of surface area and pore size enhancements caused by cracking and fracturing of the particles due to stresses imposed on the particles by the rapid combustion of carbon deposits on the surface of the particles when the OC material was re-oxidised during the 3rd cycle oxidation phase. Carbon deposition can be clearly seen in figure 6.15 of the 100Fe(S) OC material retrieved after the 15%CO_2_Pre-Red and 15%CO_2_Post-Red experiments. However, analysis of the pore size distributions via N_2 adsorption and mercury intrusion analysis showed no discernible differences between the pore size distributions and surface areas of the reacted 100Fe(S) OC material that was not exposed to the biomass pyrolysis products and the 100Fe(S) OC material that was exposed to the pyrolysis products under the different conditions.

Due to time limitations only a few repeats were possible which means an error range could not be determined for many of the results presented here. It is therefore not possible to determine whether the observed improvements in the reactivity of the OC in the cycles after the OC material was exposed to the pyrolysis products were significant or whether variation was within the experimental error. What can be stated with confidence is that there were no significant deleterious effects on the reactivity of the 100Fe(S) OC material after exposure to the biomass tars and other pyrolysis products.

6.3.4 The effects of the volatile biomass pyrolysis products on the performance of a 60Fe40Al(SAB) oxygen carrier material

Product Distribution

A larger reduction in the tar yield was observed when the pyrolysis products were exposed to the 60Fe40Al(SAB) OC material in the 2nd stage of 48-71 wt.% (relative to the equivalent experiments with a bed of sand) compared with the reduction in tar yield observed for the 100Fe(S) OC of 26.7-38.9 wt.% (fig. 6.13 (a)). The greater tar conversion efficiency was probably a result of the substantially larger surface area presented by the 60Fe40Al(SAB) OC material on which tar oxidation, gasification and cracking interactions can take place compared with the 100Fe(S) OC material (chapter 5, table 5.3).

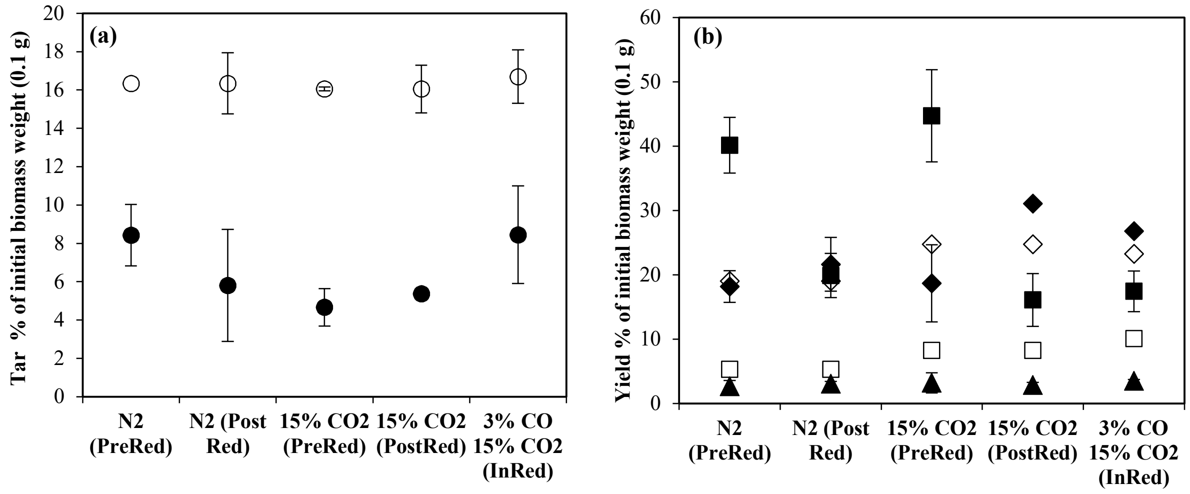

Figure 6.16. (a) Tar yields and (b) detectable gas yields from the different simulated CLC experiments in which the 60Fe40Al(SAB) OC material was exposed to volatile pyrolysis products during the 3rd cycle reduction phase at 973 K. **Experimental parameters:** ***1st stage***: **Feed** = beech wood (0.100 g, 106-150 μm), **Temperature** = 773 K, **Flow rate** = 60 $ml_N\ s^{-1}$ (0.25 $m\ s^{-1}$), **Pressure** = 1.5 bar_a, **Carrier gas** = variable, **Biomass feed cycle no.** = 3, ***2nd stage*****: Oxygen Carrier** = 60Fe40Al(SAB) (0.75 g, 300-425 μm), **Reaction** = $Fe_2O_3 \rightarrow Fe_3O_4$, **Oxidation State of OC** = variable, **Temperature** = 973 K, **Flow rate** = 60 $ml_N\ s^{-1}$ (0.40 $m\ s^{-1}$), **Total Number of CLC Cycles** = 5. Tar (●); CO_2 (■); CO (◆) CH_4 (▲); open symbols are gas yields for analogous experiments with an inert sand bed in place of the oxygen carrier.

The yields and trends in the yields of CO_2 and CO (fig. 6.13 (b)) were very similar to those observed for the equivalent experiments involving the 100Fe(S) OC material in the 2nd stage (fig. 6.11 (b)). Exposure of the pyrolysis products to the OC material in its oxidised form resulted in a substantial increase in the yield of CO_2 as a result of interactions between the pyrolysis products and OC material in its most reactive form (Fe_2O_3). Smaller improvements in the CO_2 yields were observed when the pyrolysis products were exposed the OC material in its reduced state (Fe_3O_4 and possible $FeAl_2O_4$ see section 5.4.7) in favour of a larger increase in the CO yield. The increase in CO yield was either due to interactions between the pyrolysis products and the OC material in its less reactive reduced state (Fe_3O_4 and possible $FeAl_2O_4$) resulting in a larger proportion of incomplete, partial oxidation reactions taking place and/or; enhanced cracking and gasification of the pyrolysis products during experiments carried out with a carrier gas of 15 vol.% CO_2, bal. N_2. The introduction of 15 vol.% CO_2 into the carrier gas as a means to limit the reduction of Fe_2O_3 to Fe_3O_4 was not effective for experiments involving Al_2O_3 supported Fe_2O_3 as Fe_3O_4 can be reduced further to $FeAl_2O_4$ under these conditions.

Interestingly, the pyrolysis product yields obtained after exposure to the 60Fe40Al(SAB) OC material were similar to the equivalent yields obtained after exposure to the 100Fe(S) OC material despite the fact that the total amount of the active OC component Fe_2O_3 added to the reactor was lower in the case of the experiments involving the 60Fe40Al(SAB). The higher effectiveness of the 60Fe40Al(SAB) was most likely a result of: (i) increased contact between the OC material and pyrolysis products due to the higher surface area of the material; (ii) the improved reactivity of the supported OC (as observed in chapter 5, section 5.4.7) and/or; (iii) the improved oxygen transport capacity due to the ability of the OC material to interact with the support allowing for further reduction of Fe_3O_4 to $FeAl_2O_4$ (which is not supressed by the inclusion of 15 vol.% CO_2 in the carrier gas). The presence of Al_2O_3 has been found to enhance the reduction reactivity of Fe_3O_4 with CO allowing the formation of $FeAl_2O_4$ compared with the reduction reactivity of Fe_3O_4 in the absence of Al_2O_3 where only $Fe_{0.97}O$ can be formed (Abad et al., 2007b).

Methane yields were low and remained fairly constant between 2.7-3.5 wt.%. The yields were not affected by the introduction of the 60Fe40Al(SAB) relative to the experiments in which the 2nd reactor stage contained an inert sand bed.

The effect of pyrolysis product exposure on the reactivity of the 60Fe40Al(SAB) OC

The opposite trend in the reactivity of the 100Fe(S) OC material was observed for the 60Fe40Al(SAB) OC (fig. 6.14). In almost all cases, the reactivity of the OC material after exposure to the pyrolysis products was slightly lower relative to the reactivity of the OC material measured during the cycles before exposure to the pyrolysis products and to the reactivity of the OC material that was not exposed to the pyrolysis products. The error ranges for these measurements were large (relative standard deviation of up to 25 %) such that the variation in the rates of reduction observed in the cycles after the 60Fe40Al(SAB) was exposed to the pyrolysis products under the different conditions were within the experimental error.

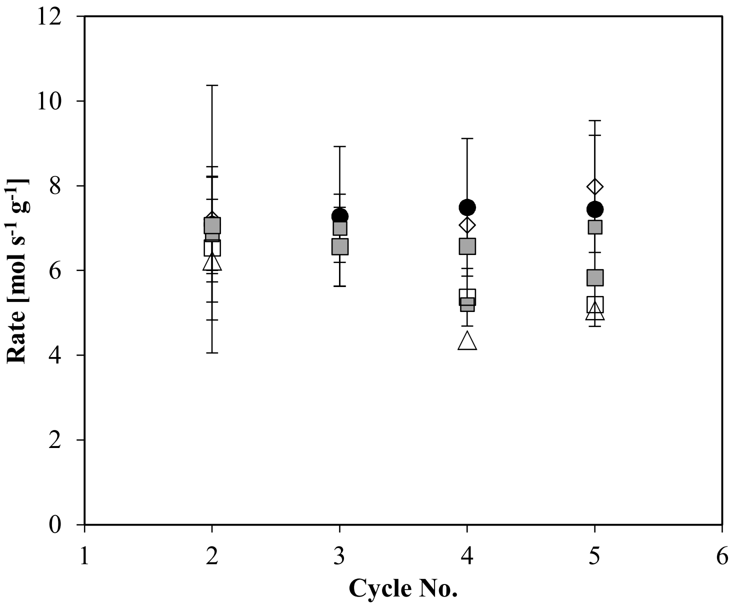

Figure 6.17. Rate of reduction ($Fe_2O_3 \rightarrow Fe_3O_4$) with CO as a function of cycle number for the simulated CLC experiments in which the 60Fe40Al(SAB) OC material was exposed to volatile pyrolysis products during the 3rd cycle reduction phase at 973 K. 5 cycle experiment with no exposure to pyrolysis products (●); 100%N$_2$_PreRed (◇);100%N$_2$_PostRed (◈); 15%CO$_2$_PreRed (□);15%CO$_2$_PostRed (▣); 3%CO15%CO$_2$_InRed (△).

Experimental parameters: ***1st stage***: **Feed** = beech wood (0.100 g, 106-150 µm), **Temperature** = 773 K, **Flow rate** = 60 $ml_N\ s^{-1}$ (0.25 $m\ s^{-1}$), **Pressure** = 1.5 bar_a, **Carrier gas** = variable, **Biomass feed cycle no.** = 3, ***2nd stage***: **Oxygen Carrier** = 60Fe40Al(SAC) (0.75 g, 300-425 µm), **Reaction** = $Fe_2O_3 \rightarrow Fe_3O_4$, **Oxidation State of OC** = variable, **Temperature** = 973 K, **Flow rate** = 60 $ml_N\ s^{-1}$ (0.40 $m\ s^{-1}$), **Total Number of CLC Cycles** = 5.

The 60Fe40Al(SAC) OC material had a much lower bulk density than the 100Fe(S) OC material which meant the length of the bed produced by adding 0.75 g of the OC material into the 2nd stage of the reactor was different. The length of the 100Fe(S) bed was ~ 0.5 mm (equivalent to 1-2 particles in height) whereas the length of the bed created by 0.75 g of the 60Fe40Al(SAB) was larger at ~ 4 mm. The pressure drop through the bed of 60Fe40Al(SAB) will have been greater than the 100Fe(S) OC bed and will therefore have been more prone to issues associated with gas bypass and channelling. Gas bypass and channelling results in a non-uniform flow of the gas through the bed and an underutilisation of certain sections of the bed. The reduced contact between the gas and the OC material will result in a lower observed maximum rate of reduction and a reaction that takes place over a longer period of time. It is also possible that the temporal disruption to the pressure and flow profile through the reactor caused by the biomass feeding may have aided the formation of channels through the bed contributing to the depressed rate of reduction with CO observed for cycles 4 and 5 after the OC material was exposed to the pyrolysis products in the 3rd cycle (fig. 6.14).

The extent of gas bypass will also affect the distribution of products retrieved after exposure of the bed to the pyrolysis products. The larger errors observed in both the product distributions and maximum rates of reduction for the experiments involving the 60Fe40Al OC material (compared with the equivalent study involving the 100Fe(S) OC) is therefore likely to be a result of different extents of gas bypass and channelling in the different experiments.

6.3.5 Carbon Deposition

The OC material retrieved after exposure to the pyrolysis products in the 3rd reduction cycle appeared to be coated with a thin layer of black carbon (fig. 6.15). The observed carbon deposition was likely due thermal/catalytic decomposition of the hydrocarbon species produced during pyrolysis in the first stage on the surface of the oxygen carrier material (Mendiara et al., 2011). Small samples of each of the 100Fe(S) and 60Fe(SAB) OC materials retrieved after exposure to the pyrolysis products were submitted for elemental (CHN) analysis in an attempt to quantify the extents of carbon deposition (table 6.4).

The results of elemental analysis revealed that the extent of carbon deposition was greatest in the case of the 60FeAl(SAB) OC material compared with the 100Fe(S) material. Carbon deposition on the surface OC material accounted for 2.7-5.5 wt.% and 7.3-9.9 wt.% of the initial biomass feed mass for the 100Fe(S) and 60Fe40Al(SAB) OC particles respectively. The extent of carbon deposition was also higher when the OC materials were exposed to the pyrolysis products in their reduced form (*i.e.* the Post-Red experimental conditions) (table 6.4).

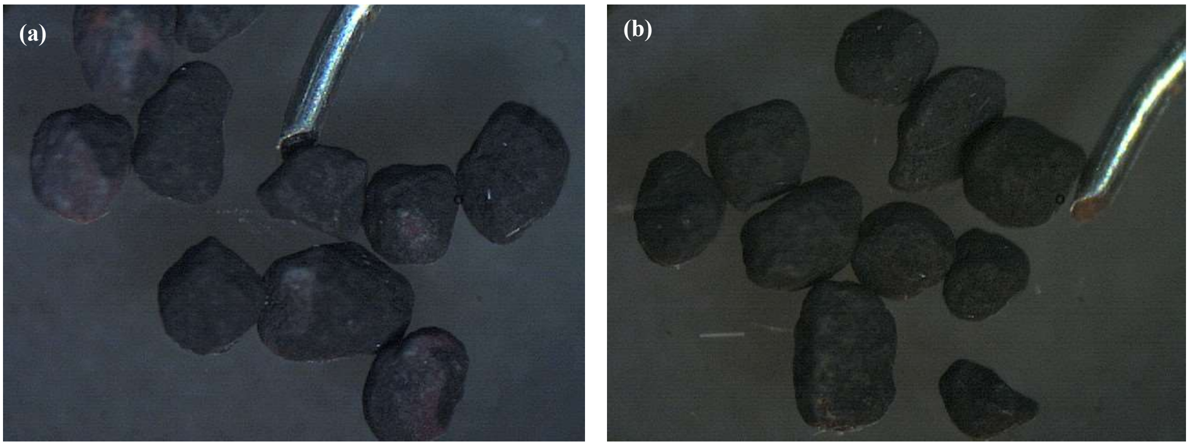

Figure 6.18. Light microscope images of (a-b) the coked 100Fe(S) OC particles and (c-d) coked 60Fe40Al OC particles retrieved after exposure to the biomass pyrolysis products under conditions of (a,c) 15%CO$_2$_Pre-Red and (b,d) 15%CO$_2$_Post-Red.

Table 6.4. Extent of carbon deposition on the surface of the OC materials retrieved after exposure to the biomass pyrolysis products under the different conditions measured via elemental CHN analysis.

Biomass feed condition	Carbon content of coked OC [wt.%]		Carbon deposition as percentage of initial biomass feed weight [wt.%]*	
	100Fe(S)	60Fe40Al(SAB)	100Fe(S)	60Fe40Al(SAB)
100%N2_Pre-Red	0.53	1.05	3.551	7.35
100%N2_Post-Red	0.82	1.41	5.494	9.87
15%CO2_Pre-Red	< 0.3	1.04	-	7.28
15%CO2_Post-Red	0.69	1.28	4.623	8.96
3%CO15%CO2_In-Red	0.4	1.2	2.68	8.4

* Assumes that carbon deposition was uniformly distributed across all the surfaces of the OC particles in the 2nd stage reactor bed.

6.4 Discussion and Conclusions

The results presented in this chapter confirm that the presence of large quantities of tars in the fuel gas for a chemical-looping combustion process is indeed a problem that can lead to significant coking of the oxygen carrier. Carbon deposition can cause temporary deactivation of the oxygen carrier material and will result in a reduction in the carbon capture efficiency of a CLC process as the carbon deposits will be burnt off in the air reactor releasing CO_2 that cannot be captured. Both materials investigated in this study were affected by carbon deposition but the effect was greatest for the 60Fe40Al(SAB) oxygen carrier where carbon deposition accounted for 7.3-9.9 % of the initial biomass weight fed into the system. Carbon deposition was marginally lower when the OC material was exposed to the biomass tars and other pyrolysis products in its oxidised form but the improvement was small. This indicates that only a small reduction in the carbon deposition extent would be possible by controlling the oxidation state of the OC material in the system.

The presence of both oxygen carrier materials in the 2nd stage of the reactor at 973 K reduced the amount of tars exiting the reactor compared with analogous experiments in which the pyrolysis products were exposed to an inert sand bed. The tar cracking effect of the 60Fe40Al(SAB) OC material appeared to be greater than the 100Fe(S) OC material although the reduction in the tar yield was roughly equivalent to the increase in carbon deposition observed for the 60Fe40Al(SAB) OC compared with the 100Fe(S) OC material. The tar cracking effect of the oxygen carriers appeared to be independent of the oxidation state in which the oxygen carrier was exposed to the volatile biomass pyrolysis products (i.e. Fe_2O_3 or Fe_3O_4). This indicates that the enhanced elimination of tars in the presence of the OC material was due to enhanced thermal or catalytic cracking on the surface of the OC material rather than the result of tars directly reacting with the OC material. The increased yields of CO_2 that were observed when the biomass tars were exposed to the OC materials in their oxidised forms was likely due to the oxidation of lighter, previously undetected gaseous hydrocarbons and/or the oxidation of the products produced from the tar cracking interactions that took place on the surface of the OC materials.

Further work is necessary to investigate the effect of higher temperatures that are more comparable to the sorts of temperatures that an OC material would be exposed to in a commercial CLC system. The presence of steam should also be studied to determine whether the addition of steam could be used to improve tar conversion whilst at the same time reducing carbon deposition.

Gas yield measurements revealed that exposing the pyrolysis products to the OC in its oxidised form resulted in a greater conversion to CO_2 as is desirable in a CLC process. A lower conversion to CO_2 was observed when the pyrolysis products were exposed to the reduced OC materials with interactions appearing to favour production of CO. Conversion of the tars and pyrolysis products to CO is particularly desirable for applications of chemical-looping reforming (CLR) and biomass syngas upgrading. Further work is therefore necessary to explore the possibility of using a process based on chemical-looping for biomass syngas upgrading and reforming for the production of a tar-free bio-derived fuel gas.

Chapter 7

Summary of Conclusions

The development of a commercially viable carbon capture and sequestration (CCS) technology for fossil fuel power generation is vital if the anticipated effects of global warning are to be avoided. A key challenge facing the development of CCS technology is that CO_2 must be obtained from power stations in a pure stream due to the limited geological space available for CO_2 sequestration. To achieve this, most carbon capture technologies use energy intensive gas separation techniques such as air liquefaction to generate O_2 or solvent based chemical systems for extracting CO_2 from syngas or flue gases.

Chemical-looping combustion (CLC) is a combustion process that intrinsically generates a flue stream of near-pure CO_2 circumventing the need for gas separation processes such that in theory, no energy is expended for gas separation. The development of a CLC process utilising biomass is of particular interest as it has the potential to result in negative CO_2 emissions *i.e.* a net removal of CO_2 from the atmosphere. Most CLC research has focused on gaseous fuels and extended pilot scale trials have demonstrated the feasibility of natural gas CLC for large scale power generation [1]. CLC using solid fuels or gasified solid fuels is more complex and less well understood as larger amounts of contaminants are introduced into the system such as light hydrocarbons, tar vapours, alkali compound vapours, sulfur and nitrogen containing species and ash. However to date, only a few studies have been carried out/published investigating the use of biomass as a fuel for CLC.

This thesis documents the progress made towards the development of a robust laboratory based system for testing the effects of biomass tars on the long term performance of a chemical-looping combustion process. The work completed in this thesis can be divided into two main areas: the first involved developing optimised fabrication strategies for the production of inexpensive iron-based oxygen carrier particles of high reactivity and robust physical characteristics that could be used in CLC systems utilising biomass as the fuel. The second research focus involved the development of a reactor and analysis protocol for studying the interactions between biomass pyrolysis tars and the cheap, synthetic iron-based oxygen carrier materials.

7.1 The influence of biomass properties and pyrolysis conditions on the pyrolysis product distribution

Chapter 3 reports and discusses the results from experimental investigations into the effects of biomass type, elevated temperatures (973-1173 K) and presence of cheap potentially catalytic solid material on the product distribution from the slow pyrolysis of biomass. This work was carried out as part of the initial training into: (i) the operation of high-temperature hot-rod reactors; (ii) procedures for conducting biomass pyrolysis experiments to achieve repeatable results; (iii) protocols for treating and isolating pyrolysis tars; and (iv) protocols for handling and analysing the pyrolysis tars and other recoverable pyrolysis products. It was also the intention to use the experience gained conducting the preliminary work discussed in chapter 3 to assess the suitability of the pre-existing 2-stage fixed-bed reactor for studying interactions between biomass tars and chemical-looping oxygen carriers at conditions relevant to large scale CLC systems.

Results into the effects of biomass type on the product distributions obtained from the slow pyrolysis experiments in the single stage reactor indicated that the total content and composition of the ash had the largest effect on the char, tar and gas yields. Biomass species containing large amounts of ash produced the largest amount of char. Pyrolysis of two rice husk species (originating from Brazil and Thailand) produced significantly different tar and gas yields but similar char yields despite containing similar quantities of ash. The observed differences in the pyrolysis behaviour between the two rice husk species was attributed to the larger amount of potassium in the Thai rice husk. It was proposed that the potassium containing ash component acted as a catalyst for tar decomposition reactions favouring the production of gaseous products as opposed to char. Other biomass properties such as O/C ratios of the parent biomass and surface area, porosity and pore size distribution of the resultant char were found to have less influence on the pyrolysis behaviours of the biomass varieties studied in this work.

The combustion and CO_2 gasification reactivity of the resultant chars were also studied in a TGA with air at 773 K and CO_2 at 1173 K respectively. Chars with the greatest extents of macroporosity and potassium contents were found to exhibit the highest combustion reactivitites in air at 773 K. Different trends were observed for the gasification reactivities. It was found that chars containing large amounts of silica in combination with alkali metals demonstrated the lowest reactivities with CO_2 at 1173 K. This behaviour was attributed to the formation of molten alkali silicate phases that deactivated the catalytic effect of the alkali metal and blocked access to the pores reducing the available reactive surface area of the char. The reactivities of the chars in the CO_2 gasification tests appeared to correlate well with the combined content of Ca and Mg present in the char.

In the second section of chapter 3, the fixed bed reactor was used in its 2-stage configuration to investigate the effects of elevated temperatures (973-1173 K), increased surface area and presence of potentially catalytically active materials on the tar and gas yields produced from the pyrolysis of beech wood in the first stage. Subjecting the tars and other volatile pyrolysis species to elevated temperatures resulted in a dramatic reduction in the tar yield. The extent of the reduction in tar yield increased with increasing temperatures due to enhanced thermal cracking of the tars. At 1173 K, 97 wt.% of the primary pyrolysis tars produced in the first stage were eliminated. The reduction in tar yield was accompanied by a significant increase in the CO yield and smaller increases in the yields of CO_2 and CH_4. At 1173 K, 22.2 wt.% of the initial biomass weight was converted to CO, 5.2 wt.% to CH_4 and 7.6 wt.% to CO_2.

The effect of increasing the surface area within the 2nd stage at 973 K by adding in sand beds of various lengths (20-40 mm) had no additional effect on the product distribution. Adding in small amounts of calcined limestone and dolomite (20 wt.%) into the 20 mm sand beds caused additional tar cracking across all the temperatures studied. The effects were more pronounced at 973 K and 1073 K. Calcined dolomite appeared to be a slightly more effective tar cracking catalyst which was attributed to its higher surface area. Both materials were affected by coking and sintering (which worsened with increasing temperature) both of which would likely affect the long term performance of the materials as tar cracking catalysts in a commercial process.

7.2 The design, construction of a new upgraded 2-stage fixed bed reactor for investigations into the interactions between biomass tars and CLC oxygen carrier materials

A new, upgraded 2-stage fixed-bed reactor was designed and constructed in an attempt to address some of the inherent limitations of the existing reactor used for the experimental work described in chapter 3. The primary motivation for constructing a new 2-stage reactor was to allow for investigations into the effect of biomass tars on CLC oxygen carrier performance to be undertaken. The concept and mode of operation of the new reactor was the same as the existing 2-stage reactor and allowed for operation in either a single-stage or two-stage configuration. Solid fuel could be pyrolysed, gasified or combusted in the 1st stage generating a fuel or exhaust gas which could either be analysed directly (single-stage experiments) or further reacted in the 2nd stage (two-stage experiments). Ash and residual char was retained by the first stage bed support and the evolved gases and volatiles would be swept downstream into the tar trap or 2nd stage. The 2nd stage could be loaded with a bed of reactive solid particles such as oxygen carriers for investigations into chemical-looping combustion (CLC); tar cracking catalysts; or CO_2 sorbents for CO_2 capture or sorbent enhanced reforming (SER) investigations.

All flange connections and welds were replaced in the new design with Swagelok connections to allow for operation at pressures up to 30 bar_a. A system for feeding small batches solid fuels was designed and incorporated. The ability to feed solid fuels enabled much quicker heating rates to be achieved that were more consistent with the heating rates of commercial, large-scale combustion/ gasification/ pyrolysis reactor systems. The solid feeding also allowed for multiple batches of solid fuels to be fed in periodically during an experiment. An inert quartz reactor liner assembly was also designed to prevent contact between the fuel and reaction products with the potentially catalytically active Incoloy 800 HT walls of the external pressure vessel tube. A new tar trap configuration was designed to allow for efficient trapping of the tar vapours using a less severe coolant consisting of a mixture of water, ice and salt in place of liquid nitrogen. This modification enabled the use of CO_2 and steam to be introduced as reactive gases into the system which was not possible in the previous reactor as these species would have condensed and frozen in the liquid N_2 cooled trap leading to blockage formation.

A set of biomass pyrolysis commissioning experiments were undertaken to compare the results obtained with the upgraded reactor with results from the existing reactor. The effect of heating rate, biomass sample feed weight and system pressure on the pyrolysis behaviour of beech wood were investigated. The tar yield obtained from the slow pyrolysis of beechwood in the upgraded single stage reactor was 27 % (mass basis) higher than equivalent experiments in the existing reactor. The higher tar yield was attributed to reduced secondary tar cracking on the reactor walls within the upgraded reactor which validates the choice of using a quartz reactor assembly to line the internal surfaces of the Incoloy 800HT outer vessel. The char yield was slightly lower and gas yields were approximately the same.

7.3 The development and testing of iron-based oxygen carriers for applications in CLC systems utilising biomass as a fuel

Chapter 5 explored the development and optimisation of fabrication strategies based on wet granulation for the production of cheap, highly reactive and mechanically robust iron oxide-based oxygen carrier materials for CLC systems utilising biomass or gasified biomass as a fuel. Three different wet granulation methods were trialled: a method based on incipient wetness; and two methods in which the particles were formed by extrusion of a paste of the raw materials through either a mechanical screw extruder or using a sieve to control the diameter of the extrudates and resultant particles. A rigorous testing protocol was established to assess the physical and chemical properties of the synthesised oxygen carrier materials and their suitability for use in large-scale systems.

The reduction kinetics (the rate limiting step in the CLC of gaseous fuels) of the different OC materials prepared in this work were assessed using a thermogravimetric analyser (TGA). A simple particle model based on the concept of effectiveness factor was applied to determine the intrinsic kinetic information. The activation energy and pre-exponential factor were calculated for values of k_i in the temperature range of 723-973 K with a 90 % confidence interval. The activation energy for the reduction of a 100 wt.% Fe_2O_3 oxygen carrier material was found to be 59 ± 8 kJ mol^{-1} which was in very close agreement with the literature and other similar studies at Imperial using a spouted, fluidised bed reactor.

This work demonstrates that it is possible to obtain accurate kinetic measurements in the timeframe of hours to days compared with the timeframe of weeks required to complete an entire kinetic study using the spouted fluidised bed reactor. The implications of this are that kinetic studies of simple gas-solid systems could be conducted in the TGA freeing up the more versatile and flexible pressurised fluidised bed reactors at Imperial College for studies that cannot be carried out in the TGA such as: CLC with in-situ gasification of solid fuels; CLC at elevated pressures or studies into the effects of sulfur containing species on CLC systems.

The fabrication technique was found to have a dramatic effect on the reactivity of the 100 wt.% OC materials indicating that substantial improvements to the performance could potentially be achieved by making small, simple modifications to the fabrication technique. Studies of a 100 wt.% Fe_2O_3 oxygen carrier at elevated temperatures (972-1173 K) revealed that the thermal stability was low with the reactivity decreasing with increasing temperatures above 973 K. The addition of 40 wt.% α-Al_2O_3 as a supporting material increased the reactivity and thermal stability of the OC material in almost all cases although the reactivity of the 60 wt.% Fe_2O_3/ 40 wt.% α-Al_2O_3 studied at the elevated temperature range did show a slight decline in reactivity with increasing temperature above 1023 K.

A range of different Al_2O_3 precursor materials were also investigated for producing the 40 wt.% Al_2O_3 loading in the 60 wt.% Fe_2O_3 oxygen carrier material. The precursor material had a substantial effect on both the reactivity and morphological properties of the resultant OC particles. Producing 60 wt.% Fe_2O_3/40 wt.% Al_2O_3 OC particles from an $Al(OH)_3$ precursor gave the most porous OC material with the highest surface area. This OC material was also the most reactive at temperatures above 973 K demonstrating the highest activation energy of all the materials studied of 72 ± 8 kJ mol^{-1} for the temperature range 823-1073 K. No deterioration in the reactivity of the material was observed at temperatures up to 1173 K. In fact, the activation energy increased to 123 kJ.mol^{-1} for the temperature range 1073-1173K. This behaviour was attributed to the further reduction of Fe_3O_4 to $FeAl_2O_4$ which involved a solid state reaction and became more pronounced above the Tammann temperature of Fe_3O_4. This theory was supported by the increase observed in the conversion with increasing temperature above what was theoretically possible when only considering the reduction of Fe_2O_3 to Fe_3O_4. If the proposed theory is correct, it would indicate that the formation of $FeAl_2O_4$ is beneficial acting to enhance the thermal stability, reactivity and oxygen transfer capacity of the iron oxide based oxygen carrier material.

7.4 Investigations into the interactions between iron oxide-base oxygen carrier materials and biomass tars

Chapter 6 presents preliminary experimental work investigating interactions between iron oxide-based oxygen carrier materials and biomass tars in the upgraded 2-stage, fixed-bed reactor. Oxygen carrier materials were loaded into the 2nd stage of the reactor and exposed to a gas stream containing large amounts of tars produced from the pyrolysis of beech wood in the 1st stage of the reactor. The effect on the pyrolysis product distribution and reactivity of the OC materials after exposure to the volatile pyrolysis products were measured. Two oxygen carrier materials were investigated: a 100 wt.% Fe_2O_3 OC and a 60 wt.% Fe_2O_3 OC material supported with 40 wt.% Al_2O_3 (prepared from an $Al(OH)_3$ precursor). The effect of carrier gas composition and oxidation state of the OC material were also studied.

Exposure of the biomass pyrolysis products to the oxygen carrier materials at 973 K reduced the amount of tars recovered compared with analogous experiments in which the volatile pyrolysis products were exposed to an inert bed of sand. The tar cracking effect of the alumina supported iron oxide OC material appeared to be greater than the pure iron oxide OC material although the reduction in the tar yield was roughly equivalent to the increase in carbon deposition observed for the alumina supported iron oxide OC compared with the pure iron oxide OC material. Carbon deposition ranged between 2.7-5.5 wt.% (of the initial mass of the biomass pyrolysed in the 1st stage) for the pure iron oxide OC and 7.4-9.9 wt.% for the alumina supported iron oxide OC material. The tar cracking effect of the oxygen carriers appeared to be independent of the oxidation state in which the oxygen carrier was exposed to the volatile biomass pyrolysis products (i.e. Fe_2O_3 or Fe_3O_4). No obvious deleterious effects were observed in the reactivity of the OC materials after the OC materials were exposed to the biomass tars and other volatile pyrolysis products.

Gas yield measurements revealed that exposing the pyrolysis products to the OC in its oxidised form resulted in a greater conversion to CO_2 as is desirable in a CLC process. A lower conversion to CO_2 was observed when the pyrolysis products were exposed to the reduced OC materials with interactions appearing to favour production of CO. Conversion of the tars and pyrolysis products to CO is particularly desirable for applications of chemical-looping reforming (CLR) and biomass syngas upgrading. Further work is therefore necessary to explore the possibility of using a process based on chemical-looping for biomass syngas upgrading and reforming for the production of a tar-free bio-derived fuel gas.

Due to time constraints, only a few experimental conditions could be investigated, however this work serves the purpose of providing a proof-of-concept for the use of the upgraded 2-stage fixed-bed reactor for studying interactions between CLC oxygen carrier materials and biomass tars. Detailed suggestions for future work are presented in section 7.5.

7.5 Suggestions for future work

This thesis provides the proof-of-concept concept for the use of an upgraded 2-stage fixed-bed reactor for studying interactions between CLC oxygen carrier materials and biomass tars. However, the full potential of this systems is still to be realised. There is a considerable amount of work left to complete in order to gain a thorough insight into the interactions that take place between biomass derived tars and CLC oxygen carrier materials. This section highlights the main areas that require further work.

- Additional oxygen carrier materials should be developed and tested using the testing protocols outlined in chapter 5. Attempts should be made to develop dual function particles that act as both oxygen carriers and tar cracking catalysts. This may involve developing oxygen carrier particles that incorporate a small amount of a known tar cracking catalyst such as CaO, Ni or MgO. A recent study has shown that the use of a CuO-based OC material with CLOU functionality may be highly effective at eliminating tars during the CLC of biomass (Adánez-Rubio et al., 2014). With this in mind work could focus on development of mixed Mn and Fe-based OC materials with CLOU functionality that offer superior thermal stabilities compared with Cu-based CLOU OC materials.
- An additional set of experiments should be undertaken to compare the tar cracking effectiveness of CLC oxygen carriers with some known tar cracking catalysts. The results from this study will help to assess whether the enhanced cracking of the tars by the iron oxide-based OC materials observed in this work was a result of an enhanced thermal, catalytic or reactive oxidative cracking mechanism between the oxidised OC material and biomass tars.
- The investigations into the interactions between biomass tars and CLC oxygen carriers was only carried out at a single temperature of 973 K. The effect on the performance of the OC materials, tar conversion efficiency and extent of coking should be studied at the higher temperatures of 973-1273 K that are more relevant to CLC applications. Other process parameters that would be worthwhile investigating are: the effect of total system pressure; presence of steam and/or CO_2; ratio of biomass to oxygen carrier material; the effect of tars derived from other biomass varieties; and the effect of tars produced during the gasification of biomass rather than pyrolysis.
- Extended cycle tests need to be carried out at conditions relevant to CLC (*i.e.* > 1123 K) to determine oxygen carrier performance over repeated oxidation and reduction cycling with multiple exposures to gases contained large quantities of tars. The effect on the oxygen carrier

performance, product distribution and trace element contamination of the oxygen carrier material should be studied.

- Strategies for minimising carbon deposition on the surface of the oxygen carrier materials could also be studied. This may involve investigating the presence of steam which could potentially act as a gasification agent removing carbon deposits from the surface of the oxygen carrier material as they form.
- Additional analytical techniques should be trialled in an attempt to gain further insight types of species and functional groups present in the recovered tars. Techniques such as GC-MS, HPLC-MS, H^1-NMR, HSQC-NMR, 31P-NMR and FTIR could all be used to identify functional groups and some of the individual components of the tars making it possible to measure how these components are affected by altering process conditions. This will help to improve understanding of the tar cracking and reforming processes that are taking place in the presence of the OC materials and develop mechanisms to describe these interactions.

References

AARNA, I. & SUUBERG, E. M. 1998. Changes in reactive surface area and porosity during char oxidation. *Symposium (International) on Combustion,* 27**,** 2933-2939.

ABAD, A., ADÁNEZ-RUBIO, I., GAYÁN, P., GARCÍA-LABIANO, F., DE DIEGO, L. F. & ADÁNEZ, J. 2012. Demonstration of chemical-looping with oxygen uncoupling (CLOU) process in a 1.5kW th continuously operating unit using a Cu-based oxygen-carrier. *International Journal of Greenhouse Gas Control,* 6**,** 189-200.

ABAD, A., ADANEZ, J., GARCÍA-LABIANO, F., DE DIEGO, L. F., GAYÁN, P. & CELAYA, J. 2007a. Mapping of the range of operational conditions for Cu-, Fe-, and Ni-based oxygen carriers in chemical-looping combustion. *Chemical Engineering Science,* 62**,** 533-549.

ABAD, A., GARCÍA-LABIANO, F., DE DIEGO, L. F., GAYÁN, P. & ADÁNEZ, J. 2007b. Reduction kinetics of Cu-, Ni-, and Fe-based oxygen carriers using syngas (CO + H_2) for chemical-looping combustion. *Energy & Fuels,* 21**,** 1843-1853.

ADAMSON, A.W. & GAST, A.P., 1997. *Physical Chemistry of Surfaces, 6th Edition*. John Wiley & Sons.

ADÁNEZ-RUBIO, I., ABAD, A., GAYÁN, P., DE DIEGO, L. F., GARCÍA-LABIANO, F. & ADÁNEZ, J. 2014. Biomass combustion with CO_2 capture by chemical looping with oxygen uncoupling (CLOU). *Fuel Processing Technology,* 124**,** 104-114.

ADÁNEZ-RUBIO, I., GAYÁN, P., GARCÍA-LABIANO, F., LUIS, F., ADÁNEZ, J. & ABAD, A. 2011. Development of CuO-based oxygen-carrier materials suitable for chemical-looping with oxygen uncoupling (CLOU) process. *Energy Procedia,* 4**,** 417-424.

ADÁNEZ, J., ABAD, A., GARCÍA-LABIANO, F., GAYÁN, P. & DE DIEGO, L. 2012. Progress in chemical-looping combustion and reforming technologies. *Progress in Energy and Combustion Science,* 38**,** 215–282.

ADÁNEZ, J., DE DIEGO, L. F., GARCÍA-LABIANO, F., GAYÁN, P., ABAD, A. & PALACIOS, J. M. 2004. Selection of oxygen carriers for chemical-looping combustion. *Energy & Fuels,* 18**,** 371-377.

ADÁNEZ, J., GARCÍA-LABIANO, F., DE DIEGO, L. F., GAYÁN, P., CELAYA, J. & ABAD, A. 2006. Nickel-copper oxygen carriers to reach zero CO and H_2 emissions in chemical-looping combustion. *Industrial & Engineering Chemistry Research,* 45**,** 2617-2625.

ANHEDEN, M. & SVEDBERG, G. 1998. Exergy analysis of chemical-looping combustion systems. *Energy Conversion and Management,* 39**,** 1967-1980.

ARJMAND, M., LEION, H., MATTISSON, T. & LYNGFELT, A. 2014. Investigation of different manganese ores as oxygen carriers in chemical-looping combustion (CLC) for solid fuels. *Applied Energy,* 113**,** 1883-1894.

ASIF, M. & PARRY, S. J. 1989. Elimination of reagent blank problems in the fire-assay pre-concentration of the platinum group elements and gold with a nickel sulfide bead of less than one gram mass. *ANALYST,* 114**,** 1057-1059.

AZAR, C., JOHANSSON, D. J. A. & MATTSSON, N. 2013. Meeting global temperature targets-the role of bioenergy with carbon capture and storage. *Environmental Research Letters,* 8**,** 8.

BAKKEN, E., STOLEN, S., NORBY, T., GLENNE, R. & BUDD, M. 2004. Redox energetics of $SrFeO_3$-delta - a coulometric titration study. *Solid State Ionics,* 167**,** 367-377.

BAUKAL JR, C. E. 2012. *The John Zink Hamworthy Combustion Handbook: Volume 1-Fundamentals*, CRC Press.

BENTSEN, N. S., FELBY, C. & THORSEN, B. J. 2014. Agricultural residue production and potentials for energy and materials services. *Progress in Energy and Combustion Science,* 40**,** 59-73.

BERGUERAND, N. & LYNGFELT, A. 2009. Chemical-looping combustion of petroleum coke using ilmenite in a 10 kW(th) unit-high-temperature operation. *Energy & Fuels,* 23**,** 5257-5268.

BERGUERAND, N., LYNGFELT, A., MATTISSON, T. & MARKSTROM, P. 2011. Chemical looping combustion of solid fuels in a 10 kW(th) unit. *Oil & Gas Science and Technology-Revue D Ifp Energies Nouvelles,* 66**,** 181-191.

BIRD, R. B., STEWART, W. E. & LIGHTFOOT, E. N. 2007. *Transport phenomena*, J. Wiley & Sons.

BOHN, C. 2010. *The production of pure hydrogen with simultaneous capture of carbon dioxide.* PhD Thesis, University of Cambridge, Cambridge, U.K.

BOHN, C. D., CLEETON, J. P., MÜLLER, C. R., CHUANG, S. Y., SCOTT, S. A. & DENNIS, J. S. 2010. Stabilizing iron oxide used in cycles of reduction and oxidation for hydrogen production. *Energy & Fuels,* 24**,** 4025-4033.

BOHN, C. D., SCOTT, S. A., MÜLLER, C. R., CLEETON, J. P., HAYHURST, A. N., DAVIDSON, J. F. & DENNIS, J. S. 2008. Production of very pure hydrogen with simultaneous capture of carbon dioxide using the redox reactions of iron oxides in packed beds. *Industrial & Engineering Chemistry Research,* 47**,** 7623-7630.

BOLTON, C., SNAPE, C. E., OBRIEN, R. J. & KANDIYOTI, R. 1987. Influence of carrier gas-flow and heating rates in fixed-bed hydropyrolysis of coal. *Fuel,* 66**,** 1413-1417.

BOOT-HANDFORD, M. E., ABANADES, J. C., ANTHONY, E. J., BLUNT, M. J., BRANDANI, S., MAC DOWELL, N., FERNÁNDEZ, J. R., FERRARI, M.-C., GROSS, R., HALLETT, J. P., HASZELDINE, R. S., HEPTONSTALL, P., LYNGFELT, A., MAKUCH, Z., MANGANO, E., PORTER, R. T. J., POURKASHANIAN, M., ROCHELLE, G. T., SHAH, N., YAO, J. G. & FENNELL, P. S. 2014. Carbon capture and storage update. *Energy & Environmental Science,* 7**,** 130-189.

BOUSINGAULT, J. B. 1852. Le gaz oxygène contenu dans l'air atmospherique. *Annales de chimie et de physique,* 35 (3rd series)**,** 5-54.

BP 2011. *Statistical review of world energy*. London, BP Plc.

BP 2015. *Statistical review of world energy*. London, BP Plc.

BRANDVOLL, O. & BOLLAND, O. 2004. Inherent CO_2 capture using chemical looping combustion in a natural gas fired power cycle. *Journal of Engineering for Gas Turbines and Power-Transactions of the Asme,* 126**,** 316-321.

BRIDGWATER, A. 2008. *Progress in thermochemical biomass conversion*, J. Wiley & Sons.

BRIDGWATER, A. V., MEIER, D. & RADLEIN, D. 1999. An overview of fast pyrolysis of biomass. *Organic Geochemistry,* 30**,** 1479-1493.

BROWN, T. 2010. *Chemical-looping Combustion with Solid Fuels.* PhD Thesis, Cambridge University, Cambridge, U.K.

BRUNAUER, S., 1943. *The Adsorption of Gases and Vapors. Vol. 1, Physical Adsorption*. Princeton University Press, Princeton, NJ, U.S.A.

BRUNAUER, S., EMMETT, P.H., & TELLER, E., 1938. Adsorption of gases in multimolecular layers. *Journal of the American Chemical Society*, 60, 309.

CHO, P., MATTISSON, T. & LYNGFELT, A. 2004. Comparison of iron-, nickel-, copper- and manganese-based oxygen carriers for chemical-looping combustion. *Fuel,* 83**,** 1215-1225.

CHO, P., MATTISSON, T. & LYNGFELT, A. 2005. Carbon formation on nickel and iron oxide-containing oxygen carriers for chemical-looping combustion. *Industrial & Engineering Chemistry Research,* 44**,** 668-676.

CHO, P. M., TOBIAS; LYNGFELT, ANDERS 2002. Reactivity of iron oxide with methane in a laboratory fluidized bed-application of chemical-looping combustion. *Seventh International Conference on Circulating Fluidized Beds.* Niagra Falls, Ontario.

CHUANG, S. Y., DENNIS, J. S., HAYHURST, A. N. & SCOTT, S. A. 2008. Development and performance of Cu-based oxygen carriers for chemical-looping combustion. *Combustion and Flame,* 154**,** 109-121.

COLLOT, A. G., ZHUO, Y., DUGWELL, D. R. & KANDIYOTI, R. 1999. Co-pyrolysis and co-gasification of coal and biomass in bench-scale fixed-bed and fluidised bed reactors. *Fuel,* 78**,** 667-679.

CORBELLA, B. M., DE DIEGO, L. F., GARCÍA-LABIANO, F., ADÁNEZ, J. & PALACIOS, J. M. 2005a. The performance in a fixed bed reactor of copper-based oxides on titania as oxygen carriers for chemical looping combustion of methane. *Energy & Fuels,* 19**,** 433-441.

CORBELLA, B. M., DE DIEGO, L. F., GARCÍA-LABIANO, F., ADÁNEZ, J. & PALACIOS, J. M. 2005b. Characterization study and five-cycle tests in a fixed-bed reactor of titania-supported nickel oxide as oxygen carriers for the chemical-looping combustion of methane. *Environmental Science & Technology,* 39**,** 5796-5803.

DABAI, F., PATERSON, N., MILIAN, M., FENNELL, P. & KANDIYOTI, R. 2014. Tar formation and destruction in a fixed bed reactor simulating downdraft gasification: effect of reaction conditions on tar cracking products. *Energy & Fuels,* 28**,** 1970-1982.

DABAI, F., PATERSON, N., MILLAN, M., FENNELL, P. & KANDIYOTI, R. 2010. Tar formation and destruction in a fixed-bed reactor simulating downdraft gasification: equipment development and characterization of tar-cracking products. *Energy & Fuels,* 24**,** 4560-4570.

DE DIEGO, L. F., GARCÍA-LABIANO, F., ADÁNEZ, J., GAYÁN, P., ABAD, A., CORBELLA, B. M. & PALACIOS, J. M. 2004. Development of Cu-based oxygen carriers for chemical-looping combustion. *Fuel,* 83**,** 1749-1757.

DE DIEGO, L. F., GARCÍA-LABIANO, F., GAYÁN, P., CELAYA, J., PALACIOS, J. M. & ADANEZ, J. 2007. Operation of a 10 kWth chemical-looping combustor during 200 h with a CuO-Al2O3 oxygen carrier. *Fuel,* 86**,** 1036-1045.

DEGROOT, W., OSTERHELD, T. H. & RICHARDS, G. N. 1988. The influence of natural and added catalysts in the gasification of wood chars. *In:* BRIDGWATER, A. V. & KUESTER, J. L. (eds.) *Research in Thermochemical Biomass Conversion.* Springer Netherlands.

DEMIRBAS, A., GULLU, D., CAGLAR, A. & AKDENIZ, F. 1997. Estimation of calorific values of fuels from lignocellulosics. *Energy Sources,* 19**,** 765-770.

DEMIRBAS, M. F., BALAT, M. & BALAT, H. 2009. Potential contribution of biomass to the sustainable energy development. *Energy Conversion and Management,* 50**,** 1746-1760.

DENNIS, J. S., MÜLLER, C. R. & SCOTT, S. A. 2010. In situ gasification and CO_2 separation using chemical looping with a Cu-based oxygen carrier: Performance with bituminous coals. *Fuel,* 89**,** 2353-2364.

DENNIS, J. S. & SCOTT, S. A. 2010. In situ gasification of a lignite coal and CO_2 separation using chemical looping with a Cu-based oxygen carrier. *Fuel,* 89**,** 1623-1640.

DEVI, L., PTASINSKI, K. J. & JANSSEN, F. 2003. A review of the primary measures for tar elimination in biomass gasification processes. *Biomass & Bioenergy,* 24**,** 125-140.

DING, N., ZHENG, Y., LUO, C., WU, Q.-L., FU, P.-F. & ZHENG, C.-G. 2011. Development and performance of binder-supported $CaSO_4$ oxygen carriers for chemical looping combustion. *Chemical Engineering Journal,* 171**,** 1018-1026.

DUESO, C., THOMPSON, C. & METCALFE, I. 2015. High-stability, high-capacity oxygen carriers: Iron oxide-perovskite composite materials for hydrogen production by chemical looping. *Applied Energy,* 157, 382-390.

EIA, 2011. *International Energy Outlook 2011*. US Department of Energy, Washington, USA.

EKSTRÖM, C., SCHWENDIG, F., BIEDE, O., FRANCO, F., HAUPT, G., DE KOEIJER, G., PAPAPAVLOU, C. & RØKKE, P. E. 2009. Techno-economic evaluations and benchmarking of pre-combustion CO_2 capture and oxy-fuel processes developed in the european ENCAP project. *In:* GALE, J., HERZOG, H. & BRAITSCH, J. (eds.) *Greenhouse Gas Control Technologies 9.* Amsterdam: Elsevier Science Bv.

ERRI, P. & VARMA, A. 2007. Solution combustion synthesized oxygen carriers for chemical looping combustion. *Chemical Engineering Science,* 62**,** 5682-5687.

ERTL, G., KNÖZINGER, H. & WEITKAMP, J. 2008. *Preparation of solid catalysts*, John Wiley & Sons.

FAN, L.-S. 2011. *Chemical looping systems for fossil energy conversions*, John Wiley & Sons.

FUSHIMI, C., ARAKI, K., YAMAGUCHI, Y. & TSUTSUMI, A. 2003. Effect of heating rate on steam gasification of biomass. 1. Reactivity of char. *Industrial & Engineering Chemistry Research,* 42**,** 3922-3928.

FYTILI, D. & ZABANIOTOU, A. 2008. Utilization of sewage sludge in EU application of old and new methods - A review. *Renewable & Sustainable Energy Reviews,* 12**,** 116-140.

GARCÍA-LABIANO, F., DE DIEGO, L. F., ADÁNEZ, J., ABAD, A. & GAYÁN, P. 2004. Reduction and oxidation kinetics of a copper-based oxygen carrier prepared by impregnation for chemical-looping combustion. *Industrial & Engineering Chemistry Research,* 43**,** 8168-8177.

GAY-LUSSAC, L. J. 1811. *Recherches physico-chimiques*, Deterville.

GAYÁN, P., DE DIEGO, L. F., GARCÍA-LABIANO, F., ADÁNEZ, J., ABAD, A. & DUESO, C. 2008. Effect of support on reactivity and selectivity of Ni-based oxygen carriers for chemical-looping combustion. *Fuel,* 87**,** 2641-2650.

GIL, J., CABALLERO, M. A., MARTIN, J. A., AZNAR, M. P. & CORELLA, J. 1999. Biomass gasification with air in a fluidized bed: Effect of the in-bed use of dolomite under different operation conditions. *Industrial & Engineering Chemistry Research,* 38**,** 4226-4235.

GILLILAND, E., R.; LEWIS, WARREN, K., 1954. Production of pure carbon dioxide. U.S. Patent 2,665,972.

GOUGH, C. & UPHAM, P. 2011. Biomass energy with carbon capture and storage (BECCS or Bio-CCS). *Greenhouse Gases-Science and Technology,* 1**,** 324-334.

GUELL. 1993. *Development of a high-pressure wire-mesh reactor for the direct determination of tar and total volatile yields: applications to coal and biomass pyrolysis and hydropyrolysis.* PhD thesis, University of London, London, U.K.

GUO, L., ZHAO, H. B., MA, J. C., MEI, D. F. & ZHENG, C. G. 2014. Comparison of large-scale production methods of Fe_2O_3/Al_2O_3 oxygen carriers for chemical-looping combustion. *Chemical Engineering & Technology,* 37**,** 1211-1219.

HIGMAN, C. & VAN DER BURGT, M. 2008. *Gasification,* Oxford, Gulf Professional.

HOSSAIN, M. & DE LASA, H. 2008a. Chemical-looping combustion (CLC) for inherent CO_2 separations – a review. *Chemical Engineering Science,* 63**,** 4433-4451.

HOSSAIN, M. M. & DE LASA, H. I. 2007. Reactivity and stability of Co-Ni/Al_2O_3 oxygen carrier in multicycle CLC. *Aiche Journal,* 53**,** 1817-1829.

HUANG, Z., HE, F., ZHENG, A., ZHAO, K., CHANG, S., ZHAO, Z. & LI, H. 2013. Synthesis gas production from biomass gasification using steam coupling with natural hematite as oxygen carrier. *Energy,* 53**,** 244-251.

HURT, R. H., SAROFIM, A. F. & LONGWELL, J. P. 1991. The role of microporous surface area in the gasification of chars from a sub-bituminous coal. *Fuel,* 70**,** 1079-1082.

IEA-ETN 2010a. IEA ETSAP- *Technology brief E14- CO_2 capture and storage.* International Energy Association Energy Technology Network, Paris, France.

IEA-ETN. 2010b. IEA ETSAP- *Technology brief E01- coal-fired power.* International Energy Association Energy Technology Network, Paris, France.

IEA 2010b. *CO_2 Emissions From Fossil Fuel Combustion Highlights (2010 Edition)*. OECD/IEA. Paris: OECD.

IEA 2015. *World Energy Outlook Special Report 2015: Energy and Climate Change*. *In:* PRIDDLE, R. (ed.). Paris, France: International Energy Agency

IMTIAZ, Q., HOSSEINI, D. & MÜLLER, C. R. 2013. Review of oxygen carriers for chemical looping with oxygen uncoupling (CLOU): thermodynamics, material development, and synthesis. *Energy Technology,* 1**,** 633-647.

IPCC 2005. *Intergovernmental Panel on Climate Change: Special Report on Carbon Dioxide Capture and Storage*. Cambridge: Cambridge University Press, UK.

IPCC 2007. *Intergovernmental Panel on Climate Change: Synthesis Report on Climate Change*. Cambridge University Press, UK.

IPCC (PACHAURI, R. K., ALLEN, M., BARROS, V., BROOME, J., CRAMER, W., CHRIST, R., CHURCH, J., CLARKE, L., DAHE, Q. & DASGUPTA, P.) 2014. *Climate Change 2014: Synthesis Report. Contribution of Working Groups I, II and III to the Fifth Assessment Report of the Intergovernmental Panel on Climate Change*. Cambridge University Press, UK.

ISHIDA, M. & JIN, H. G. 1996. A novel chemical-looping combustor without NOx formation. *Industrial & Engineering Chemistry Research,* 35**,** 2469-2472.

ISHIDA, M., JIN, H. G. & OKAMOTO, T. 1996. A fundamental study of a new kind of medium material for chemical-looping combustion. *Energy & Fuels,* 10**,** 958-963.

ISHIDA, M., ZHENG, D. & AKEHATA, T. 1987. Evaluation of a chemical-looping-combustion power-generation system by graphic exergy analysis. *Energy,* 12**,** 147-154.

JENSEN, A., DAM-JOHANSEN, K., WÓJTOWICZ, M. A. & SERIO, M. A. 1998. TG-FTIR study of the influence of potassium chloride on wheat straw pyrolysis. *Energy & Fuels,* 12**,** 929-938.

JENSEN, P. A., FRANDSEN, F., DAM-JOHANSEN, K. & SANDER, B. 2000. Experimental investigation of the transformation and release to gas phase of potassium and chlorine during straw pyrolysis. *Energy & Fuels,* 14**,** 1280-1285.

JENSEN, W. B. 2009. The Origin of the Brin Process for the Manufacture of Oxygen. *Journal of Chemical Education,* 86**,** 1266.

JERNDAL, E., LEION, H., AXELSSON, L., EKVALL, T., HEDBERG, M., JOHANSSON, K., KÄLLÉN, M., SVENSSON, R., MATTISSON, T. & LYNGFELT, A. 2011. Using low-cost iron-based materials as oxygen carriers for chemical-looping combustion. *Oil & Gas Science and Technology - Revue IFP Energies nouvelles,* 66**,** 235-248.

JERNDAL, E., MATTISSON, T. & LYNGFELT, A. 2006. Thermal analysis of chemical-looping combustion. *Chemical Engineering Research and Design,* 84**,** 795-806.

JIN, H., OKAMOTO, T. & ISHIDA, M. 1998. Development of a novel chemical-looping combustion: Synthesis of a looping material with a double metal oxide of CoO-NiO. *Energy & Fuels,* 12**,** 1272-1277.

JIN, H. G. & ISHIDA, M. 2004. A new type of coal gas fueled chemical-looping combustion. *Fuel,* 83**,** 2411-2417.

JOHANSSON, E. 2002. *Interconnected fluidized bed for chemical-looping combustion with inherent CO2-seperation.* Technical Licentiate Thesis, Chalmers University of Technology, Göteborg, Sweden.

JOHANSSON, M. 2007. *Screening of oxygen-carrier particles based on iron-, manganese-, copper- and nickel oxides for use in chemical-looping technologies.* PhD Thesis, Chalmers University of Technology, Göteborg, Sweden.

JOHANSSON, M., MATTISSON, T. & LYNGFELT, A. 2006. Creating a synergy effect by using mixed oxides of iron- and nickel oxides in the combustion of methane in a chemical-looping combustion reactor. *Energy & Fuels,* 20**,** 2399-2407.

KANDIYOTI, R., HEROD, A. A. & BARTLE, K. 2006. *Solid fuels and heavy hydrocarbon liquids: thermal characterisation and analysis: Thermal characterisation and analysis*, Oxford, Elsevier.

KANNAN, M. P. & RICHARDS, G. N. 1990. Gasification of biomass chars in carbon dioxide: dependence of gasification rate on the indigenous metal content. *Fuel,* 69**,** 747-753.

KELLER, M., LEION, H., MATTISSON, T. & THUNMAN, H. 2014. Investigation of natural and synthetic bed materials for their utilization in chemical looping reforming for tar elimination in biomass-derived gasification gas. *Energy & Fuels,* 28**,** 3833-3840.

KIERZKOWSKA, A., BOHN, C., SCOTT, S., CLEETON, J., DENNIS, J. & MÜLLER, C. 2010. Development of iron oxide carriers for chemical looping combustion using sol− gel. *Industrial & Engineering Chemistry Research,* 49**,** 5383-5391.

KUMAR, A., JONES, D. D. & HANNA, M. A. 2009. Thermochemical biomass gasification: A review of the current status of the technology. *Energies,* 2**,** 556-581.

LAMBERT, A., BRIAULT, P. & COMTE, E. 2010. Spinel mixed oxides as oxygen carriers for chemical looping combustion. *Energy Procedia (GHGT-10)*

LANGMUIR, I. 1916. The constitution and fundamental properties of solids and liquids. Part I. Solids. *Journal of the American Chemical Society,* 38**,** 2221-2295.

LARSSON, A., ISRAELSSON, M., LIND, F., SEEMANN, M. & THUNMAN, H. 2014. Using ilmenite to reduce the tar yield in a dual fluidized bed gasification system. *Energy & Fuels,* 28**,** 2632-2644.

LEHMANN, J. & JOSEPH, S. 2012. *Biochar for environmental management: science and technology*, Earthscan Books Ltd, Routledge.

LEION, H., LARRING, Y., BAKKEN, E., BREDESEN, R., MATTISSON, T. & LYNGFELT, A. 2009a. Use of $CaMn_{0.875}Ti_{0.125}O_3$ as oxygen carrier in chemical-looping with oxygen uncoupling. *Energy & Fuels,* 23**,** 5276-5283.

LEION, H., LYNGFELT, A. & MATTISSON, T. 2009b. Solid fuels in chemical-looping combustion using a NiO-based oxygen carrier. *Chemical Engineering Research & Design,* 87**,** 1543-1550.

LEION, H., MATTISSON, T. & LYNGFELT, A. 2007. The use of petroleum coke as fuel in chemical-looping combustion. *Fuel,* 86**,** 1947-1958.

LEION, H., MATTISSON, T. & LYNGFELT, A. 2009c. Use of ores and industrial products as oxygen carriers in chemical-looping combustion. *Energy and Fuels,* 23**,** 2307-2315.

LIND, F., BERGUERAND, N., SEEMANN, M. & THUNMAN, H. 2013. Ilmenite and nickel as catalysts for upgrading of raw gas derived from biomass gasification. *Energy & Fuels,* 27**,** 997-1007.

LIND, F., SEEMANN, M. & THUNMAN, H. 2011. Continuous catalytic tar reforming of biomass derived raw gas with simultaneous catalyst regeneration. *Industrial & Engineering Chemistry Research,* 50**,** 11553-11562.

LIU, G.-S. & NIKSA, S. 2004. Coal conversion submodels for design applications at elevated pressures. Part II. Char gasification. *Progress in Energy and Combustion Science,* 30**,** 679-717.

LOPES, G. B. 2013. *Práticas do gerenciamento de resíduos nas indústrias de confecções da região da rua teresa–petrópolis.* Dissertação (Mestrado), Universidade Federal do Rio de Janeiro, Rio de Janeiro, Brazil.

LU, Q., LI, W.-Z. & ZHU, X.-F. 2009. Overview of fuel properties of biomass fast pyrolysis oils. *Energy Conversion and Management,* 50**,** 1376-1383.

LUO, S., MAJUMDER, A., CHUNG, E., XU, D., BAYHAM, S., SUN, Z., ZENG, L. & FAN, L.-S. 2013. Conversion of woody biomass materials by chemical looping process- kinetics, light tar cracking, and moving bed reactor behavior. *Industrial & Engineering Chemistry Research,* 52**,** 14116-14124.

LYNGFELT, A. 2011. Oxygen carriers for chemical looping combustion-4000 h of operational experience. *Oil & Gas Science and Technology-Revue D Ifp Energies Nouvelles,* 66**,** 161-172.

LYNGFELT, A., LECKNER, B. & MATTISSON, T. 2001. A fluidized-bed combustion process with inherent CO_2 separation; Application of chemical-looping combustion. *Chemical Engineering Science,* 56**,** 3101-3113.

LYNGFELT, A. & MATTISSON, T. 2011. Materials for chemical-looping combustion. *In:* STOLTEN, D. & SCHERER, V. (eds.) Efficient Carbon Capture for Coal Power Plants. *Chemical Engineering & Technology*, *35*, 407-407.

MATTISSON, T., JÄRDNÄS, A. & LYNGFELT, A. 2003. Reactivity of some metal oxides supported on alumina with alternating methane and oxygen application for chemical-looping combustion. *Energy & Fuels,* 17**,** 643-651.

MATTISSON, T., JOHANSSON, M. & LYNGFELT, A. 2004a. Multicycle reduction and oxidation of different types of iron oxide particles - Application to chemical-looping combustion. *Energy & Fuels,* 18**,** 628-637.

MATTISSON, T., JOHANSSON, M. & LYNGFELT, A. 2006. CO_2 capture from coal combustion using chemical-looping combustion - Reactivity investigation of Fe, Ni and Mn based oxygen carriers using syngas. *In:* Proceedings of the 31st International Technical Conference on Coal Utilization & Fuel Systems, May 21-26, Clearwater, FL, U.S.A.

MATTISSON, T., JOHANSSON, M. & LYNGFELT, A. 2006b. The use of NiO as an oxygen carrier in chemical-looping combustion. *Fuel,* 85**,** 736-747.

MATTISSON, T., LEION, H. & LYNGFELT, A. 2009a. Chemical-looping with oxygen uncoupling using CuO/ZrO_2 with petroleum coke. *Fuel,* 88**,** 683-690.

MATTISSON, T., LYNGFELT, A. & CHO, P. 2001. The use of iron oxide as an oxygen carrier in chemical-looping combustion of methane with inherent separation of CO2. *Fuel,* 80**,** 1953-1962.

MATTISSON, T., LYNGFELT, A. & LEION, H. 2009b. Chemical-looping with oxygen uncoupling for combustion of solid fuels. *International Journal of Greenhouse Gas Control,* 3**,** 11-19.

MCKENDRY, P. 2002a. Energy production from biomass (part 1): overview of biomass. *Bioresource Technology,* 83**,** 37-46.

MCKENDRY, P. 2002b. Energy production from biomass (part 3): gasification technologies. *Bioresource Technology,* 83**,** 55-63.

MEI, D., ABAD, A., ZHAO, H., ADÁNEZ, J. & ZHENG, C. 2014. On a highly reactive Fe_2O_3/Al_2O_3 oxygen carrier for in situ gasification chemical looping combustion. *Energy & Fuels,* 28**,** 7043-7052.

MENDIARA, T., ABAD, A., DE DIEGO, L. F., GARCÍA-LABIANO, F., GAYÁN, P. & ADÁNEZ, J. 2013. Biomass combustion in a CLC system using an iron ore as an oxygen carrier. *International Journal of Greenhouse Gas Control,* 19**,** 322-330.

MENDIARA, T., JOHANSEN, J. M., UTRILLA, R., GERALDO, P., JENSEN, A. D. & GLARBORG, P. 2011. Evaluation of different oxygen carriers for biomass tar reforming (I): Carbon deposition in experiments with toluene. *Fuel,* 90**,** 1049-1060.

MILNE, T. A., ABATZOGLOU, N. & EVANS, R. J. 1998a. *Biomass gasifier "tars": their nature, formation, and conversion*, National Renewable Energy Laboratory Golden, CO, U.S.A.

MOILANEN, A. 2006. *Thermogravimetric characterisations of biomass and waste for gasification processes*, VTT Technical Research Centre of Finland, Espoo, Finland.

MONTEIRO NUNES, S. M., PATERSON, N., DUGWELL, D. R. & KANDIYOTI, R. 2007. Tar formation and destruction in a simulated downdraft, fixed-bed gasifier: Reactor design and initial results. *Energy & Fuels,* 21**,** 3028-3035.

MONTEIRO NUNES, S. M., PATERSON, N., HEROD, A., DUGWELL, D. R. & KANDIYOTI, R. 2008. Tar formation and destruction in a fixed bed reactor simulating downdraft gasification: optimization of conditions. *Energy & Fuels,* 22**,** 1955-1964.

NOORMAN, S., ANNALAND, M. V. & KUIPERS, H. 2007. Packed bed reactor technology for chemical-looping combustion. *Industrial & Engineering Chemistry Research,* 46**,** 4212-4220.

OASMAA, A. & CZERNIK, S. 1999. Fuel oil quality of biomass pyrolysis oils state of the art for the end users. *Energy & Fuels,* 13**,** 914-921.

ORTIZ, M., GAYÁN, P., LUIS, F., GARCÍA-LABIANO, F., ABAD, A., PANS, M. A. & ADÁNEZ, J. 2011. Hydrogen production with CO_2 capture by coupling steam reforming of methane and chemical-looping combustion: use of an iron-based waste product as oxygen carrier burning a PSA tail gas. *Journal of Power Sources,* 196**,** 4370-4381.

ÖZÇIMEN, D. 2013. *An approach to the characterization of biochar and bio-oil*. Report, Yildiz Technical University, Istanbul, Turkey.

PELTON, A. & BLANDER, M. 1986. Thermodynamic analysis of ordered liquid solutions by a modified quasichemical approach—Application to silicate slags. *Metallurgical Transactions B,* 17**,** 805-815.

PHILPOT, C. 1970. Influence of mineral content on the pyrolysis of plant materials. *Forest Science,* 16**,** 461-471.

PINDORIA, R. V., LIM, J.-Y., HAWKES, J. E., LAZARO, M.-J., HEROD, A. A. & KANDIYOTI, R. 1997. Structural characterization of biomass pyrolysis tars/oils from eucalyptus wood waste: effect of H_2 pressure and sample configuration. *Fuel,* 76**,** 1013-1023.

RAVEENDRAN, K. & GANESH, A. 1998. Adsorption characteristics and pore-development of biomass-pyrolysis char. *Fuel,* 77**,** 769-781.

RAVEENDRAN, K., GANESH, A. & KHILAR, K. C. 1995. Influence of mineral matter on biomass pyrolysis characteristics. *Fuel,* 74**,** 1812-1822.

RAVEENDRAN, K., GANESH, A. & KHILAR, K. C. 1996. Pyrolysis characteristics of biomass and biomass components. *Fuel,* 75**,** 987-998.

REED, T. B., & DAS, A. 1988. *Handbook of biomass downdraft gasifier engine systems*, Biomass Energy Foundation, U.S.A.

REED, T. B., GAUR, S., 2001. *A Survey of Biomass Gasification 2001: Gasifier Projects and Manufacturers Around the World*, National Renewable Energy Laboratory and Biomass Energy Foundation, U.S.A.

RICHTER, H. J. & KNOCHE, K. F. 1983. Reversibility of combustion processes. *ACS Symposium Series,* 235**,** 71-85.

RUBEL, A., ZHANG, Y., LIU, K. & NEATHERY, J. 2011. Effect of ash on oxygen carriers for the application of chemical looping combustion to a high carbon char. *Oil & Gas Science and Technology-Revue D Ifp Energies Nouvelles,* 66**,** 291-300.

RYDÉN, M., CLEVERSTAM, E., LYNGFELT, A. & MATTISSON, T. 2009. Waste products from the steel industry with NiO as additive as oxygen carrier for chemical-looping combustion. *International Journal of Greenhouse Gas Control,* 3**,** 693-703.

RYDÉN, M., JOHANSSON, M., CLEVERSTAM, E., LYNGFELT, A. & MATTISSON, T. 2010. Ilmenite with addition of NiO as oxygen carrier for chemical-looping combustion. *Fuel,* 89**,** 3523-3533.

RYDÉN, M., LEION, H., MATTISSON, T. & LYNGFELT, A. 2014. Combined oxides as oxygen-carrier material for chemical-looping with oxygen uncoupling. *Applied Energy,* 113**,** 1924-1932.

RYDÉN, M., LYNGFELT, A. & MATTISSON, T. 2011. $CaMn_{0.875}Ti_{0.125}O_3$ as oxygen carrier for chemical-looping combustion with oxygen uncoupling (CLOU)-Experiments in a continuously operating fluidized-bed reactor system. *International Journal of Greenhouse Gas Control,* 5**,** 356-366.

RYDÉN, M., LYNGFELT, A. & MATTISSON, T. 2011. Combined manganese/iron oxides as oxygen carrier for chemical looping combustion with oxygen uncoupling (CLOU) in a circulating fluidized bed reactor system. *Energy Procedia,* 4**,** 341-348.

RYDÉN, M., LYNGFELT, A., MATTISSON, T., CHEN, D., HOLMEN, A. & BJÖRGUM, E. 2008. Novel oxygen-carrier materials for chemical-looping combustion and chemical-looping reforming; $La_xSr_{1-x}Fe_yCo_{1-y}O_{3-\delta}$ perovskites and mixed-metal oxides of NiO, Fe_2O_3 and Mn_3O_4. *International Journal of Greenhouse Gas Control,* 2**,** 21-36.

SARSHAR, Z., SUN, Z., ZHAO, D. & KALIAGUINE, S. 2012. Development of sinter-resistant Core–Shell $LaMn_xFe_{1-x}O_3$@$mSiO_2$ oxygen carriers for chemical looping combustion. *Energy & Fuels,* 26**,** 3091-3102.

SATTERFIELD, C. N. 1970. *Mass transfer in heterogeneous catalysis*, The MIT Press, U.S.A.

SCOTT, S. A., DENNIS, J. S., HAYHURST, A. N. & BROWN, T. 2006. In situ gasification of a solid fuel and CO_2 separation using chemical looping. *AIChE Journal,* 52**,** 3325-3328.

SENNECA, O. 2007. Kinetics of pyrolysis, combustion and gasification of three biomass fuels. *Fuel Processing Technology,* 88**,** 87-97.

SHAH, M. M. & CHRISTIE, M. 2007. Oxyfuel combustion using OTM for CO_2 capture from coal power plants. *The 2nd Workshop on International Oxy-combustion Research Network.* Windsor, CT, U.S.A.

SHEN, L., GAO, Z., WU, J. & XIAO, J. 2010. Sulfur behavior in chemical looping combustion with NiO/Al_2O_3 oxygen carrier. *Combustion and Flame,* 157**,** 853-863.

SHEN, L., WU, J., XIAO, J., SONG, Q. & XIAO, R. 2009. Chemical-looping combustion of biomass in a 10 kWth reactor with iron oxide as an oxygen carrier. *Energy & Fuels,* 23**,** 2498-2505.

SHEN, L., ZHENG, M., XIAO, J. & XIAO, R. 2008. A mechanistic investigation of a calcium-based oxygen carrier for chemical looping combustion. *Combustion and Flame,* 154**,** 489-506.

SHULMAN, A., CLEVERSTAM, E., MATTISSON, T. & LYNGFELT, A. 2009. Manganese/iron, manganese/nickel, and manganese/silicon oxides used in chemical-looping with oxygen uncoupling (CLOU) for combustion of methane. *Energy & Fuels,* 23**,** 5269-5275.

SOMRANG, Y. 2012. *Effect of operating conditions on product distributions and bio-oil ageing in biomass pyrolysis.* PhD Thesis, Imperial College London, London, U.K.

SON, S. R. & KIM, S. D. 2006. Chemical-looping combustion with NiO and Fe_2O_3 in a thermobalance and circulating fluidized bed reactor with double loops. *Industrial & Engineering Chemistry Research,* 45**,** 2689-2696.

SONG, Q., LIU, W., BOHN, C. D., HARPER, R. N., SIVANIAH, E., SCOTT, S. A. & DENNIS, J. S. 2013. A high performance oxygen storage material for chemical looping processes with CO_2 capture. *Energy & Environmental Science,* 6**,** 288-298.

SONG, Q., XIAO, R., DENG, Z., SHEN, L., XIAO, J. & ZHANG, M. 2008a. Effect of temperature on reduction of $CaSO_4$ oxygen carrier in chemical-looping combustion of simulated coal gas in a fluidized bed reactor. *Industrial & Engineering Chemistry Research,* 47**,** 8148-8159.

SONG, Q., XIAO, R., DENG, Z., ZHANG, H., SHEN, L., XIAO, J. & ZHANG, M. 2008b. Chemical-looping combustion of methane with $CaSO_4$ oxygen carrier in a fixed bed reactor. *Energy Conversion and Management,* 49**,** 3178-3187.

SØRENSEN, L. H., FJELLERUP, J. S., HENRIKSEN, U. B., MOILANEN, A. & WINTHER, E. 2000. *An Evaluation of Char Reactivity and Ash Properties in Biomass Gasification: Fundamental Processes in Biomass Gasification*, ReaTech, Surrey, U.K.

SPIEGL, N. 2010. *Oxy-fuel gasification in fluidised beds.* PhD Thesis, Imperial College London, London, U.K.

STERN, N. 2006. *The Stern Review Report on the Economics of Climate Change*. Cambridge University Press, Cambridge, U.K.

STUDENT 1908. Probable error of a correlation coefficient. *Biometrika,* 6**,** 302-310.

SUTTON, D., KELLEHER, B. & ROSS, J. R. H. 2001. Review of literature on catalysts for biomass gasification. *Fuel Processing Technology,* 73**,** 155-173.

TAKEGOSHI, E., HIRASAWA, Y., IMURA, S. & SHIMAZAKI, T. 1984. Measurement of thermal properties of iron oxide pellets. *International journal of thermophysics,* 5**,** 219-228.

TEYSSIE, G., LEION, H., SCHWEBEL, G. L., LYNGFELT, A. & MATTISSON, T. 2011. Influence of lime addition to ilmenite in chemical-looping combustion (CLC) with solid fuels. *Energy & Fuels,* 25**,** 3843-3853.

THUNMAN, H., LIND, F., BREITHOLTZ, C., BERGUERAND, N. & SEEMANN, M. 2013. Using an oxygen-carrier as bed material for combustion of biomass in a 12-MWth circulating fluidized-bed boiler. *Fuel,* 113**,** 300-309.

VAN VUUREN, D. P., DEETMAN, S., VAN VLIET, J., VAN DEN BERG, M., VAN RUIJVEN, B. J. & KOELBL, B. 2013. The role of negative CO_2 emissions for reaching 2 degrees C- Insights from integrated assessment modelling. *Climatic Change,* 118**,** 15-27.

VENDERBOSCH, R. H. & PRINS, W. 2010. Fast pyrolysis technology development. *Biofuels, Bioproducts and Biorefining,* 4**,** 178-208.

VILLA, R., CRISTIANI, C., GROPPI, G., LIETTI, L., FORZATTI, P., CORNARO, U. & ROSSINI, S. 2003. Ni based mixed oxide materials for CH_4 oxidation under redox cycle conditions. *Journal of Molecular Catalysis a-Chemical,* 204**,** 637-646.

WARNECKE, R. 2000. Gasification of biomass: comparison of fixed bed and fluidized bed gasifier. *Biomass & Bioenergy,* 18**,** 489-497.

WEBB, P. A., ORR, C. & CORPORATION, M. I. 1997. *Analytical methods in fine particle technology*, Micromeritics Instrument Corporation.

WEERACHANCHAI, P., HORIO, M. & TANGSATHITKULCHAI, C. 2009. Effects of gasifying conditions and bed materials on fluidized bed steam gasification of wood biomass. *Bioresource Technology,* 100**,** 1419-1427.

WOLF, J., ANHEDEN, M. & YAN, J. Y. 2005. Comparison of nickel- and iron-based oxygen carriers in chemical looping combustion for CO_2 capture in power generation. *Fuel,* 84**,** 993-1006.

YAMAN, S. 2004. Pyrolysis of biomass to produce fuels and chemical feedstocks. *Energy Conversion and Management,* 45**,** 651-671.

YANG, H., YAN, R., CHEN, H., ZHENG, C., LEE, D. H. & LIANG, D. T. 2006. In-depth investigation of biomass pyrolysis based on three major components: hemicellulose, cellulose and lignin. *Energy & Fuels,* 20**,** 388-393.

YASSIN, L., LETTIERI, P., SIMONS, S. & GERMANA, A. 2005. Energy recovery from thermal processing of waste: a review. *Proceedings of the ICE-Engineering Sustainability,* 158**,** 97-103.

ZAFAR, Q., ABAD, A., MATTISSON, T., GEVERT, B. & STRAND, M. 2007. Reduction and oxidation kinetics of Mn_3O_4/Mg-ZrO_2 oxygen carrier particles for chemical-looping combustion. *Chemical Engineering Science,* 62**,** 6556-6567.

ZANZI, R., SJÖSTRÖM, K. & BJÖRNBOM, E. 2002. Rapid pyrolysis of agricultural residues at high temperature. *Biomass and Bioenergy,* 23**,** 357-366.

ZHANG, Z. 2014. *The effect of sulfur on chemical looping combustion with iron oxides.* PhD Thesis, Imperial College London, London, U.K.

Appendices

Appendix A

A.1 Additional Information relating to Analytical Techniques used for particle characterisation

A.1.1 Nitrogen Adsorption/Desorption Analysis

Pore surface area (BET) and pore volume distribution (BJH) measurements of the recovered chars and bed materials were determined using a Micromeritics Tristar 3000 N_2 sorption analyzer. Samples were degassed at 473 K under a constant flow of helium for 4 hours prior to analysis to remove any adsorbed species on the surface of the samples that would interfere with the analysis. Samples were then loaded into the sample tube (penetrometer) and cooled to 77.35 K with liquid nitrogen. N_2 adsorption/desorption analysis is a continuous flow process that measures the volume of N_2 adsorbed as the pressure of N_2 over the sample is increased from atmospheric to the saturation vapour pressure. Adsorption is an exothermic process that increases with decreasing temperature and increasing pressure. Desorption information is obtained by slowly decreasing the pressure over the sample back to atmospheric pressure.

The N_2 adsorption isotherms for a selection of different materials studied in this thesis are presented in figure A1 as the ratio of the actual gas pressure (p) to the vapour pressure of the adsorbing gas (p_o) as a function of volume of gas (at STP) adsorbed (v_a). All the isotherms are of Type 4 form indicating that the materials were porous (albeit with varying degrees of porosity) and that the porosity was created by relatively large pores (Bunauer, 1943). At very low pressures, the volume of N_2 adsorbed (v_a) rose rapidly as a monolayer was formed before decreasing to a slower, more stable rate as p/p_o reached ~ 0.05. Between P/P_o of 0.05 to around 0.7-0.9 (depending on the material), v_a increased steadily with increasing pressure as a result of multi-layer formation. As p/p_o approached unity, the volume of gas adsorbed rose dramatically as bulk condensation begins.

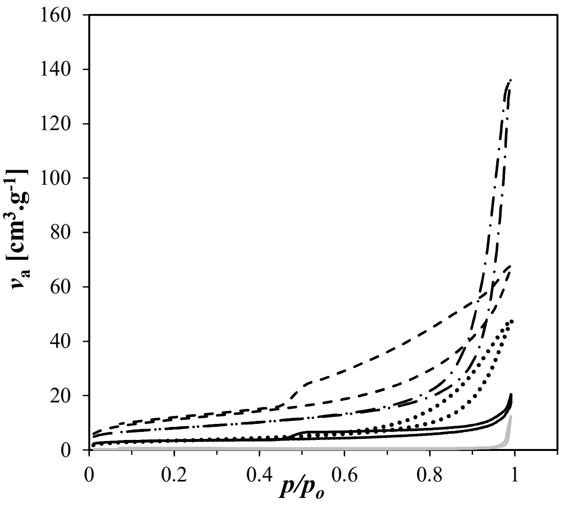

Figure A1. Nitrogen sorption isotherms for a range of different materials investigated in this thesis. BRH char (——), TIR char (- - - -), calcined limestone (··········), 100Fe(S) (——), 60Fe40Al(SAB) (— · —).

All the isotherms presented in figure A1 display hysteresis loops i.e. the desorption curves does not retrace the adsorption curves. Hysteresis loops are indicative of meso- and macroporous materials (i.e. containing pores with openings greater than 2 nm and 50 nm respectively) and are a result of differences in the mechanisms of bulk condensation and evaporation within the pores (Webb et al., 1997). Condensation within meso- and macropores progresses from the surface of the pore wall towards the centre of the pore whereas evaporation takes place from a liquid surface with different geometry.

It should also be noted that none of the hysteresis loops in the isotherms presented in figure A1 were closed indicating that this analysis was not able to provide an upper pore size limit for any of the materials presented here *i.e.* all of the materials contained pores that were larger in width than the upper resolution of this analysis of ~ 200 nm (Webb et al., 1997). Mercury intrusion porosimetry (MIP) was used to gain information related to the porous region created by larger pores > 200 nm in width (section A.1.4). Structural information relating to the surface areas and porosity of the materials was extracted from the respective adsorption isotherms.

A.1.2 Brunauer-Emmett-Teller (BET) Surface Area Theory

BET theory is an extension of Langmuir theory that incorporates the concept of multilayer adsorption allowing for the surface area of a material to be calculated from N_2 adsoprtion/desorption measurements. Langmuir's basic assumptions for monolayer adsorption is that the rate of condensation on the surface of a solid is proportional to the number of vacant sites and the rate of evaporation is proportional to the number of occupied sites both of which are equal at equilibrium (Langmuir, 1916). Brunauer et al. (1938) included additional terms to describe the heats of adsorption and rate constants which are assumed to be equal for all layers excluding the first layer. This assumption can be rationalised by considering that the first adsorption layer is formed as a result of interactions between gas species and the surface of the solid whereas all subsequent layers are formed by adsorption onto other adsorbed gas molecules. Based on these assumptions, Brunauer et al. derived equation A1 to describe this multilayer adsorption system.

$$\frac{v}{v_m} = \frac{n}{n_m} = \frac{c\, p/p_o}{(1 - p/p_o)[1 + (c-1)\, p/p_o]} \qquad \text{Equation A1}$$

Where

$$c = e^{(q_1 - q_L)/RT} \qquad \text{Equation A2}$$

Here, v is the volume of gas adsorbed (STP) per gram, n is the number of moles of gas adsorbed per gram with the subscript 'm' denoting the quantity of gas adsorbed for a complete layer, c is a constant defined by equation x where q_1 is the heat of adsorption for the interaction between the adsorbing gas molecule and solid of the sorbent, q_L is the heat of condensation onto the surface of the adsorbed liquid, R is the ideal gas constant and T is the absolute temperature.

Plotting $(p/p_o)/n(1 - p/p_o)$ against p/p_o for the p/p_o range of 0.05 to 0.2 i.e. where monolayer is being formed should yield a straight line from which n_m, v_m and c can be obtained (Adamson, 1997). The specific surface area (S) of the solid can then be calculated using equation A3 where N_A is Avogadro's number and σ_0 is the area occupied by a single adsorbate molecule.

$$n_m = \frac{S}{N_A \sigma_0} \qquad \text{Equation A3}$$

A.1.3 Barrett-Joyner-Halender (BJH) Pore Size Distribution Analysis

Pore size distributions for the range 2-200 nm was estimated using a method developed by Barrett, Joyner and Halender (BJH) (Barrett, 1951). The method calculates the pore size distribution from the change in volume of gas adsorbed for a stepwise decrease in p/p_o from 0.995 (where all pores are assumed to be filled) to 0.05 obtained from the desorptive branch of the isotherm. All pores were assumed to be straight and cylindrical (i.e. a straight cylindrical pore model was used) and the capillary thickness and thickness the adsorbed layer on the pore walls were estimated using relationships proposed by Lord Kelvin (Thomson, 1871) and Halsey (1948) respectively.

In this work, pore size distributions were presented as the log differential pore volume (dV_p) as a function of the pore diameter dV_p/d(log D_p). Plotting pore size distributions in this way with pore size plotted on a logarithmic x-axis means that peaks provide a far better indication of pore volume regardless of whether the sample contains large or small pores with narrow pore size distributions or wide pore size distributions thus allowing for easier interpretation and comparison of MIP data obtained from different related samples (Webb et al., 1997).

A.1.4 Mercury Intrusion Porosimetry (MIP) Analysis

Pore volume distribution in the macroporous range was investigated via mercury intrusion porosimetry (MIP) using a Micromeretics IV 9500 series analyser. MIP is an analytical technique that involves forcing mercury into the pores of a porous material under an applied gas pressure. Mercury is a non-wetting liquid and therefore will only enter pores when forced to do so i.e. mercury will not penetrate pores via capillary action. MIP analysis measures the cumulative intrusion volume as a function of applied external pressure. Figure A2 presents plots of the cumulative intrusion volume as a function of applied external pressure for a selection of different materials studied in this thesis. The size of a pore that mercury will penetrate is inversely proportional to the applied pressure and can be calculated using the Washburn equation (eq. A4) which assumes that all pores are of straight and cylindrical geometry (Webb et al., 1997).

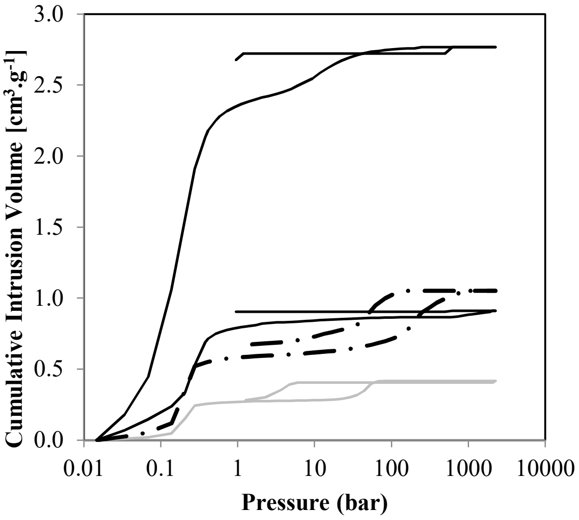

Figure A2. Intrusion/extrusion curves for mercury intrusion porosimetry analysis for a range of different materials investigated in this thesis. BRH char (——), TIR char (- - - -), 100Fe(S) (——), 60Fe40Al(SAB) (— · —).

$$D_p = \frac{-4\gamma\ cos\theta}{P_g} \qquad \text{Equation A4}$$

Here D_p is the pore diameter, γ is the surface tension of mercury, θ is the contact angle and P_g is the applied gas pressure. A contact angle of 130° is used for all analyses here and is the most widely used value for analyses where specific information is not available. A surface tension of 485 dynes.cm^{-1} was also used which is the surface tension of mercury at 293 K under vacuum.

MIP has a resolution of around 0.003-360 μm however it can often be very difficult to distinguish between inter-particle porosity and interstitial porosity (void space created between the particles due to the way in which they were packed in the sample tube) (Webb et al., 1997). Analysis of the cumulative intrusion volume versus pressure plots can sometimes provide some indication of where the cut off between interstitial and inter-particle pore space may lie. For example, the curves representing the analysis of the 100Fe(S) and 60Fe40Al(SAB) OC materials shows two steep rises at low pressure and high pressure respectively separated by region in which the curve plateaus. These curves are indicative of samples consisting of relatively coarse porous grains where the rise at low pressure is caused by the filling of void space created in between the grains and the rise at the high pressure is a result of intrusion into the pore space within the particles.

The MIP cumulative intrusion versus pressure curves for the char samples depicted in figure A2 are more difficult to interpret and are indicative of samples consisting of small particles with relatively large pores. Based on the analysis of the cumulative intrusion volume versus pressure plots and previous work at Imperial College involving CLC and OC development and testing, an upper pore size limit of 10 µm was imposed in this work. Analysis of the SEM images of the chars (section 3.3.1, fig. 3.7) also indicated that imposing an upper pore size limit of 10 µm was reasonable when analysing the porosity of the char samples.

MIP pore size distributions are presented as the log differential pore volume (dV_p) as a function of the pore diameter dV_p/d(log D_p) for reasons outlined above in section A.1.3.

A.1.5 Porosity and density calculations

Calculation of the intrinsic reduction rate kinetics from the observed kinetics requires information relating the physical structure of the material including surface area, porosity and envelope density. Surface area is obtained directly from N_2 sorption measurements. The porosity of the OC materials (ε) can be calculated according to equation A5 and is the ratio of the volume of pore space (V_p) to the total volume of the particle (i.e. the sum of the solid volume (V_s) and pore space).

$$\varepsilon = \frac{V_p}{V_s + V_p} \qquad \text{Equation A5}$$

Here, pore space volume (V_p) is determined from the MIP measurements as the cumulative intrusion volume for pores up to the upper pore size limit of 10 µm (see section A.1.4). The solid volume of the particle (V_s) is the inverse of the skeletal density (ρ_{skel}) which is the density of the particle excluding pore and interstitial space between particles within the bulk sample. The skeletal density(ρ_{skel}) was measured via helium adsorption analysis (Micrometrics, Accupyc 1330). The envelope density (ρ_{env}), which is the density of the particle including both the solid and pore volume, can then be obtained from the porosity and skeletal density according to equation A6.

$$\rho_{env} = \rho_{skel}\,(1 - \varepsilon) \qquad \text{Equation A6}$$

A.2 Tabulated results summary for experiments discussed in chapter 3

Table A1: Identified products from the pyrolysis of the different types of biomass investigated in chapter 3.
<u>**Experimental Parameters:**</u> ***1st stage***: **biomass feed**: variable (1.000g, 106-150 µm), **carrier gas** = He, **superficial velocity** = 0.1 m s^{-1}, **inlet pressure** = 2.2 bar_a, **heating rate** = 1 Ks^{-1}, **hold temperature** = 773 K, **hold time** = 900 s. ***2nd stage***: N/A.

Biomass Type		**Percentage of initial biomass feed weight (1.000 g)^{daf}**					
		Tar	**Char**	**CO_2**	**CO**	**CH_4**	**Mass Balance**
Beech Wood (BW)	$\bar{x}$	**36.3**	**22.6**	**4.0**	**2.5**	**0.3**	**61.7**
	σ	0	21.9	0.1	0.7	0	-
	c_v [%]	0	97.0	2.5	28.3	0	-
Brazilian Rice Husk (BRH)	$\bar{x}$	**37.8**	**26.8**	**5.0**	**1.7**	**0.2**	**66.6**
	σ	0.4	0.7	-	0.1	0	-
	c_v [%]	1.1	2.6	-	5.7	0	-
Thai Rice Husk (TRH)	$\bar{x}$	**22.6**	**27.5**	**4.3**	**1.3**	**0.1**	**51.5**
	σ	0.1	0.3	-	0.1	0	-
	c_v [%]	0.4	1.1	-	7.4	0	-
Textile Industry Residue (TIR)	$\bar{x}$	**30.4**	**45.9**	**4.1**	**0.2**	**0.2**	**76.7**
	σ	0.1	0.1	-	0	0	-
	c_v [%]	0.3	0.2	-	0	0	-

Table A2: The effect of 2nd stage temperature on the product distribution of beech wood pyrolysis.
<u>**Experimental Parameters:**</u> ***1st stage***: **biomass feed** = beech wood (1.000g, 106-150 µm), **carrier gas** = He, **superficial velocity** = 0.1 m s^{-1}, **inlet pressure** = 2.2 bar_a, **heating rate** = 1 K s^{-1}, **hold temperature** = 773 K, **hold time** = 900 s. ***2nd stage***: **temperature** = variable, **superficial velocity** = 0.25 m s^{-1}, **inlet pressure** =2.1 bar_a, **bed material** = N/A.

2nd Stage Temperature [K]		**Percentage (wt.%) of initial biomass feed weight (1.000 g)^{daf}**					
		Tar	**Char**	**CO_2**	**CO**	**CH_4**	**Mass Balance**
973	$\bar{x}$	**8.3**	**20.7**	**5.4**	**15.5**	**2.2**	**52.1**
	σ	0.4	0.8	0	1.8	0.4	-
	c_v [%]	4.8	3.9	0	11.6	18.2	-
1073	$\bar{x}$	**2.8**	**20.9**	**4.3**	**20.3**	**7.7**	**56**
	σ	0.2	0.3	0.1	0.8	0.1	-
	c_v [%]	7.1	1.4	2.3	3.9	1.3	-
1173	$\bar{x}$	**1.0**	**21.5**	**5.2**	**22.8**	**7.6**	**58.1**
	σ	0	0.1	0.1	1.9	0	-
	c_v [%]	0	0.5	2	8.3	0	-

Table A3: The effect of different 2nd stage sand bed lengths on the product distribution of beech wood pyrolysis at 973 K.
Experimental Parameters: ***1st stage***: **biomass feed** = beech wood (1.000 g, 106-150 μm), **carrier gas** = He, **superficial velocity** = 0.1 m.s^{-1}, **inlet pressure** = 2.2 bar, **heating rate** = 1 K s^{-1}, **hold temperature** = 773 K, **hold time** = 900 s. ***2nd stage***: **superficial velocity** = 0.25 m s^{-1}, **inlet pressure** = 2.1 bar$_a$, **temperature** = 973 K, **bed material** = sand (500-700 μm), **bed length** = variable.

2nd stage Bed		**Percentage (wt.%) of initial biomass feed weight (1.000 g)^{daf}**					
		Tar	**Char**	**CO_2**	**CO**	**CH_4**	**Mass Balance**
N/A	**$\bar{x}$**	**8.3**	**20.7**	**5.4**	**15.5**	**2.2**	**52.1**
	σ	0.4	0.8	0	1.8	0.4	-
	c_v [%]	4.8	3.9	0	11.6	18.2	-
20 mm sand	**$\bar{x}$**	**8.0**	**21.5**	**5.9**	**16.5**	**2.3**	**54.2**
	σ	0.6	1.1	0.1	1.1	0.1	-
	c_v [%]	7.5	5.1	1.7	6.7	4.3	-
30 mm sand	**$\bar{x}$**	**7.8**	**21.1**	**5.1**	**15.1**	**2.2**	**51.3**
	σ	0.4	1	0.4	1.8	0.1	-
	c_v [%]	5.1	4.7	7.8	11.9	4.5	-
40 mm sand	**$\bar{x}$**	**8.4**	**21.1**	**4.6**	**16.9**	**2.2**	**53.2**
	σ	0.2	1.3	1.1	0.4	0	-
	c_v [%]	2.4	6.2	23.9	2.4	0	-

Table A4: The effect of different 2nd stage solid bed materials on the product distribution of beech wood pyrolysis at 973 K. **Experimental Parameters:** ***1st stage***: **feed** = beech wood (1.000 g, 106-150 μm), **carrier gas** = He, **superficial velocity** = 0.1 m s^{-1}, **inlet pressure** = 2.2 bar_a, **heating rate** = 1 K s^{-1}, **hold temperature** = 773 K, **hold time** = 900 s. ***2nd stage***: **superficial velocity** = 0.25 m s^{-1}, **inlet pressure** = 2.1 bar_a, **temperature** = 973 K, **bedding material** = variable, **bed particle size** = 355-425 μm (except sand = 500-700 μm).

2nd Stage Bed		**Percentage (wt.%) of initial biomass feed weight (1.000 g)^{daf}**					
		Tar	**Char**	**CO_2**	**CO**	**CH_4**	**Mass Balance**
N/A	$\bar{x}$	**8.3**	**20.7**	**5.4**	**15.5**	**2.2**	**52.1**
	σ	0.4	0.8	0	1.8	0.4	-
	c_v [%]	4.8	3.9	0	11.6	18.2	-
Sand (2 cm)	$\bar{x}$	**8.0**	**21.5**	**5.9**	**16.5**	**2.3**	**54.2**
	σ	0.6	1.1	0.1	1.1	0.1	-
	c_v [%]	7.5	5.1	1.7	6.7	4.3	-
20%LS bed	$\bar{x}$	**6.2**	**20.9**	**6.8**	**14.7**	**2.3**	**50.9**
	σ	0.6	0.5	0.4	0.4	0.1	-
	c_v [%]	9.7	2.4	5.9	2.7	4.3	-
10%Dol bed	$\bar{x}$	**7.6**	**21.6**	**7.5**	**14.7**	**2.3**	**53.7**
	σ	0.3	1.1	1.6	1.3	0.1	-
	c_v [%]	3.9	5.1	21.3	8.8	4.3	-
20%Dol bed	$\bar{x}$	**5.4**	**21.9**	**8.4**	**14.9**	**2.6**	**53.2**
	σ	0.2	0	1.3	0	0.1	-
	c_v [%]	3.7	0	15.5	0	3.8	-
40%Dol bed	$\bar{x}$	**5.2**	**21.1**	**9.3**	**14.3**	**2.7**	**52.6**
	σ	0.2	0.6	1.7	0.9	0.1	-
	c_v [%]	3.8	2.8	18.3	6.3	3.7	-

Table A5: The effect of different 2nd stage solid bed materials on the product distribution of beech wood pyrolysis at 1073 K. **Experimental Parameters:** ***1st stage***: **feed** = beech wood (1.000 g, 106-150 μm), **carrier gas** = He, **superficial velocity** = 0.1 m s^{-1}, **inlet pressure** = 2.2 bar$_a$, **heating rate** = 1 K s^{-1}, **hold temperature** = 773 K, **hold time** = 900 s. ***2nd stage***: **superficial velocity** = 0.25 m s^{-1}, **inlet pressure** = 2.1 bar$_a$, **temperature** = 1073 K, **bedding material** = variable, **bed particle size** = 355-425 μm (except sand = 500-700 μm).

2nd Stage Bed		Percentage (wt.%) of initial biomass feed weight (1.000 g)^{daf}					
		Tar	**Char**	**CO_2**	**CO**	**CH_4**	**Mass Balance**
N/A	$\bar{x}$	**2.8**	**20.9**	**4.3**	**20.3**	**7.7**	**56.0**
	σ	0.2	0.3	0.1	0.8	0.1	-
	c_v [%]	7.1	1.4	2	3.9	1.3	-
2cm sand	$\bar{x}$	**2.6**	**21.1**	**4.2**	**21.5**	**7.7**	**57.1**
	σ	0.2	0.3	0.1	0.8	0.1	-
	c_v [%]	7.7	1.4	2	3.7	1.3	-
20%LS bed	$\bar{x}$	**1.6**	**21.2**	**4.2**	**19.9**	**10.6**	**57.5**
	σ	0.1	0.3	0.8	0.4	0	-
	c_v [%]	6.3	1.4	19	2.0	0	-
20%Dol bed	$\bar{x}$	**1.5**	**21.6**	**4.4**	**20.2**	**13.7**	**61.4**
	σ	0.4	0.2	1.4	0.7	0.1	-
	c_v [%]	26.7	0.9	32	3.5	0.7	-

Table A6: The effect of different 2nd stage solid bed materials on the product distribution of beech wood pyrolysis at 1173 K. **Experimental Parameters:** ***1st stage***: **feed** = beech wood (1.000 g, 106-150 μm), **carrier gas** = He, **superficial velocity** = 0.1 m s^{-1}, **inlet pressure** = 2.2 bar$_a$, **heating rate** = 1 K s^{-1}, **hold temperature** = 773 K, **hold time** = 900 s. ***2nd stage***: **superficial velocity** = 0.25 m s^{-1}, **inlet pressure** = 2.1 bar$_a$, **temperature** = 1173 K, **bedding material** = variable, **bed particle size** = 355-425 μm (except sand = 500-700 μm).

2nd Stage Bed		Percentage of initial biomass feed weight (1.000 g)^{daf}					
		Tar	**Char**	**CO_2**	**CO**	**CH_4**	**Mass Balance**
N/A	$\bar{x}$	**1.0**	**21.5**	**5.2**	**22.8**	**7.6**	**58.1**
	σ	0	0.1	0.1	1.9	0	-
	c_v [%]	0	0.5	2	8.3	0	-
2cm sand	$\bar{x}$	**0.9**	**20.8**	**4.8**	**23.0**	**8.3**	**57.8**
	σ	0.2	0.2	0.8	1.1	0	-
	c_v [%]	22.2	1.0	17	4.8	0	-
20%LS bed	$\bar{x}$	**0.8**	**21.5**	**5.2**	**22.0**	**13.1**	**62.6**
	σ	0.1	0.6	1.3	1.6	0.2	-
	c_v [%]	12.5	2.8	25	7.3	1.5	-
20%Dol bed	$\bar{x}$	**0.6**	**21.6**	**5.2**	**22.3**	**13.2**	**62.9**
	σ	0.1	0.5	1.3	1.4	0.4	-
	c_v [%]	16.7	2.3	25	6.3	3.0	-

Appendix B

B.1 Solid fuel feeder design process

Two different feeder designs were investigated for feeding solid fuel into the upgraded hot-rod reactor. The first design tested was for continuous feeding and was based on the design used by Spiegl (2010) (fig. B.1). The feeder consisted of a sealed pressure hopper connected to a Swagelok packingless plug valve that had been modified to behave as a rotary cup feeder valve. The port of the packingless plug valve was blocked using a gas tight cement to create two feed cups (as illustrated in the inset of figure B.1). The valve handle was also removed and connected to a variable speed motor. The outlet of the rotary valve was connected to a T-piece that allowed for a gas flow to be introduced for sweeping the solid fuel particles to the inlet of the reactor.

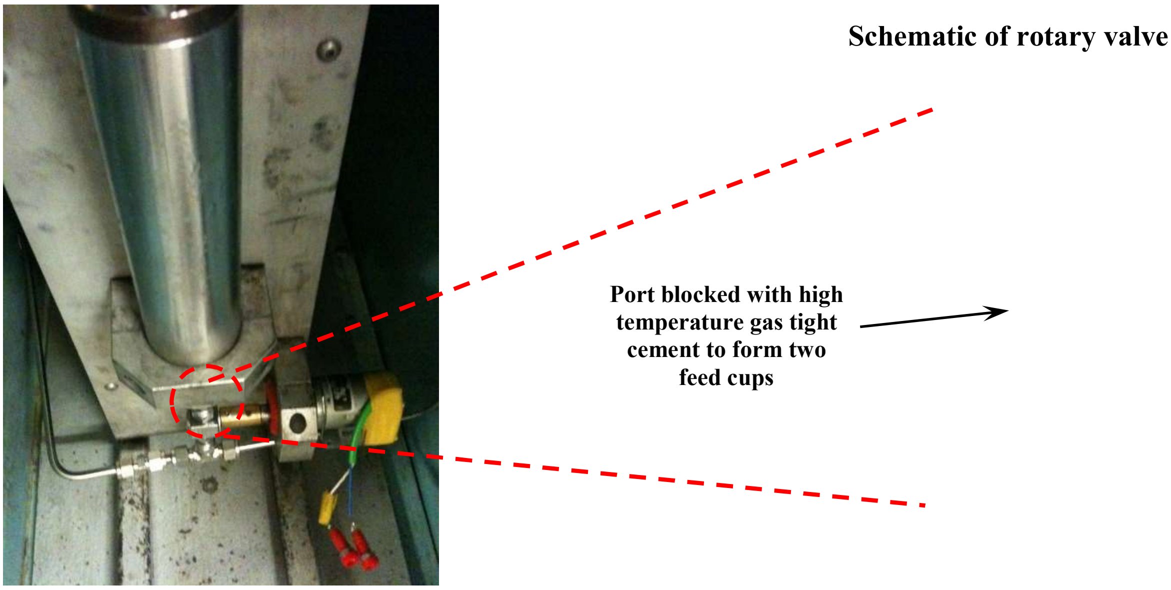

Figure B.2. Photograph of the continuous solid fuel feeding system (left) with a close up schematic of the rotary valve (right).

Optimum feeder operating parameters were identified through preliminary testing. Maintaining the pressure in the solid fuel hopper at 0.5 bar above the reactor pressure provided a pressure drop across the rotary feeding valve resulting in a repeatable feed rate tested over a period of up to 30 feeds. A gas sweep flow of 30 $ml_N.s^{-1}$ was also found to be the minimum flow necessary to sweep and entrain the fuel particles in the gas flow into the reactor, preventing a build-up/blockage forming in the T-piece fitting below the rotary valve.

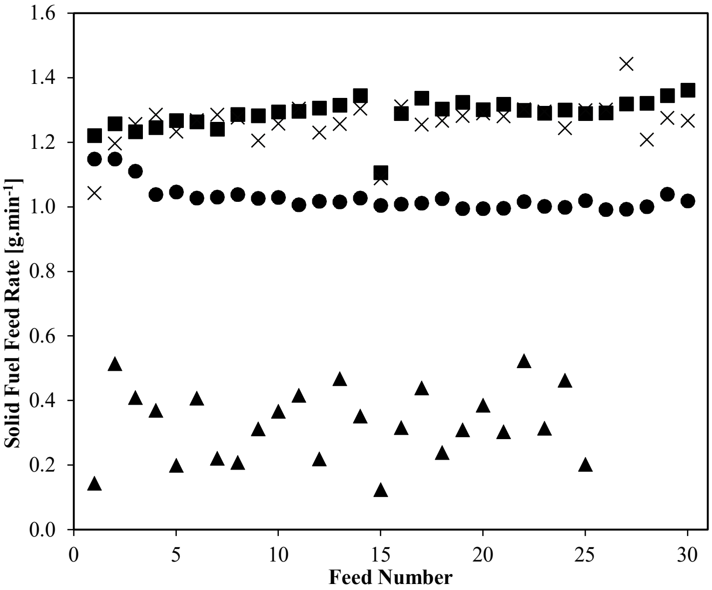

Figure B.2. Coal feeding rate as a function of feed number (feed repetition) and coal particle size. **Solid fuel feeding parameters: Pressure (coal hopper):**1.5 bara; **Feed time**: 60 s; **Sweep flow**: 30 mln.s^{-1}; **Coal Type**: Longannet (blend); **Coal particle size:**150-212 μm (×); 106-150 μm (●) 75-106 μm (■); < 75 μm (▲).

A blended coal obtained from the Longannet power station (Fife, UK) was used during the preliminary testing of the continuous feeder. Four different coal particle size fractions were investigated all of which (except the < 75 μm size fraction) could be fed at a repeatable rate over up to 30 x 60 s feed periods with a relative error in the feed rate of < 5 % (fig.B.2). Attempts to feed beech wood particles with the continuous feeder failed. The fibrous nature of the biomass particles caused bridging and blockage formation within the fuel hopper. It was also not possible to maintain a pressure drop through the fuel hopper as a result of the lower packing density (and therefore larger interstitial void volume) of the beech wood particles in the fuel hopper.

Attempts to resolve the problems associated with the continuous feeding of biomass were put on hold in favour of a batch-wise fuel feeder design (fig B.3). Samples were loaded into the solid fuel sample feed vessel and purged with N_2 (20 ml$_N$.s^{-1}) for a minimum of 5 min to ensure any reactive gases (i.e. O_2 from the air) were removed prior to the fuel feed. The fuel feed involved pressuring the gas line prior to the sample feed vessel to 0.5 bar above the set point pressure of the reactor. When signalled (by the reactor control program), the lower valve between the reactor and the sample valve was opened to cause a burst of gas to enter the sample feed tube, breaking up the packed fuel sample bed. The valve to the pressurised feeder inlet gas line was then opened causing the solid fuel particles to be entrained in the gas flow and fired into the reactor. Once the feeding segment was complete, the two valves could be shut-off allowing for the sample feed cylinder to be re-loaded if necessary.

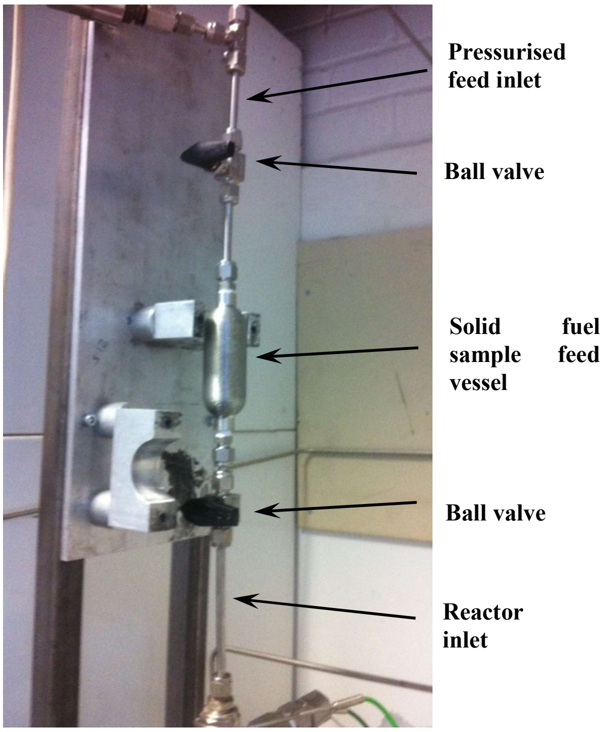

Figure B.3. Annotated photograph of the batchwise solid fuel feeder used for feeding biomass into the upgraded hot-rod reactor.

B.2 Steam generator design process

A steam generator was designed for investigation into the effects of steam gasification and chemical-looping H_2 production (fig B.4). The steam generator design involved bubbling N_2 through a pressure vessel containing water, constructed from stainless steel tubing and Swagelok fittings. A constant volume of water was maintained in the steam generator using an isocratic pump to replace the water lost as vapour ensuring steady state operation and a consistent steam output. The concentration of steam in the gas exiting the steam generator was controlled by controlling the temperature of the water inventory and the fraction of the total flow rate of N_2 going through the steam generator. A humidity probe located downstream of the steam generator enabled accurate measurement of the steam concentration in the gas entering the reactor. It was also possible to switch the steam input on and off using solenoid valves. The gas lines after the steam generator are all trace heated to a temperature above the saturation vapour pressure of the gas stream to prevent steam condensing out in the gas lines which could lead to blockages and the destabilisation of the inlet steam concentrations.

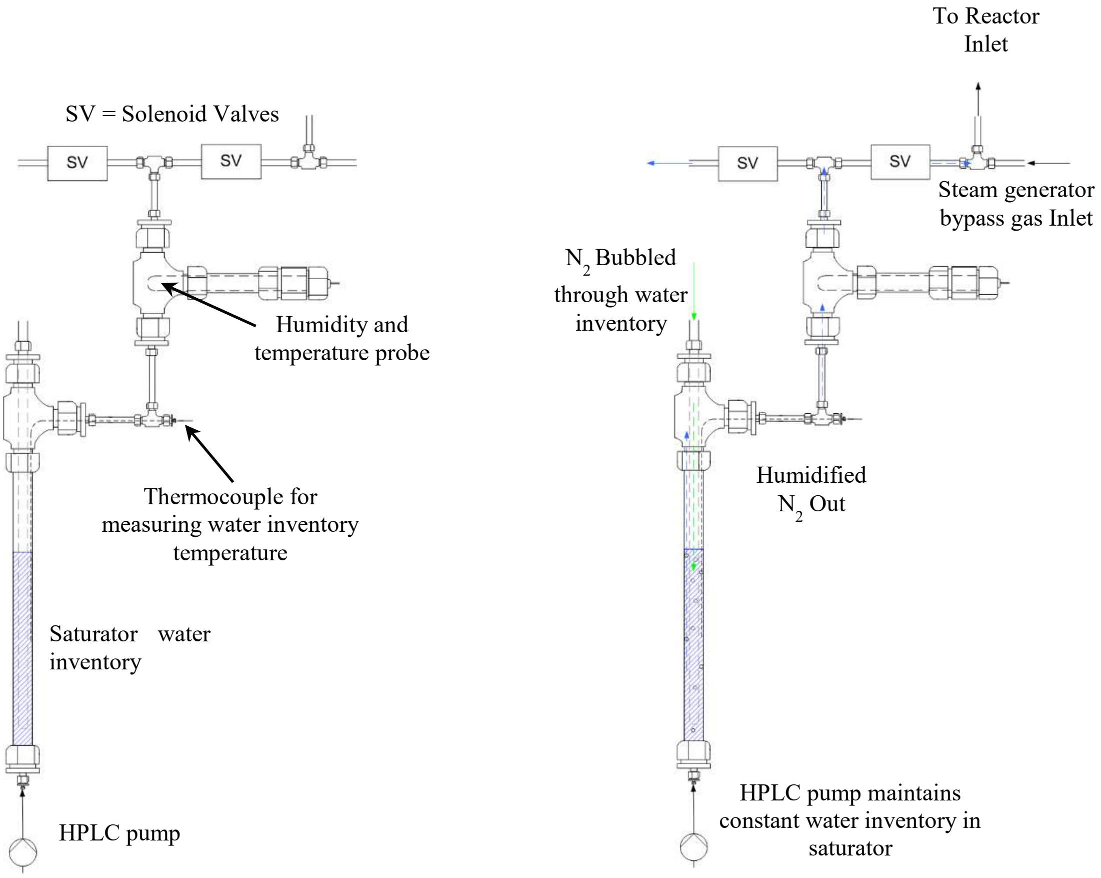

Figure B.4. Schematic of the original steam generator design showing (a) main components and (b) mode of operation.

Figure B.5 presents the average stable steam concentration measured at the inlet of the reactor over a period of 20 min as a function of the water inventory temperature. Relative errors were less than 5 % of the measured steam concentration for all parameters tested. The theoretical maximum steam concentration calculated from the saturation vapour pressure in N_2 at the steam generator temperature has also been provided for reference.

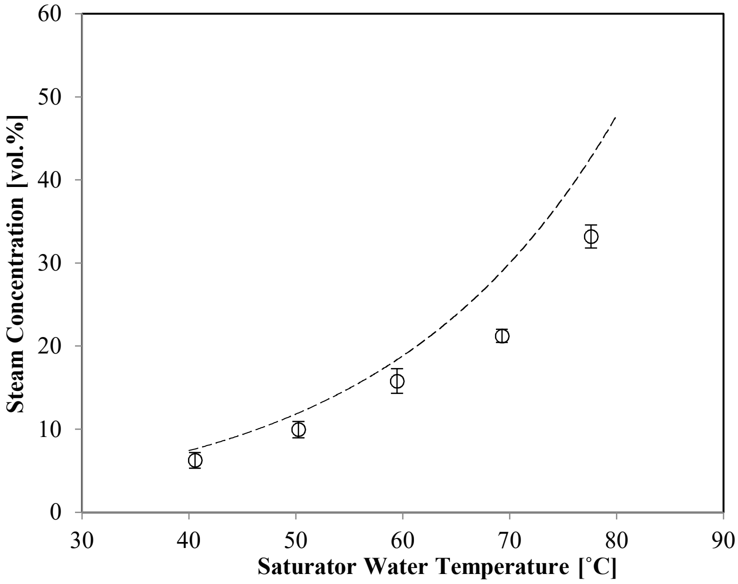

Figure B.5. Average steam concentration at the steam generator outlet (open symbols) measured over 20 minutes of continuous operation and theoretical steam concentration based on the saturation vapour pressure (dashed line) as a function of saturator water temperature with a N_2 flow of 30 $ml_N.s^{-1}$.

The steam generator operation was very stable over reasonably long periods > 20 min when the reactor was operated under steady conditions however, solid fuel feeding caused a dramatic destabilisation of the steam concentration as illustrated by figure B.6 that lasted for approximately 120 s. Destabilisation is likely the result of the solid fuel feed causing an upset of the pressure profile through the system which may have caused an ingress of some of water through the steam generator to the steam probe resulting in a wildly fluctuating signal. During the solid feed and the period immediately proceeding the solid fuel feed are the periods where measurement and control of a stable steam concentration are most important as this is the period in which steam gasification is taking place. Attempts were made to overcome this problem including reducing the feed pressure and installing a check valve after the steam generator to prevent back flow but little success was achieved. The steam generator design process was subsequently put on hold.

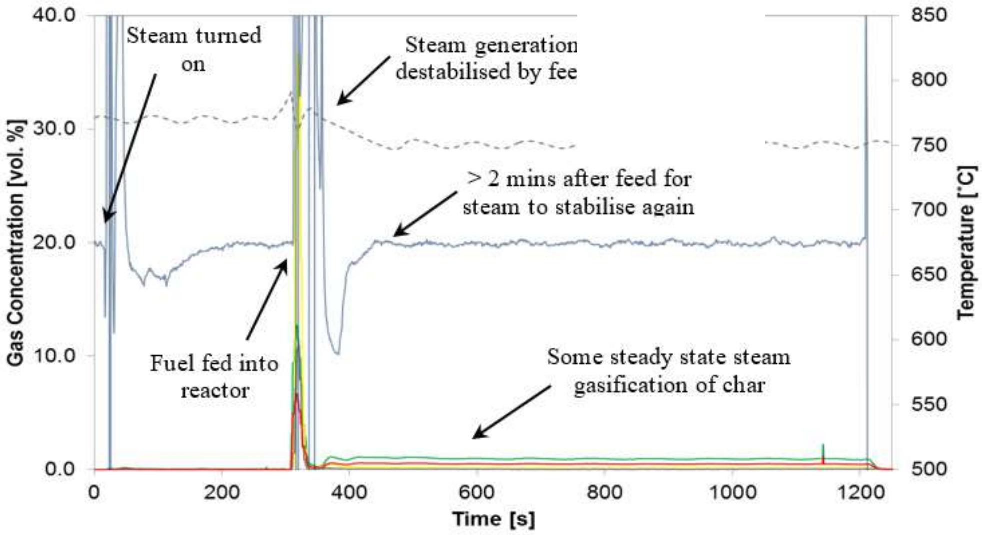

Figure B.6. Concentration profiles as a function of time for the different gas concentrations measured at the outlet and steam concentration measured at the inlet during a commissioning biomass-steam gasification commissioning experiment. <u>**Experimental parameters:**</u> ***1st stage:*** **Feed** = beech wood (1.000g, 106-150 μm), **feed weight** = 1.000 g, **inlet gas** = 20 mol.% steam, 80 mol.% N_2, **superficial velocity** = 0.1 m s^{-1} (48 ml_N s^{-1}), **inlet pressure** = 1.5 bar_a, **temperature** = 1023 K, **hold time** = 900 s. ***2nd stage***: N/A. CO_2 (——); CO (——); CH_4 (——); H_2 (——); Steam (——) temperature (----).

A new steam generator has been designed that avoids the requirement of a water inventory (fig. B.7) been developed but is yet to be tested. The steam concentration would be maintained by injecting water directly into a heated chamber via an isocratic pump. The steam concentration would be controlled via the isocratic pump flow rate. A heated chamber packed with stainless steel balls would be positioned after the water inlet pump to act as a buffer zone that and damp any fluctuations that may arise as a result of dripping water directly into the steam generator.

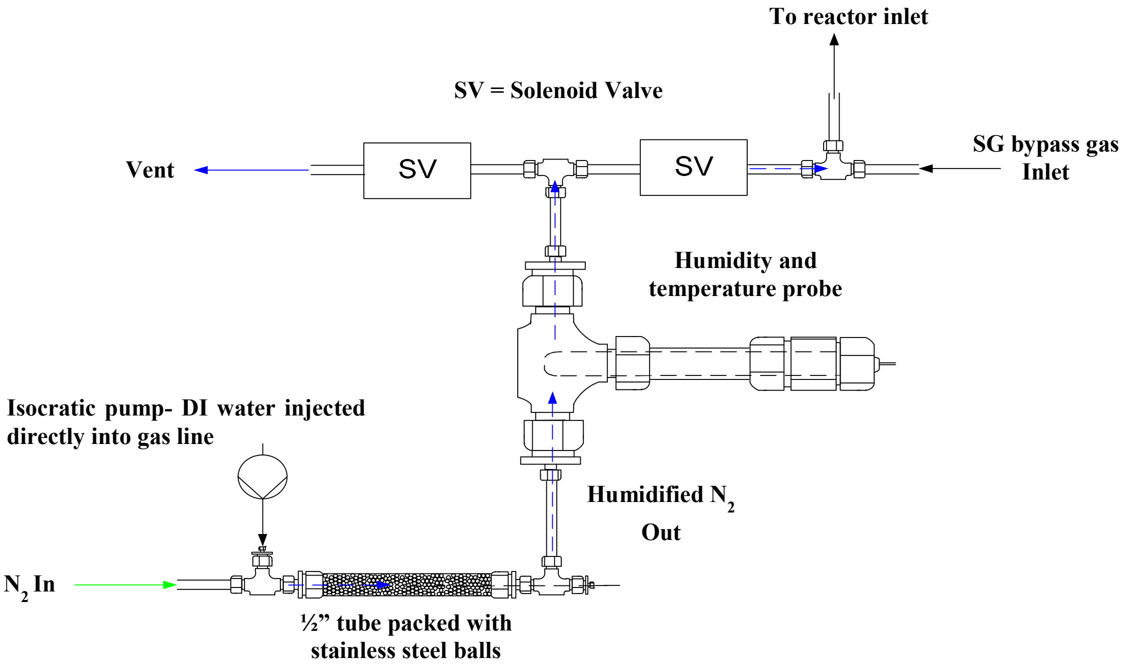

Figure B.7. Alternative steam generator design that will be implemented in the future showing both the constituent parts and mode of operation.

B.2 Tar trap design process

The initial tar trap design (fig. B.8 (a)) was based on the tar trap and moisture trap designs previously used by Spiegl (2010) and Zhang (2014) respectively. The tar trap consisted of a 450 mm stainless steel tube (½” OD) inserted through a T-piece fitting into a 500 mm stainless steel tube (1” OD) which had been capped off at the other end. The gases exiting the reactor entered the tar trap through the inner ½” tube and exited through the annulus formed between the inner ½” tube and outer 1” tube. The trap was designed to provide a void space at the base to allow for the collection of a liquid phase away from the path of the gas that might otherwise lead to the formation of a blockage, increased pressure drop through the reactor or re-evaporation of the liquid phase reducing the efficiency of the trap. The tar trap was cooled to ~ -2 °C by submerging in an ice and salt bath to condense the tars and water vapour contained in the reactor flue gas. The annulus of the trap was packed with a packing material to increase the internal surface area ensuring efficient trapping of the tars in the form of aerosol droplets. A guard tube at the exit of the trap was packed with glass wool to collect and trap any condensable vapours that were not trapped effectively in the cooled section of the trap.

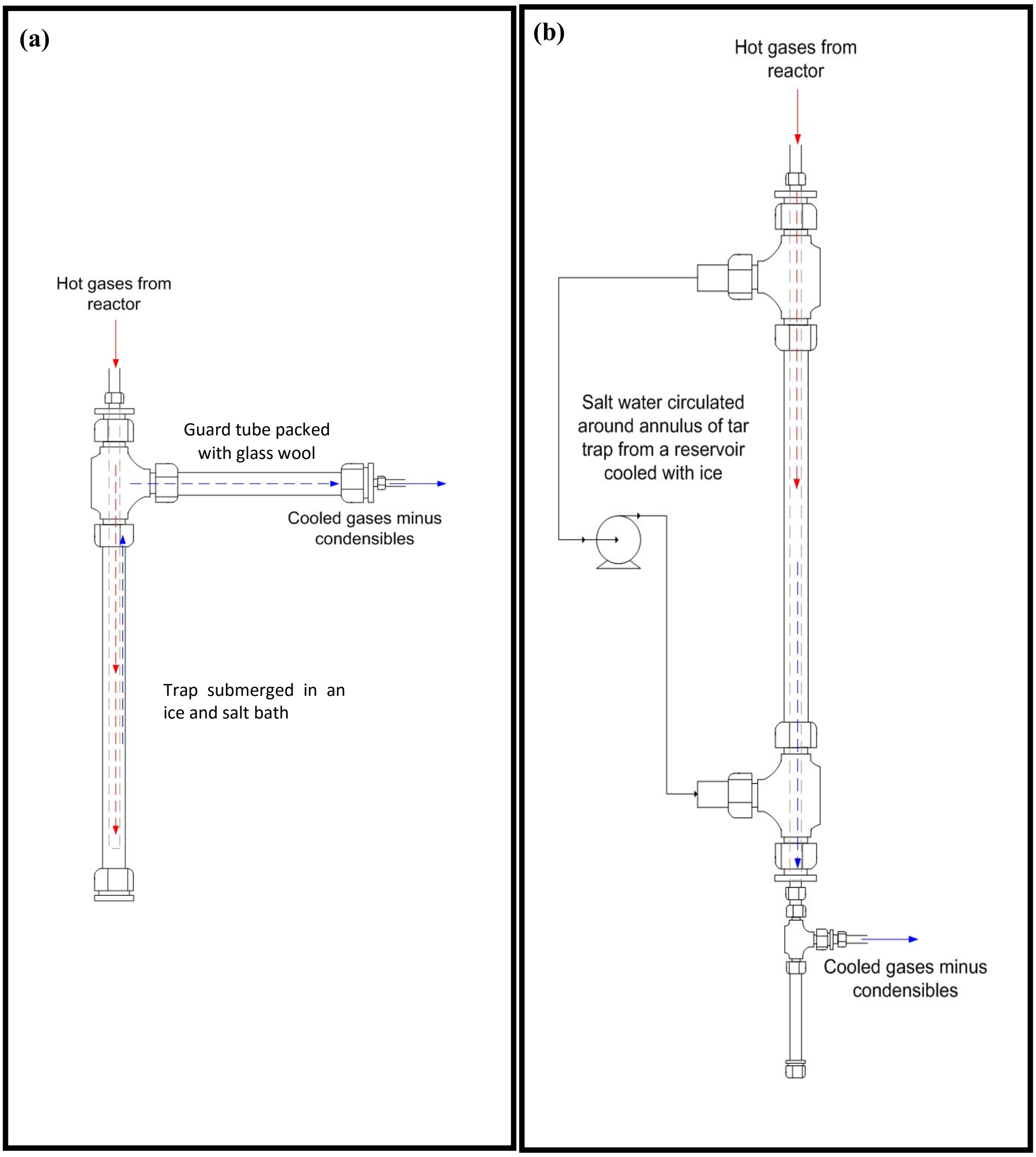

Figure B.8 Schematic of (a) initial tar trap design and (b) modified tar trap design.

Four different materials were investigated as potential packing materials for the annulus of the tar trap: (i) stainless steel wire mesh (as used for the tar trap of the original reactor and in the tar trap used by Spiegl (2010)), (ii) stainless steel ball bearings (as used in the moisture trap employed by Zhang (2014)), (iii) stainless steel wire wool and (iv) glass wool. Preliminary investigations revealed that glass wool was the most suitable packing material for the tar trap with > 95 % of the retrieved tar yield condensing in the trap and glass wool. The tar trapping efficiency of the other materials was much worse. In all cases, > 40 % of the tars were retrieved from the glass wool packing in the guard tube.

The trap design was also changed to that the annular heat-exchanger design presented in figure B.8 (b) which consisted of a 1000 mm stainless steel (½” OD) inner tube with a 1” OD outer tube connected around the outside of the ½” tube via 2 x 1” T-piece Swagelok connections. The gas exited the reactor through the internal ½” tube. The trap was cooled by pumping water (chilled to ~ -2 ˚C with ice and salt) around the annulus between outer wall of the internal ½” tube and internal wall of the external 1” tube as illustrated in the schematic provided in figure B.1 (b). The exit was loosely packed with ~ 6 g of glass wool to increase the internal surface area ensuring efficient trapping of the tars vapours in the form of aerosol droplets. The tar trap design based on an annular heat-exchanger allowed for improved heat transfer and more rapid cooling of the gases exiting the reactor and better control of the trap temperature since the cooling reservoir (ice, water and salt bath) was more accessible and easier to top up with ice. The trap was also easier and less time consuming to wash out when collecting the tar.

B.4 Tabulated results summary for experiments discussed in chapter 4

Table B1: Comparison of the pyrolysis production distribution from the slow pyrolysis of beech wood in the original single-stage reactor with the yields obtained from the slow and fast pyrolysis experiments in the new, upgraded reactor. **Original reactor:** ***1st stage***: **biomass feed**: beech wood (1.000g, 106-150 μm), **carrier gas** = He, **superficial velocity** = 0.25 $m\ s^{-1}$, **inlet pressure** = 1.5 bar_a, **heating rate** = 1 $K\ s^{-1}$, **hold temperature** = 773 K, **hold time** = 900 s. ***2nd stage***: N/A. **Upgraded reactor**: ***1st stage***: **biomass feed**: beech wood (1.000g, 106-150 μm), **carrier gas** = He, **superficial velocity** = 0.1 $m\ s^{-1}$, **inlet pressure** = 2.2 bar_a, **heating rate** = 1 $K\ s^{-1}$, **hold temperature** = 773 K, **hold time** = 600 s. ***2nd stage***: N/A.

		Percentage of initial biomass feed weight (0.100 g) ^{daf}						
		Tar	**Char (C content)***	**Char$^+$**	**CO_2**	**CO**	**CH_4**	**Mass Balance**
Slow pyrolysis, 1 $K\ s^{-1}$ (original reactor)	x̄	**36.3**	**-**	**22.6**	**4.0**	**2.5**	**0.3**	**61.7**
	Σ	0	-	21.9	0.1	0.7	0	-
	c_v [%]	0	-	97.0	2.5	28.3	0	-
Slow pyrolysis, 1 $K\ s^{-1}$ (upgraded reactor, beech wood pre-loaded)	x̄	**46.2**	**14.7**	**18.4**	**5.0**	**2.1**	**1.0**	**73.3**
	σ	3.2	1.7	-	1.6	1.3	0.4	-
	c_v [%]	7.1	11.6	-	33.1	64.0	41.2	-
Fast pyrolysis, (beech wood shot into reactor at 773 K)	x̄	**47.4**	**12.2**	**15.0**	**5.8**	**3.4**	**0.6**	**72.9**
	σ	3.5	1.1	-	1.1	0.8	0.4	-
	c_v [%]	7.5	8.8	-	20.0	24.8	55.7	-

Table B2: Pyrolysis production distributions as a function of sample feed weight from the fast pyrolysis of beech wood.

Operating parameters: ***1st stage***: **biomass feed** = beech wood (106-150 µm), **feed weight** = variable, **carrier gas** = N_2, **controlled system pressure** = 1.5 bar$_a$, **superficial velocity** = 0.25 m s^{-1}, **temperature** = 773 K, **hold time** = 600 s.

Biomass loading [g]		Percentage of initial biomass feed weight (1.000 g)^{daf}						
		Tar	Char (C content)*	Char$^+$	CO_2	CO	CH_4	Mass Balance
0.1	$\bar{x}$	**46.3**	**10.5**	**20.3**	**5.1**	**3.7**	**0.2**	**75.6**
	Σ	3.7	1.8	-	0.5	0.3	0.1	-
	c_v [%]	8.2	17.7	-	9.4	8.3	67.9	-
0.2	$\bar{x}$	**42.8**	**9.4**	**16.5**	**8.1**	**5.1**	**0.7**	**73.8**
	Σ	0.3	-	-	1.8	0.9	0.1	-
	c_v [%]	0.7	-	-	23.1	18.9	13.3	-
0.5	$\bar{x}$	**43.0**	**12.5**	**19.0**	**6.1**	**4.2**	**0.7**	**73.5**
	Σ	1.2	-	-	0.4	0.4	0.1	-
	c_v [%]	3.0	-	-	7.3	9.7	18.7	-
1.0	$\bar{x}$	**47.4**	**12.2**	**15.0**	**5.8**	**3.4**	**0.6**	**72.9**
	σ	3.5	1.1	-	1.1	0.8	0.4	-
	c_v [%]	7.5	8.8	-	20.0	24.8	55.7	-

Table B3: Pyrolysis production distributions as a function of controlled system pressure from the fast pyrolysis of beech wood.

Operating parameters: ***1st stage***: **biomass feed** = beech wood (0.100g, 106 – 150 µm), **feed weight** = variable, **carrier gas** = N_2, **controlled system pressure** = variable, **superficial velocity** = 0.25 m s^{-1}, **temperature** = 773 K, **hold time** = 600 s.

Pressure [bar$_a$]		Percentage of initial biomass feed weight (1.000 g)^{daf}						
		Tar	Char (C content)*	Char$^+$	CO_2	CO	CH_4	Mass Balance
1.5	$\bar{x}$	**46.3**	**10.5**	**20.3**	**5.1**	**3.7**	**0.2**	**75.6**
	σ	3.7	1.8	-	0.5	0.3	0.1	-
	c_v [%]	8.2	17.7	-	9.4	8.3	67.9	-
3.0	$\bar{x}$	**43.8**	**10.2**	**18.2**	**5.7**	**4.8**	**0**	**73.1**
	Σ	1.3	-	-	0.1	1.4	0	-
	c_v [%]	3.0	-	-	2.5	28.9	0	-
5.0	$\bar{x}$	**41.0**	**9.0**	**12.5**	**3.9**	**5.9**	**0**	**63.9**
	Σ	1.7	-	-	0.5	1.9	0	-
	c_v [%]	4.3	-	-	11.9	32.7	0	-

Appendix C

C.1 Tabulated results summary for experiments discussed in chapter 4

Table C1: Summary table presenting the production distribution from the fast pyrolysis of 0.100g of beech wood in different gaseous environments in the upgraded single stage reactor.

Experimental parameters*: 1st stage*: **Feed** = beech wood (106-150 µm), **Feed Weight** = variable, **Carrier gas** = variable, **Pressure** = 1.5 bar_a, **Flow rate** = 60 $ml_N\ s^{-1}$ (0.25 $m\ s^{-1}$), **Temperature** = 773 K, **Hold time** = 300 s.

Inlet Gas Composition		**Percentage of initial biomass feed weight (0.100 g)^{daf}**					
		Tar	**Char (C content)***	**Char$^+$**	**CO_2**	**CO**	**CH_4**
100 vol.% N_2	$\bar{x}$	**46.3**	**10.5**	**20.3**	**5.1**	**3.7**	**0.2**
	Σ	3.7	1.8	-	0.5	0.3	0.1
	c_v [%]	8.2	17.7	-	9.4	8.3	67.9
15 vol.% CO_2, 85 vol.% N_2	$\bar{x}$	**42.9**	**18.8**	**-**	**5.5**	**4.0**	**0.5**
	Σ	2.1	2.9	-	0.6	0.2	0.2
	c_v [%]	4.9	15.4	-	10.9	3.8	32.2
3 vol.% CO, 15 vol. % CO_2, 82 vol.% N_2	$\bar{x}$	**47.4**	**12.3**	**-**	**6.8**	**4.7**	**0.3**
	Σ	0.8	0.3	-	0.2	0.5	0.1
	c_v [%]	1.8	2.5	-	3.3	10.6	26.3

Table C.2. Summary table presenting the product distribution for the fast pyrolysis of 0.100g of beech wood in different gaseous environments in the upgraded two-stage reactor with a 2nd stage sand bed at 973 K.

Experimental parameters: ***1st stage***: **Feed** = beech wood (0.100 g, 106-150 µm), **Temperature** = 773 K, **Hold time** = 300 s, **Flow rate** = 60 $ml_N\ s^{-1}$ (0.25 $m\ s^{-1}$), **Pressure** = 1.5 bar_a. **Carrier gas:** variable; ***2nd stage***: **Bed type** = sand (0.75 g, 300-425 µm); **Temperature**: 973 K; **Flow rate**: 60 $ml_n.s^{-1}$

Experiment Identifier		**Percentage of initial biomass feed weight (0.100 g)^{daf}**			
		Tar	**CO_2**	**CO**	**CH_4**
N_2_NoBed	$\bar{x}$	**19.0**	**7.6**	**20.2**	**1.9**
	σ	0.2	0.5	0.7	0.0
	c_v [%]	1.1	6.6	3.2	0.0
N_2_Sand	$\bar{x}$	**16.4**	**5.4**	**19.1**	**2.2**
	σ	0.5	0.6	2.5	0.5
	c_v [%]	2.8	10.3	12.9	22.7
15%CO_2_Sand	$\bar{x}$	**16.1**	**8.3**	**24.8**	**2.0**
	σ	0.8	0.3	2.2	0.1
	c_v [%]	4.7	3.8	8.8	2.6
3%CO15%CO_2_Sand	$\bar{x}$	**16.7**	**10.1**	**23.3**	**2.2**
	σ	0	0.5	0.8	0.15
	c_v [%]	0	5.0	3.4	7.0

Table C.3. Summary table presenting the product distribution from the different simulated CLC experiments in which the 100Fe(S) OC material is exposed to volatile pyrolysis products during the 3rd cycle reduction phase at 973 K.

Experimental parameters: **1st stage**: **Feed** = beech wood (0.100 g, 106-150 µm), **Temperature** = 773 K, **Flow rate** = 60 ml_N s^{-1} (0.25 m s^{-1}), **Pressure** = 1.5 bar_a, **Carrier gas**: variable; **Biomass feed cycle no.** = 3; ***2nd stage*****: Oxygen Carrier** = 100Fe(S) (5 mg, 150-212 µm), **Reaction** = Fe_2O_3 → Fe_3O_4, **Oxidation State of OC** = variable, **Temperature**: 973 K, **Flow rate**: 60 ml_N s^{-1} (0.40 m s^{-1}), **Total Number of CLC Cycles** = 5.

Experiment Identifier		**Percentage of initial biomass feed weight (0.100 g)^{daf}**			
		Tar	**CO_2**	**CO**	**CH_4**
N_2 (PreRed)	$\bar{x}$	**10.1**	**40.9**	**20.6**	**3.8**
	σ	1.6	2.6	0	1.3
	c_v **[%]**	15.8	6.4	0	33.3
N_2 (Post Red)	$\bar{x}$	**11.1**	**16.9**	**29.7**	**3.0**
	σ	0.1	2.1	2.2	0.5
	c_v **[%]**	0.9	12.2	7.3	15.3
15% CO_2 (PreRed)	$\bar{x}$	**11.8**	**37.1**	**24.9**	**3.6**
	σ	1.3	0.1	0.1	0.5
	c_v **[%]**	10.6	0.3	0.4	12.7
15% CO_2 (PostRed)	$\bar{x}$	**11.0**	**19.7**	**27.5**	**2.9**
	σ	1.4	0.3	2.7	0.3
	c_v **[%]**	12.7	1.5	9.8	8.8
3% CO 15% CO_2 (InRed)	$\bar{x}$	**10.2**	**18.3**	**30.0**	**4.1**
	σ	0.4	1.6	3.7	0.8
	c_v **[%]**	3.4	8.5	12.2	18.5

Table C.4. Summary table presenting maximum rate of reduction (Fe_2O_3 → Fe_3O_4) with CO as a function of cycle number for the simulated CLC experiments in which the 100Fe(S) OC material was exposed to volatile pyrolysis products during the 3rd cycle reduction phase at 973 K.

Experimental parameters: ***1st stage***: **Feed** = beech wood (0.100 g, 106-150 μm), **Temperature** = 773 K, **Flow rate** = 60 $\mathrm{ml_N}$ s^{-1} (0.25 m s^{-1}), **Carrier gas** = variable, **Biomass feed cycle no.** = 3, ***2nd stage***: **Oxygen Carrier** = 100Fe(S) (0.75 g, 300-425 μm), **Reaction** = $Fe_2O_3 \rightarrow Fe_3O_4$, **Oxidation State of OC** = variable, **Temperature** = 973 K, **Flow rate** = 60 $\mathrm{ml_N}$ s^{-1} (0.40 m s^{-1}), **Total Number of CLC Cycles**: 5.

Experiment Identifier		**Peak Rate (r') x 10^5 [mol s^{-1} g^{-1}]**			
		Cycle 2	**Cycle 3**	**Cycle 4**	**Cycle 5**
Gaseous reduction only (no biomass feed)	$\bar{x}$	**5.89**	**6.14**	**6.29**	**6.28**
	σ	0.59	0.34	0.33	0.17
	c_v [%]	9.97	5.60	5.27	2.65
N_2 (PreRed)	$\bar{x}$	**5.45**	**-**	**6.39**	**7.00**
	σ	0.53	-	-	-
	c_v [%]	9.66	-	-	-
N_2 (PostRed)	$\bar{x}$	**5.47**	**5.85**	**6.96**	**7.77**
	σ	0.12	0.39	-	-
	c_v [%]	2.21	6.69	-	-
15% CO_2 (PreRed)	$\bar{x}$	**6.13**	**-**	**7.10**	**7.15**
	σ	0.26	-	-	-
	c_v [%]	4.24	-	-	-
15% CO_2 (PostRed)	$\bar{x}$	**5.91**	**6.28**	**6.90**	**7.22**
	σ	0.08	0.02	-	-
	c_v [%]	1.34	0.26	-	-
3% CO 15% CO_2 (InRed)	$\bar{x}$	**5.52**	**-**	**6.42**	**6.84**
	σ	0.21	-	-	-
	c_v [%]	3.86	-	-	-

Table C.5. Summary table presenting the product distribution from the different simulated CLC experiments in which the 60Fe40Al(SAB) OC material is exposed to volatile pyrolysis products during the 3rd cycle reduction phase at 973 K.

Experimental parameters: **1st stage**: **Feed** = beech wood (0.100 g, 106-150 μm), **Temperature** = 773 K, **Flow rate** = 60 ml$_N$ s^{-1} (0.25 m s^{-1}), **Pressure** = 1.5 bar$_a$, **Carrier gas**: variable; **Biomass feed cycle no.** = 3; ***2nd stage*****: Oxygen Carrier** = 60Fe40Al(SAB) (5 mg, 150-212 μm), **Reaction =** $Fe_2O_3 \rightarrow Fe_3O_4$**, Oxidation State of OC =** variable**, Temperature**: 973 K, **Flow rate**: 60 ml$_N$ s^{-1} (0.40 m s^{-1}), **Total Number of CLC Cycles** = 5.

Experiment Identifier		Percentage of initial biomass feed weight (0.100 g)^{daf} Tar	CO_2	CO	CH_4
N$_2$ (PreRed)	$\bar{x}$	**8.4**	**40.2**	**18.2**	**2.7**
	σ	1.6	4.3	2.5	0.9
	c_v **[%]**	19.0	10.8	13.6	33.1
N$_2$ (PostRed)	$\bar{x}$	**5.8**	**19.9**	**21.7**	**3.1**
	σ	2.9	3.4	4.2	0.4
	c_v **[%]**	50.2	17.2	19.3	12.6
15% CO$_2$ (PreRed)	$\bar{x}$	**4.7**	**44.7**	**18.7**	**3.2**
	σ	1.0	7.2	6.0	1.6
	c_v **[%]**	20.9	16.0	32.1	48.6
15% CO$_2$ (PostRed)	$\bar{x}$	**5.4**	**16.1**	**31.1**	**2.9**
	σ	-	4.1	0.4	0.4
	c_v **[%]**	-	25.4	1.3	13.8
3% CO 15% CO$_2$ (InRed)	$\bar{x}$	**8.4**	**17.5**	**26.8**	**3.5**
	σ	2.6	3.2	0.2	0.2
	c_v **[%]**	30.2	18.1	0.6	6.1

Table C.6. Summary table presenting maximum rate of reduction ($Fe_2O_3 \rightarrow Fe_3O_4$) with CO as a function of cycle number for the simulated CLC experiments in which the 60Fe40Al(SAB) OC material was exposed to volatile pyrolysis products during the 3rd cycle reduction phase at 973 K.

Experimental parameters: ***1st stage***: **Feed** = beech wood (0.100 g, 106-150 μm), **Temperature** = 773 K, **Flow rate** = 60 $ml_N\ s^{-1}$ (0.25 $m\ s^{-1}$), **Carrier gas =** variable, **Biomass feed cycle no.** = 3, ***2nd stage*****: Oxygen Carrier** = 60Fe40Al(SAB) (0.75 g, 300-425 μm), **Reaction** = $Fe_2O_3 \rightarrow Fe_3O_4$**, Oxidation State of OC =** variable**, Temperature** = 973 K, **Flow rate** = 60 $ml_N\ s^{-1}$ (0.40 $m\ s^{-1}$), **Total Number of CLC Cycles**: 5.

		Peak Rate (r') x 10^5 [mol s^{-1} g^{-1}]			
Experiment Identifier		**Cycle 2**	**Cycle 3**	**Cycle 4**	**Cycle 5**
Gaseous reduction only (no biomass feed)	$\bar{x}$	**7.09**	**7.28**	**7.49**	**7.44**
	σ	1.36	1.65	1.63	1.75
	c_v [%]	19.2	22.6	21.7	23.5
N_2 (PreRed)	$\bar{x}$	**7.21**	**-**	**7.07**	**7.98**
	σ	3.16	-	0.43	1.56
	c_v [%]	43.8	-	6.1	19.5
N_2 (PostRed)	$\bar{x}$	**6.84**	**7.00**	**5.20**	**7.02**
	σ	0.84	0.80	-	-
	c_v [%]	12.2	11.5	-	-
15% CO_2 (PreRed)	$\bar{x}$	**6.53**	**-**	**5.37**	**5.20**
	σ	1.70	-	0.68	0.51
	c_v [%]	26.0	-	12.6	9.9
15% CO_2 (PostRed)	$\bar{x}$	**7.06**	**6.56**	**6.57**	**5.83**
	σ	1.14	0.93	-	-
	c_v [%]	16.1	14.2	-	-
3% CO 15% CO_2 (InRed)	$\bar{x}$	**6.23**	**-**	**4.35**	**5.06**
	σ	0.97	-	-	-
	c_v [%]	15.6	-	-	-

C.2 SEC and UVF Analyses of the tars recovered after exposure to the 100Fe(S) and 60Fe40Al(SAB) OC beds in the 2-stagehot rod reactor under an atmosphere of 15 mol.% CO_2, 85 mol.% N_2.

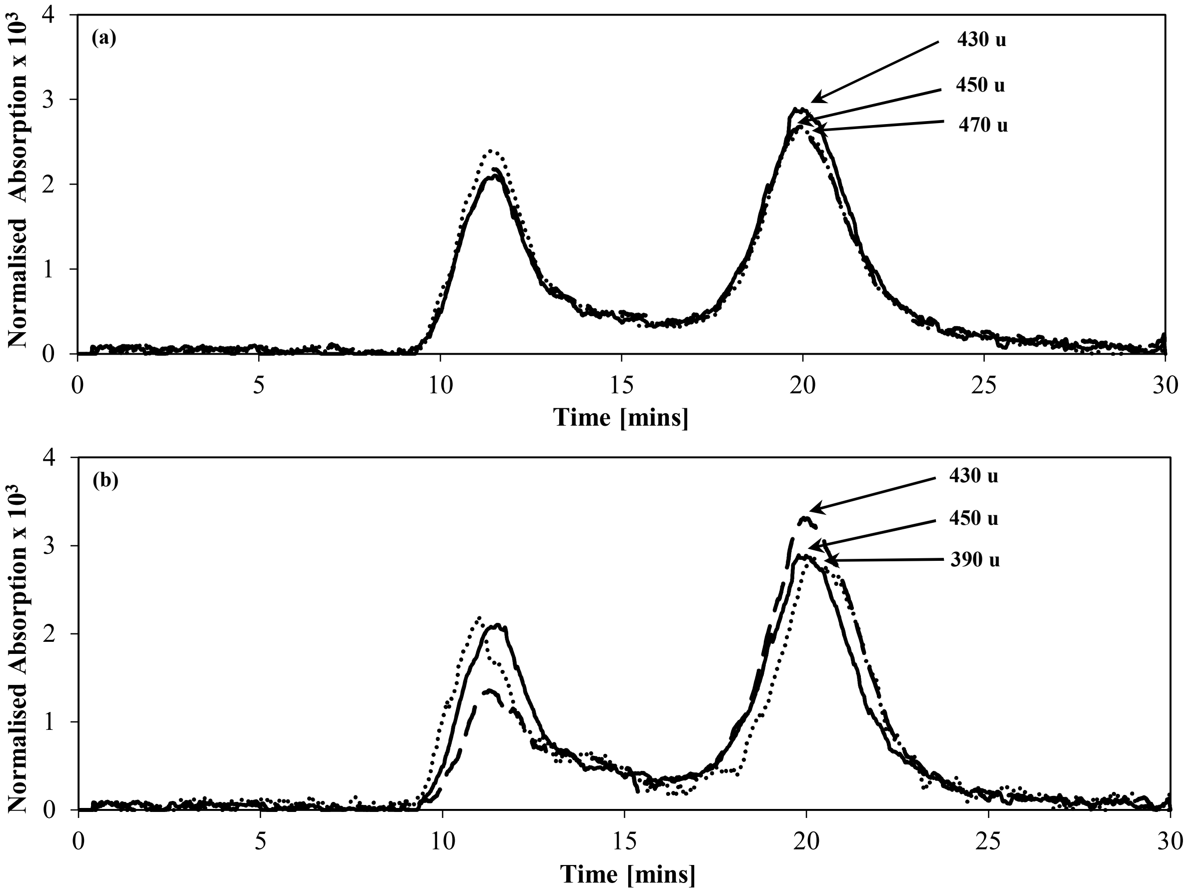

Figure C.1. SEC analyses of the tars recovered from the fast pyrolysis of 0.10 g of beech wood in the two-stage reactor loaded with (a) the 100Fe(S) OC material and (b) 60Fe40Al(SAC) OC material in both their oxidised and reduced forms under an atmosphere of 15 mol.% CO_2, balance N_2. **Experimental parameters:** ***1st stage***: **Feed** = beech wood (0.100 g, 106-150 µm); **Carrier gas** = 15 mol.% CO_2, 85 mol.% N_2, **Pressure** = 1.5 bar$_a$, **Flow rate** = 60 ml$_N$ s^{-1} (0.25 m s^{-1}), **Temperature** = 773 K, **Hold time** = 300 s. **Biomass feed cycle no.** = 3; ***2nd stage***: **Oxygen Carrier** = (a) 100Fe(S) and (b) 60Fe40Al(SAB) (5 mg, 300-425 µm); **Oxidation state** = variable; **Reaction** = $Fe_2O_3 \rightarrow Fe_3O_4$; **Temperature** = 973 K; **Flow rate** = 60 ml$_N$ s^{-1} (0.40 m s^{-1}); **Total number of CLC cycles** = 5. Sand (——); 'PreRed' conditions (- - -); 'PostRed' conditions (·········).

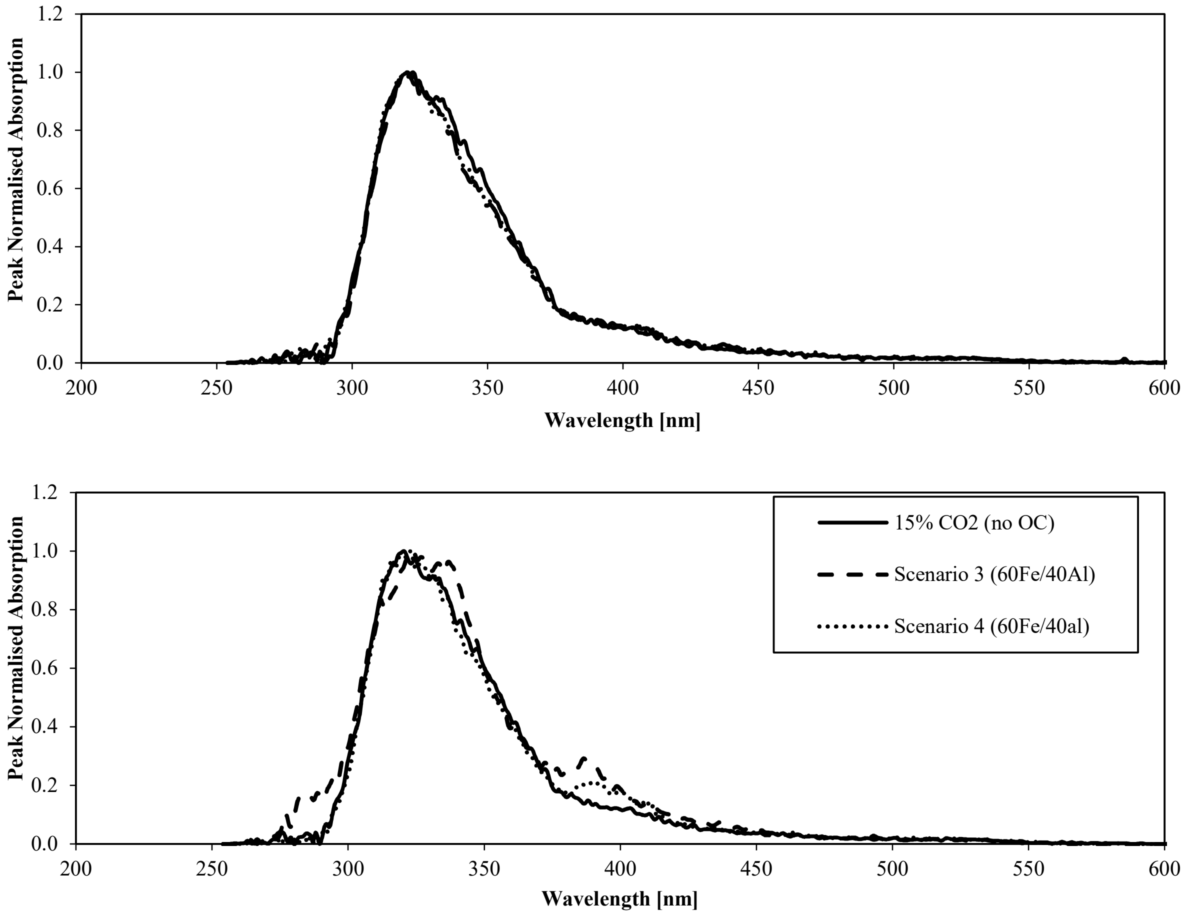

Figure C.2. UVF spectra of the tars recovered from the fast pyrolysis of 0.100 g of beech wood in the two-stage reactor loaded with (a) the 100Fe(S) OC material and (b) 60Fe40Al(SAC) OC material in both their oxidised and reduced forms under an atmosphere of 15 mol.% CO_2, balanace N_2. **<u>Experimental parameters:</u> 1st stage**: **Feed** = beech wood (0.100 g, 106-150 µm); **Carrier gas** = 15 mol.% CO_2, 85 mol.% N_2, **Pressure** = 1.5 bar$_a$, **Flow rate** = 60 ml$_N$ s^{-1} (0.25 m s^{-1}), **Temperature** = 773 K, **Hold time** = 300 s. **Biomass feed cycle no.** = 3; **2nd stage: Oxygen Carrier** = (a) 100Fe(S) and (b) 60Fe40Al(SAB) (5 mg, 300-425 µm); **Oxidation state** = variable; **Reaction** = $Fe_2O_3 \rightarrow Fe_3O_4$; **Temperature** = 973 K; **Flow rate** = 60 ml$_N$ s^{-1} (0.40 m s^{-1}); **Total number of CLC cycles** = 5. Sand (——); 'PreRed' conditions (- - -); 'PostRed' conditions (·········).